In-Situ Measurement of the Roller Bearing Inlet Meniscus Using Ultrasonic Spectroscopy

William A. Gray

A thesis submitted in partial fulfilment of the requirements for the degree of

Doctor of Philosophy

The University of Sheffield

Faculty of Engineering

Department of Mechanical Engineering

Submission Date

Autumn 2023

Acknowledgements

Firstly, I would like to thank my supervisor Professor Rob Dwyer-Joyce for the opportunity to complete this PhD. The people I have met, exciting work I have been involved in, places I have visited and doors of opportunity opened to me are all possible because of this, and I will be forever grateful for your trust and support in me.

I would like to thank the iT-CDT for hosting my project and by extension the EPSRC for partially funding my work, and all of Cohort 5 with whom I started this journey with. I wish you every success in the future. In particular, I would like to thank Dr. Arron Bird for your friendship over the past few years; for always being there to bounce ideas off and run theories by; it would not have been the same without you.

I would like to thank the Timken Co. for partly sponsoring my work, and especially to Dr. Bill Hannon and Dr. Wei Dai for their expertise, insights and encouragement of my work. To Dave and Luke, thank you for all your help with rig tinkering and experimental set-up, your expertise were always appreciated. A special mention to Dr. Gary Nicholas who from the start has helped me with all aspects of my work, motivated me to demand more of myself and driven me to be a better researcher.

To my family, thank you for all your love, faith and words of encouragement. You were my biggest cheerleaders and all the motivation I needed. And finally, to my Grandfather Rodger Poxon. I cannot put into words how much you inspired me, and fostered in me a curiosity and imagination to tackle the seemingly unfeasible. Without your love and guidance I would not be the man I am today.

Abstract

An inadequate lubricant volume at rolling contact inlets, termed contact starvation, leads to a reduced separation between opposing moving surfaces. Starvation has been linked with various failure mechanisms and can affect rolling element bearings of any size. The level of starvation can be defined by the length of the inlet meniscus, the position where lubricant films from the raceway and roller join at the inlet. Therefore, an in-situ meniscus measuring tool is key for future bearing condition monitoring systems. Currently, no other technology is capable of taking a meniscus measurement from a field bearing.

The inlet meniscus is thin, occurs over a small area, and is hidden deep within the working components of the bearing, meaning such an in-situ measurement has been previously impossible. Ultrasound, which requires no direct access to the contact and has been proven sensitive to films within the micron range in which the meniscus exists, and has been highlighted as a potential technology to take such a measurement.

In this thesis, a novel ultrasonic thin film measurement technique, capable of measuring oil and grease film thickness in-situ on a rolling element bearing raceway, has been developed. The method involves measuring the resonant frequency of the free surface film on the raceway, and using a calibrated acoustic velocity-temperature relationship, calculating the film thickness. From the measured raceway thickness and theoretical roller film, a model was created to determine the meniscus length, and thus starvation level.

The measurement technique was shown to be repeatable in a full scale wind turbine gearbox bearing test rig with both oil and grease lubrication at a range of loads, speeds and over an extended time period. The shape of the film leading into the contact inlet was generally observed to be non-uniform across the rolling axis, with the inlet film thinner at the axis centre and thicker towards the raceway edges to create a 'U' shape

distribution. This shows contacts have the potential to be fully flooded and starved at the same time, due to localised lubricant inlet conditions.

Although starvation was not repeatedly recreated in this work, for high viscosity oil lubricated contacts, a pre-starvation pattern was identified, which could be used as an indicator to future contact starvation and premature wear. The calculated starvation ratio during this pattern was of a similar magnitude to alternative starvation work in a deep groove rolling element bearing. When lubricated with grease, evidence of the channelling and clearing sub-phases of churn were observed in-situ. An inlet pattern similar to previous grease starvation and reflow contact patterns was seen, highlighting the dependence of contact separation on the inlet conditions.

A qualitative measurement of roller skew was also performed, based on the cage speed and time interval between contact passes. Sudden step changes in skew magnitude, termed skew impulses, were observed at steady state conditions, but were more common at higher bearing speeds. Results show there is a relationship between skew magnitude and lubrication state.

Contents

1 Introduction **1**
1.1 Problem Statement 2
1.1.1 The Impact of Bearing Starvation 3
1.1.1.1 Case Study: Wind Turbine Bearing Failure 4
1.2 Project Aim and Objectives 6
1.3 Thesis Layout 7

2 Rolling Element Bearings and Bearing Lubrication **11**
2.1 Roller Bearing Purpose 11
2.2 Cylindrical Roller Bearings 12
2.2.1 Cylindrical Roller Contact Mechanics 13
2.3 The Purpose of Lubrication 14
2.4 Oil lubrication 15
2.4.1 Types of Lubricating Oils 15
2.4.1.1 Mineral Oils 16
2.4.1.2 Synthetic Oils 16
2.4.2 Oil additives 16
2.5 Elastohydrodynamic Lubrication Theory 17
2.6 Grease Lubrication 18
2.6.1 Building Blocks of Grease 20
2.6.1.1 Base Oil 20
2.6.1.2 Thickener 20
2.6.1.3 Additives 20
2.6.2 Grease Churning 21
2.6.3 Oil Bleed 24
2.6.4 Film Thickness of Grease Lubricated Contacts 26
2.6.4.1 Grease Thickness at Ultra-Low Speed 28
2.7 Bearing Failures 29

2.8 Conclusion 30

3 The Principles of Ultrasound **32**

3.1 Ultrasonic Wave Propagation 32

3.1.1 Acoustic Velocity 33

3.1.2 Attenuation 34

3.2 Ultrasonic Wave Interaction with a Boundary 34

3.2.1 Time of Flight 36

3.2.2 Spring Model 38

3.2.3 Resonance Approach 40

3.3 Generation of Ultrasound 45

3.3.1 Piezoelectric Effect 45

3.3.2 Piezoelectric Elements 45

3.3.3 Huygen's Principle and the Near Field Effect 45

3.4 Measurement Referencing 47

3.5 Conclusion 49

4 Literature Review **50**

4.1 The Lubricant Inlet Meniscus 50

4.2 Starvation 51

4.2.1 Oil Starvation 51

4.2.2 Grease Starvation 56

4.2.3 Zero-Reverse Flow Boundary Condition 59

4.2.4 Relationship Between Inlet Film Thickness and Starvation . . 60

4.3 The Lubricant Outlet Meniscus 64

4.3.1 Rupture Ratio 64

4.4 In-situ Tests 65

4.5 Ultrasonic Thin Film Measurements 69

4.5.1 Ultrasonic Resonances Measurements 69

4.5.1.1 Unconstrained Films 70

4.5.1.2 Trapped Films 72

4.5.2 Bearing Spring Model Measurements 73

4.5.3 Technology Limitations 74

4.6 Roller Skew 75

4.7 Conclusion 77

5 Experimental Methods and Approaches **79**
5.1 Full-Scale Cylindrical Roller Bearing Test Rig 79
5.1.1 Bearing Lubricants 83
5.1.2 Bearing Test Matrix 83
5.2 Ultrasonic Hardware 85
5.2.1 Film-Measurement-System 85
5.2.2 Picoscope-Opmux System 86
5.3 Fundamental Data Processing 87
5.3.1 Signal Manipulation 88
5.3.1.1 Windowing 90
5.3.1.2 Zero-Padding 90
5.3.2 Calculating Reflection Coefficient 90
5.3.3 Frequency Bandwidth 91
5.4 Bearing Referencing 91
5.4.1 Air Reference 92
5.4.2 Thick Film Reference 92
5.4.3 Live Modal Reference 92
5.5 Single Frequency Reflection Coefficient Bearing Measurements 94
5.6 Influences on the Minimum Reflection Coefficient 97
5.6.1 Lubricant Presence 97
5.6.2 Lubricant Film Thickness 98
5.6.3 Contact Load 99
5.6.3.1 No Film Present 99
5.6.3.2 Lubricated Contact 100
5.6.3.3 Contact size 100
5.6.4 Finite Sensor Size 100
5.6.4.1 2-D Elastohydrodynamic Lubrication Model 101
5.7 Conclusion 105

6 Experimental Measurement of Roller Skew **107**
6.1 Impact of Roller Skew 107
6.2 Calculating Roller Skew 108
6.2.1 Calculating Roller Velocity 109
6.2.2 Calculating Contact Time 111
6.2.3 Calculating Skew Angle 112
6.3 Results 113

6.3.1 Short Duration Oil Tests 113
6.3.2 Long Duration Oil Tests 115
6.3.3 Grease Churn Results 118
6.4 Discussion 124
6.5 Conclusion 126

7 Validation of the Film Thickness - Resonant Frequency Relationship 128
7.1 Preliminary Free-Film Oil Resonance Validation 128
7.1.1 Effect of Echo Number 132
7.2 KOVOT Test Rig Design 135
7.2.1 Rig Commissioning 136
7.2.2 Ultrasonic Instrumentation 139
7.3 Experimental Method 140
7.3.1 Oil Experiments 140
7.3.2 Grease Experiments 143
7.4 Oil Film Analysis 146
7.4.1 Oil Acoustic Velocity Calibration 146
7.4.2 Oil Film Results 149
7.5 Grease Films 154
7.5.1 Grease Acoustic Velocity Calibration 154
7.5.2 Resonance Amplitude Pattern 160
7.6 Measurement Limitations, Interval and Uncertainty 162
7.6.1 Minimum Detectable Film Thickness 164
7.6.2 Maximum Detectable Film Thickness 165
7.6.3 Measurement Interval 165
7.7 Conclusion 166

8 Scouting for the Entry and Exit Film of a Cylindrical Roller Contact 168
8.1 Scouting for the Resonant Frequencies of a Raceway Film 168
8.1.1 Experiential Methodology 169
8.1.2 Ultrasonic Test Equipment 170
8.2 Piezo Element Frequency Response 170
8.2.1 Spectral Analysis of a Single Roller Pass 172
8.2.2 Comparison of Film Patterns Between Sensors 177
8.2.3 Qualitative Analysis of Speed and Load on the Raceway Film 179
8.3 Conclusion 184

9 Measurement Method for the Inner Raceway Film 186
9.1 Instrumentation of the Inner Raceway 186
9.2 Reflection Pattern Discretisation 187
9.2.1 Detecting a Reference Contact 190
9.2.2 Cross-Correlating the Reflection Pattern 191
9.2.3 Indexing Roller Passes 192
9.3 Determining the Raceway Film Thickness 192
9.3.1 Amplitude of In-Situ Resonances 192
9.3.2 Detecting Resonant Frequencies 194
9.3.3 Measured Resonant Frequency Drift 195
9.3.4 Visualising the Raceway Film 196
9.4 Calculating the Position of the Inlet Meniscus 199
9.4.1 Defining Contact Starvation 199
9.4.2 The Volume Fill Model 202
9.4.3 Volume Fill Model Improvement Parameters 204
9.4.3.1 Roller and Raceway Films 205
9.4.3.2 Bearing Cylinder Compression and Separation 206
9.4.3.3 Inclusion of Contact Compression and Raceway Film 206
9.4.4 Volume Fill Model Assumptions 208
9.5 Conclusion 209

10 Measurement of the Lubricant Meniscus Across the Rolling Axis 211
10.1 Oil Lubricated Bearing Results 211
10.1.1 Cross-Axial Inlet Film Shape 211
10.1.2 Localised Film Deviations 218
10.1.3 Mean Frontal Shape Change 219
10.1.4 Starvation Ratio 222
10.1.4.1 Singular Starved Contact 226
10.1.4.2 Bearing Stalling 228
10.1.5 Discussion 229
10.2 Grease Lubricated Bearing Results 230
10.2.1 Starvation Ratio 240
10.2.2 Discussion 242
10.3 A Model of Cylindrical Rolling Element Bearing Lubrication 244
10.3.1 Calculating Critical Raceway Films 244
10.3.2 Calculating Critical Bearing Loads 247

10.4 Conclusion 248
10.4.1 Oil Lubricated Bearing 248
10.4.2 Grease Lubricated Bearing 249
10.4.3 Lubrication Model 251

11 Discussion **252**
11.1 General Discussion on Thesis Trends 252
11.1.1 Skew Measurements 252
11.1.2 Relationship Between Inlet Film and Skew 253
11.1.3 Detecting Starvation 254
11.2 Guidance to Industry 256
11.3 Application of Technology to Other Bearings 257

12 Conclusions **259**
12.1 Thesis Motivation 259
12.2 Main Conclusions of Work 260
12.2.1 Validation Measurement of Lubricant Resonant Frequencies . 260
12.2.2 Presence of Resonances in Bearing Raceway Films 261
12.2.3 Measuring the Raceway Film Thickness 261
12.2.4 Raceway Lubricant Flow 262
12.2.5 Calculated Meniscus Position and Starvation Ratio 263
12.3 Novelty Statement 264
12.4 Future Work 265

A Appendix **268**
A.1 Resonance Detection Script 268

References **270**

List of Figures

1.1 Stribeck Curve . . . 2
1.2 UK Wind Energy Trends . . . 4
1.3 Wind turbine mean failure rate and downtime per sub-assembly failure 5

2.1 Live Modal Reference . . . 12
2.2 Cylindrical Roller Bearing Configuration Schematics . . . 13
2.3 Contributions of oil, thickener and additives to a lubricating grease . 19
2.4 Schematic of lubricant phases within a grease's lifetime . . . 22
2.5 Yield stress vs. critical energy during greased bearing operation . . . 23
2.6 Relative film thickness increase of bleed-oil compared with base oil . . 25
2.7 Film thickness vs. speed trend for grease and base oil past the ultra-low speed transition point . . . 28
2.8 Grease transition speed change with increasing temperature . . . 29
2.9 Examples of failed bearings of which improper lubrication can contribute towards . . . 30

3.1 Propagation of a longitudinal ultrasonic wave . . . 33
3.2 Pressure wave interaction with a single boundary and double boundary in (a) and (b) respectively . . . 35
3.3 Time delay between first and second reflections from an unconstrained oil film which is measurable via the TOF approach . . . 37
3.4 Visualisation of the ultrasonic spring model. Case (a) fully separated contact and case (b) mixed lubrication . . . 40
3.5 Model of resonance response at different layer thicknesses . . . 42
3.6 Construction of a plane wave front from numerous spherical wave sources 46
3.7 Schematics of beam spread from piezoelectric transducer . . . 46
3.8 Comparison of film thickness calculated via the resonance method for various film thicknesses and surface finishes . . . 48

4.1 Comparison of Meniscus Length When Fully Flooded and Starved . . 51

4.2 Starved Contact Dimensions 52
4.3 Relationship between required inlet meniscus length to achieve increasing fully flooded film thicknesses 53
4.4 Impact of meniscus length on minimum and maximum film thickness and the magnitude and position of the outlet pressure spike 54
4.5 Point Contact film thickness with varying inlet conditions 55
4.6 Transition from fully flooded to starved EHL pattern in ball-on-disc test 56
4.7 Oil bearing starvation pattern with increasing entrainment speed . . . 57
4.8 Relative film thickness of grease over-rolled at three different speeds showing three zones of lubrication 57
4.9 Measured film thickness at inner and outer raceway contact for greases and their constituent base oils under a range of speeds 59
4.10 Comparison of experimental and numerical film thickness at the centre of an EHL point contact 61
4.11 Comparison of experimental and modelled film thickness across the circumferential axis of a spherical roller inner raceway after various times 62
4.12 Schematic of the film rupture at the outlet of a contact, with a film adhering to both the roller and raceway 64
4.13 Experimental and CFD modelling approach to observing oil flow within a transparent bearing 66
4.14 In-situ measurement of the rolling bearing inlet profile change showing the onset and progression of starvation 68
4.15 Measured condensing film thickness of n-pentane using the ultrasonic resonance method 71
4.16 Comparison of lubricant reflow time with increasing viscosity oil . . . 74
4.17 Schematic of roller skew in a cylindrical roller bearing 75

5.1 Schematic and picture of the full scale cylindrical roller bearing test rig 80
5.2 Instrumented raceway linked with FMS system 82
5.3 Schematic of the laptop-PicoScope-Opmux ultrasonic hardware system used for laboratory bench-top tests 86
5.4 Example of multiple ultrasonic reflections from a single interface . . . 87
5.5 Reflection amplitude dip due to passing of a roller over the sensor measurement area 88

5.6 (a) Sample recorded reflections from an oil film and an air reference (b) reflections in the frequency domain (c) calculated reflection coefficient from Equation 3.28; the blue shaded region again shows a typical usable bandwidth 89
5.7 Comparison of signal amplitude within different bandwidth limits . . 91
5.8 Schematic of the naturally occurring steel-air boundary that exists within the bearing during operation 93
5.9 Schematic of how the live modal reference is manufactured from all signals within a data set 94
5.10 Rolling element bearing ultrasonic reflection pattern discretisation into three areas: inlet, outlet and contact 95
5.11 Schematic of the complex wave interference which leads to reflection spikes 96
5.12 Increasing lubricant film thickness affect on contact reflection coefficient with 98
5.13 Affect on reflection coefficient at a single frequency with increasing film thickness 99
5.14 Convergence study of the 2-D EHL model showing at least 244 UTR nodes are required for model convergence 103
5.15 (a) Theoretical film thickness through an EHL line contact (b) the theoretical Reflection Coefficient via the Spring Model 104
5.16 Results of EHL 2-D model for (a) VG320 and (b) VG32 105

6.1 Skew orientation Schematic 108
6.2 Calculation of roller skewing angle based on time delay between contact passing and sensor separation 109
6.3 Reflection Time Schematic 112
6.4 Mean skewing angle over a 10s duration for the VG32 and VG320 lubricated bearing 114
6.5 Schematic of the skewing orientation and film thickness at the two skew impulses seen for the VG320 lubricated bearing at 20rpm. More opaque films indicate thicker films. 116
6.6 Measured skewing angle and minimum reflection coefficient for the VG320 oil lubricated bearing operated under 400kN for (a) $6,200\mathrm{nd_m}$ and (b) $31,000\mathrm{nd_m}$ 117

6.7 Measured skewing angle and minimum reflection coefficient for the VG32 oil lubricated bearing operated under 400kN for (a) $6,200\mathrm{nd_m}$ and (b) $31,000\mathrm{nd_m}$ 119
6.8 Measured skew angle for the 460WT grease lubricated bearing 120
6.9 Mean and maximum skew angles during the churning phase for the 460WT grease lubricated bearing 122
6.10 (a) mean, (b) maximum and (c) minimum skew angle comparison for all lubricants during the long duration running tests 123
6.11 Picture of a dried grease clump next to the roller face-flange contact . 124

7.1 Predicted reflection coefficient using Equation 3.15, resonances appear as dips in R. The blue region shows a typical usable bandwidth, centred around 10MHz 129
7.2 Schematic of the thinning oil droplet experiment 130
7.3 (a) & (c) single frequency of 12MHz analysis of s3 and n10 oils respectively. Plots (b) & (d) show the spectrogram oil map of the same oils 131
7.4 Film thickness of thinning oil drops measured by time-of-flight and resonance methods 132
7.5 Different sections of a typical ultrasonic reflection 133
7.6 Different sections of a typical ultrasonic reflection 134
7.7 Schematic of the KOVOT rig, and the model representation of a lubricated raceway. The red T symbols show where thermocouples are temporarily bonded during testing 136
7.8 Vickers Bearing Test Locations 138
7.9 Picture of the KOVOT ultrasonic sensor array before cabling and epoxy was applied 140
7.10 Pictures of levelling the KOVOT rig pre-oil tests. Shown in (a) the CG60 Cromwell Circular Level (b) the Laseriner MasterLevel Box Pro 141
7.11 Schematic of Vickers test locations on the NU2244 bearing 142
7.12 Pictures of the comb gauge being dipped into a stationary oil layer. Oil is present on the 250μm tooth but not the 275μm tooth, giving a reading of $262.5\mu\mathrm{m} \pm 12.5\mu\mathrm{m}$ 142
7.13 Schematic of doctor blading style technique used to deposit grease layers 144
7.14 Example Alicona scan of a grease layer with the displayed measured profile 145

7.15 Example of a grease layer pre and post oven controlled temperature test 146
7.16 Photograph of the acoustic velocity-temperature calibration rig. Enlarged is the ultrasonic sensor embedded in an epoxy puck 147
7.17 Acoustic velocity-temperature relationship of the VG32 and VG320 oils 148
7.18 Comparison of spectral plots with upper intensity contrast limits 1.1 and 1 respectively for a & b, for the 4ml deposit test on the KOVOT test rig 149
7.19 Spectral plots of different volumes of oil deposited on the KOVOT test rig 151
7.20 Ultrasonically measured central film thickness over a 60 minute duration with four different deposit volumes 152
7.21 Comparison of the mean measured film thickness using ultrasonic sensor, film comb, and known volume deposition method 153
7.22 Acoustic velocity-temperature relationship of the Mobil SHC 460 WT grease, taken straight from the tube with no air exposure or mixing . 154
7.23 Comparison of deposited grease layer thickness measured with a wet film comb gauge, and ultrasonic sensors using the acoustic velocity of the 460WT grease and VG320 oil 155
7.24 Changing measured film thickness with increasing grease temperature 157
7.25 Measured film thickness with increasing grease temperature, calculated using modified speed-of-sound calculation technique 158
7.26 Change in 460WT grease acoustic velocity with an increase in temperature 159
7.27 Comparison of deposited grease layer thickness measured with a wet film comb gauge, and ultrasonic sensors using the calculated acoustic velocity of the 460WT grease and VG320 oil 160
7.28 Comparison of resonance dips in the reflection coefficient response of three deposited grease layers. The blue area represents a bandwidth of acceptable signal-to-noise ratio 161
7.29 Comparison of theoretical measurable thickness and interval with an increasing fundamental resonant frequency, with (a) two temperature extremes (b) different levels of signal padding at $20°C$ 165

8.1 Instrumented multi-frequency scout bearing 169
8.2 Multi-frequency non-dimensionalised frequency response 171
8.3 Frequency vs. MRC over a single contact 172

8.4 3-Dimensional view of roller pass across frequency domain 173
8.5 Spectrogram of a single roller pass 174
8.6 Drawn by eye resonances and calculated film thickness at the contact inlet and outlet 176
8.7 Multi-frequency bearing sensor spectral comparison 177
8.8 Spectral analysis of VG 320 lubricated multi-frequency bearing 181
8.9 Spectral analysis of VG 32 lubricated multi-frequency bearing 183

9.1 Schematic of the instrumented inner raceway of the multi-axis bearing 187
9.2 Example spectrogram with inlet, outlet and contact regions highlighted 188
9.3 Contact discretisation for automation of data processing 189
9.4 Example resonance plot from an in-situ measurement 193
9.5 Example of measured higher order harmonics compared with the theoretical value, calculated from $\overline{\Delta f}$ 196
9.6 Visualisation of the raceway film at the contact inlet and outlet regions. Highlighted are regions of scatter where a stable film is not present . 197
9.7 (a) shows the measured raceway film at the inlet to a contact with some scatter far away from the contact inlet. (b) shows the moving variance and determination of the raceway film detection area 198
9.8 (a) shows the measured raceway film at the inlet to a contact, which appears very stable. (b) shows the moving variance which confirms the stability 200
9.9 Observation of measured raceway film shape in area influenced by vertical interference 201
9.10 Schematic of the circle separation which governs the volume fill model approach 203
9.11 Change in s/b ratio with different complexities of the volume fill model. both plots are of the VG320 oil with (a) total bearing load of 600kN with increasing bearing speed (b) bearing speed of $31,000\mathrm{nd_m}$ and increasing load 208

10.1 Mean raceway thickness leading into the contact inlet at different axial locations when the bearing was lubricated with VG320 and VG32 oils 212

10.2 Mean raceway thickness leading into the contact inlet at different axial locations when the bearing was lubricated with VG320 and VG32 oils. The test conditions were 100kN load, operated at bearing speed of $6,200\mathrm{nd_m}$, $12,400\mathrm{nd_m}$, $18,600\mathrm{nd_m}$, $24,800\mathrm{nd_m}$ and $31,000\mathrm{nd_m}$ respectively from a to e 214
10.3 Mean raceway thickness leading into the contact inlet at different axial locations when the bearing was lubricated with VG320 and VG32 oils. The test conditions were $31,000\mathrm{nd_m}$ bearing speed, operated at applied loads of 100kN, 200kN, 300kN, 400kN and 500kN respectively from a to e 216
10.4 Mean raceway thickness leading into the contact inlet at different axial locations when the bearing was lubricated with VG320 and VG32 oils. The test conditions were $6,200\mathrm{nd_m}$ bearing speed, operated at applied loads of 100kN, 200kN, 300kN, 400kN and 500kN respectively from a to e 217
10.5 Change in frontal inner raceway film thickness with increasing speed under different loads for (a) VG32 (b) VG320 220
10.6 Change in frontal inner raceway film thickness with increasing load under different speeds for (a) VG32 (b) VG320 220
10.7 Comparison of frontal inner raceway film thickness for various load a speed cases for (a) VG32 (b) VG320 222
10.8 Theoretical Hertzian contact half-width with increasing load, calculated using Equation 2.4 223
10.9 Change in inlet meniscus position with an increased bearing speed under 600kN total load, lubricated with VG320 oil 224
10.10 Change in s/b ratio with increasing bearing speed for (a) VG32 (b) VG320 225
10.11 Change in s/b ratio with increasing bearing load for (a) VG32 (b) VG320 226
10.12 A raceway film thickness pattern at the inlet of a roller pass where the moving variance threshold was not met, and so a NaN film thickness is detected 228
10.13 Results 231
10.14 3D spectrogram plot of grease churn across the rolling axis 232
10.15 Results of the grease churn when operated at $6,200\mathrm{nd_m}$ 233
10.16 Results of the grease post-churn when operated at $6,200\mathrm{nd_m}$ repeat test 234
10.17 Results of the grease churn when operated at $12,400\mathrm{nd_m}$ 235

10.18 Results of the grease churn when operated at $18,600\mathrm{nd_m}$ 237
10.19 Results of the grease churn when operated at $24,800\mathrm{nd_m}$ 238
10.20 Results of the grease churn when operated at $31,000\mathrm{nd_m}$ 239
10.21 Starvation ratio during churn tests 241
10.22 Film thickness required to meet the (a) $5b$ and (b) zero reverse flow conditions, with the bearing operated at $nd_m = 31,000$ 246

11.1 Theorised relationship between raceway thickness and contact thickness, showing a detectable pre-starvation window of detection 255

A.1 Matlab script developed to detect resonances on bearing raceways. A series of peak passes show how noise is filtered to reduce the chance of a false detection 269

Chapter 1

Introduction

Roller bearings are either shaft or case mounted and serve the purpose of a supporting a rotating load. This means they are found in nearly every mechanical device which has some kind of rotation, making them one of the most common machinery components. These devices range from the smaller scale such as lawn mowers and automotive drive-trains to larger scales such as within a wind turbine gearbox or main bearing where bore diameters are in the meter scale. Regardless of the bearing size, a lubricant is normally required for healthy operation.

Rolling bearing elements all have rough surfaces when observed on the microscopic scale due to the presence of asperities. When these asperities touch, microscopic adhesion and abrasion causes wear to the surface, ultimately leading to bearing failure. This can be partially avoided by using a lubricant. When a lubricant is present, it floods the contacting surfaces and through a combination of film thickening due to high contact pressure which develops at the inlet, and elastic deformation of asperity tips, the contacting surfaces are separated, the amount of wear is vastly reduced, and bearing life is prolonged. However, if too much lubricant is introduced into a system, it acts as a separate resistance to rolling as the elements now have to churn through the lubricant to move. This is also damaging for bearing health as churn losses make devices less efficient, and cause cyclic temperature rises leading to the expansion and contraction of sub-surface cracks, inducing thermal thermal fatigue.

This has naturally led to a large amount of research into optimising lubricants for more efficient tribo systems, trying to balance acceptable wear levels and churning losses. Looking at a Stribeck curve in Figure 1.1 from Guorong et al. [1], the elasotohydrodynamic (EHL) regime, in which roller bearings operate, exists in the crossover between mixed lubrication and hydrodynamic lubrication, and has the minimum coefficient of friction (μ) and therefore the greatest efficiency.

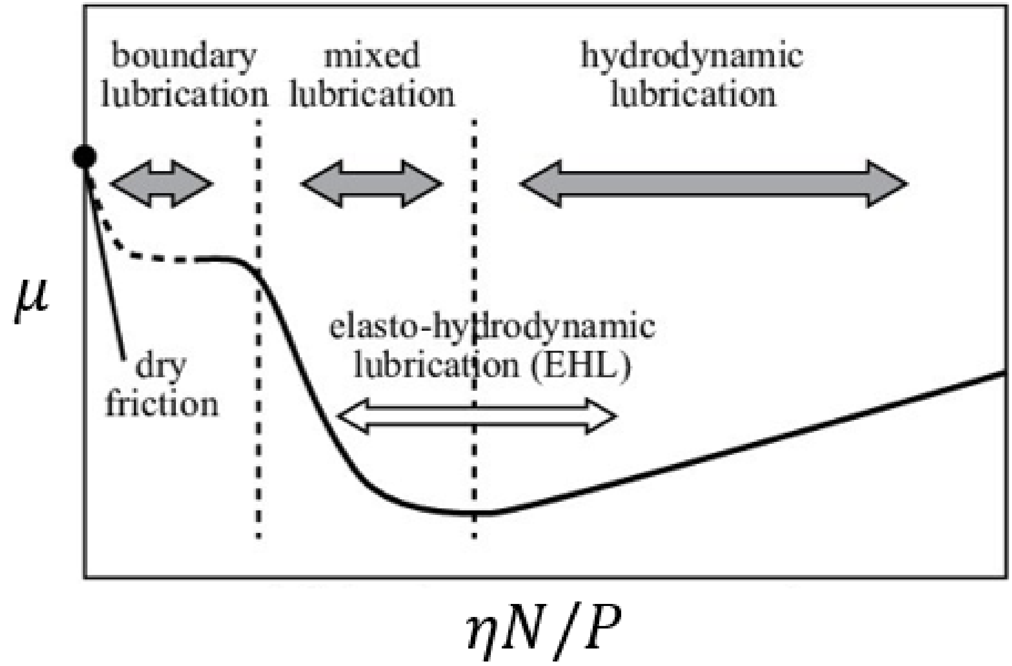

Figure 1.1: Stribeck curve plotted as Hursey number vs. Coefficient of Friction (μ), taken from Guorong et al. [1]

A key mechanism in developing a separating lubricant film is the development of a meniscus, a reservoir of lubricant at the contact entry. If present, then there can be adequate pressure build-up leading into the contact. If missing or shortened, the contact is deemed to be 'starved' of lubricant and [2] suggest the separation is reduced up to 70% of the fully flooded contact, reducing the load carrying capacity. Thus, having an understanding of a lubricant capability to develop a meniscus, and an in-situ measurement of thickness and length, enables engineers to develop more sophisticated lubricants and bearings that aid in meniscus development, as well as improved maintenance procedures for potentially starved tribo systems.

1.1 Problem Statement

The inlet meniscus is defined as the position of the oil-air boundary leading into the contact, forming when the roller and raceway films meet, and marks the start of the pressure increase into the contact that enables separation. The inlet meniscus dimensions are directly linked to contact film thickness [3, 4], however they are difficult to measure, and thus were historically considered an impractical parameter in determining lubrication state of rolling bearings [5]. This is because they are in the sub mm range, are found deep in the working components of bearings, which are also often buried inside a larger machine, and are moving oil films. That is to say, they do not remain in one location, but instead are paired with a rotating rolling element. Additionally, numerical work has shown that the length is not consistent across the entire inlet, and that local oil availability can cause a contact that is nearly fully flooded in one region to be starved in another at a single point in time [6, 7].

The inlet thickness was adopted by Chevalier et al. [8] as an alternative to length to define starvation levels in a numerical analysis of starved EHL point contact film thickness. The same thickness parameter has been used to define starvation in experimental work [5, 9, 10]. Here an optical EHL rig was modified with a second roller, preceding the contact of interest, of preset height to control film thickness into the observed contact. Accordingly, the inlet thickness is easier to control, compared with length, for laboratory experiments, but it is still impractical to measure in-situ in an operating bearing. Chen et al. [11] and Chennaoui et al. [12] used combinations of optical interferometry and ratiometric fluorescence to study inlet thickness within sapphire bearings, but again this is limited to a laboratory due to the use of unrealistic bearing materials.

There is still a lack of an in-situ measurement system employable on fully metallic field bearing. As Chennaoui et al. [12] discuss, rolling bearing contact conditions are extremely well studied and understood, yet relativity little is known about the inlet conditions which are crucial to developing adequet separation. An in-situ measurement system could therefore provide a step change in understanding further lubrication phenomenon within rolling element bearings.

1.1.1 The Impact of Bearing Starvation

Bearing starvation is the lack of adequet lubricant flow to the contact inlets to allow full hydrodynamic lubrication. When starvation occurs, the contact separation is reduced, leading to increased metal-to-metal contact and and increase in surface and subsurface wear phenomenon. The consequence of a bearing failure due to starvation is initially machinery downtime which can have upfront costs of replacing the bearing and affected parts, but then also a prolonged cost of the downtime depending on what the bearing was used in. For example, failure of machinery on a factory assembly line halts the production of parts and so the cost of failure is more than just part replacement.

Starvation is a potential problem for all common bearings that operate using oil or grease, and so there are a huge number of industries vulnerable to this lubricant failure mechanism. One industry which is particularly vulnerable is wind turbine gearboxes as maintenance is difficult due to remote access, and if starvation does occur the failure can be catastrophic due to the high loads and harsh operating conditions. This issue is discussed in more detail in the next section.

1.1.1.1 Case Study: Wind Turbine Bearing Failure

One industry that is severely affected by the absence of an in-situ measurement technique is the wind turbine industry. Figure 1.2 shows the energy trends of the UK from 2010 to 2019 [13]. Although total energy generation has been in slight decline over the previous decade, the renewable share of that generation rose from 6.9% to 37.1%. Of that renewable generation, wind farming rose from 39.3% to 53.4%. Global trends mirror those of the UK, with 93.6GW of new installations in 2021 [14], with Europe, Latin America and the Middle East showing large market growths. Although the number of turbines installed has increased, enabling the increase in energy production, so too has the size of the turbines installed. Between 1998-1999 to 2021, the *Office of Energy Efficient & Renewable Energy*, an office of the US *Department of Energy* report that the average rotor diameter has increased from $\approx$ 50m to 127.5m, giving an approximate 600% increase in swept area over the same period [15].

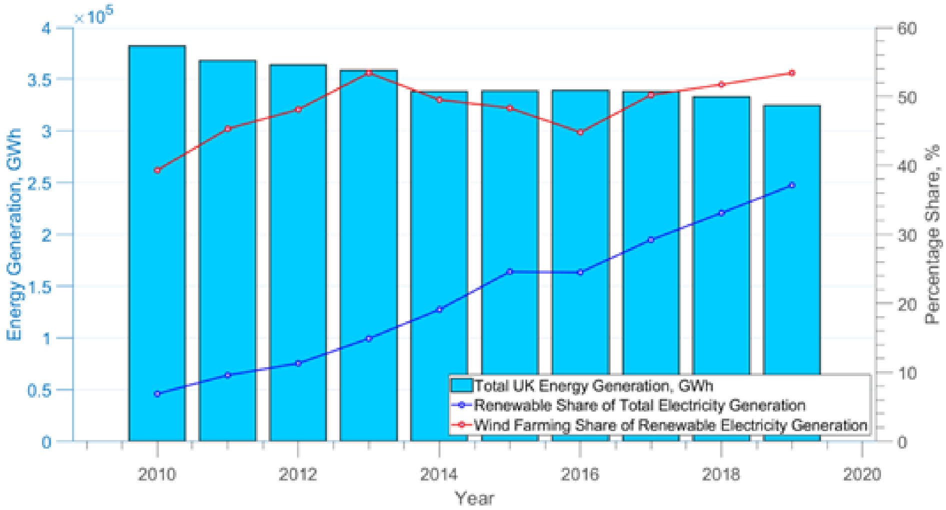

Figure 1.2: UK wind energy trends from 2010 to 2019 [13]

Although such a size increase leads to more energy production, it does not come without a downside. As blade length increases, so too does the force through the gearbox and bearings, increasing the load which bearings must withstand, thus making the working conditions harder. There is an abundance of turbines which do not meet their expected 20 year lifespan, and the majority of these premature failures are due to bearing failure [16]. Of these failures, the majority are wind turbine gearbox bearing (WTGBs) failures [17, 18]. WTGB failure is extremely costly, and increases the price of renewable energy. Figure 1.3 adapted from Faulstich et al [19]. shows that although they are not the most common occurring failure they do have the longest downtime for repair.

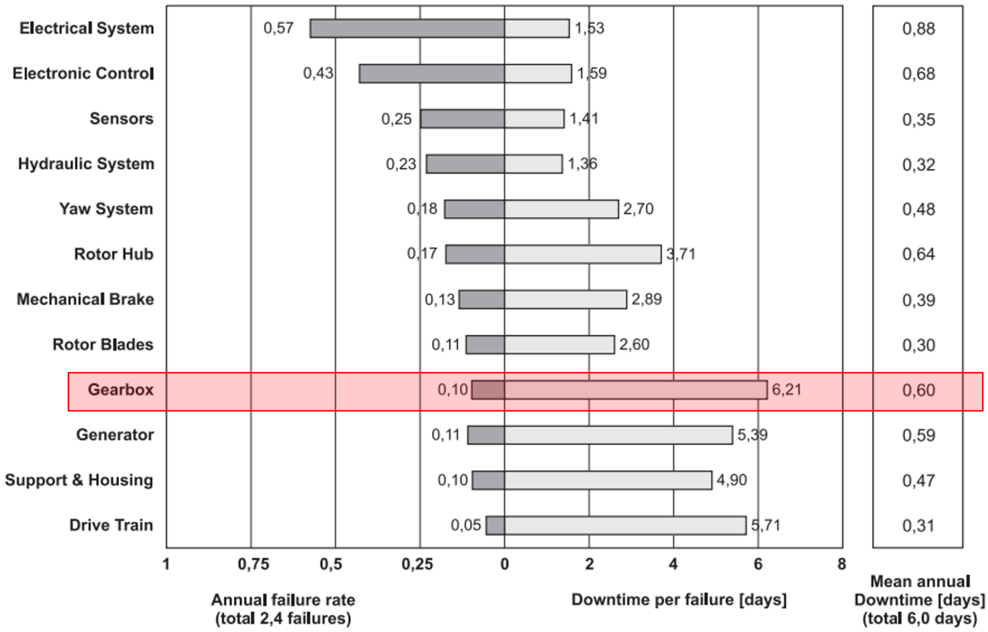

Figure 1.3: Mean failure rate and downtime per sub-assembly failure, adapted from [19]. Gearbox failure has been highlighted as having the longest downtime per event

Classically, bearings fail through rolling contact fatigue, the sustained over-rolling of loaded elements on the raceway. Over time, butterfly cracks form due to fatigue in the subsurface of the raceway material, eventually leading to spalling and bearing failure [20]. Excessive loads can also lead to plastic deformation on both the macro and micro scale [21]. However, turbine bearing failures are more complicated, and typically fail due to micropitting, smearing or white etch cracking (WEC), all of which can be caused by, or worsened by, a lack of adequate lubricating film [16, 21, 22, 23]. Although there are numerous reasons for a lack of lubricating film, it is already established that a meniscus must be present to form any film at all. Therefore, by not having an in-situ monitoring technique that is deployable for operational bearings, failure prevention will be predominantly based on design improvement from post-failure evaluations rather than live condition monitoring data.

1.2 Project Aim and Objectives

The lubricant meniscus, which acts as a reservoir of oil, is known from literature to be crucial in enabling contact separation. A depletion of this meniscus is detrimental to bearing health and causes premature wear. The aim of this project was to develop an ultrasonic technique capable of measuring the length and thickness of the lubricant inlet meniscus in-situ within a real operating metallic bearing, which is suitable for both oil and grease lubrication. This would allow the lubricant flow around a contact to be monitored, and the starvation level of the bearing determined. The impact of bearing load, speed, lubricant viscosity and lubricant type on contact starvation could then be assessed. The intention of the work is therefore being a step towards industrial in-situ measurements for maintenance purposes, and further fundamental lubrication understanding for research gain. In order to achieve the project aim, the following objectives were defined:

Develop a Novel Measurement Method for Raceway Film Thickness Develop an ultrasonic method capable of measuring raceway lubricant films in-situ, on a full scale wind turbine gearbox bearing test rig. Using the novel method, measure the raceway film thickness to observe lubricant flow around rolling bearing contacts. The method should be validated using mathematical models and bench-top experiments.

Determine the Contact Inlet Meniscus Length of Oil Lubricated Bearings From either a direct measurement or mathematical model with measurement input, determine the length and thickness of the inlet meniscus to a rolling bearing contact. From this measurement, determine the starvation level, if any, of the bearing.

Investigate the Effect of Load, Speed and Oil Viscosity on Meniscus Dimensions Based on the measurements obtained of the meniscus dimensions, draw conclusions on the effect of load, speed and oil viscosity on the inlet meniscus dimensions. This includes investigation into the mean shape and distribution changes across the rolling contact. From these conclusions, practical guidance should be given to industry stakeholders.

Monitor Grease Distribution During Churn Using the same measurement approach, assess whether grease films can be monitored in-situ. If the technology is capable, monitor the grease distribution during the initial churning phase, and assess how bearing speed affects the shape, time or magnitude of this distribution.

Explore Measurable Bearing Kinematics Although meniscus lubrication is the primary focus of this work, it would be an oversight not to explore other bearing kinematic properties, such as roller skew which can alter the lubrication state of the bearing. Therefore, a primary aim was, using the same sensors, explore these bearing kinematic properties and how their presence affects the lubrication state.

Use of Bare Piezoelectric Transducers Drawbacks of commercial ultrasonic transducers for their use of measuring bearing contacts and conditions is their relatively bulky size (meaning installation is difficult) and their upper temperature operating limit. Bare piezoelectric transducers are much smaller (in the mm range), have operating temperatures of around 200°C and can be permanently installed on components. The aim was to therefore use these 'bare' sensors so that techniques were industrially applicable.

Data Analysis Automation One practice common to ultrasonic measurements is the dependency of an industry expert to be able to interpret data, often meaning that only short time durations of data can be analysed. Alternatively, automation has been achieved but only for more basic measurements such as time of flight and minimum reflection coefficient. A main aim of this work is to improve upon the automation of data analysis, thus reducing the dependency on data 'snap-shots' and allowing a more well defined picture of lubricant conditions over a longer time period to be appreciated.

1.3 Thesis Layout

This thesis is comprised of eleven chapters, each of which address the following:

Chapter 1: Introduction This chapter introduces the industry problem that is challenged by this thesis of work, defines project aims and objects, and gives a layout of thesis structure.

Chapter 2: Rolling Element Bearings and Bearing Lubrication The background theory outlined in this chapter covers the purpose of rolling element bearings, key mechanisms which allow for their proper operation, and the consequence of failure. Bearing lubricants are then discussed and the lubricating mechanisms of oil and grease are compared.

Chapter 3: The Principles of Ultrasound This chapter covers the fundamental principles of ultrasonic waves including wave generation, propagation, influences on diminishing wave pressure and wave interaction with multi-body boundaries. The three main thickness measurement approaches are presented; the time of flight approach, the spring model and the resonance method. Each of these measurement techniques has a achievable measurement thickness range; the method and drawbacks for all are discussed.

Chapter 4: Literature Review This thesis literature review first focuses on the lubricant inlet meniscus to the rolling bearing contact. The meniscus governance on EHL contact separation is presented, and the starvation phenomenon is discussed and linked to a lack of lubricant at the contact inlet. The outlet meniscus impact on the lubricant film to the next roller is highlighted, and finally the limited in-situ meniscus measurement tests are shared. Roller Skew is highlighted as a key kinematic mechanism of a roller bearing that could impact the inlet lubricant meniscus. A broad review of ultrasonic reflectometry within bearings is presented, with measurement potential and limitations addressed. A gap in the research focusing on the ultrasonic resonant method to measure bearing raceway films, and thus infer the meniscus location, is given.

Chapter 5: Experimental Methods and Approaches This chapter reports on the full-scale wind turbine gearbox bearing test rig used for the in-situ measurement of the inlet meniscus location. The ultrasonic hardware used for the full scale testing and validation experiments is introduced. The fundamental data analysis at a single sensor frequency is introduced which enables the more complex discretisation of the bearing pattern in the later chapters of the thesis. Finally, a simple EHL model is explained which was used to determine the sensor measurement area.

Chapter 6: Experimental Measurement of Roller Skew In this chapter the roller skew mechanism is explained, and the detrimental effects on the lubricant and surface wear are explored. The chapter then reports on single frequency ultrasonic measurements taken during oil and grease lubrication, and the method of calculating roller skew based on contact time delay across the roller transverse axis.

Chapter 7 : Experimental Validation of the Surface Film Thickness - Resonant Frequency Relationship This chapter reports on the use of the ultrasonic resonant method to measure free lubricant films in a solid-lubricant-air boundary. An initial test platform is detailed where a thinning oil droplet was measured over time. Effects such as echo number and wavelet length are reported. Details are given of the Known-Oil-Volume-Test-Rig (KOVOT) design, manufacture and commissioning. The KOVOT was used to validate the measurement of thinning and stationary oil films, and to develop an acoustic velocity-temperature relationship for grease.

Chapter 8: Scouting for the Entry and Exit Film of a Cylindrical Roller Contact To explore the use of a resonance method to measure raceway films a scouting bearing was instrumented with an array of different central frequency sensors. The process and results are discussed in this chapter via a spectral data visualisation method. The work concludes that the measurement is possible, but the film varies across the rolling axis, meaning a second bearing is needed with an increased sensor number.

Chapter 9: In-Situ Measurement Method of the Inner Raceway Film Rolling bearings undergo millions of revolutions within their lifetime, and so looking at spectral plots of single passes is insightful but does not give a full lubrication picture. This chapter details the automatic discretisation of reflection patterns and calculation of the mean film raceway thickness. A numerical Volume Fill Model is then introduced which, based on some lubricant assumptions, allows for the calculation of the inlet meniscus position based on the raceway film thickness.

Chapter 10: In-Situ Measurement of the Lubricant Meniscus Across the Rolling Axis Within the chapter the results from the in-situ measurement of the inlet raceway thickness, and calculation of the meniscus position, are given. For the oil tests the viscosity, load and speed impact is assessed. For grease, the speed and time dependence are investigated. Based on the Volume Fill Model, critical film calculations are given to achieve fully flooded and zero reverse flow. Alternatively, based on a known raceway film, equations are given to calculate critical load at which fully flooded and zero reverse flow is achieved.

Discussion This chapter discusses the work presented in this thesis. Key data trends are discussed and topics such as applicability to other bearing sizes and types, if the sensors could be mounted in other positions, and how the technology might be used in industrial and academic work are all covered.

Conclusions This chapter summarises the key findings of this thesis of work, with the novelty highlighted. The ability to measure resonances in-situ with different lubricants is addressed, and conclusions on measuring lubrication state are drawn. Limitations of the method and potential future research avenues are explored.

Chapter 2

Rolling Element Bearings and Bearing Lubrication

Bearings solve a problem that is simple in principle, the support of a mechanical load applied through a rotating component such as a shaft, and allowing that rotation to occur with minimal friction. There are many types and variants of bearings, but all are designed to solve this same problem. The many design requirements such as required load supported, running speed, size constraints, working environment and others govern what bearing and lubricant system is used. Within these requirements countless other mechanisms and principles are at work, all of which aid or detract from how well the bearing performs. This means there is a huge volume of work on bearings, how to select the right type, material, lubricant, etc. which has been the focus of many books. The reader is guided to two books by Harris et al. *"Essential Concepts of Bearing Technology"* [20] and *"Advanced Concepts of Bearing Technology"* [24] which are very comprehensive. The purpose of this chapter is to discuss only the necessary concepts needed to understand the work presented in the research chapters of this thesis.

2.1 Roller Bearing Purpose

Mechanics and mechanical engineering relate to machines and devices which incorporate moving parts for some form of designed advantage [25]. Some applicable moving machines are obvious, such as bicycles, automotive vehicles and jet engines. Others are less obvious, but still very relevant, such as electrical toothbrushes, hair dryers and hard disc drives. These components cannot be fully supported with conventional bolts, screws and fastenings etc. as these would not allow movement. Instead, bearings must be used, which can support a load from a rotating component.

Rolling element bearings consist of four main components: an inner raceway, an outer raceway, the rolling elements themselves and a cage to separate the elements. The element shape is the largest deviation between bearing types, and often determines the type of load that can be accommodated (radial or axial), the magnitude of load and the operating limits of rotational speed. The most widely used bearing, because of its applicability to many scenarios, is a deep groove roller bearing, pictured in Figure 2.1a. These bearings can accommodate relatively high loads and speeds, and because the elements are symmetrical in any cross sectional plane, they can roll in any direction and can accommodate some thrust loads [20]. However, in cases where even larger radial loads are required, a cylindrical roller bearing is used.

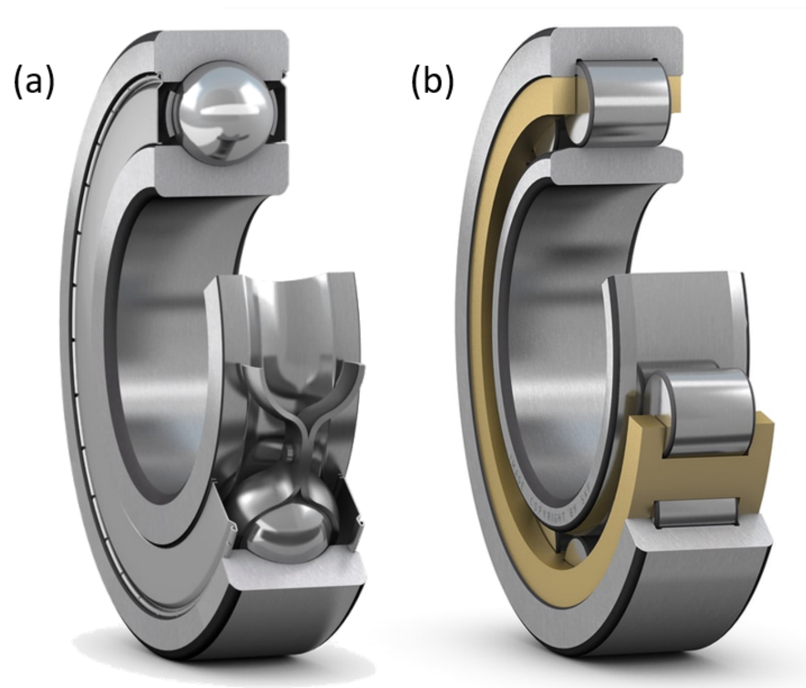

Figure 2.1: Picture of a single row deep-groove ball bearing [26] (a) and a cylindrical roller bearing [27](b)

2.2 Cylindrical Roller Bearings

Cylindrical roller bearings (CRB's) have cylindrically shaped rolling elements, instead of balls, which allows the support of greater radial loads and also higher rotational speeds [20], an example is shown in Figure 2.1b. These bearing types are often used in much larger configurations, like within a wind turbine gearbox, where loads are in the kilonewton magnitude. The disadvantage of such bearings is they generally cannot support any axial loading that may occur as there is only one plane of rotation

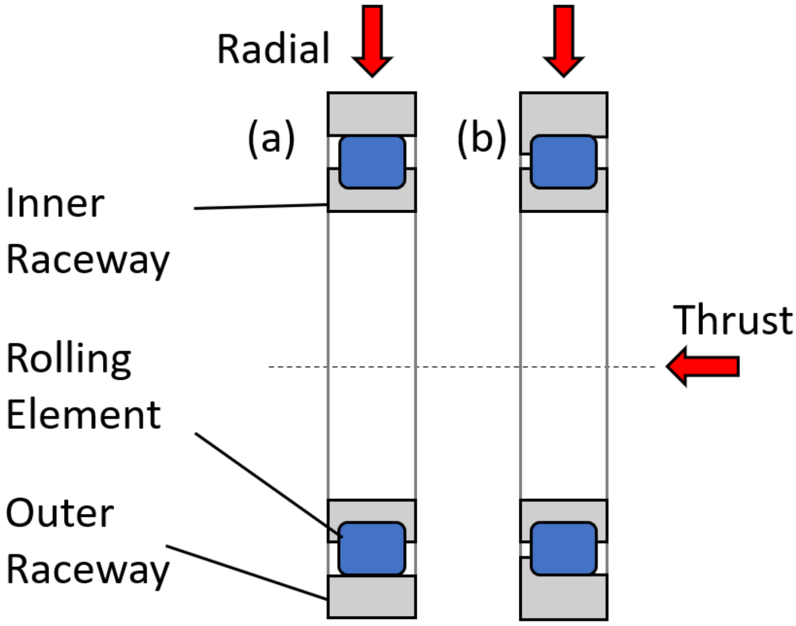

Figure 2.2: Schematics of a cylindrical roller bearing a) standard configuration b) with thrust flange

possible. For this reason, they are often allowed to float along the shaft, and if a axial force is present, a secondary thrust bearing is incorporated into the system [28]. However, some small amount of thrust load can be accommodated, through the clever use of a thrust flange, if required. Figure 2.2a & b shows the schematic of a cylindrical roller bearing without and with this thrust flange respectively.

2.2.1 Cylindrical Roller Contact Mechanics

In 1882 Hertz [29] published his original solution to solve pressure and stress distributions within non-conformal contacts. From this work, more sophisticated models have been developed to supplement the theory [30], but the Hertzian theory alone is still relevant and widely used today [31]. When no axial load is accommodated, the inner raceway-roller and outer raceway roller loads are equal. The shape of the contact and subsequent pressure distributions are governed by the shape of the bodies in contact. The inner raceway-roller contact within a CRB, which is the subject of interest for this thesis, can be modelled as a cylinder on cylinder to form a line contact. Where v and E are the Poisson's ratio and elastic modulus respectively, the reduced elastic modulus E^* is calculated as:

$$\frac{1}{E^*} = \frac{1 - v_1^2}{E_1} + \frac{1 - v_2^2}{E_2} \tag{2.1}$$

The reduced radius R' relates to the curvature of both bodies and is calculated from the radius of curvature R of the two cylinders in contact. Where subscripts 1 and 2 refer to the two bodies in contact:

$$\frac{1}{R'} = \frac{1}{R_1} + \frac{1}{R_2} \tag{2.2}$$

The load per unit length P' is calculated from the applied contact load P and the length of the contact L:

$$P' = P/L \tag{2.3}$$

From Equations 2.1 to 2.3 the contact half-width can be calculated as:

$$b = \sqrt{\frac{4P'R'}{\pi E^*}} \tag{2.4}$$

One of the major assumptions of the Hertzian model is that the contacting bodies are at rest and in equilibrium. Equation 2.4 shows that there is no speed parameter incorporated, and instead the half-width is determined solely off material and load conditions. Although a bearing contact of course has a velocity parameter, this breach of assumption is not detrimental to the result when in pure rolling.

2.3 The Purpose of Lubrication

On a macro scale, within a cylindrical rolling element bearing there exists a finite number of contact points where the rolling elements touch the inner and outer raceway. The addition of all these points, calculated using the Hertz model, would give the apparent contact area. At these locations, on a micro scale, there are thousands of much smaller contacts, where individual asperities from the rolling surfaces interact. These individual asperity contacts form the real area of contact, which is always smaller than the apparent area in a real system, where surfaces are never perfectly smooth. When asperity-asperity contact occurs in rolling surfaces the damage can be catastrophic; the purpose of lubrication is to form an intermediary separating layer between opposing bodies of motion, thus avoiding surface initiated failure mechanisms.

Some very niche journal bearing applications have unique lubricants such as air [32], water [33], or dry lubricant layers such as PTFE [34] that are intended to wear during normal operation. However, the vast majority of rolling element bearings have an oil or grease lubricant system, and it is estimated over 90% of world bearings are grease lubricated [35]. Although oils and greases serve the same purpose of causing contact separation, they do so in different ways.

2.4 Oil lubrication

Oil lubricated bearings are less common than their grease counterpart, but are somewhat simpler in nature, as grease has added rheological complexity that will be explored in the following sections. Often lubricant and machinery industry focused publications give good practical guidance on when an oil system may be used instead of grease. Fitch [36] in 2006 gave a comprehensive overview of the benefits of oil systems.

High Speed For high speed applications, oil is often a better lubricant due to its availability to flow around the bearing surfaces and reach contact points. LANXESS [37] suggest that when a bearing operates at $> 250,000\mathrm{nd_b}$ in inch, rpm (which converts to $> 6,350,000\mathrm{nd_b}$ in mm, rpm) where n is revolutions per minute and $\mathrm{d_b}$ is the bearing bore diameter, then oil should always be used. The most adopted speed convention is to normalise against the mean diameter $\mathrm{d_m}$. SKF [28] suggest that any greased cylindrical roller bearing with $\mathrm{nd_m} \geq 270,000$ is considered to be in the extremely high speed range. Grease is not capable of flooding the contact inlets at such high speeds and oil lubrication is preferred.

High Temperature Bearings are often subjected to very high temperatures either due to frictional heat with the harsh running conditions of high loads and speeds, or due to the working environment. If cooling is necessary, oil is preferred as recirculation gives a cooling affect via convection. Although many greases have high temperature resistance and dropping points above 200°C they do not circulate and so cannot provide this cooling effect.

Controlled Lubricant Level Oil pumps allow for the volume of oil delivered to a bearing to be controlled. This helps avoid contact starvation and lubricant churn. Counter to this, after grease is packed into the bearing, the churning/break-in phase displaces the majority of grease and bearings are known to often operate in the starved regime.

2.4.1 Types of Lubricating Oils

There are several different types of oils used within industry, the selection of a particular kind depends on the contact and environment conditions. The two most common are mineral oils and synthetic oils.

2.4.1.1 Mineral Oils

Williams [38] gives an introduction to mineral oils, which are commonly used for most applications. They are derived from the distillation of crude oil and are made primarily of hydrocarbons. The most commonly occurring hydrocarbon determines the oil type, and is governed by the field from which the crude oil was extracted. Paraffinic oils are made of long, branched chains of carbon atoms that are fully saturated with hydrogen. Naphthenic oils are similarly saturated, but form some ring structures, unlike paraffinic oils. Aromatic oils form similar ring structures, but with alternating single and double bonds, and are also unsaturated. All mineral oils are at risk of oxidation; the more rings formed the more oxidation takes place. As oxidation causes clumping in the oil it is detrimental to lubricant performance, meaning antioxidant additives are often used in mineral oils to delay degradation.

2.4.1.2 Synthetic Oils

Petroleum is the highest grade product from the distillation of crude oil. To produce synthetic oils, this petroleum is cracked using a combination of heat, pressure and catalysts. This cracking brakes down longer hydrocarbon chains into smaller, more uniform single bond chains that contain a single unsaturated carbon at one end of the chain. Polymerisation then controls the linking of chains, causing the formation of a lubricating oil. Polyalphaolefin (PAO) are the most commonly used synthetic oils as they have a wide range of achievable viscosities, a high viscosity index, and a large operating temperature range [39].

2.4.2 Oil additives

Rarely will a mineral or synthetic oil be used to lubricate a component without further modification via the use of additives. The purpose of an additive is to enhance beneficial qualities of oil, such as its ability to inhibit rust formation, or subdue detrimental qualities, such as oxidation rate. Some common oil additives are:

Antioxidants Oxidation causes clumping of oil and thus is detrimental to lubricating performance. Antioxidant additives can be used to inhibit this oxidation for a finite period.

Rust and Corrosion Inhibitor Rust and corrosion inhibitors protect ferrous and non-ferrous metals respectively from chemical degradation.

VI Improvers It is beneficial to have a high viscosity index (VI) oil as this allows a more stable viscosity at different operating temperatures. VI improvers can be used to increase the viscosity index, and reduce the viscosity decrease that is seen at higher temperatures for oils with a low VI.

This is not a comprehensive list, there are many other additives that aim to improve friction, oil wettability, stop foaming and more. Which additives are used is dependent on which application the oil is intended for.

2.5 Elastohydrodynamic Lubrication Theory

Bearing contacts operate under boundary or elastohydrodynamic (EHL) conditions. Looking at the Stribeck curve in Figure 1.1 this is ideal for bearing efficiency as the coefficient of friction is a minimum, meaning the least amount of resistance to rolling. However, within these regimes there is often not a thick enough contact film to fully separate surfaces, which can lead to premature wear if not fully understood. To appreciate the film thickness in the contact under these conditions, the EHL theory was formulated. The main assumptions of the theory are the contact shape, pressure distribution and asperity deformation are the same as within a dry Hertzian contact [40], and that the contact is fully flooded.

The separation is then caused by a combination of plastic deformation of asperity tips, and an increase in viscosity of a piezoviscous oil within the contact. As the contact pressure is within the gigapascal range, there is a large viscous thickening effect of the oil. However, it is the inlet viscosity which governs the level of separation, with more viscous oils typically generating thicker films if the lubricant supply is adequet. However, more viscous oils have difficulty in accessing the inlet at higher bearing speeds as they do not flow as readily, and so the if the oil is so viscous it cannot fill the inlet, starvation occurs and a thinner, impaired contact film forms if any film is formed at all.

In classical EHL theory, it is assumed a contact is fully flooded, meaning there is ample lubricant flowing into the contact inlet to feed the separating film. This is called the infinite meniscus assumption [41]. With this assumption, the contact film is governed by bearing material properties, load and speed conditions, and oil viscosity. Equation 2.5 from Dowson & Toyoda [42], developed from the minimum film equation from Dowson and Higginson [43], gives the prediction of the central film thickness within an EHL line contact.

$$\frac{h_c}{R'} = 3.11 G^{0.54} U^{0.69} W^{-0.1} \tag{2.5}$$

where h_c is the central film thickness of the contact; G, U, and W are material, speed and load parameters respectively. They are calculated from the oil pressure-viscosity coefficient α, ambient dynamic viscosity η_0, mean surface velocity $\overline{U}$, contact length L and the applied load, reduced modulus and reduced radius which were defined in Section 2.2.1. The EHL parameters are defined as:

$$G = 2\alpha E^* \tag{2.6}$$

$$U = \frac{\overline{U}\eta_0}{2E * R'} \tag{2.7}$$

$$W = \frac{P}{2E^* R' L} \tag{2.8}$$

Dowson et al. discusses extensively how load, speed, materials and inlet viscosity greatly affect the lubricant film thickness in EHL conditions [43, 44, 45, 46, 47, 41, 42, 48, 4, 49]. Clearly, the load parameter has the smallest theoretical effect as it is to the power -0.1. Materials do have a substantial affect, but as there is little variation in bearing materials (most are high carbon alloy steels) the impact between contacts is also minimal. Therefore, the governing parameter is U which encompasses both speed and viscosity; this parameter has the greatest impact on the theoretical film thickness. Predominantly, the inlet viscosity, not viscosity through the contact, governs the contact film thickness [50, 51]. Then, the quicker the entrainment velocity into the contact, the thicker the film that is developed.

2.6 Grease Lubrication

Grease is regarded as a semi-solid emulsion of thickener, base oil and additives [52]. The percentage contributions of each are given in Figure 2.3, adapted from [53]. Clearly, the majority of grease is composed of the lubricating base oil, which is the most important component. However, the thickener and additives can still drastically alter the grease performance and characteristics.

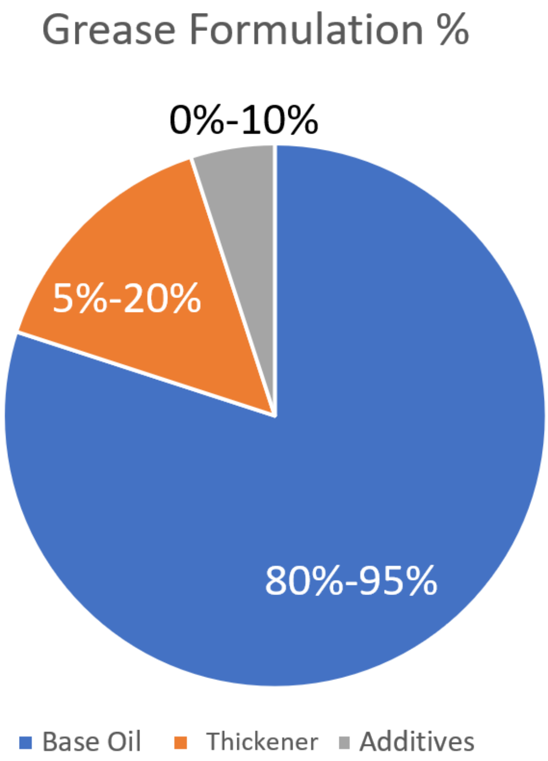

Figure 2.3: Contributions of oil, thickener and additives to a lubricating grease

Although oil lubrication is a more researched, understood lubrication method, within industry, grease is far more commonly used. The reasons for which can be found in Table 2.1. However, despite grease clearly working as a lubricant, unlike oil lubrication there is still no unified theory on how grease lubricates due to its complex rheological behaviour.

Benefits	Disadvantages
• Better starting torque as the grease does not flow away from the contact during downtime • Reduced leakage when compared with oil • Self-replenishing lubricant supply meaning little to no maintenance is required	• Can suffer from thermal degradation as the grease around the contact retains heat • For a large portion of running time the contact is starved due to reflow mechanisms

Table 2.1: Fundamental benefits and disadvantages of grease lubrication

2.6.1 Building Blocks of Grease

2.6.1.1 Base Oil

A base oil makes up the vast majority of a grease (80%−95%). The oils used in greases range from simple animal and plant oils to the more standard mineral and synthetic oils discussed in Section 2.4.1. The base oil is the most important component of grease as this is what provides the separation of surfaces, after the churning phase [54]. The purpose of thickener is essentially to act as a delivery system of this base oil to the working component. Thus, an appropriate base oil should be defined using the viscosity and viscosity index.

2.6.1.2 Thickener

Although the base oil determines the ability of a grease to lubricate a contact during the bleeding-phase, over the vast majority of the grease life, during the initial churning stage, and very slowly rotating bearings, thickener enters the contact. This gives a comparatively thicker film than oil at these operating phases. The thickener also governs the majority of grease properties other than film thickness such as tackiness, dropping point etc. Soaps are the most common grease thickener used. They dissolve into the base oil, forming bonds with the base oil chains. Soaps with longer chains have an increased solubility of oil, meaning the grease is thickened more and bleeds oil less readily. Oil separation can also be reduced by decreasing the thickener-base oil ratio [54].

Insoluble, inorganic thickeners are less common, and work by dispersing a powder into the oil that binds to the base oil chains. The main benefit to this thickener type is they have no melting point, meaning the operating temperature limit is determined purely by the oxidative capabilities of the oil, and not the dropping point of the grease [39]. This allows the grease to operate in more extreme temperature conditions when compared with a soap-thickened grease.

2.6.1.3 Additives

Additives make up the smallest volume contribution towards the overall grease, but their impact on performance can be substantial. Many additives are the same as used for a lubricating oil, as discussed in Section 2.4.2, and so will not be repeated. Grease is advantageous in that it can carry solid additive particles which can greatly improve lubricant performance, particularly under extremely heavy loading. Such particles include graphite, Teflon, zinc oxide and others, all of which can reduce surface wear [54].

2.6.2 Grease Churning

When a bearing is rotated with fresh grease, the lubricant undergoes a churning phase, whereby there is macroscopic flow of grease from the swept area, where the rollers pass, to the unswept areas either side of the contact patch [55]. As thickener enters the contact along with the base oil during churn, there is a thicker contact film during this phase when compared with just the base oil [56]. Churning can be broken down into two sub-phases. The first is the channelling phase where Chata & Lugt [35] state $90\% - 95\%$ of the grease is pushed by the elements to the un-swept area in the first few minutes. During churning the bearing temperature increases due to high drag forces, as the rollers push through the grease, as shown in references such as [57, 55] among others. This combination of high temperature and shear forces causes thermal and mechanical degradation of the grease [58].

After channel formation, there is then a clearing phase where the grease reservoirs leak back onto the track and are then re-pushed back into the channels. Clearing is the process of removing the remaining 5%-10% of grease from the swept area. This greases moves in and out of the running track during this clearing phase, but remains stationary in the unswept area when the shear force can no longer meet the grease yield stress, which marks the transition from the churning phase to the bleeding phase. Figure 2.4 shows the process of grease churn through to the bleeding phase within the bearing.

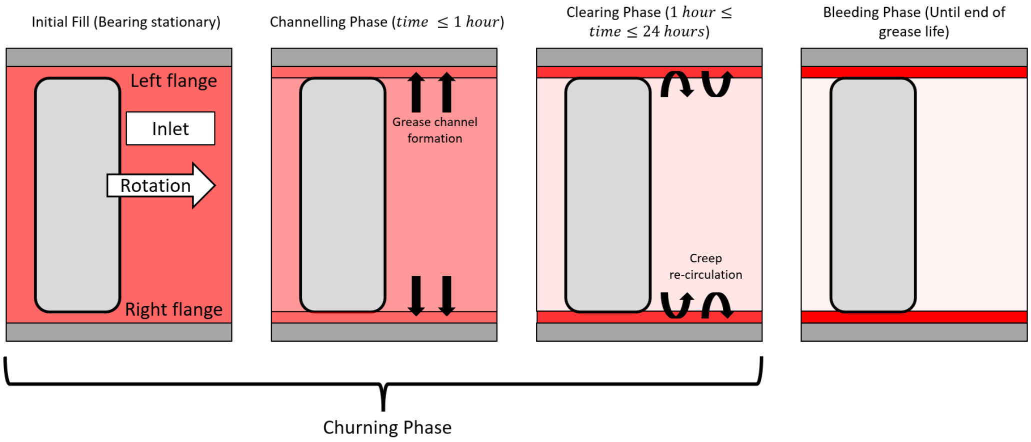

Figure 2.4: Transition from left to right of grease churning, forming side reservoirs in the unswept area, to the semi steady-state bleeding phase. The opacity of the grease relates to film thickness; during churn the film leading directly into the contact thins, and thicker lubricating reservoirs form either side of the swept area

During churn there is additional drag forces due to the grease, and so efficiency is low; a shortened churn time is therefore desirable. Churn can be monitored via bearing temperature, where there is initial rise due to the lubricant drag force, then stabilisation and finally temperature reduction as the channels are formed and the bearing enters a more steady-state bleeding phase. This temperature pattern is expected to mirror that of a frictional torque measurement, however it is noted by Chatra et al. [59] that such a measurement is difficult to take at high speeds.

As the grease is churned there will be a breakdown and degradation of thickener fibres from the original length to a shortened state. Chatra et al. [55] showed that greases that churn quickly show a gradual linear reduction in grease yield stress during churn, which stabilises when a critical energy is met. Greases that take longer to churn have no gradual decrease, and yield stress is constant until the bleeding phase, at which point there is a sudden and steep decrease, and so require a larger critical energy input to achieve churn, see Figure 2.5. The amount of fibre breakdown was linked to duration of churn; grease with higher critical energy input demands take longer to churn and therefore undergo more degradation, leading to more severe fibre breakdown.

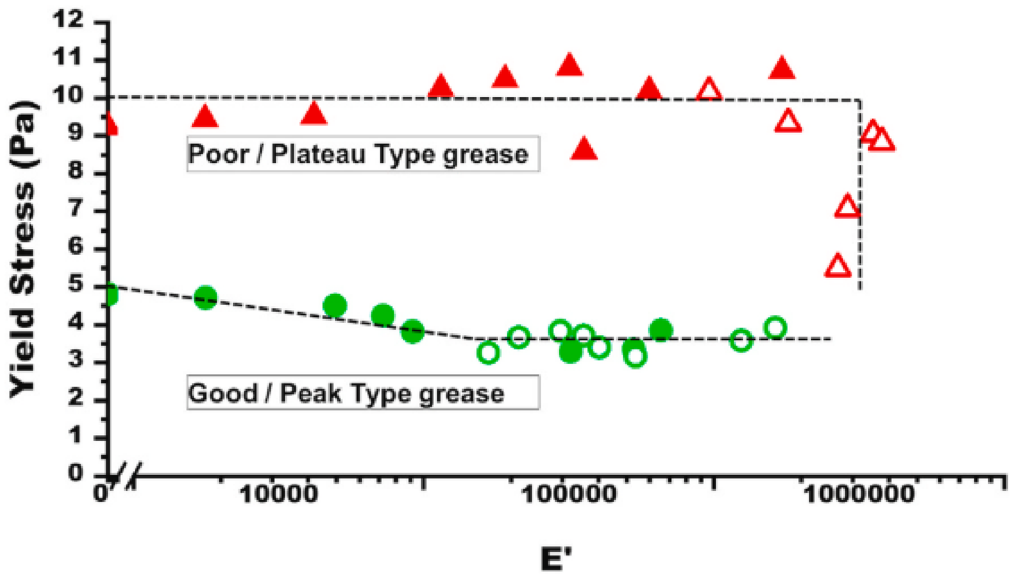

Figure 2.5: Yield stress vs. critical energy during greased bearing operation under controlled temperature conditions. Closed symbols results taken during churning phase, and open during the bleeding phase; taken from Chatra et al. [55]

Governance of churn time is complex and still not fully understood. Speed has been shown to increase the length of the churning phase [60, 35]. This is due to a more violent and dynamic side-flow from the running track to the un-swept areas. At lower speeds the velocities are reduced and so this channel formation happens smoother and quicker. With increasing load Cen & Lugt [60] observed reduced reflow times, indicative of a quicker grease churning phase. This effect is most likely driven by more aggressive shearing which ages the grease at a quicker rate and promotes more bleeding, allowing quicker stabilisation of the film. Grease fill heavily governs churn time but there can be large variations in time even with identical fills and filling procedures; Lugt et al. [57] described the churning as deterministic chaotic behaviour based upon these results. The variations have been attributed to extremely small changes in initial fill and large variations of rheology in the initial rollings [55].

There exists a monotonic relationship between temperature and oxidation rates, with oxidation causing chemical degradation to grease. Lugt et al. [61] says that hybrid bearings have lower oxidation rates due to a smaller metallic surface area within the bearing, which could potentially alter churn time. However, the work in [61] looks at grease life (not specifically the churning event) which is not reached until long after churning and so this is unverified.

Chatra et al. [55] observed that grease with a more desirable, shorter churning phase have more "microstructural flexibility" meaning that under shear the fibres are more prone to rearrangement and entanglement. Grease that took longer to churn had less microstructural flexibility and had far more fibre degradation when observed using Atomic Force Microscopy. Xu et al. [62] observed that with increased entanglement there is a higher structural strength, and therefore resistance to shear degradation.

In general, grease churn is still not fully understood and needs more research into understanding the grease/rheological properties which relate to churn time [55]. Of particular benefit would be an in-situ monitoring of grease distribution and rheological properties to help determine the causation of longer or shorter churn times.

2.6.3 Oil Bleed

For grease to work, the oil must be purged from the thickener to lubricate a contact via 'bleeding', and this 'bleed-oil' has the largest contributing factor, of any of the grease components, to lubricating the bearing [54]. Bleeding is therefore critical for bearing performance, and indeed grease manufactures optimise oils and thickeners to match the bleed requirements of the bearing. Grease bleed can occur statically due to temperature fluctuations, vibrations and storage facilities. However this is not detrimental to the grease, and mixing can re-emulsify the grease [63]. When inside a bearing, the dynamic conditions cause bleed through thermal changes and the mechanical mechanisms of surface tension, centrifugal and capillary forces [64].

The oil bleed rate defines the rate at which oil separates from the thickener to lubricate the bearing. Different bearings require different bleed rates to properly operate, but all greases must have the ability to bleed somewhat. If the bleed rate was to be $0\text{mm}^2/\text{s}$ then no oil would be released and the bearing would starve, with premature wear occurring immediately. On the contrary, if the bleed rate was very high, a majority of the oil will be released early in the grease life, reducing the oil availability in the thickener for the long term operation. Oil concentration is a key contributor to the bleed rate, and so a low oil volume will result again in premature wear once the initial release has been swept away by the rollers. Bartz showed that electric motors running at $T = 125°\text{C}$ fail when the grease loses 50% of its oil [65].

Cousseau et al. [66] compared base oil and grease lubricating performance by measuring the frictional torque in a thrust ball bearing. Results showed that the base oil performance, in comparison with the grease, was not comparative and that the base oil generated higher friction levels. However, Cousseau et al. [67] later compared the film thickness generated by a grease, its base oil, and its bleed-oil (extracted statically according to a modified IP 121 test method) and found significant difference between

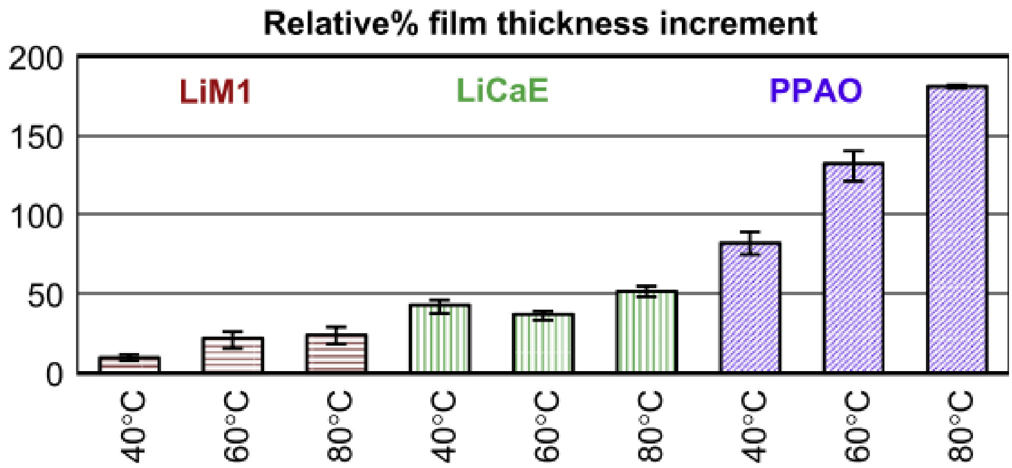

Figure 2.6: Relative film thickness increase of bleed-oil compared with base oil. Taken from Cousseau et a. [67]. LiM1 is a mineral oil, lithium thickened grease. LiCaE is an ester oil, lithium and calcium thickened grease. PPAO is a polyalphaolefin oil thickened with polypropylene and an elastomer

the bleed oil and base oil. For three greases of different base oil and thickener types, the extracted bleed-oils had different viscosity and pressure-viscosity values compared with the base oil. For Lithium thickener with a mineral base oil and lithium/calcium thickener with an ester base oil, the bleed-oil had very similar dynamic viscosities, but the pressure-viscosity coefficient α was increased by 38% to 87% based on the temperature. A PPAO polypropylene grease, co-thickened with an elastomer with a PAO base oil showed the largest change in α (between 79% and 89%) but this was reduced in comparison with the base oil. However, Figure 2.6, taken from [67], shows that all bleed-oils tested had an increase in the measured film thickness in comparison with the base oil.

Despite the PPAO having a decrease in α, this bleed-oil showed the largest increase in film thickness. Interestingly, this bleed-oil had by far the largest increase in viscosity from base oil to bleed-oil (1264% at 40°C). The findings of the study therefore support the theory presented by Crook [50] and later Cann et al. [51] that the viscosity of lubricant at the inlet meniscus is the driving factor that determines the contact film thickness. The most remarkable point of the study was the suggestion base oil is not the best indicator of a grease film thickness but instead the bleed-oil, which has very similar thickness values to the fully formulated grease and therefore can be used as a predictor of film thickness through common models such as those presented by Dowson or Hamrock.

Huang et al. [68] completed a thorough study into point contact starvation and reflow times for greases of different thickener and oil types on a ball on disc setup. The grease bleeding rate was found to be a primary contributor to reflow and therefore avoiding starvation. The base oil type (PAO, ester etc.), the base oil viscosity and the thickener type were all found to influence reflow and film thickness but in different ways. A summary of the effects can be found in Table 2.2.

Base oil type	Base oil viscosity	Thickener Type
Intermolecular attraction of oil to grease heavily influences bleed rate	Higher viscosity forms thicker film	Thickener type mainly influences the reflow thickness
If attraction is strong, less oil separates, regardless of its viscosity	Lower viscosity increases bleed rate and reduces reflow time	Lithium thickeners are broken down and sheared through the contact, meaning reflow thickness is always less than initial thickness
Lithium thickened grease has stronger intermolecular bonds with ester oils than PAO oils	Lower viscosity has a thicker **minimum** film thickness as reflow is improved	Silica grease is not broken during shearing, and so reflow thickness can match initial thickness
	Oils with lower pressure-viscosity coefficients stay more fluid within the contact, and therefore leak more readily	Diurea thickened grease showed evidence of urea absorption into the metal, and a chemical deposited layer that maintained a constant film thickness regardless of reflow

Table 2.2: Summary of effects of grease properties on bleed rate and film thickness from Huang et al. [68]

2.6.4 Film Thickness of Grease Lubricated Contacts

The thickness of greased contact films has a clear dependence on time/number of rollings which is not seen for oil lubricated contacts. This time-dependent relationship was observed in [69, 51, 70, 56] and others, and is due to starvation and replenishment phenomenon.

During the churning phase a combination of thickener and oil enter the contact, and so the contact thickness is greater than that of just base oil which occurs in the later bleeding phase [71, 72, 73]. Cen et al. [56] found a similar conclusion that at low speeds the grease film thickness is greater than that of the base oil. However, there was an observed transition speed above which the grease and base oil film thickness were comparable.

Where there is a contrast in ideas is the prediction of film thickness within grease lubricated contacts that are fully flooded; using either the base oil properties or the bleed-oil properties. It was originally assumed that the base oil properties would be a good indicator of film thickness. The design intention of the thickener is to act solely as a mode of transport for the oil to the contact, and as a retainer for oil which is not yet bled. As the thickener is degraded and separated from the oil during churn, Zhu & Neng [74] made the fair assumption that the film thickness could be calculated using the base oil properties.

Cousseau et al. [67] showed that the base oil and bleed-oil can have very different viscosities and pressure-viscosity coefficients, and thus argued that it is the bleed-oil properties which should be used to calculate film thickness. However, this has been disputed by Cen et al. [56] and Kanazawa [75] where it was found that base oil properties, not bleed-oil, were found to be appropriate for the calculation of central film thickness, so long as the bearing speed was kept high and the grease churned.

Figure 2.7 shows the work of Kanazawa et al. [75] where the film thickness of grease and its constituent base oil were measured and found to be almost identical with increasing entrainment velocity after a low speed inflection point.

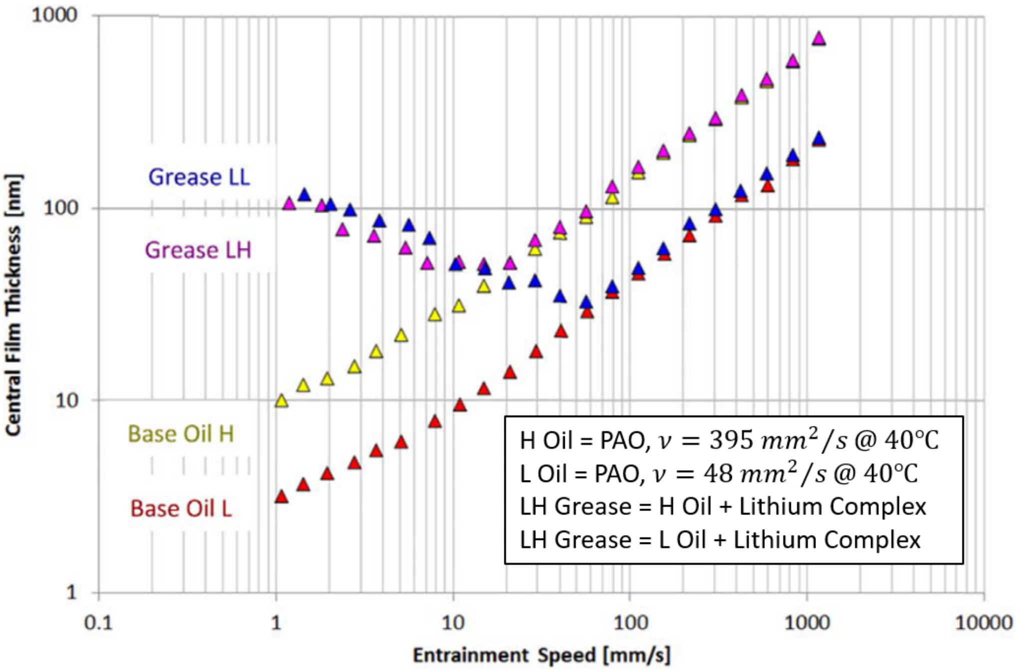

Figure 2.7: Measured central film thickness with increasing entrainment speed for grease and base oil at 70°C, adapted from [75]

2.6.4.1 Grease Thickness at Ultra-Low Speed

At ultra-low speeds grease lubricated contacts show a very stark 'V' shape pattern on a film thickness vs. speed plot, see Figure 2.8. The inflection point of this plot is often referred to as the transition speed. Above the transition speed the grease film thickness is governed entirely by the base oil and follows the same oil EHL trend [76] with an increasing film thickness with speed. Below the transition point the relationship is opposite, and there is a film increase with decreasing speed [56]. This trend occurs because at such a low speed the contact is filled with thickener agglomerations as well as base oil. Cen et al. [56] give the transition speed as around 0.01m/s.

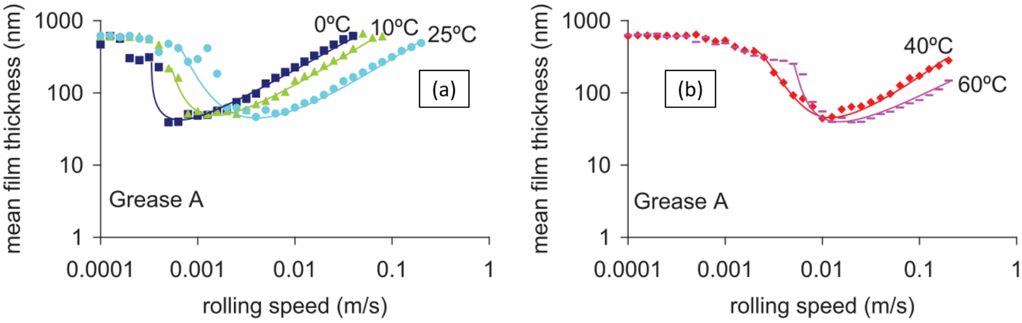

Figure 2.8: Mean film thickness of lithium based grease with increasing speed in the ultra-low speed range with (a) 0, 10 and 25°C (b) 40 and 60°C, taken from [56]

Similar transition plots for grease are shown in Figure 2.7 from Kanazawa et al. [75]. However, The inflection point in this plot is greater than 0.01m/s and varies with base oil viscosity, but the film thickness at the transition point is $30 - 60$nm. A similar trend is seen in the same study for diurea grease with varying transition speeds but similar transition thicknesses. The authors therefore argue that at lower speeds, the thickness speed inflection point is actually related to fibre agglomeration thickness, and that as the speed decreases there is deposition onto the contacting surfaces which allows the film growth.

2.7 Bearing Failures

Bearing failures are either surface or sub-surface initiated. The primary failure mechanism for bearings is rolling contact fatigue (RCF) which is used as a predictor of bearing life [28]. Even if a bearing is adequately lubricated and operated within its designed for conditions, it will still eventually fail due to the material fatigue limit via RCF. RCF occurs over time due to a high number of loaded revolutions which leads to subsurface cracks. These cracks eventually propagate to the surface leading to spalling, a surface material loss [20]. White etched cracking, a failure mechanism particularly prevalent in the wind industry, is a form of rolling contact fatigue [23]. Sub-surface failures such as RCF cracks form below the contact, in the bulk of the material and can be worsened by improper material selection, manufacturing defaults and excessive loading. Figure 2.9c & d show examples of spalling and white-etch cracking.

Surface initiated failures are primarily due to a lack of lubrication, or the incorrect lubricant used. If the wrong lubricant is used the contact is either not fully flooded leading to starvation, or a film is formed but is not adequately thick for the application. Both of these scenarios lead to increased asperity-asperity contacts and abrasive and adhesive wear phenomenon such as micropitting, smearing, fretting, gauging and more [21], see Figure 2.9a & b. A major issue with poor or improper lubrication is a temperature rise due to frictional heating. This can lead to material softening and worsening of surface wear mechanisms. Additionally, elevated temperatures reduce the elasticity of bearing steels, thus accelerating RCF [77].

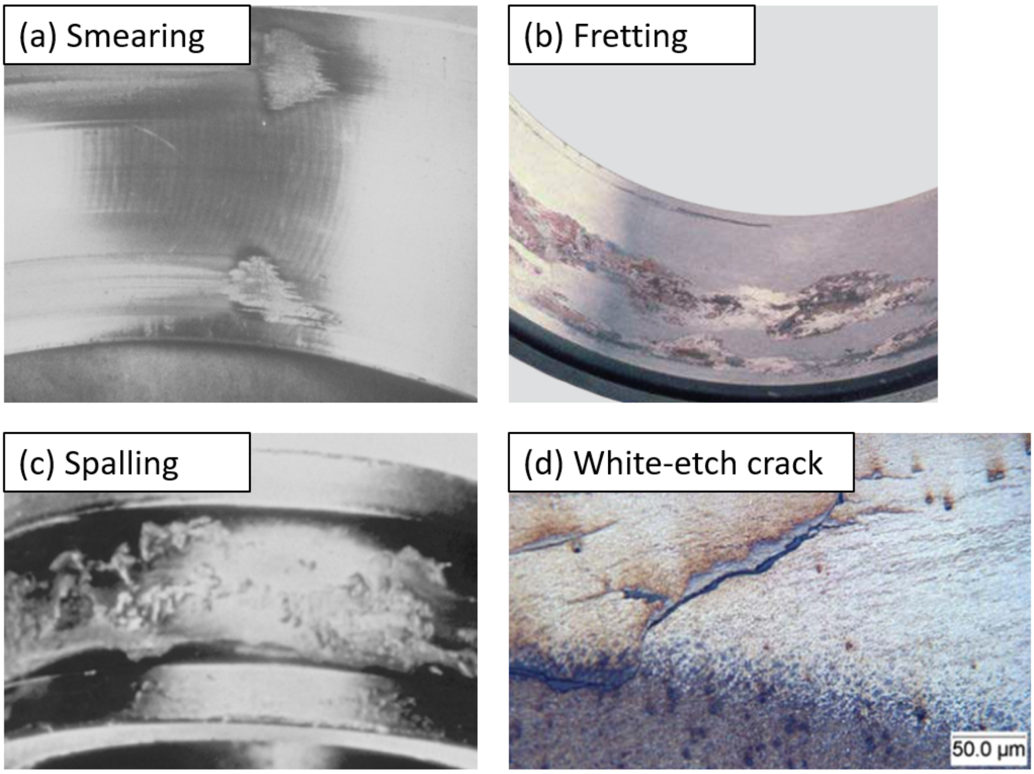

Figure 2.9: Examples of failed bearings of which improper lubrication can contribute towards [26, 21]

2.8 Conclusion

- Within this chapter, the fundamentals of bearing function and operation have been outlined, and the importance of proper lubrication conditions to avoid premature wear has been emphasised. The constituents of fully formulated oils and greases have been discussed, along with the benefits of using either one.

- Rolling element bearings require lubricant to separate the metal-metal surfaces within the contact. Due to the high contact pressure rolling element contacts operate in either mixed or EHL lubrication, often depending on the lubricant supply.

- If the lubricating system (oil or grease) does not adequately provide oil to the rolling contact, premature wear can be expected, and the bearing component will not meet its expected life.

- Oil or grease can be used depending on the application. Each have various advantages and disadvantages

- Fully formulated lubricating oils are made by combining a synthetic or mineral oil with an additive package that enhances beneficial qualities and subdues disadvantageous qualities of the oil.

- Oil lubrication has a greater body of research and is therefore more understood and able to be modelled and predicted. Grease film modelling is much more difficult due to its complex rheological behaviour.

- Grease is made from combining a fully formulated oil with a thickener, but a majority of grease (up to 95%) is still oil. Grease can contain different, solid particle additives that oils cannot, which can greatly improve lubricating performance.

- Grease first goes through a churning phase, made up of an additional channelling and clearing phase. Channelling is expected to be complete within the first hour of operation, and moves 90% to 95% of grease to the unswept areas to form reservoirs. This is followed by clearing where there is grease creep and recirculation into and out of the swept area. The bleed phase is determined by the end of the clearing phase.

- During churn there is a high level of thermal and mechanical stress upon the grease. There is no unified theory on what causes short or longer churning times; in-situ measurements of grease flow and mechanical properties would be advantageous to explore the churning mechanism.

- For grease to lubricate, bleed oil is released from the thickener due to mechanical or thermal stress. Bleed-oil differs from the base oil as characteristics of the thickener and additives are imparted into the oil.

Chapter 3

The Principles of Ultrasound

Ultrasound refers to mechanical waves above the audible human hearing range of 20kHz. This chapter introduces the generation and fundamental propagation of these waves, external factors that cause wave amplitude reduction, and the complex waveforms that reflect from boundaries with different numbers of layers and intermediary thicknesses. The reflection coefficient is a crucial parameter which gives the proportion of reflected wave amplitude in comparison with the incident wave; the calculation of the reflection coefficient is discussed. Several models, which interpret the reflection coefficient in different ways to calculate an intermediary layer thickness, such as an oil film within a machinery part, are detailed.

3.1 Ultrasonic Wave Propagation

Acoustics is the science of mechanical wave propagation through liquids, solids and gaseous substances via particle oscillations due to internal electrostatic forces and inertia [78]. The upper frequency limit for human audible hearing is 20kHz, above this limit is said to be ultrasonic [79]. Low-intensity, high frequency applications (LIHF) are those with power densities of 1W/cm^2 or lower, and frequencies in the megahertz range. LIHF applications avoid any kind of changes to the medium and instead are used for the detection, investigation and evaluation of the medium to which they are applied. Typical applications therefore involve non-destructive testing (NDT) and ultrasonic biomedical imaging [80, 81].

Krautkramer et al. [79] gives a detailed explanation of plane wave propagation, with a condensed version here. Particles within an elastic material can be thought of as single mass points attached to each other by springs. So long as a material is not stressed above its elastic limit, an ‘excitation’ or displacement can then cause an oscillation of particles leading to a vibration and the propagation of waves. In longitudinal waves, particles oscillate in the same direction as the wave travels. Figure 3.1 shows a 2D representation of this, with the wave moving from left to right. Areas of constriction, where particle planes are in compression, are always adjacent to areas of rarefaction, where planes are in tension. All particles in a single plane are in the same phase of oscillation. The wavelength, λ is the length between two particle planes in identical phase and is the inverse of the excitation frequency.

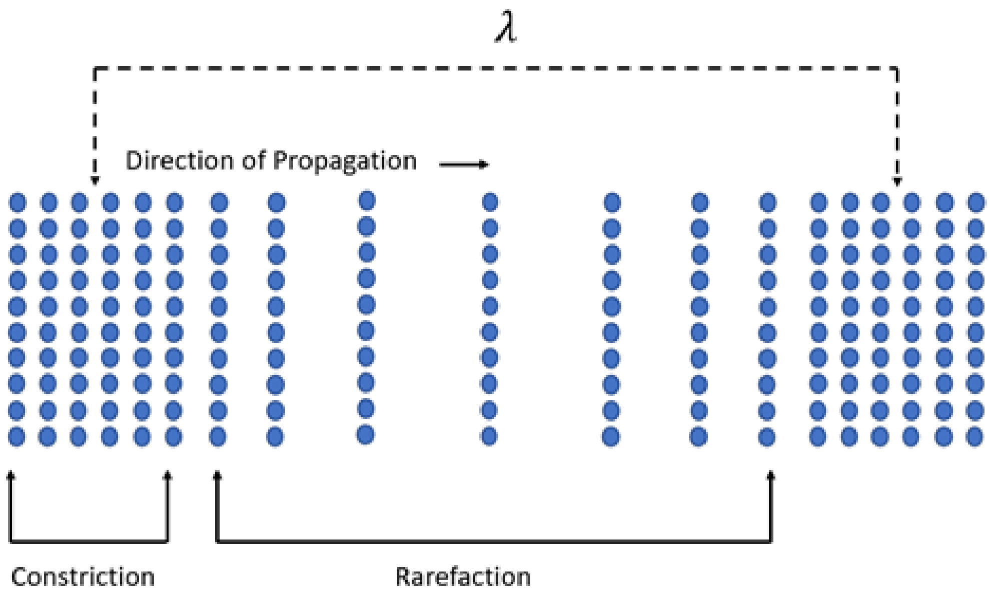

Figure 3.1: Propagation of a longitudinal ultrasonic wave

3.1.1 Acoustic Velocity

The acoustic velocity c describes how quickly a wave propagates, and can be calculated as a product of the the wavelength λ and frequency f:

$$c = \lambda f \tag{3.1}$$

The acoustic velocity varies between materials and is governed by the bulk modulus B and density ρ. Bulk modulus defines a fluid's resistance to compression; the greater the bulk modulus the greater the acoustic velocity, and the relationship is defined as:

$$B = \rho c^2 \tag{3.2}$$

Acoustic velocities can be altered by operating conditions. Stress fields can change the velocity of wave propagation due to the acoustoelastic effect. As described by Egle et al. [82], the magnitude of alteration is dependent on the level of stress, wave mode, and the wave path in relation to the stress axis. The greatest change in velocity occurs for longitudinal waves travelling parallel to the stress axis.

Temperature increases in a solid material mean that individual particles have more kinetic energy, increasing the rate of particle collisions, allowing waves to propagate faster, as described in [83]. In fluids, the temperature increase causes a decrease in fluid density, which alone would cause an increase in c. However, there is a much larger reduction in the fluid viscosity, and this results in an overall decrease in the acoustic velocity.

3.1.2 Attenuation

Attenuation is a diminishing signal effect, where the amplitude of a wave decreases as it propagates through a material. There are several key influences as to the level of attenuation, as described by Ensminger et al. [33].

Absorption The transfer of kinetic energy during particle collisions is not perfect, and some energy is transformed into heat, diminishing the total wave energy.

Scattering As no materials are truly homogeneous, when discontinuities, grain boundaries, voids, etc. of a metallic material are within the travel path of a wave, scattering occurs. Higher frequency waves with smaller wavelengths are more prone to scatter effects as the ratio between the scatter feature size and wavelength is reduced.

Beam Spread As a wave propagates particle collisions are not always perpendicular to the direction of propagation due to particle planes misalignment and shear wave influence [34]. Therefore, some particles diverge from the central travel path of the wave, which adds to the diminishment of the wave amplitude.

3.2 Ultrasonic Wave Interaction with a Boundary

When an ultrasonic wave strikes the boundary between two acoustically different materials, a portion of the wave energy will transmit into the second material, and the remainder will be reflected. Figure 3.2a shows a representation of this where p indicates a pressure wave and the subscripts i, t and r represent the incident, transmitted and reflected waves respectively.

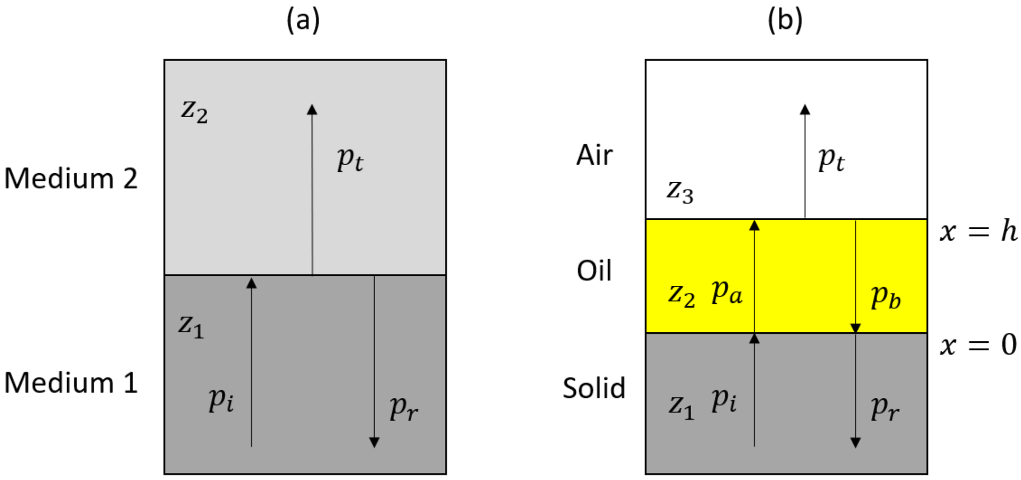

Figure 3.2: Pressure wave interaction with a single boundary and double boundary in (a) and (b) respectively

The proportion of wave energy which is transmitted and reflected is based on the acoustic impedance mismatch between the two materials. The acoustic impedance z is a measure of a material's ability to accommodate wave transmission, and is the product of its density ρ and speed of sound c:

$$z = \rho c \tag{3.3}$$

The reflection coefficient R quantifies the reflected proportion and is calculated in Equation 3.4:

$$R = \frac{z_2 - z_1}{z_2 + z_1} \tag{3.4}$$

From this equation it is clear that greater acoustic mismatches lead to a greater proportion of the wave being reflected. The proportion of wave energy transmitted is referred to as the transmission coefficient T. The theoretical maximum value for either coefficient is 1, representing either total transmission or total reflection [84].

If two materials had identical acoustic impedances, for example two steel blocks of the same grade, and both had perfectly smooth faces, when pressed together it is clear from Equation 3.4 that it would be as if no boundary existed, meaning complete transmission, and so $R = 0$. Alternatively, if two materials had greatly differing acoustic impedances, such as steel ($z_{steel} \approx 4.7 \times 10^7 \text{kg/m}^2\text{s}$) and air ($z_{air} \approx 0.4 \times 10^3 \text{kg/m}^2\text{s}$) then a majority of wave energy would be reflected, $R_{steel-air} = 0.9999872 \approx 1$.

For thin film and coating measurements the reflection from a single boundary is of no interest as these measurements are often of a two-boundary contact, as shown in Figure 3.2b, which complicates the reflection pattern. Depending on the distance between the two boundaries there are multiple ways the reflected signal is affected.

Figure 3.2b shows a schematical representation of a steel-oil-air system. Here the initial incident, transmitted and reflected wave occur across both boundaries. p_a and p_b represent the first transmitted wave across the $x = 0$ boundary and the reflected wave from the $x = h$ boundary respectively. In a real contact, as the wave splits at every boundary, there would be several reverberations of these transmitted and reflected waves within this middle oil layer.

3.2.1 Time of Flight

The time-of-flight (TOF) approach is the most basic approach to measure the middle layer of a two boundary system. When an incident wave, such as p_i in Figure 3.2b, travels through the first media, it will split into smaller amplitude transmitted and reflected waves, p_a and p_r respectively at the first boundary where $x = 0$. The p_r wave will be recorded by the sensor, but the p_a wave will continue to travel through the second media, an oil layer in this case, and split again at the boundary $x = h$. This will form a second transmitted wave p_t and reflected wave p_b. The p_b wave then travels back to the first boundary at $x = 0$, splitting again, and in doing so forms a second p_r wave which is recorded, at a delay, from the first p_r wave. Figure 3.3 shows an example reflections from an unconstrained oil film.

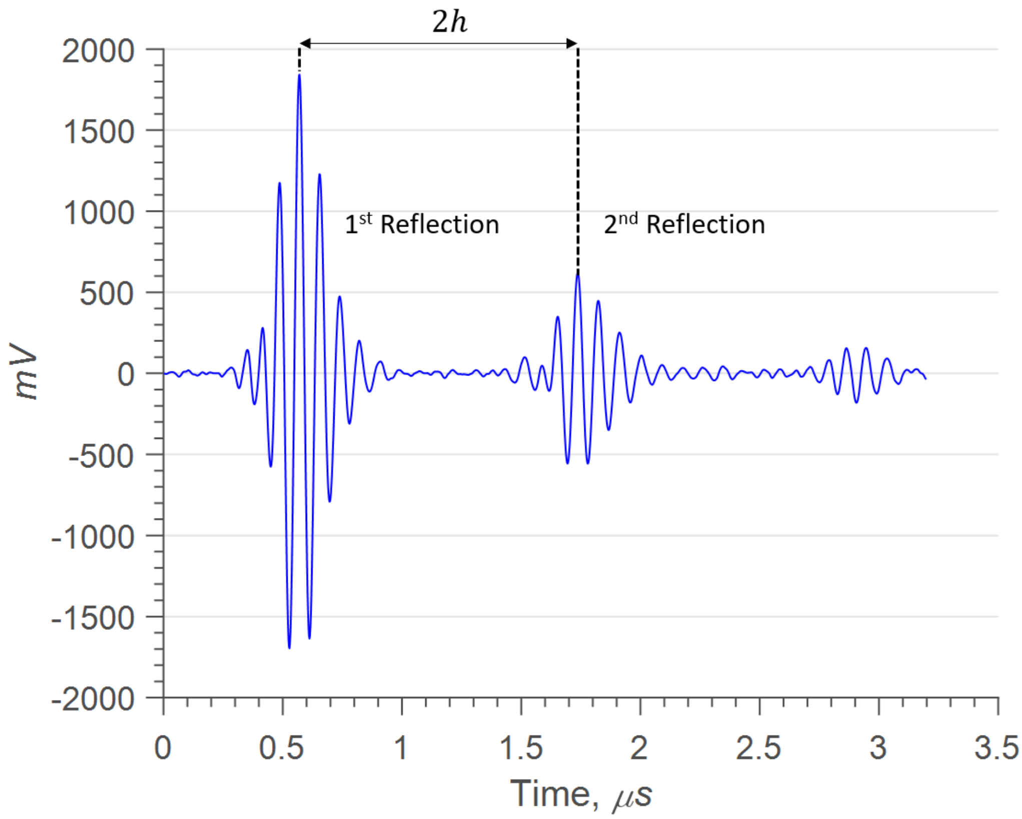

Figure 3.3: Time delay between first and second reflections from an unconstrained oil film which is measurable via the TOF approach

Between the first and second reflection the wave has travelled the distance of the second medium twice. If the velocity through he second medium is known, the layer thickness can be calculated from the time delay Δt as:

$$h = \frac{c\Delta t}{2} \tag{3.5}$$

For the example in Figure 3.3, $c = 1453$m/s and $\Delta t = 1.17\mu$s giving a film thickness $h = 847\mu$m. For the TOF method to be applicable, there must be ample spatial resolution in the time domain for the first and second reflections to be distinct from one another. With thinner films the first and second reflections overlap, becoming indistinguishable. Practically, using a 10MHz sensor a layer must be $h \geq 300\mu$m to be measurable via TOF. If any thinner the reflections overlap and a different measurement approach is required.

3.2.2 Spring Model

If the middle layer of a 3-body system becomes very thin in comparison with the wavelength, such as an EHL roller bearing contact film, the reflections from the first and second boundary overlap and become superimposed, meaning the TOF approach is not suitable. In 1971 Kendall and Tabor [85] experimentally showed that the ultrasonic wave transmission and reflection across a contact, where the middle layer is made of air, was governed by the contact stiffness K, and therefore could be modelled as a spring-mass system. Thomas & Sayles [86] state this relationship for stiffness per unit area based on the nominal contact pressure p_{nom} and the approach of the mean lines of surface roughnesses h:

$$K_s = -\frac{dp_{nom}}{dh} \tag{3.6}$$

where subscript s represents an unlubricated, solid stiffness. Equation 3.6 shows that as load increases, so too does the contact pressure, resulting in a reduced separation and therefore higher contact stiffness. Tattersall [87] then showed that the relationship between the ultrasonic reflection coefficient and contact stiffness can be modelled as:

$$R = \frac{z_1 - z_3 + i\omega(z_1 z_3/K)}{z_1 + z_3 + i\omega(z_1 z_3/K)} \tag{3.7}$$

where ω is the angular frequency, and z_1, z_3 refer to the acoustic impedances of the materials either side of the contact. The imaginary part relates to the phase and the real part to amplitude. The real part can be defined as:

$$|R| = \sqrt{\frac{(\omega z_1 z_3)^2 + K^2(z_1 - z_3)^2}{(\omega z_1 z_3)^2 + K^2(z_1 + z_3)^2}} \tag{3.8}$$

If the materials either side of the sandwiched layer are the same and have identical acoustic impedances ($z_1 = z_3$), the real portion of Equation 3.7 can be simplified to:

$$|R| = \frac{1}{\sqrt{1 + (\frac{2K}{\omega Z})^2}} \tag{3.9}$$

Drinkwater et al. [88] used the spring model to investigate the reflection from two contacting aluminium plates under a range of loads. The spatial resolution of the sensor encompassed asperity contacts of high transmission, and air gaps of low transmission, and therefore gave a mean R value across the sensing area. As load increased the solid stiffness and real asperity contact increased, causing R to reduce towards the theoretical limit of $R = 0$.

Dwyer-Joyce et al. [89] then developed the method further, including the asperity variance of summit height and asperity density per unit area into the dry contact stiffness calculation along with contact pressure and Hertzian elastic modulus. The aim of the work was to measure the film thickness in an EHL contact which means including a lubricating layer within the contact stiffness. Hosten [90] defined the liquid stiffness as:

$$K_l = \frac{B}{h} \tag{3.10}$$

where B is bulk modulus and in [89] was calculated from Bair [91]:

$$B = \left\{1 - \frac{1}{1 + B_0'} \ln \left[1 + \frac{p}{B_0}\left(1 + B_0'\right)\right]\right\} \left[B_0 + p\left(1 + B_0'\right)\right] \tag{3.11}$$

where B_0 is the bulk modulus at ambient pressure, p is applied pressure to the liquid ($p = 0$ when ambient) and B_0' is the rate of of change of B which is approximately 11 [91]. The total contact stiffness was then calculated as the product of the lubricant stiffness and dry contact stiffness ($K_t = K_l + K_s$). Measured results from a dry and lubricated contact agreed well with the model results from the mixed stiffness approach. Figure 3.4 shows a schematic of the spring model for (a) a fully lubricated case where load is supported by just K_l and (b) a mixed lubrication case where asperity contacts also add to the total stiffness value.

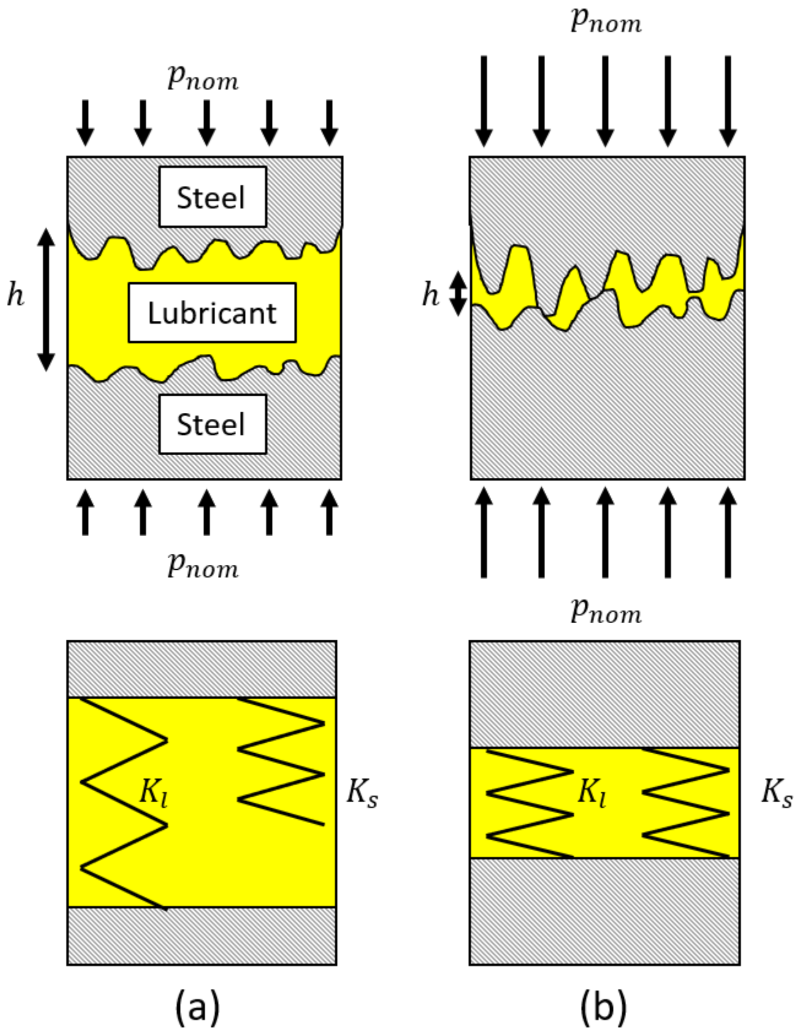

Figure 3.4: Visualisation of the ultrasonic spring model. Case (a) fully separated contact and case (b) mixed lubrication

Dwyer-Joyce et al. [84] discuss the spring model limitations. The thinnest film measurable via the spring model is governed by the frequency of sensor used and the acceptable signal-to-noise ratio (SNR) so that a reflection is distinguishable from the system noise. Using a high 60MHz sensor a 2nm film can theoretically be measured. For thicker films, as the middle layer continues to thicken the stiffness change is less prominent to the point where the spring model becomes insensitive and tends towards unity. Practically films of $h < 20\mu$m have been measured using this approach [92]

3.2.3 Resonance Approach

For films in the range greater than those detectable using the spring model, but thinner than those measurable via the TOF method, a resonance approach can be taken. The case of the complex reflection coefficient, from a layered material, in terms of pressure was given by [93]:

$$R = \frac{R_{23} + R_{23}^{(2i\alpha_2 h)}}{1 + R_{12}R_{23}^{(2i\alpha_2 h)}} \tag{3.12}$$

where R_{12} and R_{23} are the reflection coefficients at the first and second media boundaries, such as $x = 0, h$ shown in Figure 3.2b. α_2 is a coefficient referring to the second medium, defined as:

$$\alpha_2 = k_2 + i\beta \tag{3.13}$$

Where β is the attenuation coefficient and c_2 is the wave velocity through the middle layer, k_2 is the wave number calculated as:

$$k_2 = \frac{2\pi f}{c_2} \tag{3.14}$$

Although Equation 3.12 is complex, incorporating amplitude and phase, Haines et al. [94] gives an equation for the real, amplitude portion:

$$|R| = \left[\frac{(R_{23} + R_{12}e^{-2\beta h})^2 - 4R_{12}R_{23}e^{-2\beta h}\sin^2 k_2 h}{(1 + R_{12}R_{23}e^{-2\beta h})^2 - 4R_{12}R_{23}e^{-2\beta h}\sin^2 k_2 h}\right]^{1/2} \tag{3.15}$$

Figure 3.5 shows the modelled real amplitude portion of the reflection coefficient calculated from Equation 3.15 for four different oil film thicknesses.

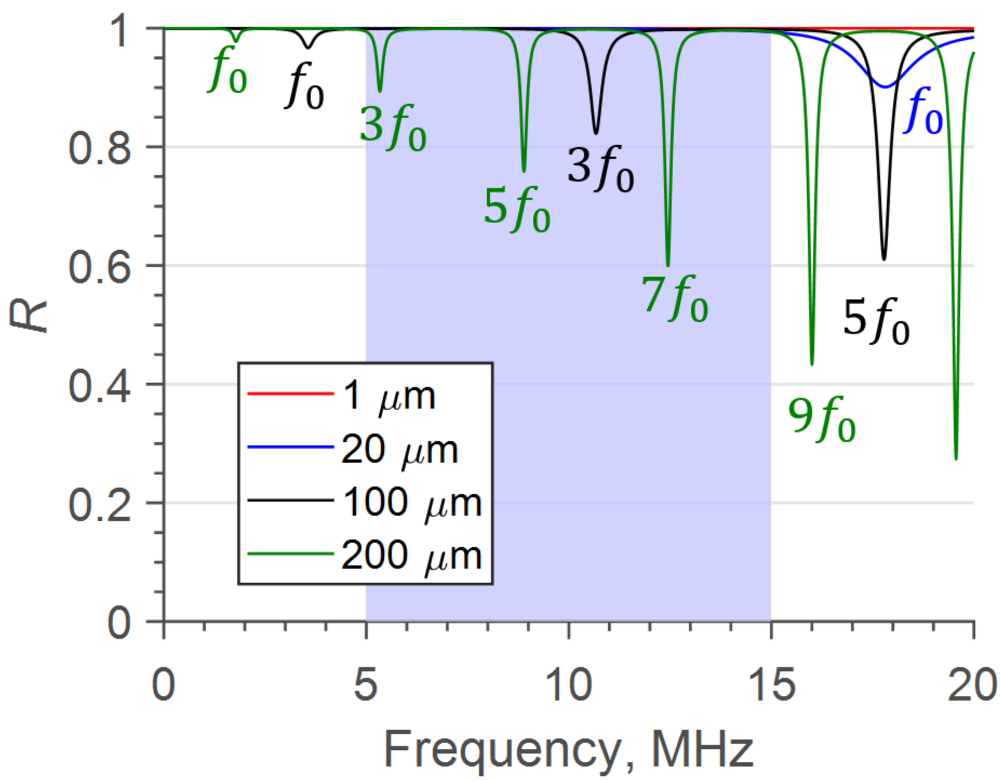

Figure 3.5: Model of resonance response at different layer thicknesses

Kinsler et al. [95] explains when a wave travelling through an acoustically soft material reaches the boundary with an acoustically harder material $z_1 < z_2$ the reflected portion of the wave is perfectly in phase with the incident wave. When $(z_1 > z_2)$ the reflected wave is 180°out of phase with the incident wave. Transmitted and incident waves across a boundary are always in phase regardless of acoustic impedances at a boundary. These rules still hold true at $x = 0, h$ in a 3-body system. However, the phase between the transmitted wave p_a from the first boundary and the reflected wave p_b from the second boundary changes based on the distance between boundaries i.e. the thickness of the middle layer.

Haines et al. [94] showed that when $z_1 > z_2 > z_3$ the middle layer resonates at odd integer multiples of the fundamental frequency $(f_o, 3f_o, 5f_o, etc.)$. These resonances are clear from Figure 3.5, and are seen as dips in R. The resonant frequencies are calculated by the following:

$$(2n + 1)f_o = \frac{(2n + 1)c_2}{4h} \tag{3.16}$$

where n is any integer value $(n = 0, 1, 2, 3, \ldots)$. At these particular frequencies, p_a and p_b interfere to create a short duration standing wave, greatly reducing the amplitude of p_r. This is then observed by a drop in the reflection coefficient. The first of these resonances is the fundamental frequency, f_o. To find the relationship between fundamental frequency f_o and film thickness, Equation 3.14 is used with $f = f_o$, multiplied by the thickness of the middle body h, and equalled to the phase change when $n = 0$:

$$\begin{aligned} k_2 h &= (2n+1)\frac{\pi}{2} \\ \therefore \frac{2\pi f_o h}{c_2} &= \frac{\pi}{2} \end{aligned} \tag{3.17}$$

And so:

$$h = \frac{c_2}{4 f_o} \tag{3.18}$$

Equation 3.18 shows that $h \propto 1/f_o$ and so the thicker films have smaller fundamental frequencies and thinner films have larger fundamental frequencies. This is shown in Figure 3.5, which compares model data of films between 1μm and 200μm. The 1μm film shows no detectable reduction in R across the presented bandwidth, demonstrating that there is a lower limitation of the resonance method. In reality, a resonance would occur if the layer could be excited by a high enough frequency, but an increased frequency leads to more attenuation, and thus a diminishing reflection amplitude. The 20μm fundamental frequency occurs at $\approx$ 18.75MHz. The thicker films have lower fundamental frequencies; for the 200μm film $f_0 \approx 1.8$MHz and further resonant dips are seen at approximately 5.4, 9, 12.6MHz which are the higher order odd harmonics. For a metal-oil-air contact resonances occur at odd integer multiples of the fundamental frequency. Other film thicknesses also have multiple resonances, though the thinner films have higher fundamental frequencies, and therefore the higher order resonances occur at even larger frequencies.

When measuring resonant frequencies it can be difficult knowing which harmonic is detected if only one dip is present, and this is discussed in the validation work of this thesis in Section 7.6 of Chapter 7. However, if multiple resonances are detected, knowing the frequency difference is $\Delta f = 2f_0$ between harmonics, the following relationship can be made where $\overline{\Delta f}$ is the mean measured frequency difference between dips:

$$h = \frac{c_2}{2\overline{\Delta f}} \tag{3.19}$$

This can be a much more practical measurement approach, especially with a limited frequency bandwidth.

Swapping c_2 for terms in Equation 3.1 into Equation 3.18 shows that the middle layer resonates at its fundamental frequency when its thickness is a quarter of that of the ultrasonic wave:

$$h = \frac{\lambda}{4} \tag{3.20}$$

This resonance occurring in media at a quarter of the interacting wavelength is seen in other wave interactions, such as coupling piezoelectric elements to water and air [96], and coupling ultrasonic matching-layers with metals in ultrasonic viscometers [97]. Higher order odd harmonics occur at higher odd integer multiples of a quarter of the wavelength. For example, where $n = 3$, using Equation 3.16:

$$\begin{aligned}
&(2 \times 3 + 1)f_o = (2 \times 3 + 1)c_2/4h \\
&7f_o = 7c_2/4h
\end{aligned}$$

A simple rearrangement of Equation 3.18 can make the frequency the subject:

$$f_o = \frac{c_2}{4h} \tag{3.21}$$

Haines [94] also shows that if $z_2 < z_3$, dips in the reflection coefficient occur at even integer multiples of the fundamental frequency $(2f_o, 4f_o, 6f_o, \dots)$ when the second layer is an integer multiple of the half wavelength, $h = \lambda/2$. Pialucha et al. [98] expanded the resonance work into measuring layer thickness of an acoustically soft material sandwiched between two acoustically harder materials. Where m is the mode of the frequency and f_m is the frequency at that mode, Equation 3.22 can be used to calculate the layer thickness.

$$h = \frac{cm}{2f_m} \tag{3.22}$$

As there is a boundary from acoustically hard to acoustically soft then acoustically soft to acoustically hard with this kind of sandwiched layer, resonances occur at all integer multiples of f_0. Resonance analysis is therefore applicable to measuring both free-film and constrained layer thicknesses, so long as the resonances occur within the sensor bandwidth.

The thinnest measurable film using a resonance approach is dependent on the bandwidth of the sensor used for testing. As $h \propto 1/f_0$ thinner films have higher resonant frequencies, and so higher frequency sensors are needed to be sensitive to the film resonance. A 20μm oil film has a resonant frequency of $f_0 \approx 18.75$MHz which is close to the practical limit of the resonance method. The thickest measurable film is dependent on the spatial resolution of resonances within the frequency domain and the number of reflections through the oil layer. With thicker films there are less echoes and thus shallower resonances which are harder to detect [99]. This is discussed further in Section 7.1.1. For the resonance approach $20\mu\text{m} \leq h \leq 600\mu\text{m}$ is appropriate as above or below this either the TOF or spring model is a more accurate film thickness measurement approach.

3.3 Generation of Ultrasound

3.3.1 Piezoelectric Effect

The piezoelectric effect is a property of some crystalline material structures with no centre of symmetry. When a pressure is applied to a piezoelectric material from a mechanical displacement, an electrical charge proportional in magnitude is formed. Likewise, if the material is subject to an electrical charge, a mechanical displacement is caused.

3.3.2 Piezoelectric Elements

Piezoelectric elements are made from polarized, crystalized ceramics that allows for the piezoelectric effect. Both sides of the element are coated in a conductive metallic substance to form two electrodes, thus allowing a current to be passed through the ceramic for element 'exciting'. The thickness of the element, s determines the sensor resonant frequency f_r at which signal amplitude will be a maximum and therefore most sensitive to test conditions. To calculate f_r Equation 3.23 is used where N_f is the frequency constant of the piezoelectric material, approximately 2000Hz/m. A typical 10MHz element can therefore be calculated to be approximately 0.2mm thick, a 5MHz element would be 0.4mm thick.

$$f_r = \frac{N_f}{s} \tag{3.23}$$

3.3.3 Huygen's Principle and the Near Field Effect

Plane waves described in Section 3.1 are actually the result of complex interference patterns from multiple spherical point sources, as described by Huygens' principle [79]. Put simply, spherical point sources, that in bulk make up the element face, generate simple elementary waves that propagate radially from the point source. As these waves interfere with each other both constructively and destructively, a plane wave front can be generated from the dominant element face, seen in Figure 3.6

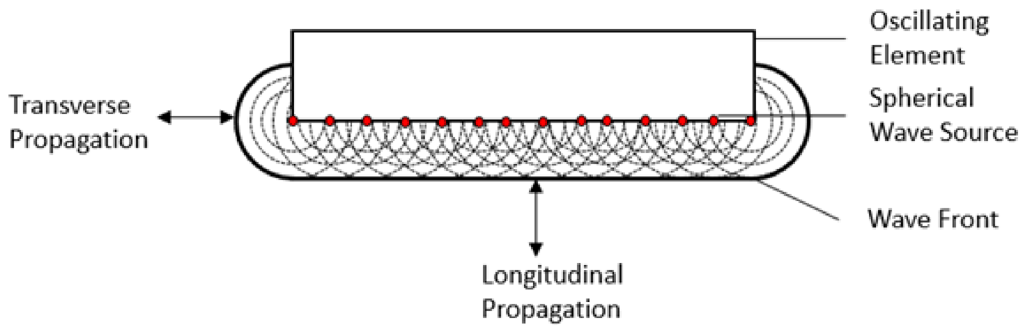

Figure 3.6: Construction of a plane wave front from numerous spherical wave sources

The plane wave develops over length N, which is known as the near field. Interference within the near field causes large fluctuations in sound pressure meaning data interpretation is very difficult in this area. After the near field a uniform plane wave of a maximum amplitude forms, which then diminishes as the wave propagates further away from the source. This area of uniformity is known as the far field and it is desirable to always test in this location for ease of result interpretation [79, 100]. Transition from near field to far field is shown in Figure 3.7, as is the simplified 3D development of a sound field.

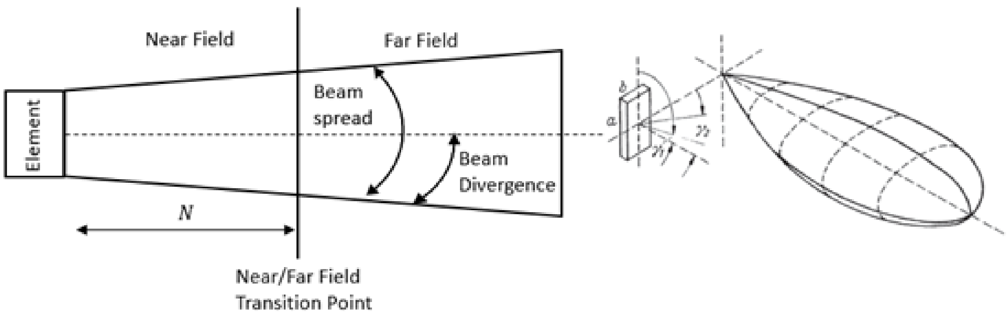

Figure 3.7: Left: Schematic of wave field from oscillating element with clear transition point. Right: Beam spread from a rectangular piezoelectric element where side lobes have been emitted, taken from [79]

The sizing of a square element influences N. Where a and b are half of a piezoelectric element length and width respectively, the dimension ratio can be calculated:

$$dimension\ ratio = \frac{b}{a} \tag{3.24}$$

This dimension ratio then corresponds to a h factor. A table of common dimension ratios and h factors can be found in [79]. If the speed of sound through a material is known, as is the frequency of the wave propagation from Equation 3.23, then the wavelength can be calculated from Equation 3.1 and so N is found from:

$$N = h(\frac{a^2}{\lambda}) \tag{3.25}$$

Element sizing also influences beam spread which contributes to the attenuation of an ultrasonic wave. Figure 3.6 shows how point sources at the element edge allow a small amount of shear propagation, even with a longitudinal element. In the far field, a combination of these propagation modes results in the mean direction of the wave being parallel to the direction of oscillation, but a spreading of the beam wave front. This diminishes the ultrasonic resolution (UTR) and reduces measurement sensitivity. Figure 3.7 Left shows a simplification of the beam spreading from the element source. The beam divergence is the angle from centre axis of the wave front to the edge at a given distance, and is therefore always half of the beam spread angle [101].

Krautkramer et al. [79] explain how for square elements, the wave front half widths, b_1 and b_2 for each plane of propagation can be calculated. Where $D_1 = 2a$ and $D_2 = 2b$ relating to element dimensions, γ indicates divergence angle and k_α is a bandwidth factor:

$$b_1 = L \cdot tan(\gamma_1) \approx L \cdot sin(\gamma_1) = LK_\alpha(\lambda/D_1) \tag{3.26}$$

$$b_2 = L \cdot tan(\gamma_2) \approx L \cdot sin(\gamma_2) = LK_\alpha(\lambda/D_2) \tag{3.27}$$

3.4 Measurement Referencing

A benefit of ultrasonic measurements is that the reflected signals are very sensitive to lots of external parameters such as temperature, stress, viscosity and film thickness. However, as ultrasonic signals will respond to these external stimuli, it can make isolating the variable of interest in post-processing difficult. For this reason, a majority of ultrasonic measurement techniques use a reference signal of just the incident wave to compare against.

When using a single sensor in a pulse-echo setup it is difficult to directly measure the incident wave due to hardware limitations of switching the sensor from a pulsing mode to a listening mode. Instead, for film thickness measurements, an air reference can be used because the reflection coefficient between steel and air

$R_{steel-air} = 0.9999872 \approx 1$ and so the recorded reflection is very close to the true incident wave [84].

With recorded ultrasonic reflections the reflection coefficient can be measured by dividing the amplitude of the measured signal by that of a reference signal while both are in the frequency domain, see Equation 3.28.

$$R = \frac{A_{mes}(f)}{A_{ref}(f)} \tag{3.28}$$

Dou et al. [102] investigated the use of an air reference by monitoring the frequency of the minimum amplitude, within a bandwidth, from the frequency amplitude spectrum and the reflection coefficient amplitude spectrum. Findings showed that if the number of echoes recorded, determined by the window length in the time domain, were low (between 2-6) then the frequency of minimum points disagreed and some errors could occur. These errors diminished with higher numbers of echoes. The work does state that there are practical considerations in terms of the number of echoes captured, such as diminishing amplitude and a need to set a finite window in post-processing. Hunter et al. [103] ran a series of calibration measurements for various ultrasonic techniques used for measuring thin films, the resonance results are shown in Figure 3.8.

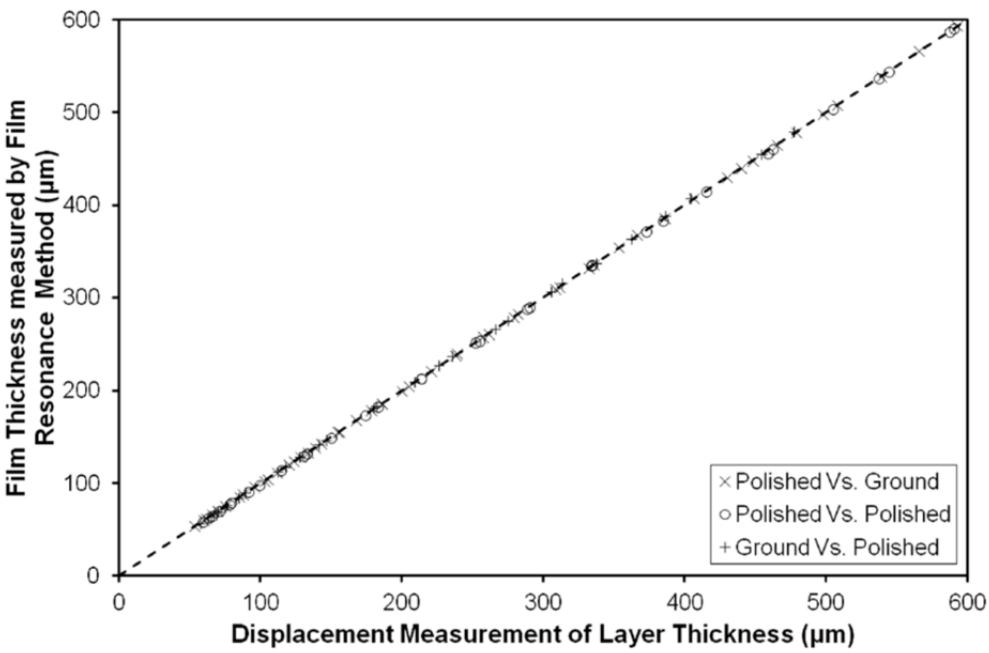

Figure 3.8: Comparison of film thickness calculated via the resonance method for various film thicknesses and surface finishes, taken from Hunter et al. [103]

The reflection coefficient was calculated using an air-reference. The tests were ran on a water layer between aluminium plates of different surface finishes, at different set distances. The resonance results are seen to be very repeatable and insensitive to the surface finish. Therefore, although a low echo number from a sandwiched layer can cause errors [102], if a practical attempt is made to window the reflected signal until these echoes diminish, errors due to using an air-reference are negligible and the technique is appropriate. More care should be taken if a very short window must be applied for whatever reason.

3.5 Conclusion

- Ultrasound refers to mechanical waves above 20kHz, the upper frequency limit for human audible hearing. LIHF waves are low intensity, not altering the mechanical structure through which they propagate, and are therefore ideal for non-destructive testing.

- Ultrasonic waves propagate via particle collisions, meaning materials with more chaotic particle orientations, such as gasses, attenuate more, especially at higher frequencies.

- When a voltage is applied to a piezoelectric element there is a mechanical vibration response which causes the ultrasonic wave. This is the piezoelectric effect.

- When a wave hits a material boundary it splits into a transmitted and reflected part. The reflection coefficient R represents the reflected proportion from the total wave amplitude, and contains information about the boundary conditions.

- In a 3 body contact, the middle layer thickness h is measurable, if the acoustic velocity is known through the layer, by processing R in different ways depending on the layer thickness. Although there are overlaps in measurement methods, when $h \geq 600\mu$m the TOF is used; if $20\mu\text{m} \leq h \leq 600\mu$m the resonance approach is used; if $h \leq 20\mu$m the spring model is used.

Chapter 4

Literature Review

In the preceding chapters the background and concepts of large scale bearings, lubrication and ultrasound have all been introduced, to provide context for this thesis of work. This chapter reviews the most relevant and up-to-date literature surrounding lubricant meniscus position, starvation and bearing skew, and outlines the difficulties with taking such measurements in-situ. Then, previous applications of ultrasonic reflectometry to thin films and bearing lubricant films are reviewed, concluding with the potential to use ultrasound as an in-situ monitoring technology in novel areas.

4.1 The Lubricant Inlet Meniscus

An issue identified with classic lubrication models is the assumption that the inlet to the contact is fully flooded, and that when considering the lubricant flow around a roller of radius r, lubricant is assumed to fill the separation of the roller from raceway up to the length r away from the contact centre [41]. The purpose of this assumption is to give ample distance for the pressure in the inlet to develop, so that any change in film thickness is due to other conditions such as load, bearing speed and viscosity. This kind of lubricant fill is known as the "infinite meniscus assumption" and is shown in Figure 4.1a.

When fully flooded, the inlet lubricant properties are very important. Crook [104, 50] used a capacitance method to monitor oil films between contact rollers and results showed that huge temperature spikes through the contact ($> 200°$C) made very little difference to the film thickness, and instead the lubricant conditions, particularly viscosity, at the inlet to the contact determined the separation.

In a real contact the meniscus has a finite length $< r$, closer to the contact entry. When the meniscus shortens to the point that the inlet pressure rise is hindered, the contact pressure is subdued and the separation is not as thick as it theoretically should

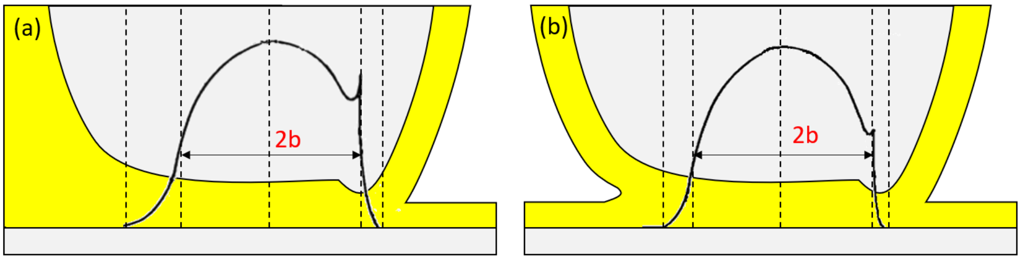

Figure 4.1: Schematic of (a) fully flooded “infinite meniscus assumption” (b) a starved contact with zero-reverse flow boundary. A sketch of the EHL contact pressure is overlaid for comparison

be meaning the contact is starved, as seen in Figure 4.1b, and the infinite meniscus assumption becomes inappropriate, particularly for grease lubricated bearings which are known to operate under starved conditions [105, 54]. Therefore, there was an emphasis to be able to study these contact areas in more detail. It has so far been difficult to accurately measure meniscus length and thickness in-situ within a rolling bearing of any kind, without component modifications. This is due to the menisci being very thin, occurring over small areas, and being hidden deep within the contact between the rolling elements and raceway.

4.2 Starvation

Starvation of a rolling contact occurs when inadequate lubricant conditions lead to a reduction in film thickness, when compared against fully-flooded conditions which are either measured or calculated from the relevant Dowson model for the contact shape [106]. Figure 4.2 shows different dimensions of a starved EHL contact that are often referred to in literature, and so is shown here for reader reference.

4.2.1 Oil Starvation

Cameron and Gohar [107] developed a very accurate optical method for measuring thin oil films in the nanometer range, which has become popular for measuring meniscus dimensions. The downside to this technique is the requirement of a transparent window to the contact which usually limits the application to laboratory ball on plate experiments. However, it allows the study of films in single ball on disc contacts within a nanometer range.

Wedeven [106] et al. was one of the first to adopt the optical method, and question how the meniscus length at the entry to the contact may affect contact film thickness.

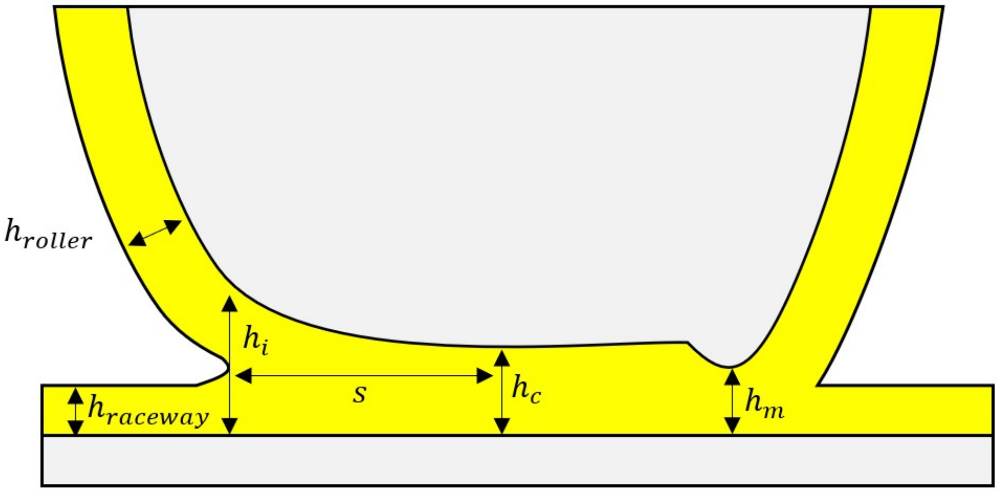

Figure 4.2: Schematic of the dimensions of a starved contact often referred to in literature. Shown is the raceway film leading into the contact ($h_{raceway}$), the roller film (h_{roller}), film thickness at the inlet meniscus (h_i), central film thickness (h_c), minimum film thickness (h_m), and the distance of the air-oil boundary from the contact centre (s)

They studied oil lubricated point contact starvation, and observed empirically that as the inlet meniscus position moved closer to the Hertzian contact zone the pressure build up was delayed and starvation occurred, resulting in the contact film thickness reducing to a proportion of the fully flooded thickness. Figure 4.3 plots central film thickness against an s/b ratio where b is the Hertzian contact half-width in the rolling direction and s is the distance from the contact centre to the inlet meniscus position.

Results shows that a longer inlet meniscus is needed to achieve a greater central film thickness. For all thicknesses, the results indicate that up to $s/b = 4.5$ the central film thickness was still increasing, meaning that starvation was still apparent within the contact. Figure 4.4 is adapted from the work of Dowson [41] and shows a similar trend of decreasing minimum and central film thickness with a shortening of the meniscus towards the contact centre.

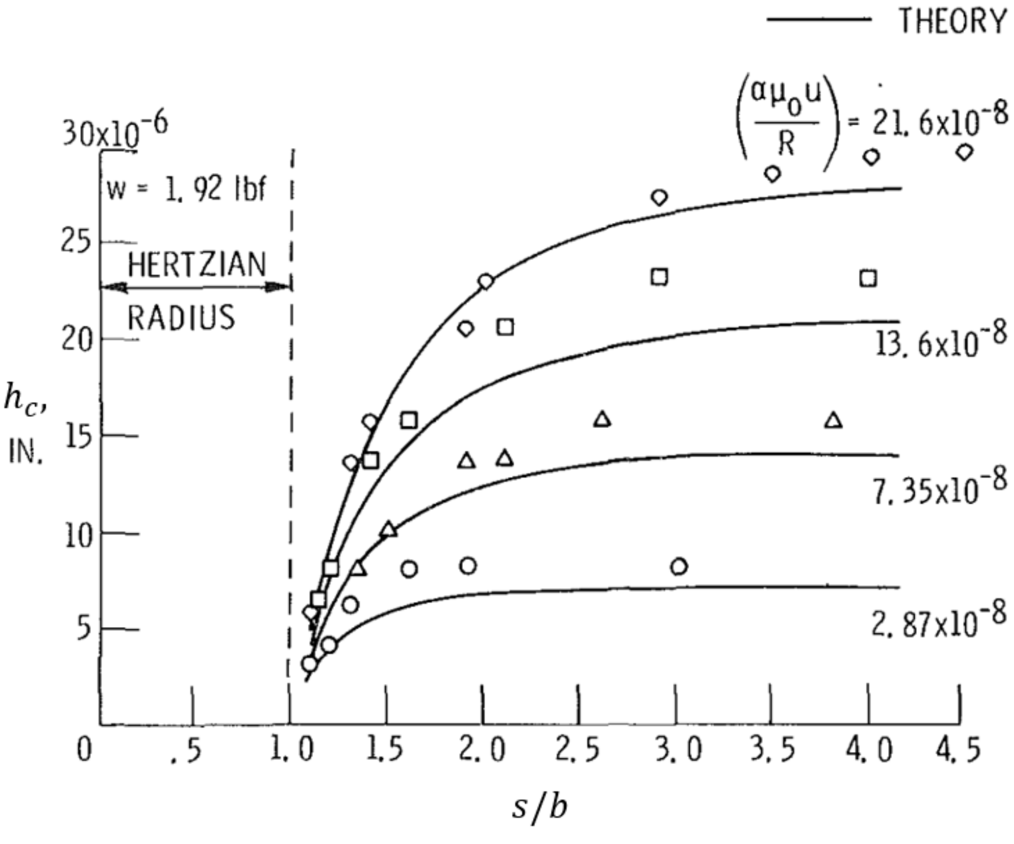

Figure 4.3: Relationship between required inlet meniscus length to achieve increasing fully flooded film thicknesses, adapted from [106]

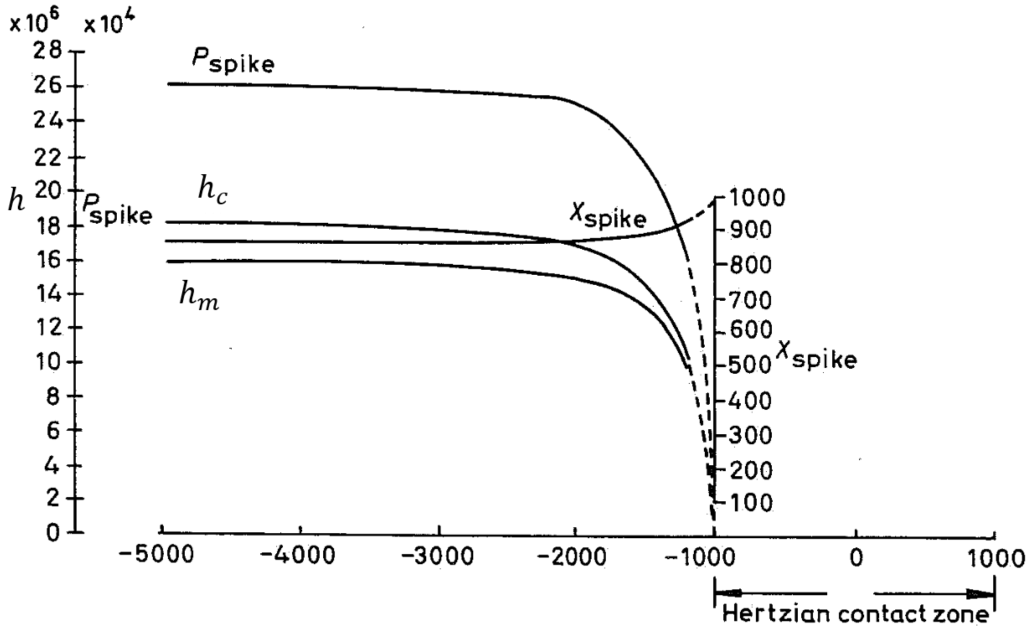

Figure 4.4: Impact of meniscus length on minimum and maximum film thickness and the magnitude and position of the outlet pressure spike, adapted from [41]

Interestingly, at $s/b = 5$ both trends plateau, suggesting that further lengthening has no affect on contact film thickness. Therefore there seems to exist an empirical relationship that if $s/b \geq 5$ the contact is fully flooded. However, if $s/b < 5$ then starvation will occur. This relationship is beneficial as it is easy to understand and visualise. However, a lack of in-situ monitoring techniques to measure the meniscus position and thus define the s/b ratio has meant this ratio has not been adopted in more recent starvation analysis.

Wedeven [106] et al. also showed that within a single point contact, some areas can be fully flood and others starved due to different local lubricant supplies. Figure 4.5 from Wedeven [106] et al. compares a classic fully flooded EHL 'horseshoe' shape in (a) to two contacts with a disturbed contact film thickness due to uneven inlet menisci in (b) and (c). Chevalier et al. [6, 7] modelled similar point contacts and also observed this variation in lubricant supply on the micro scale. This complicates the contact lubricant state, as it means a contact can be both fully flooded and starved at the same instance, resulting in an uneven film thickness within the contact.

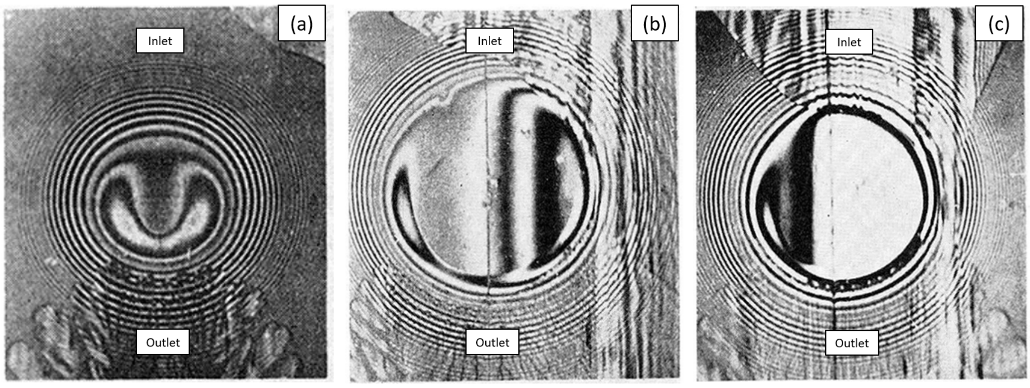

Figure 4.5: Point contact film thickness with varying inlet conditions. Plot (a) shows the classical EHL 'horseshoe' shape, plots (b) and (c) show a contact film variation due to varying inlet menisci shapes. Adapted from Wedeven [106] et al.

Wolveridge et al. [3] addressed this starvation problem with a semi-analytical approach, and findings gave the same conclusion as Wedeven et al., as the meniscus length shortens, the load carrying capacity of rollers in a bearing reduces to a proportion of the fully flooded capabilities. More recently, Kumar et al. [108] modelled contact starvation by moving the inlet meniscus position and found that shorter menisci lead to thinner contact films with higher coefficients of friction.

Cann et al. [109] studied the transition from fully flooded to starved conditions with increasing speed on a ball-on-disc test. Figure 4.6 shows that initially with a speed increase there is a film thickening as expected with fully flooded EHL conditions. With further speed increases there is impaired lubricant flow to the contact and the onset of starvation, meaning the thickness trend plateaus. Further speed increases further impair lubricant flow and so film thickness actually reduces. With increased temperatures the oil viscosity is reduced and so naturally oil flow is improved, explaining the delay of starvation to a quicker speed. In Figure 4.7 Chennaoui et al. [12] confirmed the same fully flooded to starved trend using optical interferometry in a bearing manufactured with a transparent sapphire outer raceway. Again, the onset of starvation was delayed with a lower viscosity oil due to its enhanced flow properties.

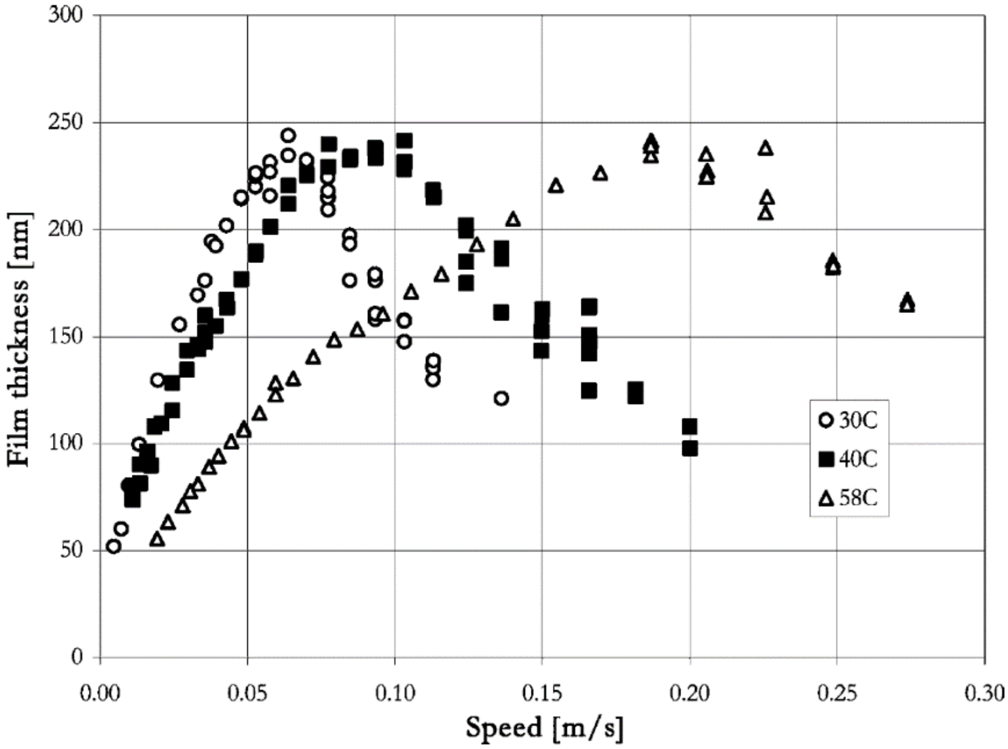

Figure 4.6: Contact film thickness with increasing speed, taken from ball-on-disc rig, showing the transition from fully flooded to starved conditions at 30, 40 and 58°C, taken from [109]

4.2.2 Grease Starvation

Grease starvation is heavily linked with the churning and bleeding phases, discussed in detail in Sections 2.6.2 and 2.6.3. Cann et al. [110] studied starvation and replenishment of grease lubricated single point contacts using optical interferometry. 0.5ml of grease was deposited on the running track of a disc over one full revolution, to ensure a distribution across the entire track. A ball was then loaded to the disc, and the disc was spun, during which the central film thickness was monitored and plotted against the number of disc rotations. The film thickness of the set volume test was divided by a measured fully flooded value h_{c_∞}, where a small grease reservoir was in place, to calculate a relative film thickness value between 0 and 1. In the tests, of different grease make-up and speed, there is a strikingly similar starvation and replenishment pattern. Figure 4.8 shows the relative film thickness change of a grease made of a 0.4Pa s paraffinic base oil and 8% lithium hydroxystearate thickener.

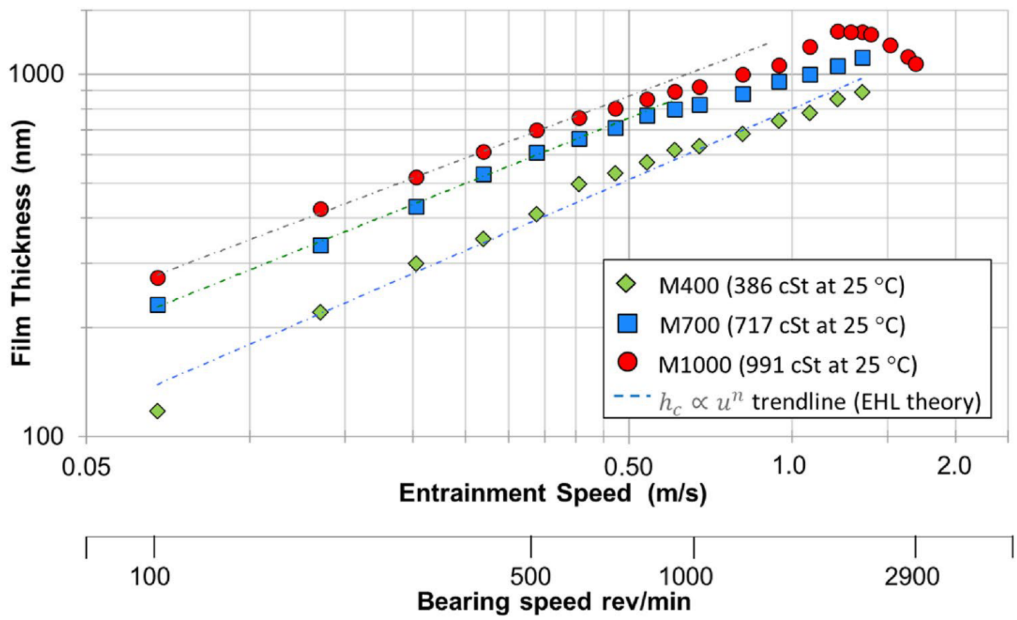

Figure 4.7: Contact centre film thickness with increasing speed within a deep groove ball bearing, showing the transition from fully flooded to starved conditions at 32°C for different viscosity oils, taken from [12]

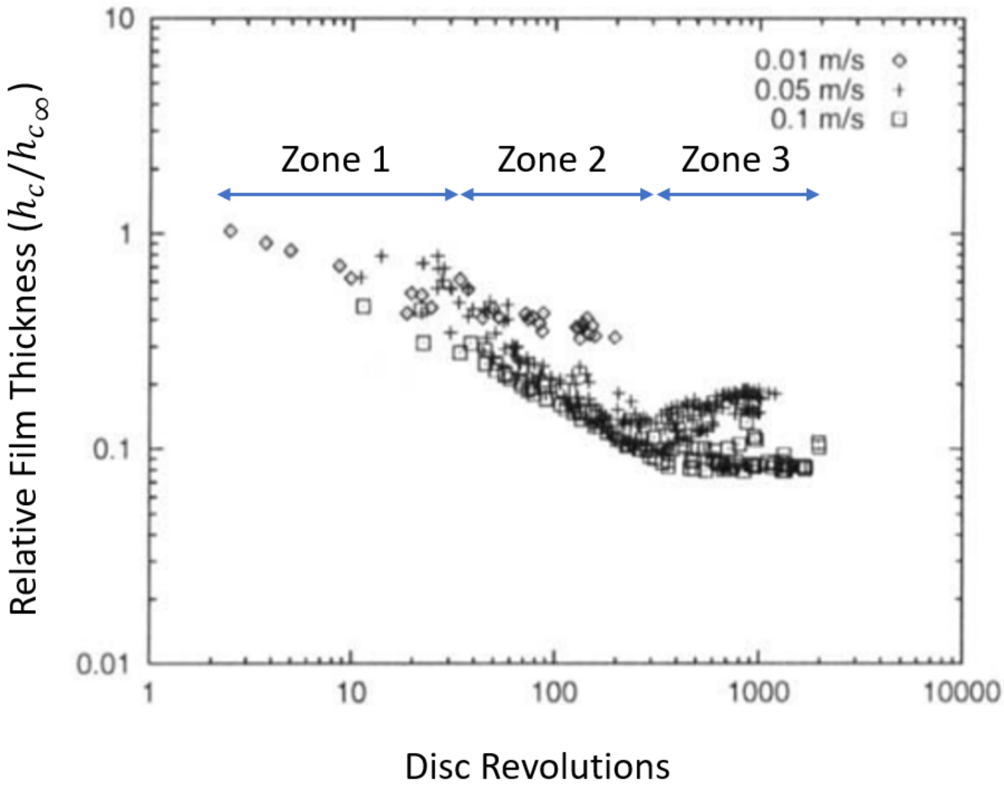

Figure 4.8: Relative film thickness of grease over-rolled at three different speeds showing three zones of lubrication, adapted from [110]

Figure 4.8 shows there is a distinct pattern of relative stability with some film thinning, followed by more severe film thinning, and then stabilisation for the three speeds tested, which the authors attributed to three different grease lubrication zones. As all speeds tested are equal to or greater than 0.01m/s, the stated transition speed [56], the thickness is not governed by the ultra-low speed mechanism discussed in Section 2.6.4.1.

Zone 1 : Initially the contact is flooded with fresh grease, but during initial over-rollings the bulk grease is pushed out of the swept area causing starvation, during which a high viscosity layer is deposited onto the surfaces. The lateral expulsion of lubricant from the deposited layer is prohibited by the shear strength of the grease in low pressure regions and because of the high increase in viscosity in the high pressure regions, meaning lubricant loss from the contact is a minimum. This deposited layer means the thickness is very similar to the fully flooded case.

Zone 2 : Zone 2 begins when the fresh grease in Zone 1 is churned, with the thickener structure breaking down and releasing oil from the grease, which is in turn lost from the contact. This results in an inadequate volume of lubricant, more severe starvation and a further reduction in film thickness.

Zone 3 : As the film reduces, less oil is expelled from the contact. Additionally, the previously bled oil now acts as a reservoir on the track to re-feed the contact, and so the film stabilises and in some cases there is film growth with this oil reflow. This is called replenishment.

Zhang & Glovnea [111] used an electrical capacitance method to monitor grease and oil contact film thickness inside a deep groove ball bearing with an increasing entrainment speed. In the work the authors separately isolate each raceway so a comparison can be made between the inner and outer raceway film thickness. Figure 4.9 shows how the inner and outer contact film changed for two greases, and their constituent base oils, for a range of speeds. Much like in Figures 4.6 and 4.7 there is a plateau in thickness with increasing speed due to the onset of starvation. What is noteworthy is for this particular case the grease film is thicker than the oil film at all speeds, which the authors attribute to an advantageous vibrational effect which promotes grease bleeds and oil reflow. However, this vibrational affect was not the focus of the study, does not apply to all bearings, and further work will be needed to investigate this.

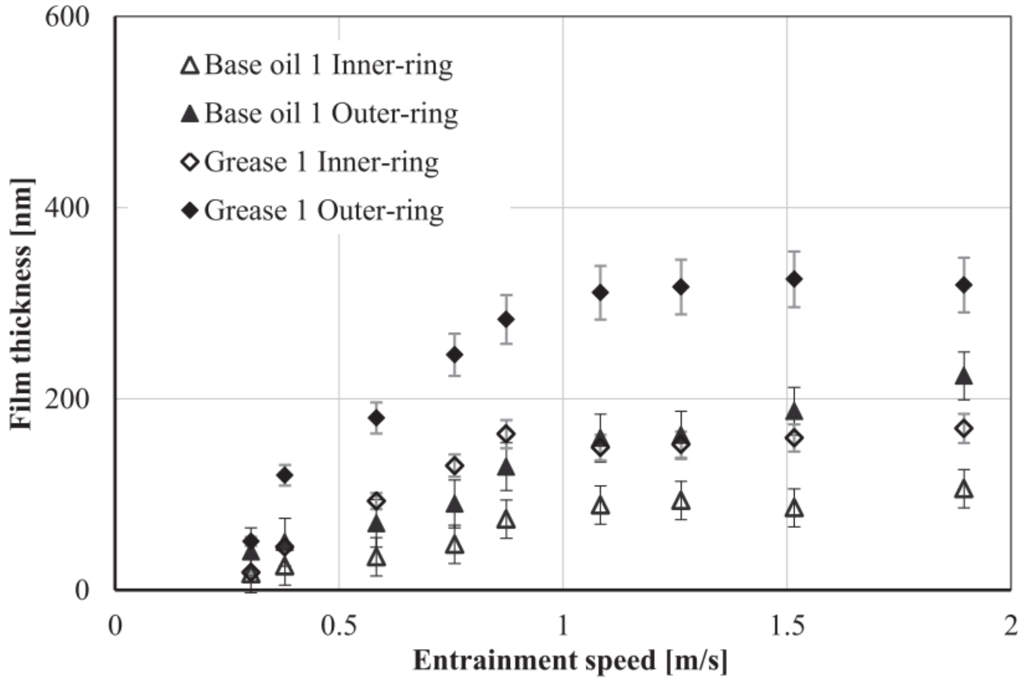

Figure 4.9: Measured contact film thickness at inner and outer raceway within a deep groove ball bearing lubricated with greases and their constituent base oils under a range of speeds, taken from [111]

4.2.3 Zero-Reverse Flow Boundary Condition

The zero-reverse flow boundary condition was suggested by Luader [112] when he noticed that the air-oil boundary (where the inlet meniscus position occurs) for a lubricated flywheel pressed to a steel plate formed at different lengths from the contact centre based on the load and speed conditions. He concluded that the contact pressure which enables separation begins to develop at this air-oil boundary, which marks the inlet meniscus, at a point where the lubricant velocity is zero, and thus all lubricant present passes through the contact.

The zero-reverse boundary condition is met when the air-lubricant boundary is a half Hertzian width distance away from the contact centre. When this occurs, both Saman [113] and Aihara & Dowson [2] concluded that the central film thickness $h_c = 0.7h_{c_\infty}$ in pure rolling and $h_c = 0.46h_{c_\infty}$ in pure sliding. Saman [113] who studied the lubrication deposition between rotating twin disks, also noted the random movement of oil droplets about the inlet region which were either lost through the discs or adsorbed in lubricant reservoir bands. In reviewing the work, Dowson [41] suggested this movement is the lubricant redistributing to adhere to the zero-reverse flow boundary condition. Dowson then concluded the review of work from the time as the zero-reverse flow boundary condition being an adequate practical assumption for contacts that are severely starved, but do contain some lubrication.

4.2.4 Relationship Between Inlet Film Thickness and Starvation

Rather than define starvation as the distance away of the inlet meniscus to the contact centre, in 1980 Elrod [114] defined starvation through the available oil on a surface, leading into the contact, labelled $h_{raceway}$ in Figure 4.2. This was deemed necessary as although the length away from the Hertzian contact zone can be used as a predictor of starvation in models [3], it is not practical to measure, and it ignores experimental observations that the meniscus is not a straight line, and in fact the length differs at different points along the Hertzian contact [106]. Elrod's algorithm used the Reynolds equation in two different domains. In the first, when the contact is fully flooded, the Reynolds equation is applied as normal. In the second, when a contact is starved, two lubricant layers are adhering to the ball and plate, and are separated by an air layer. This situation was still solved using the Reynolds equation, but with an additional filling rate parameter to represent this change in fill. Where the oil layers are sandwiching an air layer the pressure is atmospheric, and thus the contact pressure build-up is delayed which is known to occur in starved contacts.

Based on Elrod's algorithm, Chevalier et al. [6] numerically modelled starvation in an EHL point contact by varying the initial surface film thickness leading into the contact. The relationship between velocity and number of over-rollings was investigated. The main conclusion was that in EHL point contacts the centre starves due to a lack of lubricant, and that replenishment is fed mainly from the lubricant side lobes on the track. The work was expanded on with further numerical and experimental work in [7]. Conclusions were the inlet meniscus position was determined by the availability of surface oil, and the previous theory of central depletion with relatively thick side lobes, in point contacts, was verified. In the work Chevalier et al. used a depletion parameter $\gamma = \overline{\rho} H^3/\overline{\eta}$, where $\overline{\rho}$, H and $\overline{\eta}$ are the dimensionless density, film thickness and viscosity respectively. The parameter was used to describe the film thickness reduction in the contact centre due to starvation. In 1998 Chevalier et al. [8] produced a third piece of work on the starvation phenomenon, and found that controlling the inlet film thickness was an acceptable way to model starvation, and that numerical results agreed very well with experimental ones, as shown in Figure 4.10. The figure highlights how a contact centre can be starved and yet the side lobes fully flooded due to oil replenishment. Additionally, it was found that within the EHL regime $2 \geq \gamma \leq 5$, which has been validated in further studies.

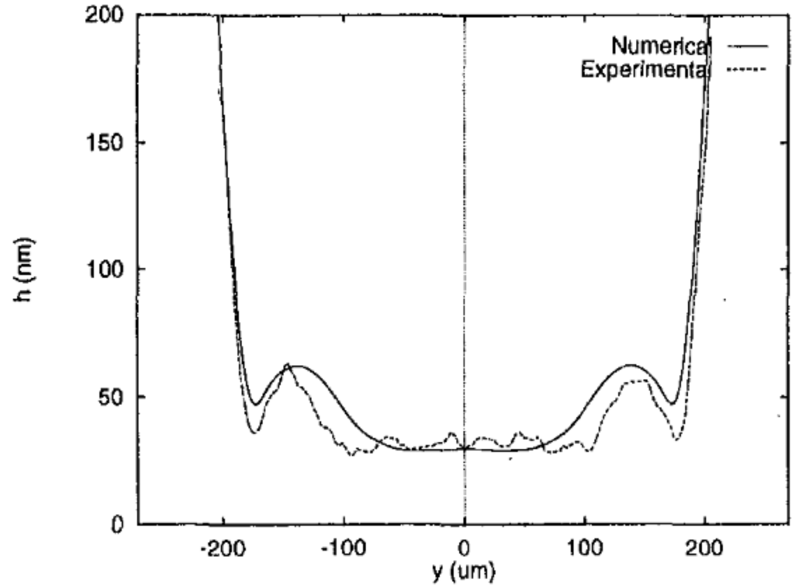

Figure 4.10: Comparison of experimental and numerical film thickness at the centre of an EHL point contact, taken from [8]. The rolling direction is into the page. The plot shows the centre is starved and yet the side lobes are fully flooded.

Damiens et al. [115] investigated starvation in elliptical contacts experimentally, analytically and numerically, based on the work of Elrod [114] and linked dimensionless material and load Moes parameters [116] to the film reduction parameter suggested by and Chevalier et al. [8]. Again, the thickness of the oil layer leading into the contact was used to determine the starvation level, and was varied based on the number of overrollings of the element. Interestingly, the ellipticity increase, when compared with the point contact of Chevalier's work, increased the γ parameter, indicating that side-leakage was reduced. This is due to a reduced pressure gradient in the y direction (due to the length of the contact) and an increased distance for the lubricant to travel from the centre. Also concluded from the study is that γ is linked both to the controlled inlet thickness value and to the meniscus inlet length, which was deemed the governing parameter in earlier studies. The work concluded that the Moes parameters were linked with side flow and film thickness, and that the reduction parameter was also linked with oil supply.

Cann et al. [109] offered an alternative starvation parameter:

$$SD = \frac{\eta_0 u a}{h_{raceway} \sigma_s} \tag{4.1}$$

Where $\eta_0 u$ (base oil viscosity and speed) was a viscosity parameter studied by Chiu [117] in its relationship with starvation; a, $h_{raceway\infty}$ and σ_s are the contact radius, raceway thickness and surface tension respectively. The work concludes that when $SD < 1.5$ the contact is fully flooded. When $SD > 1.5$, $h_c/h_{c\infty} = (1.5/SD)^{1.67}$, i.e. starvation occurs and the contact film depletes.

The studies of Chevalier et al. [8], Damiens et al. [115] and Cann et al. [109] prove that the thickness of an oil film going into the contact is crucial for achieving fully-flooded conditions. However, these studies were of contact fundamentals and excluded two considerations. Firstly, replenishment from the track to the contact was ignored, which is known to be a main re-lubrication mechanism within a bearing. Secondly, the geometry of the bearings was ignored as the studies were of rolling elements on flat plates.

van Zoelen et al. [118] addressed this second point by investigating oil layer distribution on bearing raceways, which forms the inlet films which have been highlighted as a governing parameter for bearing starvation. Both tapered and spherical raceways were modelled and experimentally measured, with good agreement across the majority of the raceway in the circumferential distance, see Figure 4.11. Of particular note is the non-uniformity on the spherical raceway, with a thickening of lubricant towards one edge.

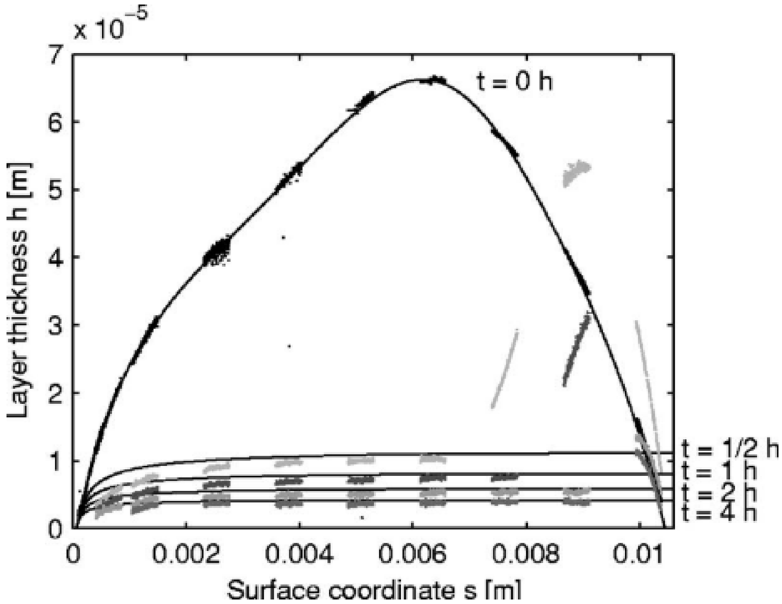

Figure 4.11: Comparison of experimental and modelled film thickness across the circumferential axis of a spherical roller inner raceway after various times. The straight line represents the model data, the points are experimental values. During the test the raceway was rotating at 1000rpm. Plot taken from van Zoelen et al. [118]

van Zoelen et al. [119] built upon this work, again using inlet thickness to define starvation level, and developed a model to predict central film thickness depletion in circular and elliptical contacts. The main difference of this model, when compared with those of Chevalier et al. [8] and Damiens et al. [115] is that time is used instead of the number of overrollings. The authors reasoning for this is that the number of overrollings within a bearing can be complicated to calculate and is not easily defined due to the different frequencies at which parts rotate. One noteworthy point from the work, with increased contact loading, numerical and experimental results show that film thickness decay is reduced, meaning the onset of starvation is delayed and a bearing can run for longer with a thicker central film thickness. This is due to a reduction in mass flux through the contact with an increased load. Referring to Cann et al. [110], who attributed a lack of side-leakage in fresh grease to the high viscosity of lubricant in the contact, a higher load could theoretically increase this viscosity, further impairing side-leakage when compared with a lighter loaded contact.

With the previously mentioned studies, the film thickness leading to the inlet of the contact is of crucial importance. However, the experimental work did not control this parameter, and so further experimental work was necessary. Svoboda et al. [5] used thin film optical interferometry to study point contact starvation, where starvation was controlled by using an initial elliptical roller, with a set gap height from the rotating plate, to control the film thickness going into the inlet of the contact of interest. The appropriate rupture ratio (Section 4.3.1) was calculated for the operating Slide-to-Roll ratios (SRR) to calculate this film thickness. The work validated that the thickness of the oil layer going into the contact had a relationship with the inlet filling, and that by reducing this film thickness the contact could be starved.

This work was expanded on by Koštál et al. [9] to investigate starvation in contacts of varying ellipticity, again controlling the starvation via the oil film thickness at the inlet. Again, the film leading to the inlet was controlled by an initial elliptical roller, with a contact width much greater than that of the contact of interest to stop reflow interfering with the subsequent inlet film. The time between contact was reduced to $0.2s$ and fluorescent microscopy was used to validate that reflow could not occur in this time, thus ensuring a constant, known film thickness entering the contact of interest. The different starvation levels were defined by the ratio of oil leading into the contact to the fully flooded central film thickness. For each starvation level, the contact with the higher ellipticity, narrower in the rolling direction, showed a thicker film in the central contact region when compared with the fully flooded value. Experimental results of the paper agree well with the theoretical relationships described by Chevalier et al. [8]. The authors conclude that as starvation occurs and the inlet meniscus position moves towards the Hertzian contact zone, side-leakage is reduced. However, for a set volume of oil, the more elliptical contact will expel less oil from the contact and therefore be less starved. Although these results are applicable for bearings that are very starved, or have very high running speeds, the authors comment that replenishment mechanism has been deliberately excluded from the tests. In a bearing, where the first contact is not substantially wider, but instead all contact patches are equal, replenishment may have a much bigger role, and the ellipticity pattern seen in this study may not be applicable. This again highlights the need for in-situ tests on full scale bearing rigs.

4.3 The Lubricant Outlet Meniscus

The focus of this thesis is on the meniscus conditions at the inlet to a contact. However, it is worth mentioning that a meniscus also occurs at the outlet, exit side of the contact. In understanding the lubrication of rolling elements it is necessary to consider this outlet meniscus, as lubricant from this region joins lubricant that flows back onto the rolling track via replenishment and forms the inlet meniscus to the subsequent contact.

4.3.1 Rupture Ratio

Once lubricant has passed through a contact, the film is distributed between the rolling element and the raceway, and the ratio between these films is the rupture ratio Δ. Figure 4.12 shows a schematic of this film rupture at a contact outlet.

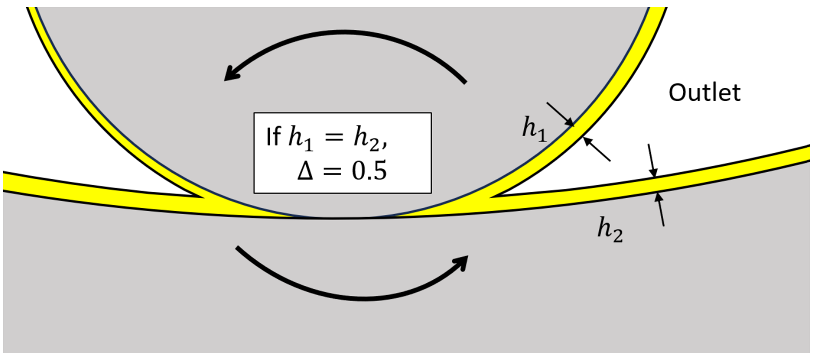

Figure 4.12: Schematic of the film rupture at the outlet of a contact, with a film adhering to both the roller and raceway

Bruyere et al. [120] developed a two-phase flow model using the Navier-Stokes equation to study the rupture ratio with different SRRs. The work was only done on hydrodynamically lubricated contacts, where the separation film was in the 10's μm range, but the principles are still applicable to EHL. The work concluded that the rupture ratio was determined only by SRR and that lubricant surface tension had no impact on film distribution. When in pure rolling (SRR = 0) the film was evenly distributed between the two surfaces. If sliding was present, whichever surface had the quickest velocity developed the thicker film. Koštál et al. [121] studied the rupture ratio experimentally in EHL contacts using fluorescent microscopy. Their study concluded also that when SRR = 0 there is an even distribution of the film at the outlet, and that if slip occurs, the slower moving surface has a thinner adhered film. The capillary number, a single parameter that encompasses the lubricant viscosity at atmospheric pressure (η_0), surface tension (σ) and velocity (U) can be defined as:

$$Ca = \frac{\eta_0 U}{\sigma} \tag{4.2}$$

Six different oils with Ca values between 3.2 and 13.6 were tested, and although variance was detected, there was no clear correlation, again suggesting that rupture ratio is driven purely by SRR conditions and not lubricant conditions. Koštál et al. [9] went on to develop an empirical formula for the rupture ratio, which is inclusive of side-flow, unlike the theoretical model of Bruyere:

$$\Delta = 0.0108 \cdot \mathrm{SRR} + 0.5 \tag{4.3}$$

Clearly, when SRR = 0 in pure rolling, this equation shows $\Delta = 0.5$ and the distribution of lubricant at the outlet is evenly split.

As the oil layer in the contact is so thin, as predicted by Hamrock and Dowson [4], the amount of lubricant adhering to the raceway after a roller has passed will be in the nanometer range. This highlights why replenishment is such an important lubricant mechanism in forming a substantial inlet film for the next contact.

4.4 In-situ Tests

Current technologies for measuring inlet and contact film thicknesses focus on optical interferometry [106, 5, 122] and electrical capacitance [50, 60, 123]. These approaches are capable of measuring contact lubricant films with varying levels of success, but all are limited to the laboratory, often on single contacts, due to their spacial requirements and/or need to have direct access to the contact. Due to the difficulty in measuring lubricant distribution and specifically inlet meniscus dimensions in-situ, there has been a lull in research. This is in terms of work that focuses on developing measurement methods, and modelling work that would use such a measurement as there was likely an expectation that such models could not be experimentally validated. Consequently, there is still a demand for an approach to measure inlet meniscus length and thickness in-situ, thus determining the lubricant fill and bearing health.

To date, the author is not aware of any in-situ monitoring of the meniscus or lubricant flow in operational field bearings, or lab based metallic bearings run under field conditions. This is due to a considered lack of appropriate technology to do so. However, in a recent study from Chen et al. [11], a bearing was manufactured from a transparent resin and glass and the oil distribution was observed using laser-induced fluorescence. A computational fluid dynamics (CFD) model was made to validate the results. A schematic and picture of the bearing are shown in Figure 4.13a & b respectively, and the CFD schematic is shown in Figure 4.13c.

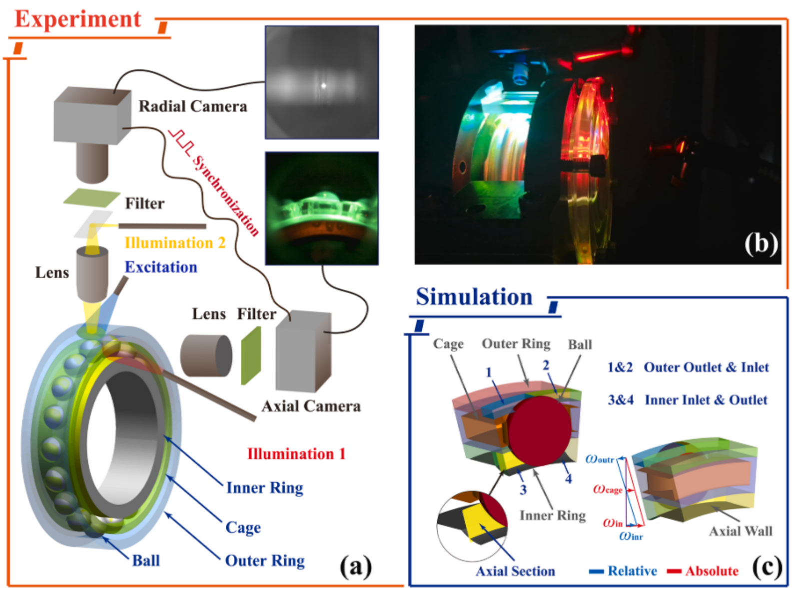

Figure 4.13: In-situ oil flow measurements performed by Chen et al. [11] showing (a) experimental setup of optical measurements (b) picture of the rig during measurements (c) schematic of the complimentary CFD model. Figure taken from Chen et al. [11]

In the experiments, 1ml of oil was added to the bearing cavity, and there was no further supply during the tests. Results show that the level of starvation of the ball increases with bearing speed, viscosity and Ca, and that this oil decay is related to a movement of oil away from the running track, towards side lobes. This agrees with the previous single point contact work of Chevalier et al. [8], meaning this study somewhat validates the use of single point contacts to study starvation in EHL roller bearing contact. They also observe that at high bearing speeds the contact centre is depleted with a thicker film on the side bands, which agrees with the previous literature shown in Figure 4.10. The paper concludes that the Ca value is closely linked with oil layer decay, which in turn may potentially lead to lubricant starvation.

Chennaoui et al. [12] also used a transparent outer raceway bearing to map lubricant film thickness around a contact, which included studying the relationship between inlet meniscus length and the level of contact starvation. Optical interferometry was used to measure EHL contact film thickness and specific laser induced fluorescence was used to measure and quantify distribution leading into the contact. Figure 4.14 shows the contact centre line profile of oil leading into the contact with increasing bearing speeds of 100, 1000 and 2000rpm from (a) to (c) respectively. The oil shown here is the M1000 plotted in Figure 4.7, from the same study. At 100rpm Figure 4.7 shows the contact was fully flooded as there is still an increase in central film thickness with bearing speed. Figure 4.14a shows that $s/b = 11.2$ at this speed, again indicating fully flooded conditions. At 1000rpm Figure 4.7 still shows an increasing central film thickness but the gradient is not as steep, suggesting starvation onset. At this speed 4.14b shows that $s/b = 7.1$. This is greater than the $s/b = 5$ ratio observed by Dowson [41] but as there is still an increasing contact thickness trend it could not be said that the contact was starved, it was simply entering the starvation mode. At 2000rpm and greater Figure 4.7 clearly shows the thickness plateau and then decrease indicating contact starvation. At this speed 4.14c shows that $s/b = 3.0$ which is less than the previously defined $s/b = 5$ for fully flooded conditions, again confirming contact starvation.

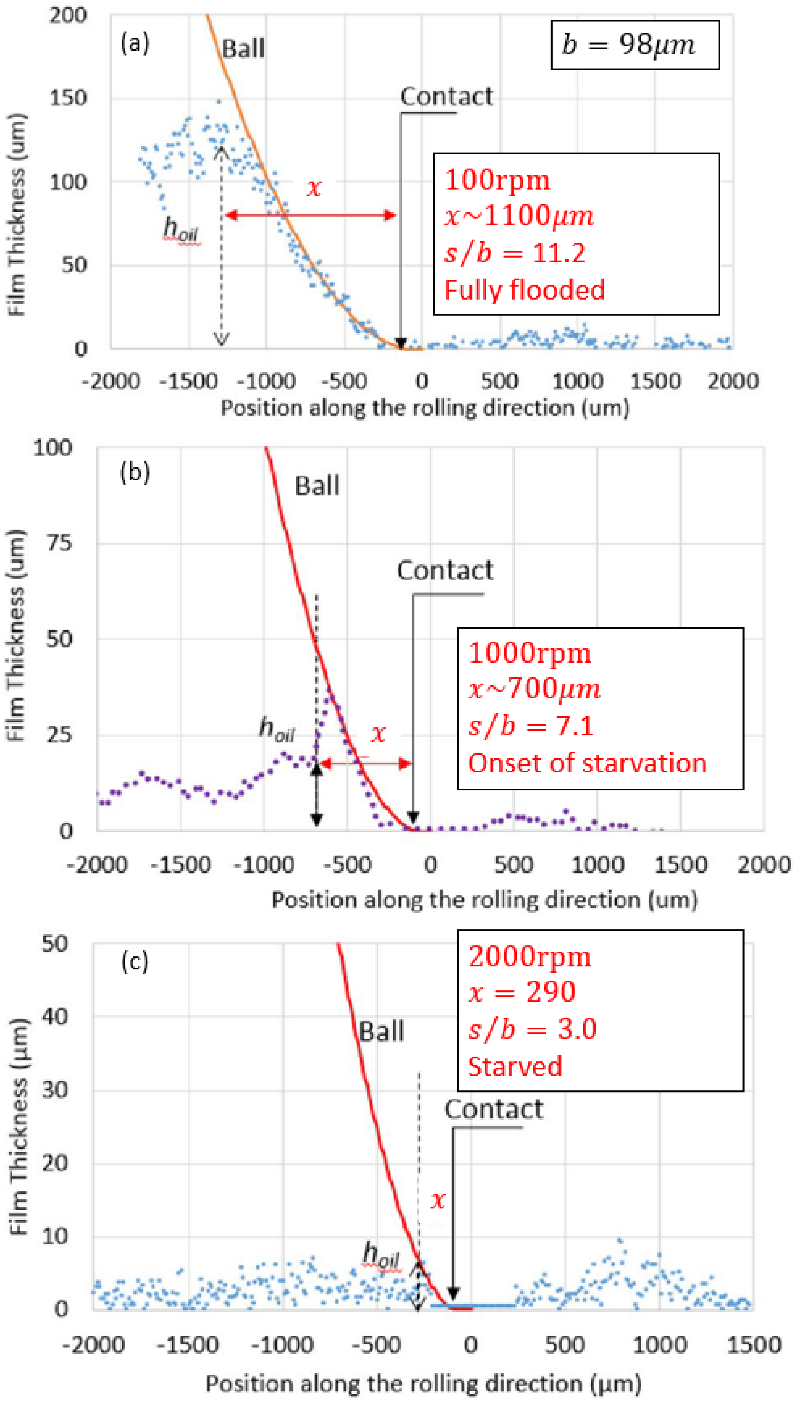

Figure 4.14: Profile of film thickness along the centre line of the rolling contact, adapted from [12], with calculated s/b ratio and stated starvation level of contact. From (a) to (c) the bearing speed was increased, leading to onset and progression of starvation

Sakai et al. [124] used a neutron imaging technique (NIT) to measure grease distribution within a metallic bearing after fresh grease had gone through a running-in period. The measurement time resolution limited tests to stationary, non-rotating bearings, but no bearing modifications were required. Spatial resolution was limited to 60μm but this was adequate to see how different thickener types altered grease distribution. Using the NIT method, the work concluded that lithium complex grease has most adherence to the cage surfaces and thus gave low bearing torque values. A lithium soap thickened grease had much stronger adherence to the balls which increased rolling resistance and made the bearing less efficient. This NIT approach therefore has potential to monitor lubricant distribution on larger bearings, but more work is needed to reduce both the spatial and time resolutions, so that distribution can be visualised during churning, and to a greater degree of accuracy. Thus, there is still a need for in-situ film monitoring of unmodified bearings which are representative of those used in the field.

4.5 Ultrasonic Thin Film Measurements

In the last two decades ultrasonic sensors have been gaining momentum as an alternative technology to measure bearing lubricant conditions [84, 125]. This is due largely to their low cost, simplicity, and ability to propagate waves through solid and liquid media, meaning direct contact access is not required. As discussed in Chapter 3, ultrasonic waves do not require a 'window' to the contact, meaning that they have potential to take these in-situ raceway thickness measurements.

In 2003 Dwyer-Joyce et al. [84] published a comprehensive approach to measuring lubricant films in bearing systems. The paper covers two approaches, the spring model and the resonance approach, the fundamentals of which were introduced in Chapter 3. Both approaches will be talked about in more detail.

4.5.1 Ultrasonic Resonances Measurements

An ultrasonic resonance approach is a form of ultrasonic spectroscopy where a reflected signal from a thin layer between 20μm $\geq h \geq$ 600μm, analysed in the frequency domain, has observable amplitude reductions at certain frequencies. The amplitude reductions are governed by the harmonics of the layer of interest, which are themselves governed by layer thickness through which the ultrasonic wave travels.

Although resonance measurements are often stated as using a continuum model approach, this is not actually true, as pointed out by Dou et al. [99]. In the work it is explained that the continuum model is a constant incident wave acting upon a layer, and when the frequency of the wave matches the resonant frequency of the layer, all of the wave is transmitted through, resulting in an observed reflection coefficient of 0. However, in lots of ultrasonic tests, the wave is not continuos, and piezo elements are operated in a pulse-echo manner. As a single element has to transmit and receive, the wave cannot be continuos and instead it is often a pulse wave. The authors describe that although a minima is still observed at the resonant frequency of the oil layer of interest, the formation mechanism governing this minima is due to wave superposition and opposing phase changes which cancel out, rather than actual layer resonance and incident wave transmission. However, by increasing the number of echoes received from the oil layer, the authors showed that the superposition model tends towards the continuum model with echo numbers of $n = 50$. For this reason, all approaches of this kind within this thesis will be referred to as a resonance approach.

4.5.1.1 Unconstrained Films

Chen et al. [126] used the ultrasonic resonance method to measure condensing water films of stable and unstable thicknesses. The experimental setup consisted of an ultrasonically instrumented copper block with either a polyethylene rim to conduct fluid wave experiments or a plastic ring for stationary film measurements. The purpose of the rim or ring is to contain the fluid. The first experiment was of a stable film fed by a controlled mechanical drip mechanism. The volume of fluid and ring dimensions were used to calculate the film height, which was then compared with the ultrasonically measured film height. Across a range of film thicknesses from 0.01mm to 8.7mm there was a percentage error less than 3% which reduced to 1.5% over 0.5mm. Fluid wave experiments were then carried out, where a single sensor was used to monitor the changing film thickness. The ultrasonic measurements were accurate enough to differentiate between the wave peak and trough, and from those thicknesses calculate a wave speed which agreed well with an optical shadowgraph of the same wave. The final portion of the work was to measure condensing films of n-pentane on the top and bottom of the test plate, results shown in Figure 4.13.

When condensing on the top face in Figure 4.15a, the film can grow naturally and results show an almost linear increase in film thickness from 25μm to 350μm. When the film condensed on the bottom plate in Figure 4.15b a much more violent pattern is shown, and the film thickness has a zig-zag pattern to it. The authors attribute this pattern to droplets forming near the sensor location and then breaking away once their mass becomes too great to be held to the plate by surface tension.

To investigate this droplet formation and breakaway in more detail the authors developed a numerical model to study the measurement of uneven surface film ge-

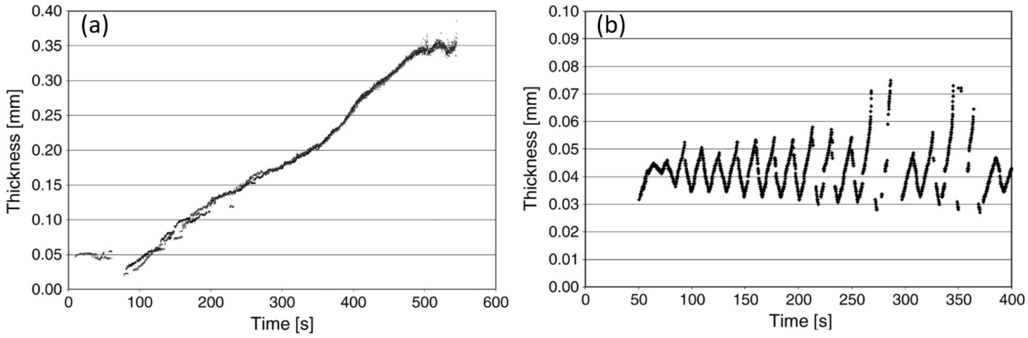

Figure 4.15: Measured film thickness of n-pentane using the ultrasonic resonance method from a single sensor when (a) the condensing film grew on the top face of the test plate (b) the condensing film grew on the bottom face of the test plate with droplet loss. Taken from Chen et al. [126]

ometries. The model results of a film over the measurement area, show that if the centre-edge difference reaches 45% the spectral peaks, used in this work for resonance detection, widen and lower in amplitude to the point where they could not conceivably be detected. However, if taking a measurement of a film with a centre-edge difference $< 45\%$ the measurement will be of the thickness directly above the sensor location. This finding is pivotal in showing the ultrasonic resonance method can measure free-surface films of varying thickness accurately, even if the film layer is not completely stable.

Al-Aufi et al. [127] used multiple ultrasonic reflectometry approaches to measure stationary and dynamic layers. For thin films, the ultrasonic resonance method and a TOF baseline correction (TOF-BC) method were used. The TOF-BC method, developed by Park et al. [128], offers a simplistic way to measure thin films through a time-of-flight approach, even with superimposed signals. First a reference signal is recorded of a solid-fluid layer where the fluid layer is much larger than the acoustic wavelength. Therefore, the first recorded signal is just of the solid-fluid boundary with no interference from the fluid-air boundary. When a thin layer is present, with superimposed waves, the recorded baseline is subtracted to form a new wavefront. Comparing the time difference of the first peak between the new wavefront and baseline allows for the thickness calculation. When testing stationary oil films, the resonance and TOF-BC approaches thickness measurements agree very well, with TOF-BC being more accurate below 200μm and the resonance approach more accurate for thicker films. When studying dynamic films such as those containing waves in Figure (20) of [127], the authors suggest that the frequency approach is not appropriate due to an increase in spectral peaks, making resonance detection hard. However, they observe the signal in the frequency amplitude spectrum, not the reflection coefficient amplitude spectrum, and also do not define the surface deviation that the spectrum is taken from. It is also suggested that the accuracy of the TOF-BC corrected approach suffers from uneven film thicknesses, and it is shown that the approach can under-calculate film thicknesses of a dynamic film. However, ultrasonic reflectometry is clearly shown to be sensitive to thin, dynamic films by Chen et al. [126].

4.5.1.2 Trapped Films

The potential to use the resonance approach to measure trapped lubricant films has been explored. Tohmyoh and Suzuki [129] applied the ultrasonic resonance technique to steel coatings. The purpose of the work was to attempt to measure a coating on an inaccessible face, after which a component cross-section could be taken to validate the measurement. Three coatings of known thicknesses 15.2μm, 15.3μm, 17.2μm were measured with a 50MHz and 100MHz commercial ultrasonic probes, submerged into a water bath for a more refined beam width. The thickness measurements were shown to be accurate, with a percentage error between 0.7% and 2.3% for the 50MHz sensor, and 0.7% and 4.9% for the 100MHz sensor.

Dwyer-Joyce et al. [92] used ultrasonic reflectometry to measure the oil films in journal bearings at the thinnest film region. The two approaches considered were the spring model, and the resonance approach. The authors note that the resonance approach is more desirable as the calculation requires less meta information about the contact to calculate thickness, and also that the measurement is insensitive to amplitude, only the frequency of resonance is needed. However, during a validation experiment an oil film between two shims of known separation was measured. The thinnest film measurable was 64μm which is an order of magnitude bigger than the expected film in the bearing, and theoretically no film under 10μm could be measured, which was still too thick.

Beamish and Dwyer-Joyce [130] instead then used the resonance approach to measure the thickest film in a dynamically loaded journal bearing. Results showed that as load increased, so too did the measured film thickness, due to a reduction in minimum film thickness 180° away from the sensor location. Likewise, a reduction in load led to a reduction in the measured film thickness, and across all loading patterns there was a good trend between the measured film thickness and applied load.

Beamish [131] in his thesis used ultrasonic reflectometry to measure the film thickness around the full 360°, and used the resonance approach to measure the fundamental frequency of the thickest films that were calculated between around $65 - 80\mu$m.

In this work Beamish highlights that a larger bandwidth can detect a greater range of thicknesses, but has an impaired signal-to-noise ratio, and thus is more susceptible to false readings. Beamish also notes that when running starvation tests, there is a noticeable reduction in the resonance approach measured film thickness.

To the authors knowledge, the only published work of using the ultrasonic resonance approach for bearing film thickness measurements has been done on the previously mentioned journal bearings. There is a lack of work on rolling element bearings. However, in the next section the spring model will be discussed, an alternative ultrasonic reflectometry approach which has a wide range of applications.

4.5.2 Bearing Spring Model Measurements

The spring model, introduced in Chapter 3 has a wide body of published work on bearing measurements. In his thesis, Howard [132] used bare piezoelectric sensors bonded to a bearing inner raceway to monitor the roller-raceway contact in-situ via the spring model approach. When contact stiffness increases, the reflection coefficient decreases as per Equation 3.7. Howard measured this change in R with an increased load on the bearing. However, the R values measured were an order of magnitude larger than those predicted by the model of Dwyer-Joyce et al. [89], and there was a disproportionately larger drop in R with increased load when compared with the theoretical values. Both of these observations were attributed to the use of bare piezoelectric elements, which unlike previously mentioned work with commercial transducers, could not be focused, meaning the sensor measurement area was larger than the EHL contact area. As shown in [88], the recorded R value is an average of all the sensing area, and thus for Howard's work, the low R value expected in the contact was blurred by the high reflectance value of the steel-air interface at either side of the contact. Also, when load increased, the sensing area remains the same but the contact width increases, meaning more of the sensing area is encompassing the contact region, explaining the disproportionately large drop in R with increasing load.

Nicholas et al. [133] used the same bare piezoelectric elements as Howard, and showed the reflection coefficient, observed at a single frequency over time, was sensitive to not only load, but also the lubricating film at the inlet and outlet of rolling contacts. Figure 4.16 shows R drops from 1 to ≈ 0.95 at the inlet to the contact. The drop is due to an oil layer on the raceway, that has a higher acoustic impedance than air, and so less of the signal is reflected back. Nicholas et al. [133] used the time where the reflection coefficient was reduced to infer reflow time, the time taken

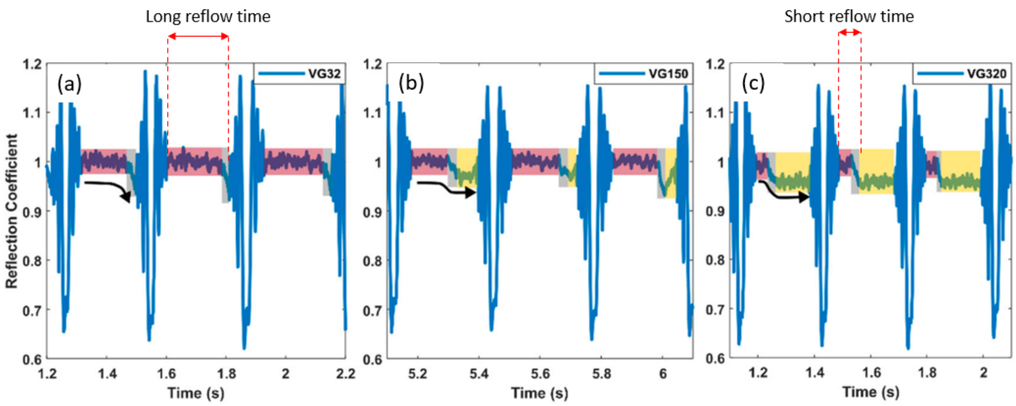

Figure 4.16: Reflection coefficient pattern for a test bearing lubricated with three different viscosity oils. As the viscosity increases, the lubrication reflow time decreases [133]

for the oil to flow around the roller to form a meniscus at the inlet. Oil comparison showed decreasing reflow time with an increasing viscosity which is counter-intuitive as the lower viscosity oils have less internal resistance to movement. However, this measurement is limited to a sensitivity of $0.95 \leq R \leq 1$. This means the analysis is useful, but only qualitative and somewhat blunt to the lubrication complexities such as film thickness, shape and length.

4.5.3 Technology Limitations

Schirru & Varga [134] and Dou et al. [125] have published two recent, comprehensive overviews of using ultrasonic reflectometry to measure tribological contacts. Both papers address limitations in applying such technology, the three main ones are summarised as follows:

Miniturisation Ultrasonic sensor size is related to the central frequency, with higher frequency sensors being smaller in thickness, length and width. However, even 10MHz sensors have a minimum face of around 2mm $\times$ 5mm. Given that the beam will spread away from the sensor face, the area of measurement is larger than many tribological interfaces, such as a rolling element bearing contact.

Wave Guiding Wave guiding or steering is a way to reduce the area of measurement of a sensor, to one smaller than a tribological contact. Currently this is achieved via a curved sensor face and water bath, such as in the work by Ibrahim et al. [135]. This is a complex, bulky instrumentation that is not ideal for use on in-field tribological assessment.

Contact Operating Conditions Ultrasonic reflections are demonstrably sensitive to film thickness. However, the reflection coefficient is also sensitive to temperature [103], pressure [95, 131] and oil contamination or particle deposition [136]. Therefore, difficulties can arise in decoupling the desired measurement variable from other interferences.

4.6 Roller Skew

In ideal operation of a cylindrical roller bearing the rolling elements roll perfectly perpendicular along the track between the inner and outer raceway. Harris et al. [137, 20, 24] discuss that raceway loading and geometry imperfections cause misalignment, which can create axial forces on the bearing. Combined with bearing rotation, a friction force occurs at the roller end-flange contact which then leads to roller skew, a pivoting of the roller about the axis normal to the roller-raceway contact. They then discuss how skew can truncate the roller end-flange contact, causing higher edge stresses and poor lubrication. Additionally, as a roller skews, the roller end-flange contact point moves towards the flange edge. It is undesirable for the contact to be coincident with the flange edge as this causes high contact stress and impaired lubricant performance. Figure 4.17 compares an ideal roller on the left side, to the skewed roller on the right.

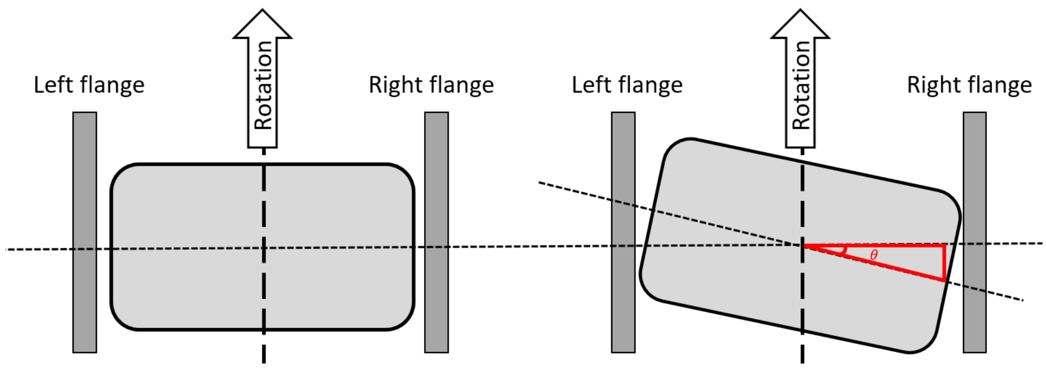

Figure 4.17: Schematic of roller skew in a cylindrical roller bearing

Skew has been measured using surface mounted Kelvin contact potential difference (CPD) probes in tapered rolling bearings [138] and spherical rolling bearings [139]. Results show that skew increases with an increasing rotation speed and higher viscosity lubricant. Skew is a maximum at the contact load zone entry and exit, and a minimum at the point of maximum load. A numerical model from Liu et al. [140]

showed an increase in skew angle with a larger rotation rate, outer raceway radius and roller length, and also with a decrease in radial load. Liu et al. [141] then investigated how load impacts change lubrication state of a skewed roller. Findings show a skewed roller has a thinner film than an ideal roller when load impacted, which is also inconsistent across the roller axis leading to roller tilt.

Like with many bearing kinematic mechanisms, there is a lack of true in-situ measurements. However, skew is a simple concept, and does not require meta data such as film thickness or contact pressure to calculate. Instead, only the ability to measure a roller-raceway contact, the time lag between contacts at either side of a roller, and the roller velocity is needed, from which the tangent skew angle can be calculated. Ultrasound can measure the roller contact pass time very accurately as there is a large change in acoustic impedance matching as the roller passes, when compared with no roller present, as explained in Section 3.2. The acoustic mismatch, and therefore recorded contact, would still be present with any other bearing material such as ceramics in a hybrid bearing. Due to the high capture rate of ultrasonic data acquisition systems it would also be possible to monitor individual roller skew values, not just a mean representation of the entire bearing. This makes ultrasound a viable potential technology for skew measurements.

However, There are drawbacks to the ultrasonic approach. If using in-situ permanently bonded sensors, only the skew at a fixed location is measurable. To assess skew at another angular position would require another set of sensors instrumenting. Additionally, other mechanisms relating to skew would be hard to measure. Roller tilt for example is more complicated as it is determined by a film thickness delta across the contact, and previous work by Howard [132] has shown this to be nearly impossible to measure with in-situ bare piezoelectric elements due to the sensor sizing. However, relative change in thickness, which is linked to the magnitude of R is possible, showing the potential for a qualitative measurement.

Roller slip would be another valuable in-situ measurement but this would be more difficult to perform using ultrasound. The ultrasonic response is sensitive to the fact that there is a contact between components which causes a reduction in the reflected pressure wave; in terms of a bearing the contact is between a raceway and roller. However, the contact is insensitive to which part of the roller or raceway is touching, so that a rolling contact and sliding contact, with the same contact dimensions, travelling at the same speed, would theoretically have an identical ultrasonic response. Therefore, a roller slipping as it passes the ultrasonic sensor measurement are would not be obvious. A mechanism such as contact lengthening due to slip could be a topic for future research, but is beyond the scope of this thesis.

4.7 Conclusion

- Starvation can occur in real contacts and leads to the excess rubbing of component surfaces, resulting in accelerated wear and a premature failure of the bearing when compared with its expected life.

- With a fixed oil quantity, overrolling of a contact leads to film thickness decay, and eventual starvation. Starvation is therefore linked with a lack of oil availability.

- For film decay to take place it is suggested the bearing speed must be in the thousands of revolutions-per-minute range, or the capillary number greater than 2.5 [11]. However, bearings operating at lower speeds are still known to starve, suggesting that starvation is not governed by oil availability alone.

- If there is adequate lubrication so that the oil layer does not decay and is present at the contact inlet, starvation is then determined by how filled the inlet region is.

- The volume of fill can be non-dimensionally quantified by the distance of the air-oil boundary away from the contact centre, divided by the Hertzian contact width.

- When the inlet meniscus forms at $5\times$ the Hertzian contact half-width away from the contact centre, there is adequate distance for contact pressure to rise and the contact is deemed fully flooded, so $h_c = h_{c\infty}$ [41].

- As inlet meniscus moves towards the contact centre and the pressure rise is delayed, not as much separation is possible, meaning $h_c < h_{c\infty}$. When the meniscus forms at the edge of the Hertzian contact zone the zero-reverse flow condition is met and $h_c = 0.7h_{c\infty}$.

- Therefore, when the meniscus length is $b \leq s \leq 5b$ the central film thickness is $0.7h_{c\infty} \leq h_c \leq h_{c\infty}$.

- The inlet volume film is governed by the layer adhering to the roller and raceway. At contact outlets the film is ruptured so only a thin film adheres to the roller, but lubricant replenishment means much larger films can exist on the raceway. Inlet volume fill is therefore determined primarily by the available oil on the roller race leading into the contact when replenishment can take place. In-situ measurements of the oil film thickness on the raceway leading into the contact are obviously very desirable.

- In-situ bearing measurements of contact film thickness is currently hindered by the size of commercial transducers and lack of focusing options for bare piezoelectric transducers. This limitation is highlighted in the recent reviews of ultrasonic technologies for monitoring tribological contacts by Dou et al. [125] and Schirru and Varga [134].

- Bare piezoelectric elements are sensitive to bearing conditions and have industrial value in qualitatively monitoring the change in reflection coefficient. Roller skew has been highlighted as a bearing kinematic mechanism that could potentially be measured using bare piezoelectric elements in-situ.

- Skew has been linked to accelerated wear and impaired lubricant performance making it a desirable to measure, and is often accompanied by tilt.

- The inlet meniscus shows that the raceway film is critical in determining the inlet fill, and thus the starvation level of a contact. As these films occur over a relatively large area, bare piezoelectric elements are potentially applicable for this kind of in-situ measurement. This has not yet been attempted in any published literature and is therefore a novel and innovative use of ultrasonic measurement techniques.

Chapter 5

Experimental Methods and Approaches

In this chapter, the wind turbine gearbox bearing test rig is described, along with the lubricants and ultrasonic hardware used to perform in-situ raceway film thickness and skew tests. Then, the fundamental data analysis of ultrasonic reflections at a single frequency is described, as are the impact of a lubricant film presence, film thickness and contact load. Lastly, a 2D EHL model, used to reverse engineer the measurement area of an ultrasonic transducer, is introduced.

5.1 Full-Scale Cylindrical Roller Bearing Test Rig

All of the bearing tests in this work were run on a full-scale CRB test rig, shown in Figure 5.1, taken from [142]. The bespoke rig was designed and manufactured by Ricardo UK Ltd and housed at the University of Sheffield, described in [132]. The rig houses a shaft mounted NU2244 cylindrical roller bearing which is representative of a CRB that supports a low speed shaft in a 2.5MW − 3MW wind turbine gearbox. The bearing has a bore diameter of 220mm, a mean diameter of 310mm and has fifteen cylindrical rollers of 54mm diameter and 82mm length. During testing the inner raceway remains stationary, the outer raceway being belt driven up to a maximum of 100 revolutions-per-minute (rpm). This setup is to specifically recreate the nature of a bearing within a wind turbine epicyclic gearbox which operates in this manner, and was the focus of previous work by Howard [132] for which the rig was initially built. However, this thesis of work is also applicable outside of the wind turbine industry, and there is no detrimental impact of this setup as the necessary bearing rotation is still present. The ultrasonic method described within the further chapters of this

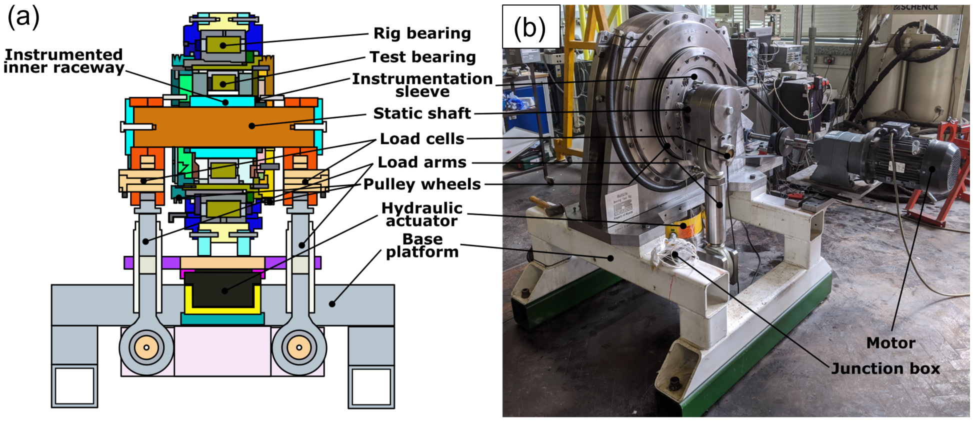

Figure 5.1: Cylindrical roller bearing test rig (a) schematic (b) photograph, taken from [142]

work would be applicable to a bearing with a rotating inner raceway and stationary outer raceway.

A hall effect sensor monitored the rotation of the outer raceway of the test bearing whilst a purely radial load was applied to the shaft via two linkages. Load cells within each linkage gave load feedback. During oil testing a hydraulic pump fed lubricant between the raceways, at 60° from the bottom-dead-centre. A scavenger pump was used to collect and recirculate this oil feed so that the bearing had a constant lubricant supply. A pressure transducer in the inlet to the oil pump ensured there was lubricant flow during testing. The load, rotational speed and oil pump were all controlled through a LabVIEW interface.

The rig design intention was for the bottom, heavy loaded region to be swamped with oil to provide advantageous lubrication conditions for the contacts in this region. In actuality, as the rollers rotate they wade through the oil creating wedges, and recirculation is still need from the outlet of one roller contact to the inlet of the next. The effect is more pronounced at higher bearing speeds and it means fully flooded conditions cannot be assumed. However, some level of beneficial side-flow can be assumed to be present for the oil lubricated results, but again not as dominant at higher bearing speeds. A key noteworthy point is that the oil availability of the monitored contact at the bottom of the bearing is larger than the availability of the contact at the top of the bearing, where oil has to adhere to the rollers and raceway and be dragged around the bearing circumference in order to lubricate. For the grease tests, the oil pump was removed and 1/3 of the bearing free space was filled with grease with spread across the roller faces and cage area, with the intention of providing an advantageous spread for optimum lubrication. However, no grease shields were in place during the tests.

Within this thesis of work no modifications were made to the rig other than ultrasonic instrumentation of components. Two ultrasonically instrumented bearings were made for this thesis, with sensors bonded to the inner face of the inner raceway. Sensors were mounted onto the inner raceway as it remains stationary during the test, simplifying both cabling from the rig and data interpretation. The instrumentation of the first raceway discussed in Section 8.1 was performed by the author of this thesis. The instrumentation of the raceway discussed in Section 9.1 was performed by researchers at the University of Sheffield, in consultation with the thesis author.

For this second raceway, a single k-type thermocouple was bonded on the inner bore of the inner raceway, at a position next to the central ultrasonic sensor. Only one thermocouple could be used due to space restrictions limiting cable access. This sensor was used to determine the in-situ lubricant temperature for acoustic-velocity calculation and to determine grease churn time in Chapter 10. Obviously, there is likely some delay in temperature from the contact face of the inner-raceway to the measurement location, but this was the closest access to the moving parts without altering the fundamental mechanisms of the bearing.

The instrumented inner raceway used for meniscus measurements in Chapter 10 is shown in Figure 5.2a. For rig assembly, the instrumented raceway was mounted onto a bearing carrier before being shaft mounted. The bearing carrier had a machined instrumentation slot ≈ 10mm wide and ≈ 5mm deep which accommodates the sensors, but limited testing to bare ultrasonic piezoelectric elements rather than commercial probes. Although it is not ideal to have an intermediary piece between the raceway bore and shaft as it introduces the potential for extra radial play into the system, during all inspections of components there were no visible signs of fretting damage on the bearing carrier, shaft or inner raceway suggesting that a solid, movement free fit was achieved through the inner raceway mounting system.

The raceway was mounted in such a way that a guiding bolt ensures the position of the sensors is at the bottom dead-centre, so that as the rollers pass the sensor location the recorded contact was at the moment of maximum load. When excited, a wave transmitted from the ultrasonic element, through the raceway material and reflects from the inner raceway-roller contact. The same sensors were used to both transmit waves and record the return reflections which were sensitive to the lubricant conditions.

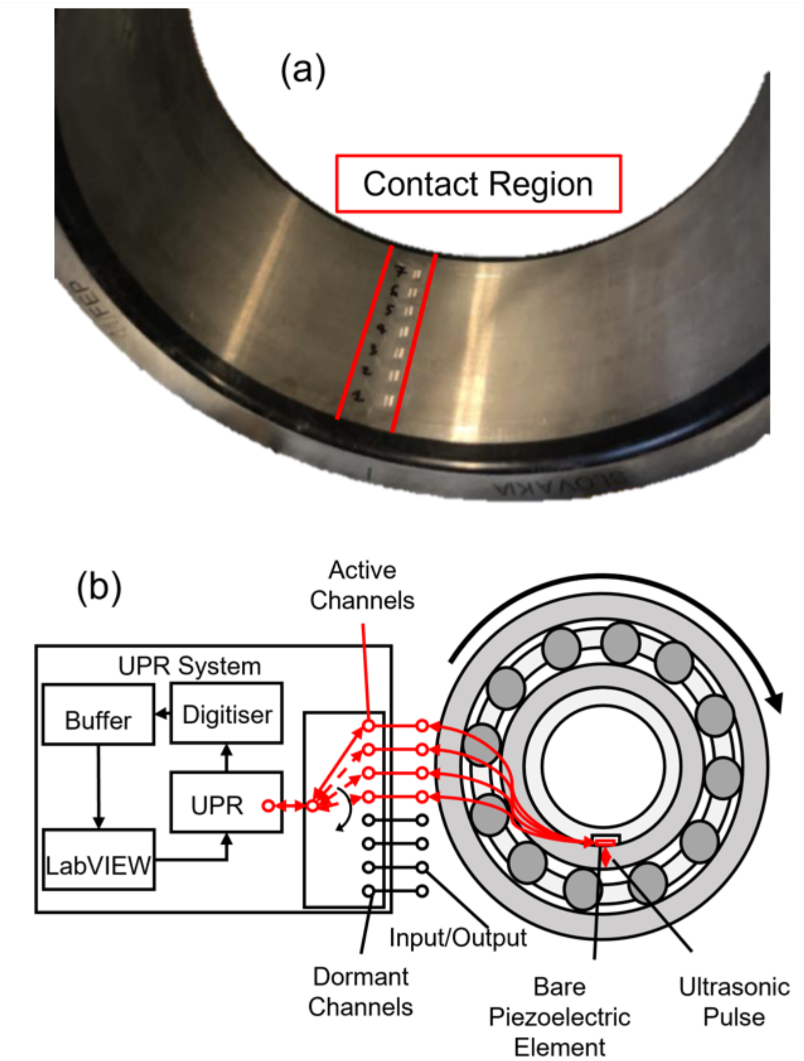

Figure 5.2: (a) Roller bearing inner raceway with a row of ultrasonic piezo elements instrumented on the inner, non-contact face (b) Schematic of ultrasonic pulser-receiver linked with instrumented bearings, adapted from [132]

Properties	Hyspin VG 32	Alpha SP 320	Mobil SHC 460 WT
Type	Oil	Oil	Grease
Viscosity at 20°C	—	335cSt	—
Viscosity at 40°C	32cSt	328cSt	460cSt
Viscosity at 100°C	5.3cSt	24cSt	> 16cSt
Density at 15°C	870kg/m^3	860kg/m^3	900kg/m^3
NLGI	—	—	1.5

Table 5.1: Properties of lubricating oils and grease used for bearing tests, taken from manufacturer data sheets and Howard [132]

5.1.1 Bearing Lubricants

For the bearing tests, two oils were used, *Alpha SP 320* (VG320) and the less viscous *Hyspin VG 32* (VG32). The VG320 oil is a typical oil that would be used to lubricate the rolling contacts within a wind turbine gearbox bearing. VG32 is a much lower viscosity lubricant, and was used for comparison. Additionally, *Mobil SHC 460 WT* (460WT) grease was tested, which is a PAO oil with lithium complex thickener, typically found in the main bearing of wind turbines. By using lubricants of different viscosities and type it was possible to investigate the potential to detect raceway resonances in different applications and the effects on meniscus dimensions. Lubricant properties can be found in Table 5.1.

5.1.2 Bearing Test Matrix

Two test durations were identified for the bearing work, based on the lubricant type and the mechanism being investigated. For the oils, a series of short 10s tests were completed. These were performed from unloaded to 600kN of pure radial load applied in steps of $100kN$, and at speeds of 20rpm to 100rpm in 20rpm increments. Incorporating the bearing size, this calculates as $6,200\mathrm{nd_m}$ to $31,000\mathrm{nd_m}$.The full matrix is shown in Table 5.2. The VG32 oil was only run to 500kN as the bearing stalled at the higher load.

As there is no time dependence with oil lubrication, tests could be run in a quick sweep manner. Each sweep was performed by setting the bearing load and allowing the system to stabilise, then capturing data at the five different speeds. Between changing speed steps the rotation rate was also allowed to stabilise. For the heavier loaded cases the order of sweep was intentionally set at 100rpm to generate the thickest theoretical film and then the speed reduced in an attempt to avoid rig seizure. A speed sweep at a single load took approximately ten minutes to complete. The temperature change, monitored at the sensor location on the inner raceway, showed $\Delta T < 1°C$ for all speed sweeps completed at a single load. The temperature difference between 100kN and 500kN was approximately 4°C, and all tests had mean temperatures of $27°C \leq T \leq 32°C$.

Test Sequence	Lubricant	Speed, rpm	Load, kN	Purpose
1	Hyspin VG 32	20 - 100	0 - 500	In-Situ Meniscus Measurements
2	Alpha SP 320	20 - 100	0 - 600	In-Situ Meniscus Measurements

Table 5.2: Test matrix for the oil, short duration tests

The second test matrix in Table 5.3 incorporated a grease lubricant, which due to its complex rheology is time dependent. The focus of these tests was primarily to observe the churn effect on the meniscus film and skew angle. When churning, the grease rheology is complex and chaotic as grease fibres are severely broken and the bearing lubrication state shifts towards starvation [54]. For each test speed, the grease was deemed churned when the bearing temperature had a less than $1°C$ change over a 15 minute period, based on *The Timken Co.* standard laboratory procedure for churning greases. Between tests, the grease was left inside the bearing and the rig was allowed to cool and the grease relax overnight. Some tests extended beyond the duration of churn, as discussed in the Section 10.2 of the results Chapter 10.

To enable data acquisition over the complete churning phase the capture time was reduced to 5s but repeat captures were taken every 30s until churn had been achieved. The only repeat test condition was between test sequence 1 and 2 to compare the distribution of post-churn grease after it had relaxed overnight. Within the same test matrix both oils were subjected to the same load, the same extremities of speed, and operated over comparable durations as the grease. As the oil flow is not time dependent, the purpose of these tests were purely as a comparison to grease in terms of skewing angles.

Test Sequence	Lubricant	Speed, rpm	Load, kN	Duration, min	Purpose
1	Mobil SHC 460 WT	20	400	123.5	In-Situ Meniscus and Skew Angle Measurement
2	Mobil SHC 460 WT	20	400	49.5	In-Situ Meniscus and Skew Angle Measurement
3	Mobil SHC 460 WT	40	400	129.5	In-Situ Meniscus and Skew Angle Measurement
4	Mobil SHC 460 WT	60	400	149.5	In-Situ Meniscus and Skew Angle Measurement
5	Mobil SHC 460 WT	80	400	224.5	In-Situ Meniscus and Skew Angle Measurement
6	Mobil SHC 460 WT	100	400	331.5	In-Situ Meniscus and Skew Angle Measurement
7	Hyspin VG 32	20	400	240	In-Situ Skew Angle Measurement
8	Hyspin VG 32	100	400	240	In-Situ Skew Angle Measurement
9	Alpha SP 320	20	400	240	In-Situ Skew Angle Measurement
10	Alpha SP 320	100	400	240	In-Situ Skew Angle Measurement

Table 5.3: Test matrix for the oil and grease, long duration tests

5.2 Ultrasonic Hardware

5.2.1 Film-Measurement-System

The ultrasonic data-acquisition system and hardware used for bearing tests was a *Film-Measurement-System* (FMS) from *Tribosonics Ltd.* which comprised of a personal computer with an in-built ultrasonic pulser receiver (UPR), amplifier and digitiser. The UPR could excite ultrasonic sensors using a square wave at a rate of 80kHz known as the global pulse rate (GPR), and the digitiser allowed for the digitisation of reflections at a frequency of 100MHz. The GPR is split over a possible 8 active channels and so if all channels are used, each channel pulse rate can be a maximum of 10kHz. Due to the high capture rate, a buffer was used to temporarily store recorded reflections before being permanently saved onto a hard drive. The UPR was controlled through a LabVIEW programme which allowed different pulse widths, delays, ranges and filters to be applied to each channel. This allowed for the optimisation of the excitation signal for the largest amplitude with the widest bandwidth. It also enabled just the first reflection to be recorded which reduced data storage demands. Figure 5.2b shows a schematic of the UPR system linked up with the test bearing.

5.2.2 Picoscope-Opmux System

For laboratory tests such as those detailed in Chapter 7 such a high pulse rate was unnecessary, meaning the FMS system, which is often in very high demand for other research projects, was unsuitable. Figure 5.3 shows a replacement kit made of a 5000 series PicoScope with an Optel opMux Ultrasonic Multiplexer (Opmux). The picoscope was controlled through a LabVIEW programme, in which a specific sequence of channel excitation orders, number of pulses, duration of pulse etc. was loaded through a sequence table. The PicoScope was used to trigger the Opmux, which in turn excited the relevant sensors, in a manner dependent on the sequence table conditions. The analogue voltage signals were returned from the Opmux to the picoscope where they were digitised, and stored through the LabView VI on the controlling laptop PC. By using the Opmux system, as opposed to just the PicoScope, the number of active channels was increased from 1 to 8, and the potential excitation voltage was in 100's of volts range, instead of just 4V as with the PicoScope.

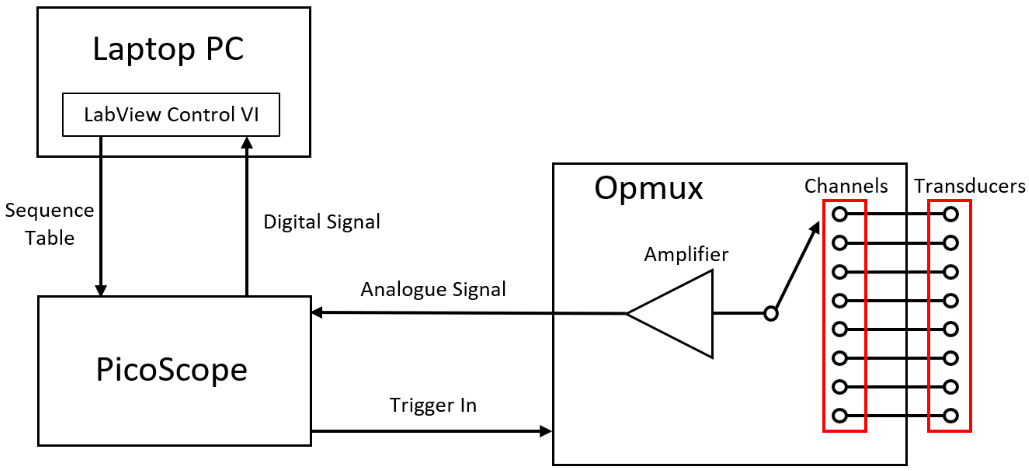

Figure 5.3: Schematic of the laptop-PicoScope-Opmux ultrasonic hardware system used for laboratory bench-top tests

5.3 Fundamental Data Processing

When an ultrasonic wave is incident upon a boundary, it is established that a part of that wave will reflect, and ultimately strike the transducer face. Due to the piezo-electric effect, this causes a voltage differential across the transducer, which is then digitised and recorded. However, the wave will reflect back-and-forth from the boundary of interest and transducer face, meaning a series of reflections are recorded, as shown in Figure 5.4. Of these reflections, the first always has the best signal-to-noise ratio, and thus a wider usable frequency bandwidth. As thousands of captures were taken per second in the bearing tests, it was unfeasible to capture multiple reflections from multiple sensors for a duration of seconds without losing data as the sensor would be excited again whilst still listening. Therefore, there was a trade-off to be made when determining the capture widow; that is how much of the signal received is actually recorded. If a large capture window is needed where multiple reflections are seen, the pulse rate of the ultrasonic hardware must be reduced. If a high pulse rate is necessary because of a dynamic nature of a test, such as the rotation of the bearing, the capture window must be shortened. In Figure 5.4 a typical bearing capture window is shown, which envelopes just the first reflection.

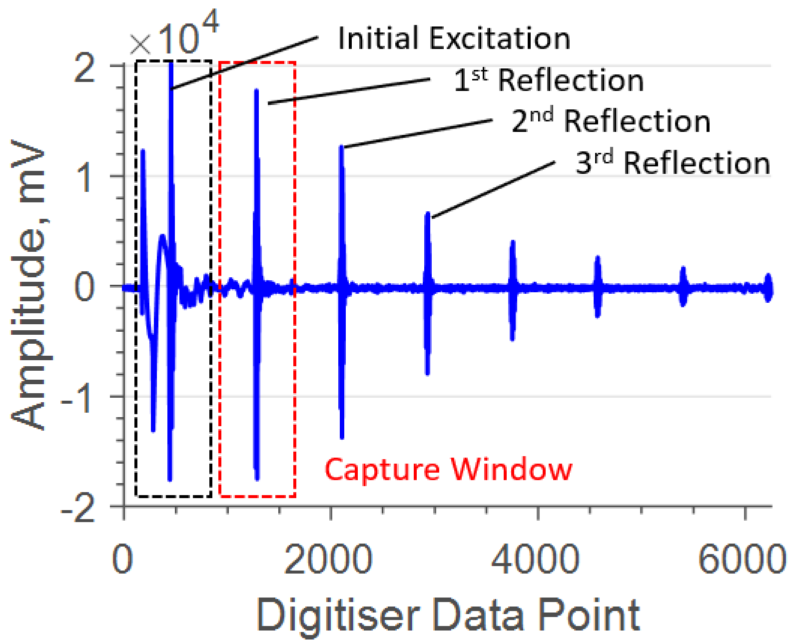

Figure 5.4: Example of multiple ultrasonic reflections from a single interface

During bearing operation the ultrasonic sensors were repeatedly excited and then listening for reflections, and a pre-determined delay and range value was set to envelope just the first digitised reflection, which was then stored and the rest of the data discarded. These reflections were stored as a long sequence of data, referred to as an A-scan stack; Figure 5.5 shows such a stack from a single sensor. When there is no rolling element over the sensor, there is high reflectance from the steel-air interface. As the roller moves over the sensor location there is a stiff steel-oil-steel contact which allows more transmission, meaning the reflected amplitude reduces, seen as a dip in the stack. The zoomed in portion shows some of the 10's thousands of individual reflections that the A-scan stack is made of. Although the contact pattern shown is interesting, very little can be gained from an amplitude change in the time-domain, and further analysis in the frequency domain is required.

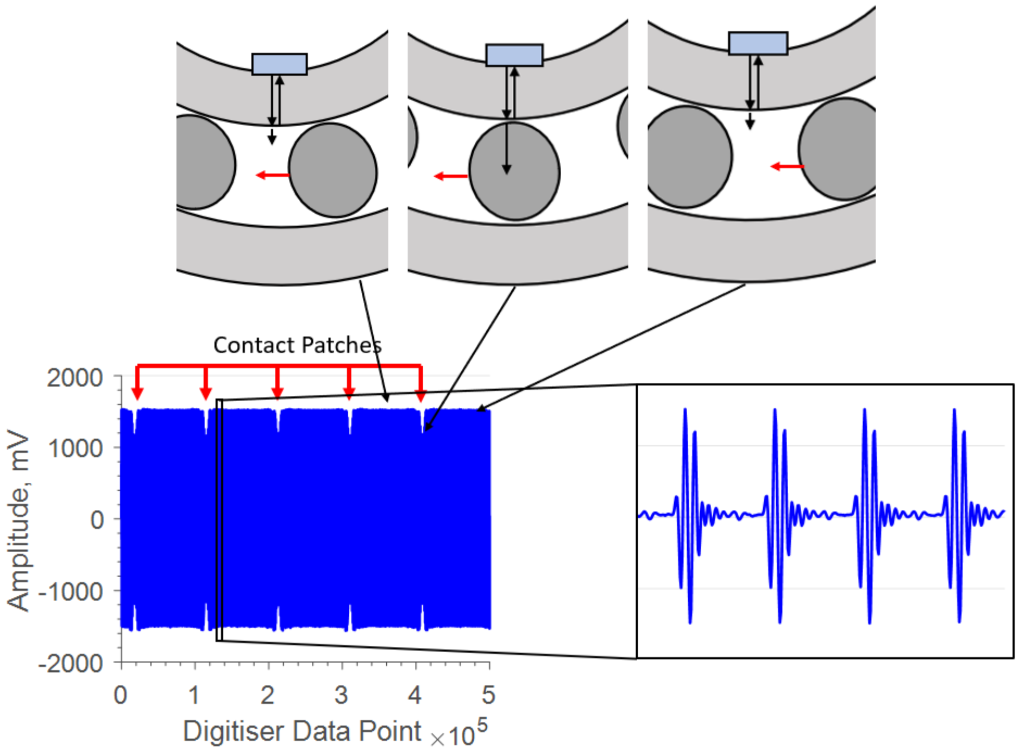

Figure 5.5: Reflection amplitude dip due to passing of a roller over the sensor measurement area

5.3.1 Signal Manipulation

Figure 5.6a shows how a measurement signal, from a free surface oil layer, compares to a reference signal from a bench-top validation test. Clearly there is an amplitude reduction and signal time extension with the presence of an oil film within the time domain, but the change is blunt and the potential analysis is limited.

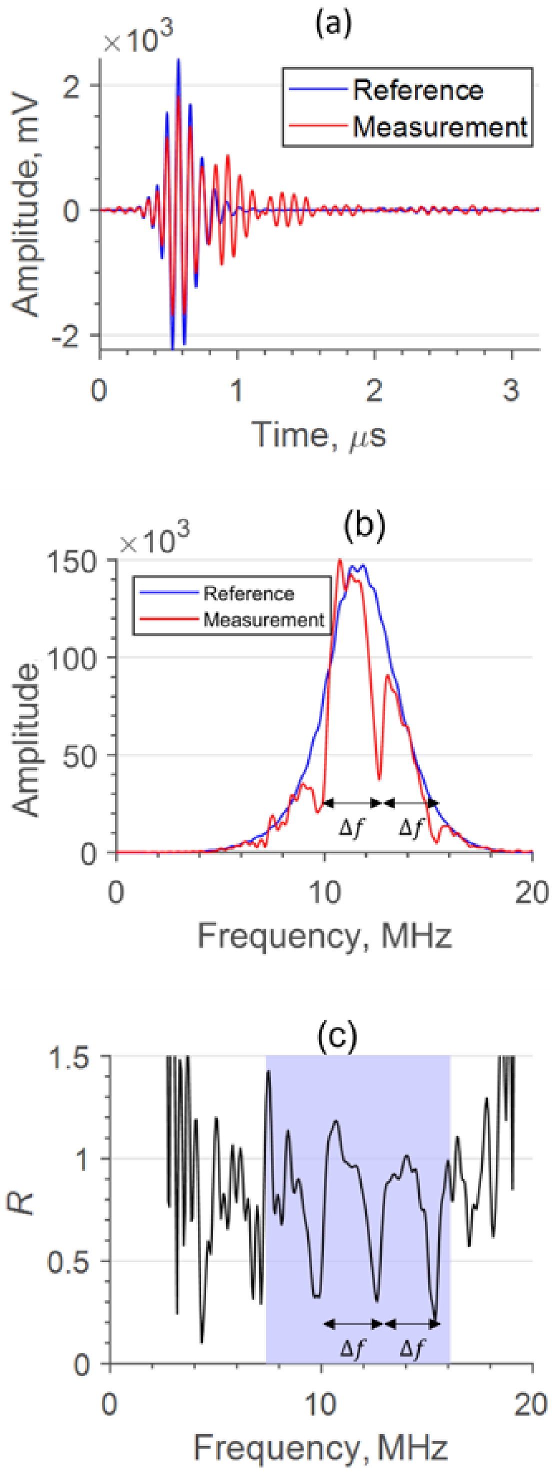

Figure 5.6: (a) Sample recorded reflections from an oil film and an air reference (b) reflections in the frequency domain (c) calculated reflection coefficient from Equation 3.28; the blue shaded region again shows a typical usable bandwidth

Figure 5.6b shows the signal transformed into the frequency domain using the fast Fourier transform, and the signal change is much more apparent, with reductions in amplitude at certain frequencies due to oil layer resonance. The frequency between resonances, marked Δf is highlighted on the figure, will be explored in much more detail in Chapter 7 and onwards. What is of note here, is that the reflection is far more sensitive to oil films in the frequency domain, and so all signals are converted in initial data processing.

The quality of a signal in the frequency domain is based on the quality of signal in the time-domain. Each reflection within the A-scan data stack must be treated individually, and some slight manipulation can greatly improve the frequency response.

5.3.1.1 Windowing

Due to the nature of a ultrasonic pulse-echo capture, reflection wavelets only exist for a short number of cycles before resting about a zero point. Therefore, so long as an adequate capture window is defined that encapsulates the rise and fall of the first reflection wavelet until it equilibrates about a zero value, no further windowing is necessary.

5.3.1.2 Zero-Padding

Kihong & Hammond [143] discuss the benefits of the Zero-Padding technique. Zero-padding is an analysis technique used to interpolate between Fourier transform bins in the frequency domain, thus increasing spectral resolution. However, padding can not increase the true resolution; if there are two frequencies that cannot be distinguished only a longer capture length or quicker digitisation rate can improve upon this. Padding has the secondary benefit of increasing computation time by matching the signal length to FFT algorithm, so long as the final signal length is equal to 2^n where n is a real integer number.

5.3.2 Calculating Reflection Coefficient

The reflection coefficient represents the proportion of wave energy reflected from a boundary, compared with the total incident energy. Equations 3.4 and 3.12 give the theoretical reflection coefficient from a two-media and three-media boundary respectively. Equation 3.28, copied below, shows how R can be obtained from measured data and Figure 5.6c shows the measured reflection coefficient for a validation test resonant oil film. Resonant dips in the plot are clear.

$$R = \frac{A_{mes}(f)}{A_{ref}(f)}$$

5.3.3 Frequency Bandwidth

Figure 5.7 shows the frequency response from a piezoelectric element with a manufactured central frequency of 10MHz. This stated frequency is dependent on the thickness of the ceramic as per Equation 3.23. When a voltage is applied to this element, it will naturally resonate at or close to this frequency, but on a FFT plot the resonant frequency occurs at the peak of the curve. However, the element will vibrate over a range of frequencies either side of the centre. The usable frequencies can be defined by a proportion of the signal amplitude of the maximum frequency response, and is defined as the bandwidth. Within this bandwidth, there is an acceptable SNR, and a range of frequencies at which signals can be further analysed. Larger bandwidths have a greater range of frequencies, but at a diminished SNR. Also, the relationship between bandwidth amplitude and the frequency range is not linear to the extent where larger and larger bandwidths only include very few additional frequencies.

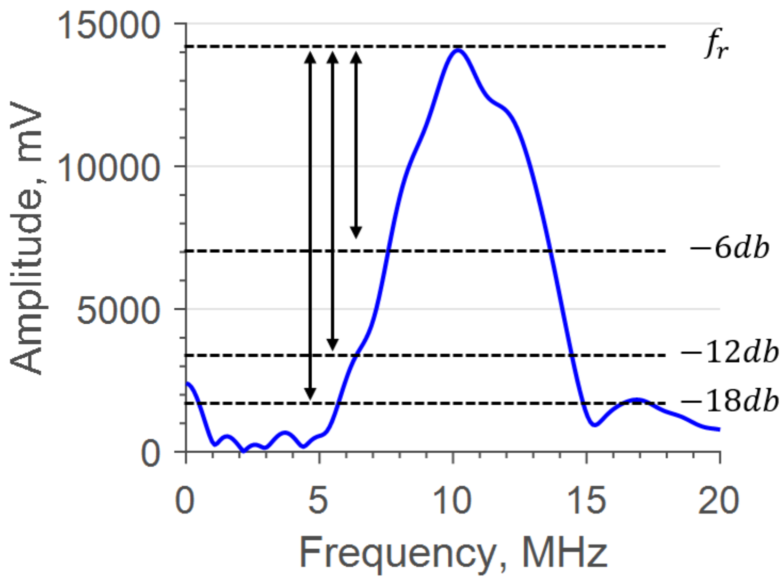

Figure 5.7: Comparison of signal amplitude within different bandwidth limits

5.4 Bearing Referencing

As following chapters will show, ultrasonic reflection signals are susceptible to influences from lubrication presence and thickness, contact size and load; all of which are of interest to engineers. However, the signals are also influenced by practicalities such as the thickness and quality of the bonding layer that sticks a sensor to a surface [144], the temperature at which the sensor is operating [145], the degradation of the sensors over time as they are used, or a change to the substrate material the sensor is bonded to (e.g. from wear). Consequently, a reference is required. There are several approaches to this.

5.4.1 Air Reference

An 'air' reference is common practice, where measurements are taken using the sensor outside of any contact, without any lubricant presence, under a full range of operating temperatures. The reflection therefore encompasses all kinds of bonding and temperature influences, and any change to the signal during testing is assumed to be caused by the lubricant/contact conditions. As previously mentioned however, sensors can degrade over time and so best practice is to take air references on a regular basis between tests. This kind of referencing is therefore possible, all be it cumbersome, in a laboratory setting. In Industry though, the cost of dismantling and machinery down time necessary to take the air reference often out-weighs any benefit to in-situ monitoring and so the air reference technique can become inappropriate.

5.4.2 Thick Film Reference

If an air reference signal is not possible or impractical, an alternative is a thick film reference. This requires an oil layer far thicker than the ultrasonic wavelength so that the reflection amplitude is consistent over the usable frequency range and abides by Equation 3.4. When taking measurements of thin films, defined here as within the same magnitude of the ultrasonic wavelength, then resonances will appear in the frequency domain that will differentiate the measurement signal from the reference, regardless of the general amplitude change.

5.4.3 Live Modal Reference

The issue with both an air reference or thick film reference is that calibration curves are required which not only increase the amount of post-processing, but are also difficult to define for effects such as sensor degradation over time. A different approach is a live modal reference, developed by Howard [132], which attempts to artificially create an air reference in-situ, and works on the assumption that in-between rolling element bearings, the raceway surface is mostly free of lubricant and so a steel-air

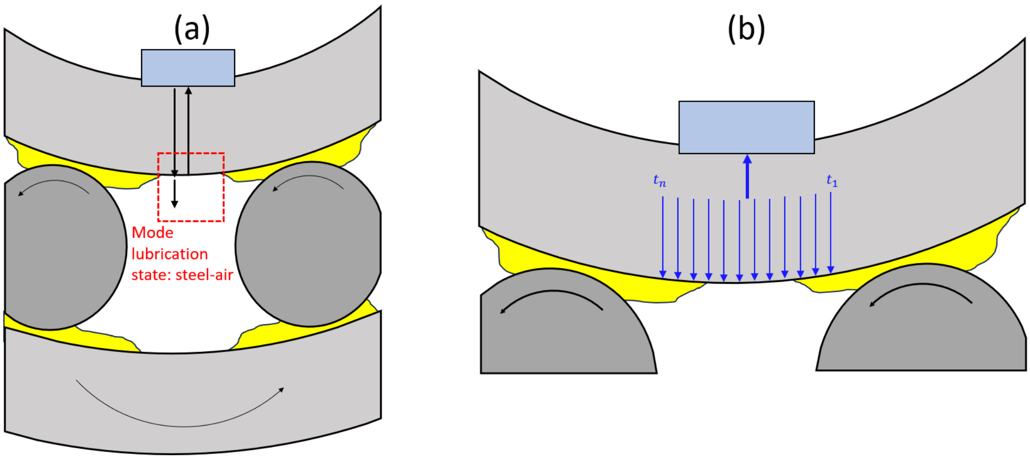

Figure 5.8: Schematic of the naturally occurring steel-air boundary that exists within the bearing during operation

boundary exists. Figure 5.8a shows where the steel-air boundary exists within the bearing.

This area of steel-air is also assumed to be the most common occurring lubricant state within the bearing, i.e. the mode lubrication state, as within the menisci and contacts the signal amplitude changes greatly, and over short distances. Figure 5.8b shows how reflections are taken through the entire rotation of the bearing, from time t_1 to t_n when the capture stops. For bearing testing t_n is typically 5s to 10s and encapsulates tens to hundreds of bearing revolutions, depending on the operating speed. To create the reference an A-scan stack, shown in Figure 5.5, is first spliced into individual reflections and then stacked to create a matrix with a length equal to the number of reflections and width equal to the number of data points within each reflection. The mode value at each reflection point location is calculated to then create the modal reference. Figure 5.9 gives a visual representation of this calculation where A is the reflection amplitude, x_n the x axis position for each reflection and t_n is the time at which each individual reflection occurs. The benefit to this approach is dismantling and downtime for referencing is not necessary as the air reference is created in-situ. So long as test durations are kept short it can be assumed the capture was taken under constant temperature and any sensor degradation that does take place is already referenced for, meaning no further calibration is needed. This referencing approach has therefore been used in previously mentioned ultrasonic measurements of wind turbine bearings [146, 133]. There is a substantial drawback to this approach however, which is if at no point during the test the central raceway region between rollers becomes free from oil, the modal reference will be of a thin lubricant

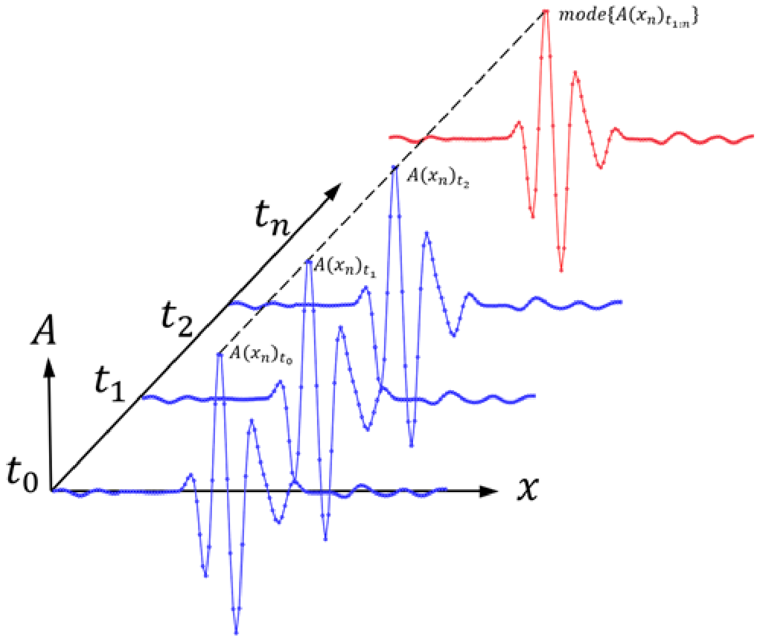

Figure 5.9: Schematic of how the live modal reference is manufactured from all signals within a data set

oil. This can reduce the amplitude of measurement signals, which means a baseline correction is needed in post-processing if amplitude is of importance. However, this is not necessary for the resonant method used in Chapter 10 as the frequency at which the resonance occurs, not the resonance amplitude, is what is used to determine film thickness.

5.5 Single Frequency Reflection Coefficient Bearing Measurements

A well established way to analyse bearing kinematics using ultrasonic sensors is at a single frequency, often the sensor central frequency as this has the greatest SNR. This technique has been used by Howard [132] and Nicholas et al. [147, 146, 142, 133] to measure load and lubrication state in large wind turbine gearbox bearings. To analyse at a single frequency, each reflection within a data stack is windowed, zero-padded, transformed to the frequency domain via a fast Fourier transform, and is then divided by a reference signal in the frequency domain to calculate the reflection coefficient R as per Equation 3.28. Figure 5.10 shows the reflection coefficient change as four rolling elements passed over a sensor location. The schematic shows the lubricant/contact state at different points during the rotation to explain the reflection amplitude change.

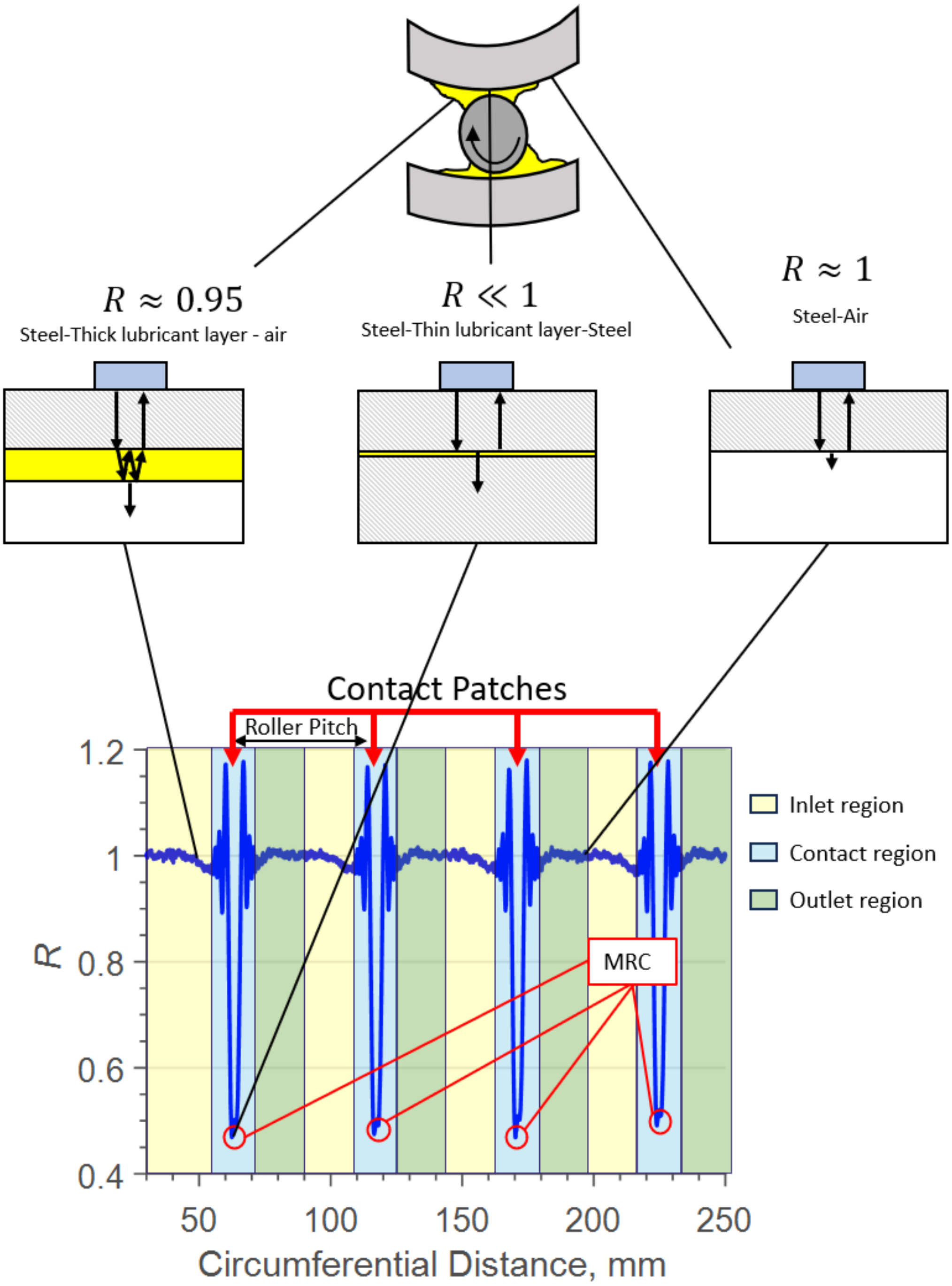

Figure 5.10: Rolling element bearing ultrasonic reflection pattern discretisation into three areas: inlet, outlet and contact

The mode value $R = 1$ across the plot, indicating from Equation 3.4 there is a large acoustic mismatch. This occurs away from the contact or lubricant films, where the raceway is essentially parched, and so the reflection is from a steel-air boundary. This is the region used to generate the live modal reference, as shown in Figure 5.8.

The blue regions are where the roller was directly over the sensor location. As the bearing operates in EHL lubrication, the contact film is extremely thin ($\leq 1\mu$m) and very stiff due to the bearing load. The Spring Model in Equation 3.7 shows that this high stiffness will allow for a large amount of wave transmission through the film and into the roller, and so the pressure of the reflected wave is greatly reduced. At the very bottom of each contact patch, the minimum reflection coefficient (MRC) has been highlighted. This value can allow for quantitative analysis between individual rollers within a single test, or the mean MRC value across tests.

For each contact there are large spikes in R greater than the theoretical limit of $R = 1$ either side of the contact. In his thesis, Howard [132] theorised that this pattern was due to multiple wave reverberations between the curved convex radii of the rolling element and raceway, allowing constructive interference to return larger amplitude waves than the ones generated. Figure 5.11 shows how these interfering waves can develop.

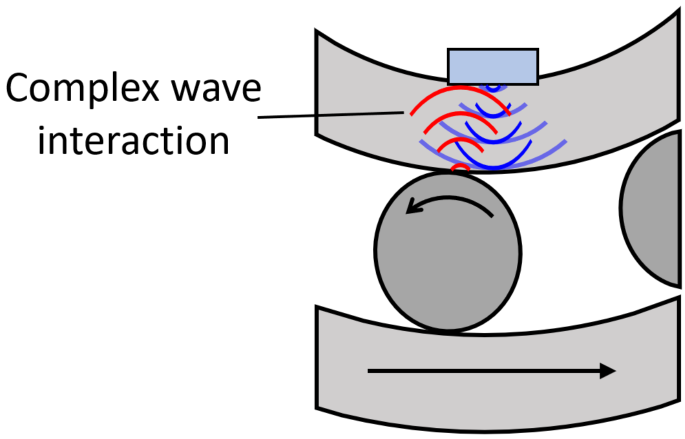

Figure 5.11: Schematic of the complex wave interference which leads to reflection spikes; adapted from Howard [132]

Zhu [148] studied ultrasonic measurements of dry, stationary contacts of a curved nature, and the same pattern was observed. Clarke [149] modelled curved boundaries in contact, and again concluded that the spikes are a result of complex interference. Thus, it is concluded that the vertical interference pattern is a direct result of the complex contact geometries and not the lubricant presence. Getting meaningful results out of the area of vertical interference would be very difficult and require an investment of time beyond the scope of this thesis. However, it is beneficial to recognise this pattern, so that it may not negatively impact results from the usable portions of data.

In Figure 5.10 to the left of each contact is an inlet region, and to the right is an outlet region. Looking first at the inlet in yellow, far from the contact $R = 1$ indicating the previously mentioned steel-air boundary. However, closer to the contact region there is a shift to $R \approx 0.95$. This is caused by an oil film developing on the raceway at the contact inlet. This pattern is mirrored on the outlet side, where initially $R \approx 0.95$ before increasing to $R = 1$ away from the contact. It was mentioned in Section 4.5.2 of the literature review that this kind of pattern has been used to analyse lubricant flow in wind turbine bearings by Nicholas et al. [133].

5.6 Influences on the Minimum Reflection Coefficient

When taking in-situ measurements using a single frequency analysis approach, the magnitude of the MRC is used to compare contact conditions. There are three major contributing factors which affect this magnitude:

1. The *presence* of a lubricant
2. The *thickness* of the lubricant film
3. The *load* applied to the contact

These will all be discussed in further detail.

5.6.1 Lubricant Presence

Referring to the principles of ultrasound, the amount of reflection from a material boundary is dependent on the acoustic mismatch of the contacting media and contact conditions. In the case of a roller-raceway contact, the media have identical acoustic impedances. If the surfaces were then perfectly smooth and the sensing area was smaller than the contact patch, using the Equation 3.4 $R = 0$, there would be no reflection. This case is essentially the same as a wave travelling through a single, unbroken block of steel. There is no boundary and so nothing to reflect from.

In bearing contacts, boundaries are not perfectly smooth due to the presence of asperities. This means that the apparent area of contact is smaller than the real area of contact. If we could look inside the contact on a micro scale, one would see that some asperities are touching, and at these points there is total transmission, $R = 0$. At other points, there is no contact at all and instead total reflection, $R = 1$. Ultrasonic waves have a finite area, and so the reflection recorded is an average of the micro areas of total reflection and total transmission.

Sticking with the same hypothetical contact, if the air pockets were to be filled with a typical lubricating oil, $Z_{oil} \sim 1.2 \times 10^6 kg/m^2s$, then $R_{steel-oil} \approx 0.95$. This means the reflected amplitude is approximately 5% less, a small but noticeable difference. A reflection from this contact, without any change to the number or size of asperity contacts, would therefore be smaller than the unlubricated steel-air example.

5.6.2 Lubricant Film Thickness

Figure 5.12 shows an example affect of a contact with a thin and thick lubricant film. The thicker film contact has a larger R value meaning there is less reflected energy. When the lubricant film is thicker, the number of high transmission asperity contacts reduces, and so R increases.

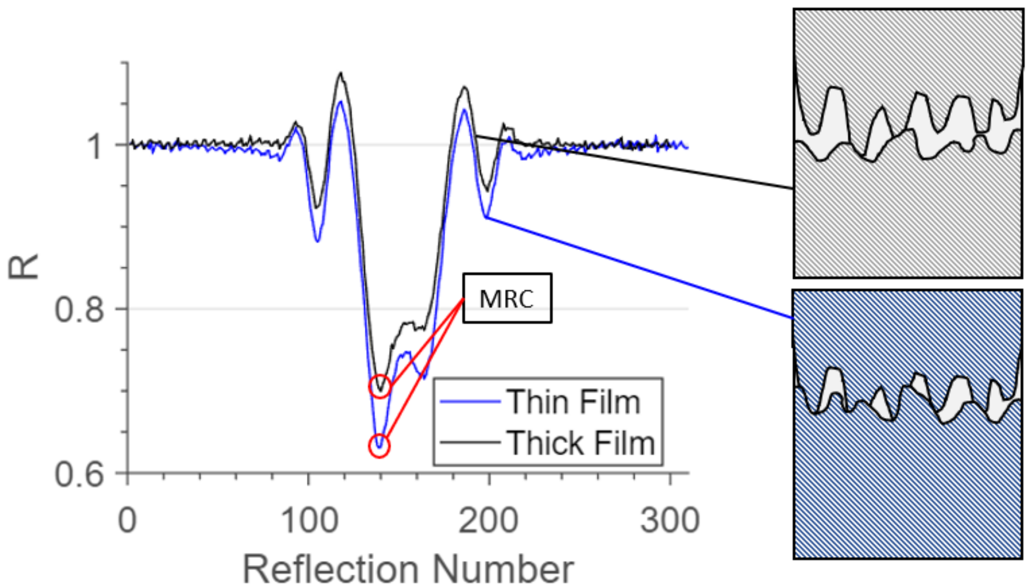

Figure 5.12: Increasing lubricant film thickness affect on contact reflection coefficient with

Once no asperity-asperity contacts exist, further separation will still cause a reduction in R due to a stiffness reduction within the contact, but the increase is not monotonic and will plateau towards $R \approx 0.95$ as the film becomes thick to the point that Equation 3.9 is superseded by Equation 3.4 for applicability. Figure, 5.13 is a theoretical plot of Equation 3.9 which shows this plateau.

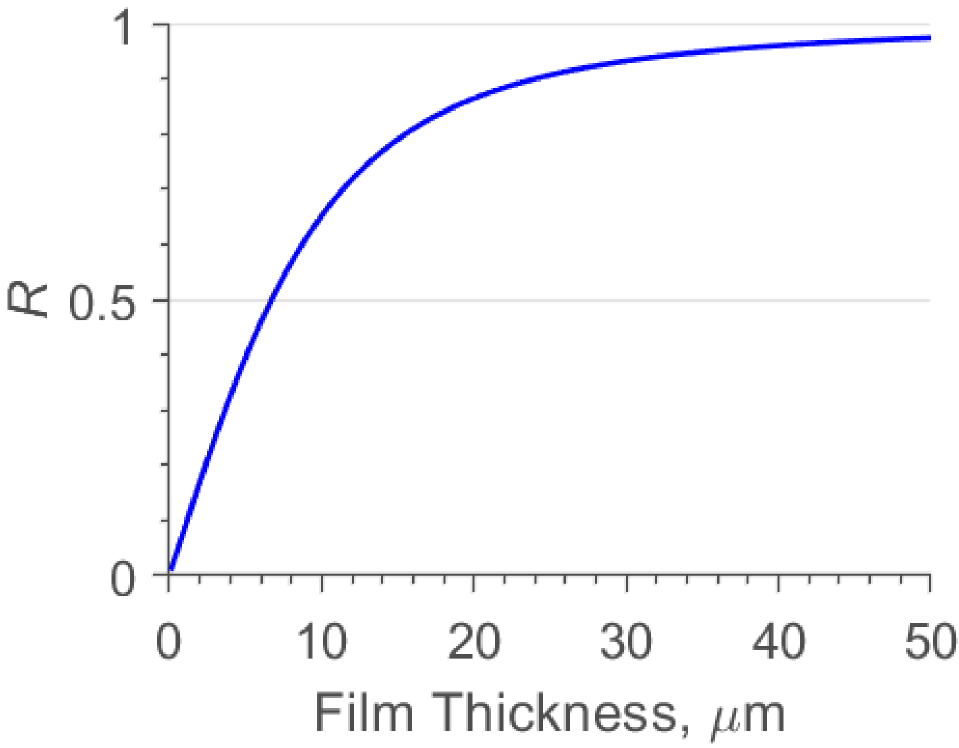

Figure 5.13: Affect on reflection coefficient at a single frequency with increasing film thickness

5.6.3 Contact Load

The contact load is the final major contributing factor to the amplitude of reflection recorded. The magnitude of impact is different depending on the presence of a lubricating film.

5.6.3.1 No Film Present

If no lubricant film is present, the impact of load on reflection is clearer. Within the contact of nominally flat surfaces, the contact separation is related to the load [150]. Equation 3.6 from Section 3.2.2 shows that contact stiffness increases with load, essentially meaning that the real contact area increases towards the apparent contact area, with less air pockets within the contact, resulting in a increased wave transmission. Hence, the amplitude of the reflected wave decreases with increasing load.

5.6.3.2 Lubricated Contact

Within a lubricated contact, the implications of a changing load are slightly more complex. Firstly, it is known from the work of Hamrock & Dowson [49] that an increase in load will reduce the central and minimum film thicknesses, albeit by a very small amount. The more paramount effect however is the increase in viscosity that takes place. Within an EHL contact, the contact pressure on the lubricant can be of the GPa magnitude. If a lubricant has a dynamic viscosity of $0.032\text{Pa} \cdot \text{s}$ and a pressure viscosity coefficient of $2.076 \times 10^{-8} m^2/N$ then under 1 GPa of pressure the viscosity would increase to $3.455 \times 10^7 \text{Pa} \cdot \text{s}$. The contact is then of course, extremely stiff. The implications of this is that the acoustic mismatch across the contact is reduced, allowing more transmission and therefore reduced reflection.

5.6.3.3 Contact size

Whether the contact is lubricated or dry, it is known from the Hertz theory that the contact size will increase with increasing load. As ultrasonic sensors have a finite measurement area, this is an important consideration, discussed in the next Section 5.6.4.

5.6.4 Finite Sensor Size

As a piezoelectric element has a finite surface area, when excited the transmitted wave too has a finite frontal area which increases as the wave moves away from the sensor. However, the finite area of the sensor means that not all of the reflected wave from a contact is recorded, only the wave that reflects onto the sensor face. In a perfectly parallel contact, only the wave that travels normal to, and reflects at angles within the sensor face area is reflected back towards the piezoelectric element, and so the ultrasonic measurement resolution area (UMR) is equal to the sensor face area.

This is not true of a contact that contains a concave radius of curvature, such as that of a bearing. Due to the curvature, it is feasible that parts of the beam with divergence angles $\theta > 0deg$ will be reflected onto the sensor face, as well as the beam portion that is normal to the contact. Therefore, the UMR is larger than the sensor face area. To calculate this UMR would be very difficult due to the unknowns such as the adhesive thickness that glues the elements to a component, any flexion in the element, and the complex contact geometries. Instead, a 2-D Elastohydrodynamic model was developed to investigate this problem.

5.6.4.1 2-D Elastohydrodynamic Lubrication Model

The purpose of the model was first to discretize a contact into a series of nodes, and then at each node calculate parameters such as film thickness and stiffness. Theoretically, the reflection coefficient could then be calculated for each of these nodes, inferring what a varyingly small ultrasonic sensor would measure at that point. Different UMR's of the same contact condition were then simulated by taking an average value of the reflection coefficient at different nodes. The more nodes included in the averaging represents an increased UMR.

To calculate the film thickness in the contact centre, Dowson-Higginson-Toyoda Equations 2.5, 2.6, 2.7 and 2.8 were used. These equations are reliant on other parameters. The first is the roller load parameter P, calculated from:

$$P = \frac{5W}{Z} \tag{5.1}$$

where W is total load applied and Z is the number of rollers. The second variable is the speed parameter $\overline{U}$, calculable from the mean surface speed of the roller and raceway. The final variable is the atmospheric dynamic viscosity parameter for the oil entering the contact, noted as η_0. Using the supplier stated values of kinematic viscosity at $40°C$ and $100°C$, ASTM D341 [151] was used to calculate the kinematic viscosity at the operating temperature of the inner raceway. The standard gives the temperature-viscosity extrapolated relationship as:

$$\log\log(\nu + 0.7) = A - B\,\log(T_k) \tag{5.2}$$

Between 2cSt $\leq \nu \leq 2 \times 10^7$cSt, where A and B are calculable oil constants, ν is the kinematic viscosity and T_k is temperature in Kelvin. All log values are to base 10. Given a set temperature, Equation 5.2 can be rearranged to make ν the subject, allowing a temperature input to calculate a viscosity:

$$\nu = 10^{10^{A-B\,\log(T)}} - 0.7 \tag{5.3}$$

An equation to calculate the density of the oil at the recorded temperature is given by Khonsari and Booser [152] as:

$$\rho = \rho_0(1 - 0.00063(T - T_0)) \tag{5.4}$$

where ρ is density, ρ_0 is the reference density, T is the test temperature and T_0 is the reference temperature. The atmospheric dynamic viscosity η can then be calculated from the kinematic viscosity and lubricant density through the following relationship:

$$\eta = \nu \cdot \rho \tag{5.5}$$

For the model, the inlet region was assumed fully flooded, and calculated using a divergent wedge theory as described in [38]:

$$h = h_c \frac{4\sqrt{2}}{3} \frac{b^2}{2R'} (\xi - 1)^{3/2}, \text{ where } \xi = |x_i/b| \tag{5.6}$$

Pure rolling was assumed as the measurement is taken at the point of maximum load, meaning $SRR = 0$ and so according to Equation 4.3 $\Delta = 0$, and thus the outlet thickness was equalled to $h_c/2$.

It is essential to understand the pressure distribution across the contact as this affects contact stiffness, which in turn alters the theoretical reflection coefficient. Across the contact, the Hertzian pressure distribution was applied, with a single node elevated to 1.5$\times$ the maximum to resemble the pressure spike, as per [153]. At the inlet and outlet the pressure was assumed to be atmospheric. As the pressure at the inlet to the beginning of the parabolic contact pressure increases so rapidly, the change was modelled as a step rather than a progressive gradient. The same principle was applied to the outlet. This does not negatively affect the model accuracy as the stiffness, and therefore influence on reflection coefficient, in the inlet pressure is negligible compared with the contact, and therefore has minimal influence on the averaged UMR.

centre to outlet changes so rapidly,

The model was run for load and speed conditions at which the Lamda ratio $\lambda \geq 1$ ensuring full separation, so only the liquid stiffness had to be calculated from Equation 3.10. Bair [91] states that Tait's equation, Equation 5.7, is the most accurate for modelling this steep pressure increase and incorporating thermal effects. In the equation p, B_0 and B_0' denote pressure, ambient bulk modulus and bulk modulus rate of change with pressure respectively.

$$B = 1 - \frac{1}{1 + B_0'} ln[1 + \frac{p}{B_0}(1 + B_0')][B_0 + p(1 + B_0')] \tag{5.7}$$

Bair [91] also states that although B_0' does have some dependence on temperature, the values for some known fluids are all approximately 11 and that by using this assumption a general equation can be used for numerical solutions of EHL calculations for a large range of pressures and temperatures.

To determine an appropriate number of meshing nodes a convergence study was performed. A UTR = 0.72mm was set, as calculated by Howard in his thesis [132]. As the constriction point was set as just a single node, this means the UTR can span three regions at once; the central region, constriction, and outlet region. The convergence study was completed by setting the UTR to be made of an equal node number, and then comparing the model reflection coefficient of the UTR with an extra central parallel region node (P dominant) or extra outlet region node (O dominant). Results in Figure 5.14 show that at least 244 UTR nodes are required for convergence.

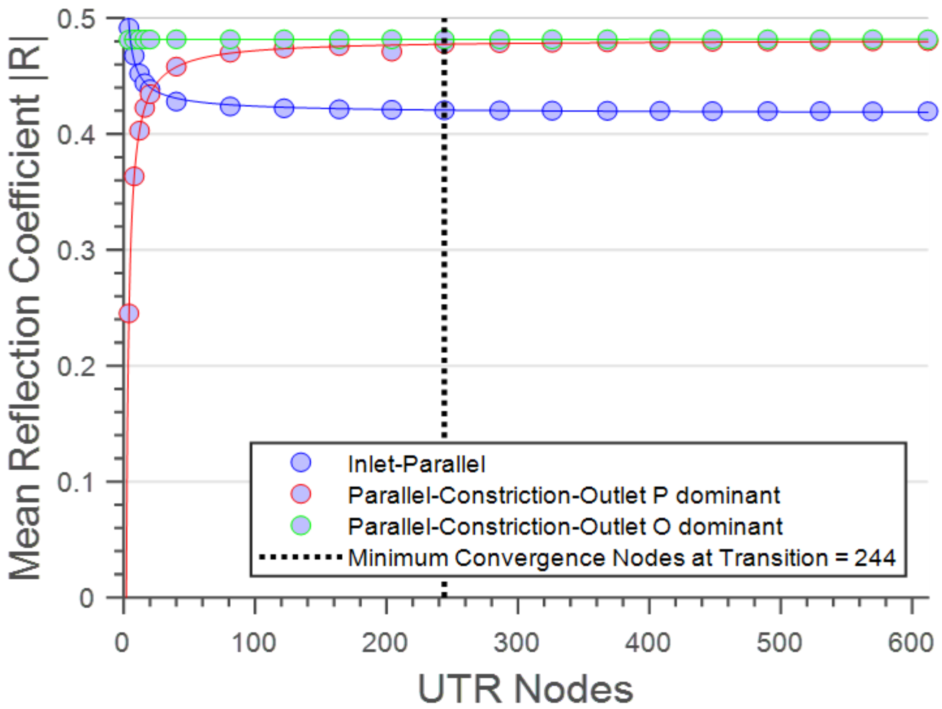

Figure 5.14: Convergence study of the 2-D EHL model showing at least 244 UTR nodes are required for model convergence

Figure 5.15a shows the theoretical film thickness across a single contact. The y-scale is plotted as a log so that the shape can be appreciated. To adhere to the infinite meniscus assumption the inlet is assumed filled up to $5b$ away from the contact centre. At the outlet, reflow around a roller is not considered and so the outlet film is determined by the rupture ratio of the contact film. Figure 5.15b shows the theoretical reflection coefficient, calculated from applying Equation 3.8 to this theoretical film.

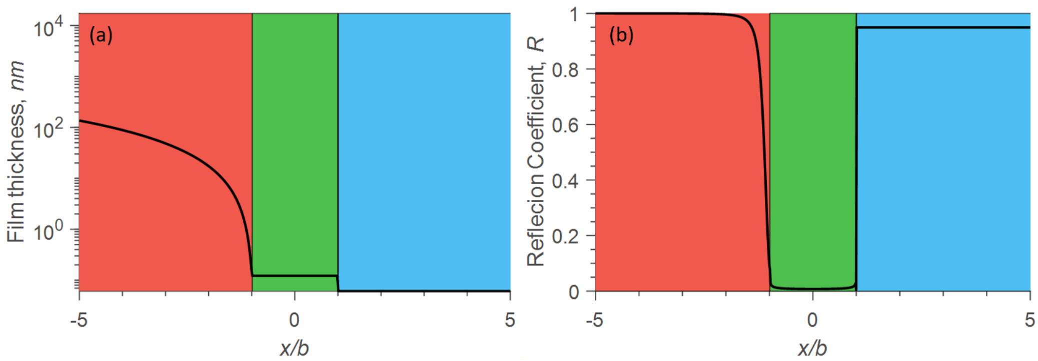

Figure 5.15: (a) Theoretical film thickness through an EHL line contact (b) the theoretical Reflection Coefficient via the Spring Model

Clearly there is a reduction in R leading into the high stiffness contact, and R does not return to 1 at the outlet due to the thin film coating.

Figure 5.16 shows a comparison of measured data and model data with different 2D resolutions. In blue is the exact model values if an increasingly small sensor array could measure a passing contact. R is close to 1 outside of the contact, and close to 0 within the contact with a clear dip towards the outlet where the pressure spike occurs. In purple the UTR is the theoretical width of the beam front, calculated from Hyugen's principle. As this is so wide, the UTR is dominated by areas of high reflectance either side of the contact and so the contact pattern is completely lost. Clearly then, the true width is between these two values. With a measurement UTR = 3mm there is very close agreement with a measured value. It is difficult to reverse engineer the UTR in this manner due to both the shape change observed in measured contact patterns, and the variability in the reflection coefficient amplitude. However, an estimation of 3mm^2 is a good reference point.

The model shows that the measured reflection coefficient within the contact is higher than the theoretical value, and this discrepancy occurs due to reflection coefficient blurring as areas of high reflectance outside of the contact are also encapsulated within the measurement. Therefore, the MRC amplitude should be used only for qualitative trend analysis.

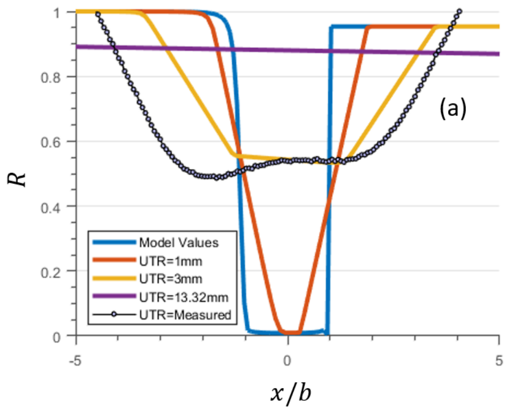

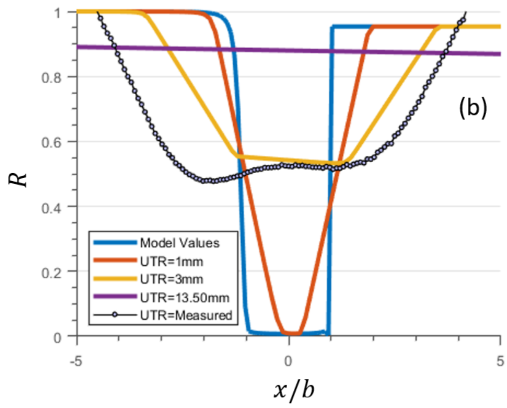

Figure 5.16: Results of EHL 2-D model for (a) VG320 and (b) VG32

5.7 Conclusion

- The rig used for full scale testing is a wind turbine gearbox cylindrical roller bearing test rig; The NU2244 CRB is typical of those found on the slow speed shaft of a 2.5MW to 3MW turbine.

- The rig can be operated at 20, 40, 60, 80 and 100 rpm, with a mean diameter of 310mm this gives a speed range of $6,200\mathrm{nd_m}$ to $31,000\mathrm{nd_m}$. The maximum radial applied load in this work was 600kN; no axial load was present.

- The rig can be operated using oil lubricant, where the bottom, heavy loaded region acts as a sump. However, as rollers plough through this oil, reflow time is still important and fully flooded conditions cannot be assumed. Alternatively, the bearing can be lubricated with grease, using a 1/3 free space fill and a spreading which is advantageous to lubrication.

- Within the bearing data there exists a natural air reference between roller passes, which can be extracted by examining the modal reflection wave and used as a live reference.

- When a roller passes the sensor location the stiff contact allows lots of transmission and so less wave energy is reflected. This roller pass shape can be quantified via the Minimum Reflection Coefficient (MRC).

- The MRC is affected by the presence of a lubricant layer, the thickness of the lubricant layer, the contact load and the finite sensor size.

- Due to small contact widths, which are less than the measurement area size, the MRC value is blurred by areas of high reflectance either side of the contact zone. This makes MRC analysis qualitative.
- Either side of the measured rolling contacts are areas of large vertical interference. This occurs due to complex wave reverberations thickness measurements within this region unfeasible.
- A 2-D EHL contact was developed which suggests the measurement width in the rolling direction is $\approx$ 3mm.

Chapter 6

Experimental Measurement of Roller Skew

In this chapter a new method for measuring roller skew is explained and results from long duration tests using oil and grease are compared and discussed. The potential impact of skew on the lubrication state of the bearing is outlined, and limitations of the measurement method and potential future work is shared.

6.1 Impact of Roller Skew

Roller skew is the pivoting of a roller about an axis normal to the roller-raceway contact. An understanding of skew orientation is prudent to understanding lubricant flow around the bearing as skewed rollers are known to have inconsistent lubricant films across the rolling axis [141]. A skewed roller has the potential to cause excessive wear at face-flange contacts through impaired lubrication. However, depending on the direction of rolling, and the face-flange contact in question, skewing can be either beneficial or detrimental. When the skewing angle forms an opening in the rolling direction, a divergent wedge film is formed which can help lubricate the rolling contact. Figure 6.1 shows the defined skewing orientations used in this thesis. A clockwise pivoting motion is defined as a positive angle, and causes a wedge to form on the left side, enhancing the lubrication in this region by promoting lubricant flow. However, at the opposite face a closed contact is formed, where no wedge is developed and thus lubrication is hindered. An anti-clockwise pivoting is defined as a negative skew angle, and instead aids lubrication on the right side and hinders on the left. In tapered rolling bearings it is ideal for the wedge to form at the main flange as this is more load bearing. In a CRB, as there is a plane of symmetry through the rolling axis, a positive wedge will always be accompanied by a negative one, and so any amount of skew is negative to the health of the bearing.

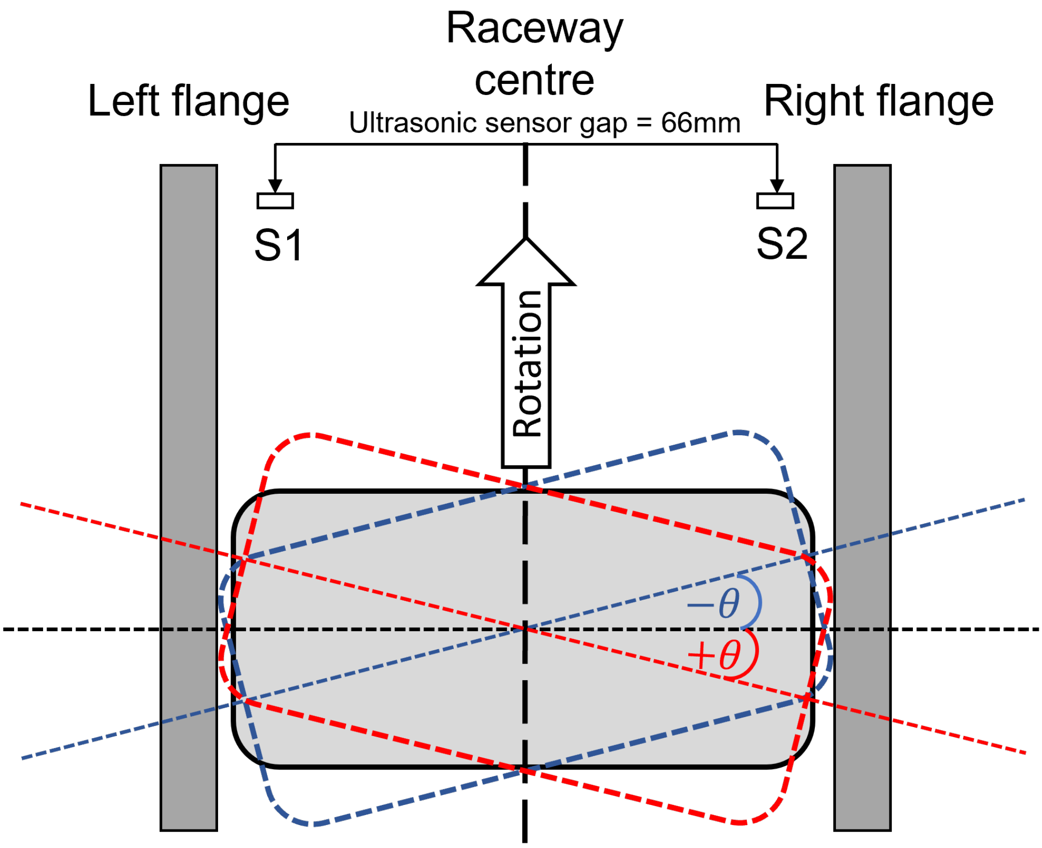

Figure 6.1: A schematic of roller skewing orientation with reference to the bearing flanges, where red indicates a positive skewing angle and blue a negative one.

6.2 Calculating Roller Skew

Figure 6.2 shows the approach to measuring skew, using the time delay Δt between contacts of two sensors, positioned towards both face-flange contacts, at the point of maximum load. It was assumed for this purpose that the point of maximum load coincided with the minimum reflection coefficient of each contact. By then measuring the revolutions-per-minute of the bearing and thus calculating a linear velocity V, this time delay can be used to calculate a skew distance Δs as $\Delta s = \Delta t \times V$. The skewing angle was then calculated as the tangential between this skew distance and the known sensor spacing.

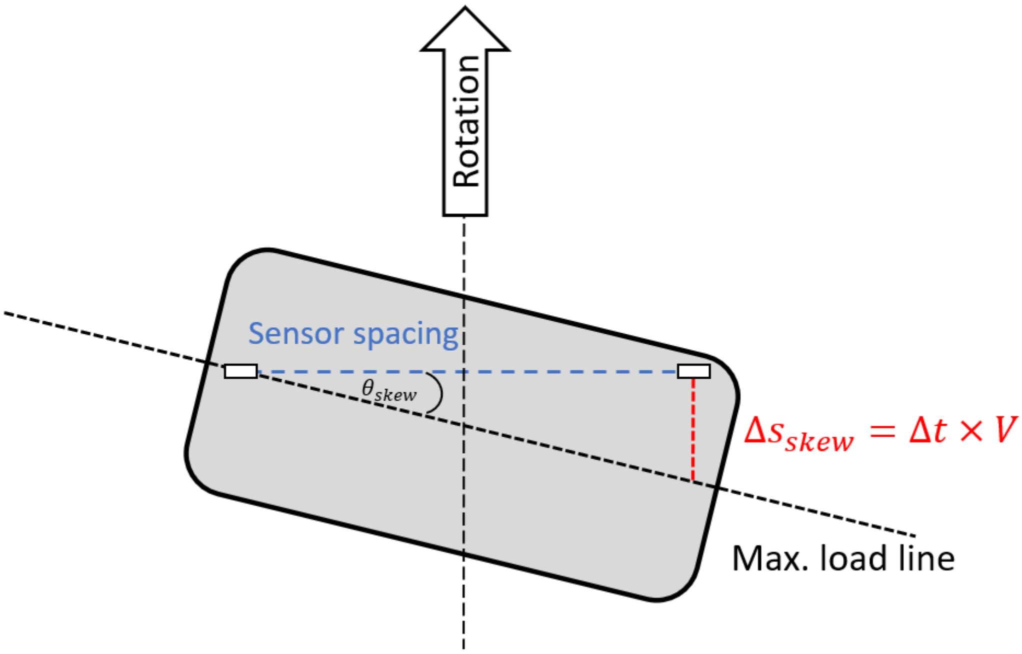

Figure 6.2: Calculation of roller skewing angle based on time delay between contact passing and sensor separation

6.2.1 Calculating Roller Velocity

As the bearing rotates, rollers pass over the sensor locations, with each contact showing a minimum reflection coefficient (MRC) value. For a given capture window, the mean number of reflections between MRC's is calculated. This value is then multiplied by the *Pulse Repetition Time* PRT, calculated from the inverse of the *Channel Pulse Rate* CPR, to calculate the average time between contacts, noted as Δt. This Δt is in turn, the inverse of the *ball pass inner frequency* BPF_i. The BPF_i relates to the driven shaft speed, in this case the bearing outer raceway n_o, and bearing dimensional parameters within the coefficient γ in Equation 6.1 [154]:

$$BPF_i = \frac{1}{\Delta t} = \frac{zn_o}{120}(1 + \gamma) \tag{6.1}$$

γ can be defined as:

$$\gamma = (d/D_p)\cos\varphi \tag{6.2}$$

Where φ, d and D_p are the contact angle, roller diameter and pitch diameter respectively. Within cylindrical roller bearings $\varphi = 0$ and so $\cos\varphi = 1$. Equation 6.2 is then simplified to:

$$\gamma = d/D_p \tag{6.3}$$

To make n_o the subject, Equation 6.1 is rearranged to:

$$n_o = \frac{120BPF_i}{z(1+\gamma)} \tag{6.4}$$

The outer raceway rpm relates to the inner raceway rpm n_i and the cage rpm n_m by Equation 6.5 [24]:

$$n_m = \frac{1}{2}[n_i(1-\gamma) + n_o(1-\gamma)] \tag{6.5}$$

As the inner raceway is stationary during testing, $n_i = 0$ and so the above simplifies to:

$$n_m = \frac{1}{2}[n_o(1-\gamma)] \tag{6.6}$$

Which can be rearranged to:

$$n_o = \frac{2n_m}{1-\gamma} \tag{6.7}$$

Subbing Equation 6.7 into Equation 6.4:

$$n_o = \frac{2n_m}{1-\gamma} = \frac{120BPF_i}{z(1+\gamma)} \tag{6.8}$$

This is then simplified and rearranged to:

$$n_m = \frac{60 \times BPF_i}{z} \tag{6.9}$$

The angular velocity of the cage was then calculated as:

$$\omega_m = n_m \frac{2\pi}{60} \tag{6.10}$$

The linear velocity of the raceway-roller contacts V_c is then calculated as:

$$V_c = \omega_m \times R_c \tag{6.11}$$

Where R_c is the radius from the bearing centre to the roller-raceway contact.

6.2.2 Calculating Contact Time

During operation of the Film Measurement System (FMS) all active channels are sequentially excited with a single trigger, and this excitation process repeats a user-defined number of times. Therefore, with 2 active channels, and a channel pulse rate of 10kHz there will actually be $20,000$ excitations (Global Pulse Rate = 20kHz), constantly flipping between the first and second channel. If the number of active channels increased to 4, the channel pulse rate would reduce to 5000, and the excitation sequence would be channel $1, 2, 3, 4, 1, 2, ...$ Every whole channel excitation can be referred to as a single FMS pulse.

As ultrasonic data streams from a bearing are so large, a data buffer is required to temporarily store the measured voltages, before being permanently stored on the hard-drive. To reduce the amount of data stored, other NI DAQ measurements such as temperature are taken at a frequency equal to the buffer capture rate, as the time between buffer collections are small and changes are negligible. Each buffer collection, rather than reflection, is then given a time stamp. However, each global reflection time stamp can be calculated from the duration of the buffer capture, the number of FMS pulses stored, and the number of active channels. For the channels being used in the skew measurement, the channel reflection number of the minimum reflection coefficient is needed. As only a single channel is observed during this MRC detection, this channel reflection number correlates to the FMS pulse number (FMP).

Figure 6.3 shows a simplified schematic to explain the order of reflections. In the example there is a single buffer with a duration of 1.2s (this is magnitudes larger than real values but simplifies the explanation), with 4 active channels, and the third channel being investigated for the MRC value. The MRC occurs at the second FMS pulse. The time between individual reflections within a single buffer is:

$$\Delta t = \frac{\Delta B_t}{no.\, reflections} \tag{6.12}$$

where B_t is buffer time and so ΔB_t is buffer duration. The reflection number at which the MRC value occurs can be calculated as:

$$reflection_x = (FMP - 1) \times no.\, active\, channels + Chn.\, no \tag{6.13}$$

where x refers to whichever reflection in question. Incorporating the buffer time stamp, where n is the buffer number, the time at which the MRC occurs can be calculated as:

$$t_{reflection} = B_t(n) + [(FMP - 1) \times no.\, active\, channels + (Chn.\, no.)] \times \frac{\Delta B_t}{no.\, reflections} \tag{6.14}$$

Applied to the example given in Figure 6.3, the time stamp of this reflection is:

$$t_{reflection} = B_t(1) + [(2-1) \times 4+] \times \frac{1.2}{12}$$

and so if $B_t(1) = 0$ then $t_{reflection} = 0.7$.

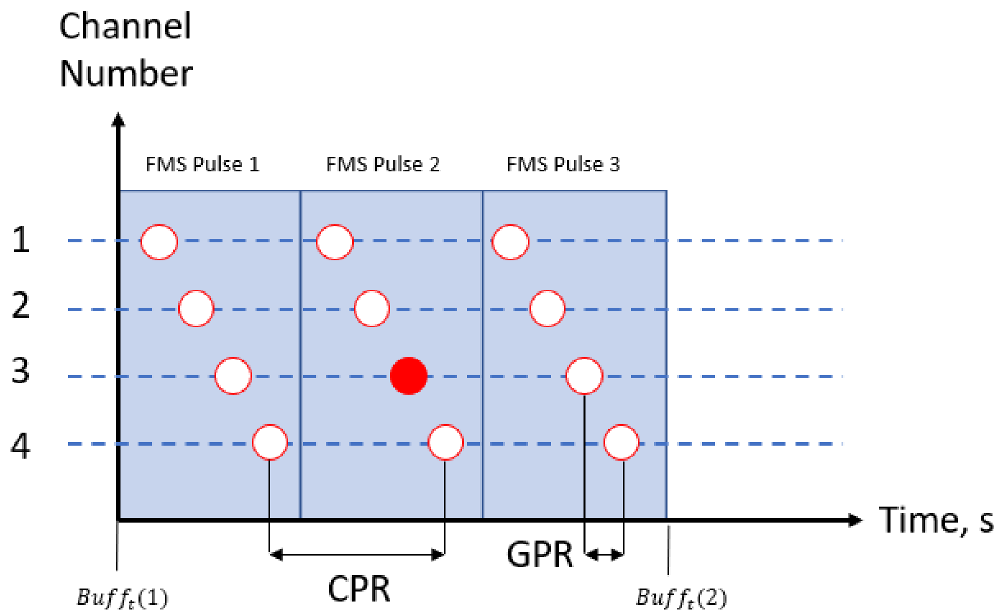

Figure 6.3: A schematic of reflection time within a single buffer capture from the FMS. GPR and CPR are the global and channel pulse rate respectively

To calculate skew, 2 sensors are needed, each with the relative MRC time stamp calculated. With these times, the contact delay due to skew will become apparent. However, even if the roller is running perfectly parallel with the spin direction, there will always be some delay. This is caused by the pulse delay of the FMS, as only one channel is excited at any given moment. To calculate the delay due to the FMS, the number of delays between active channels is multiplied by the inverse of the GPR. The corrected skew time is then calculated by subtracting this delay from the measured delay. As the GPR can fluctuate during testing, it is important to compute this FMS delay for each individual buffer capture.

$$t_{skew} = \Delta t_{reflection} - \text{FMS Delay} \tag{6.15}$$

6.2.3 Calculating Skew Angle

Using Equations 6.11 and 6.15 the skewing distance can be calculated for each roller pass:

$$s_{skew} = V \times t_{skew} \tag{6.16}$$

For each capture window of either 5s or 10s depending on the test, the mean skewing distance was calculated along with the MRC value for the two channels. Pythagoras theorem could then be used, along with the known distance between sensors, to calculate the skew angle and orientation. There are two main assumptions for this approach, the first is the roller is travelling linearly across a flat surface, not a curved surface as the raceway is. However, as the scale of skew is so small, it is a fair assumption in this scenario. The second is that the sensors are in-line and properly spaced, as deviations away from their stated position would obviously affect the measured result. If the sensors had a greater or smaller in-line separation this would have given a smaller or larger skew angle respectively. As skew was not the main focus of this thesis of work, there was inadequate time to develop a calibration method, and so the measurements are all relative.

6.3 Results

6.3.1 Short Duration Oil Tests

The skew angle over the short duration 10s tests of the first bearing test matrix, shown in Table 5.2, were investigated, and the results shown in Figure 6.4. The mean angle was calculated by measuring the skew angle of all roller passes within the 10s duration as they past the measurement zone and taking the average of these angles. There are two noteworthy points from plot. The first is that the skewing angle is clearly related to bearing load, speed and the viscosity of lubricating oil. This agrees with [137, 20, 24, 138, 139] that the aforementioned parameters have some governance over the skew of CRB's.

The second is that for all tests other than VG32 running at $31,000\mathrm{nd_m}$ under loads of 400kN and upwards, the measured skewing angle is positive. Increasing bearing speed and load, or decreasing lubricant viscosity shifts the angle in a negative orientation, but in most cases not past the 0deg threshold. There is no obvious mechanism behind which these parameters influence skew. The increasing load and speed would reduce bearing slip, which is associated with skew, and so the decreasing trend makes sense. However, increasing viscosity, so long as fully flooded conditions are met, should also reduce slip, but the opposite, increased skew trend is seen in the results. Further research would be needed with a more extensive test campaign to investigate these patterns further.

One caveat to the work is the skew angles measured are very small, meaning ultrasonic sensor alignment is crucial. Theoretically, a skew angle of 3×10^{-3}deg

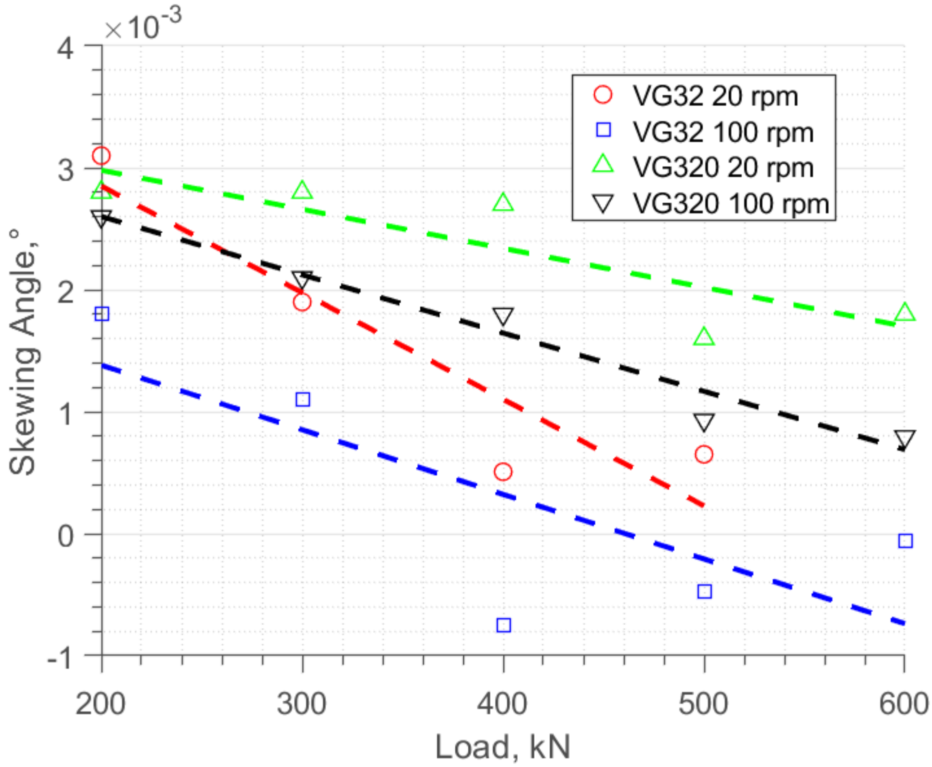

Figure 6.4: Mean skewing angle over a 10s duration for the VG32 and VG320 lubricated bearing

(5×10^{-2}mRad) would be measured if there was a misalignment of just 3μm in the axis perpendicular to the axial plane. Obviously, this kind of misalignment could be expected on sensor positioning. However, the fact that all measured values are within the millidegree range suggests that the sensors were aligned extremely well. This is further emphasised in Figure 6.7a as when the two sensors R values match, the measured skew angle is ≈ 0deg. However, the misalignment potential means the true skew angle cannot be determined, and only a qualitative analysis of the angle change is appropriate from these results. Further work would be needed to determine the accuracy of the true skewing angle.

6.3.2 Long Duration Oil Tests

Figure 6.5 shows how the skewing angle changes over a four hour duration with the bearing lubricated with VG320 oil and operated at 20rpm, test 9 of Table 5.3. It is noted that the skew scale threshold has been limited about the magnitude of interest, but for this plot and the following skew plots, a few skew values with magnitudes far larger than the trend have been omitted. The outlier values are due to a script failure, not actual large skew impulses, and by setting appropriate thresholds the meaningful trend changes in skew can be appreciated. Also shown is the change in R for each sensor, which is calculated from the mean MRC value for that capture window. Initially the skew angle is around 1×10^{-3}deg. Then, at 0.8 hours into the test, there is a step change in skew angle to 2.5×10^{-3}deg. This is accompanied by a drop in R on the right hand side, while the left side continues to increase. For the next 3 hours the skew angle remains constant, while there is an increase in R of 0.035 on both sensors. 3.8 hours into the test there is a second skew impulse but towards the opposite, negative orientation. This impulse is accompanied by a drop in the left side R value, and instead the right side seems unaffected. Essentially, the second skew impulse is a mirror of the first. These skew impulses, where there are step changes in skewing angle, are marked on the plot as SI_1 and SI_2. The two schematics show an exaggerated state of skew orientation after both impulses.

The skew-R pattern shows that an impulse towards a positive, clockwise orientation results in a reduction in R on the right-hand side. Counter to that, if the roller moves towards a negative, anticlockwise orientation, the left-hand axis experiences a reduction in R. It is important to note that the skew angle does not have to cross the measured 0deg threshold for this reduction to take place. In Section 5.6 the influences on the contact reflection amplitude were discussed with lubricant presence, film thickness and contact load highlighted as the governing parameters. In the skew

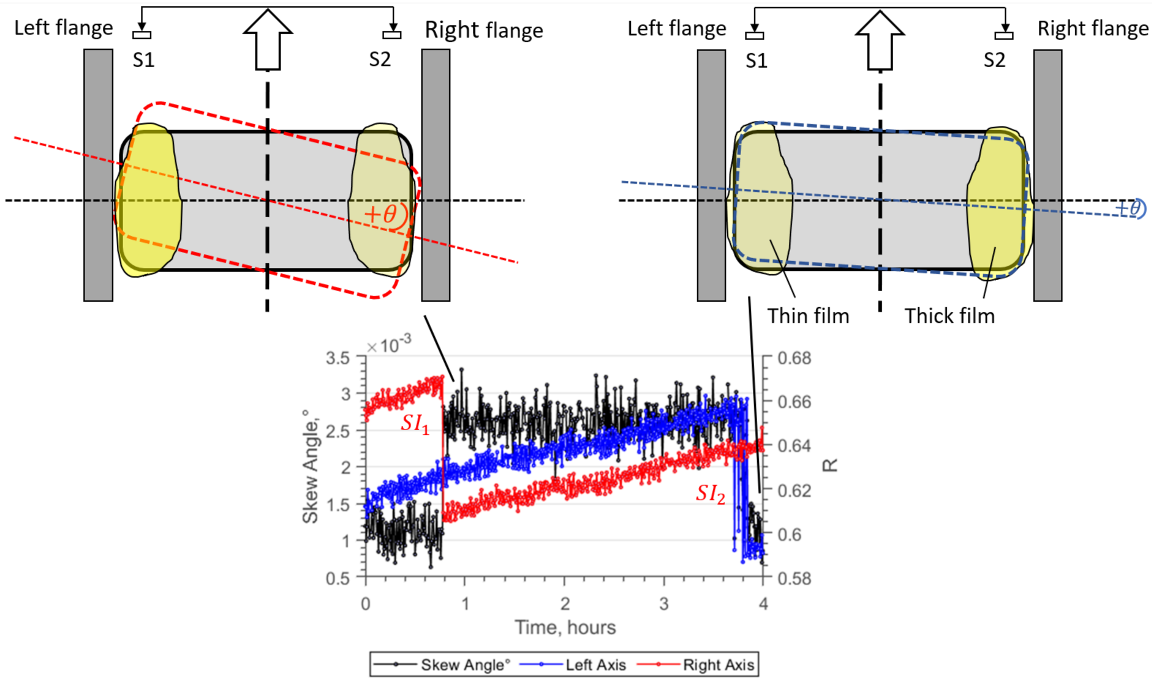

Figure 6.5: Schematic of the skewing orientation and film thickness at the two skew impulses seen for the VG320 lubricated bearing at 20rpm. More opaque films indicate thicker films.

tests, the bearing was lubricated and was under constant load and speed for the test duration. Therefore, a change in R is most likely due to a film thickness change within the contact, and a reduction in R suggests more wave transmission through the contact, the result of a thinner oil film. This then suggests that when a skew impulse occurs, the film on the roller side that is trying to trail reduces, as represented by the opacity of the oil films in the two schematics. This uneven distribution of film across the roller axis was noted in the model work of Liu et al. [140].

Figure 6.6 shows the skew results for the VG320 lubricated bearing for both 20rpm ($6,200\mathrm{nd_m}$) and 100rpm ($31,000\mathrm{nd_m}$) for a and b respectively. For the higher speed case in 6.6b, the same relationship is seen between the orientation of a skew impulse and a film thinning on the edge trying to trail. Unlike the lower speed case, there is evidence at the 1 hour mark of a drop in reflection coefficient with only a minor change in skew amplitude. This suggests that a change in skew does not need to be drastic to trigger a film thinning on one edge. Another feature seen in Figure 6.6b and no other skew results is a drop in both the left and right side R values together at ≈ 2.5 hours into the test. As both sensors show a decrease, this is unrelated to the skew angle, suggesting that a skew angle change is not the only governing mechanism to change the R magnitude under steady state conditions.

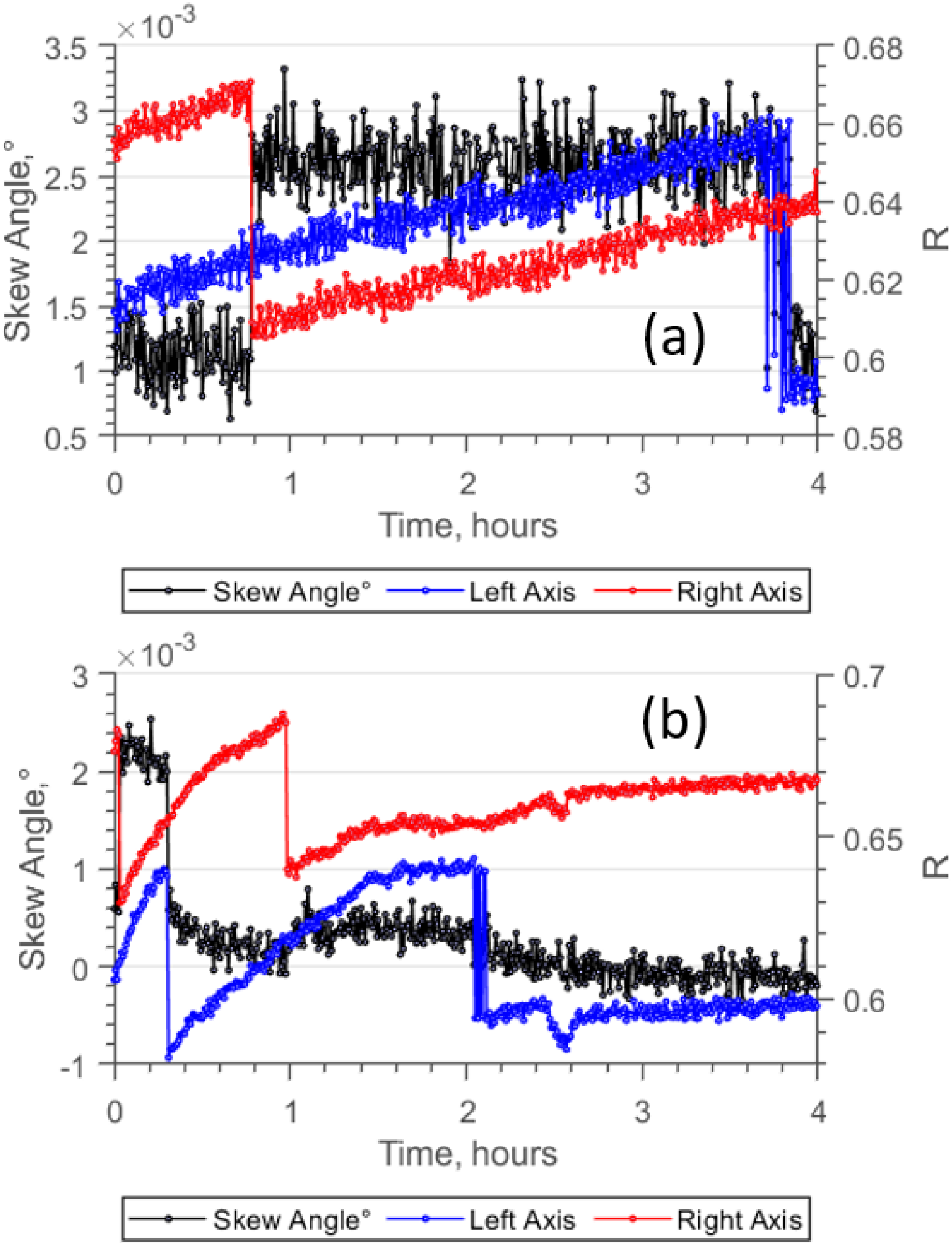

Figure 6.6: Measured skewing angle and minimum reflection coefficient for the VG320 oil lubricated bearing operated under 400kN for (a) $6,200nd_m$ and (b) $31,000nd_m$

Figure 6.7 shows the skewing results for the VG32 lubricated bearing, Table 5.3 tests 7 and 8. In Figure 6.7a right at the beginning of the plot the skew angle $\theta_{skew} \approx 0\text{deg}$ and both sensor R values are closely matched around 0.67. At around 6 minutes into the test there is a sudden skewing impulse which increases the skewing angle to $\theta_{skew} \approx 2 \times 10^{-3}\text{deg}$. This skew impulse is accompanied by a drop in R on the right side axis of 0.06 suggesting film thinning, again while the left side appears unaltered as with the more viscous oil. For the next 2.5 hours this new skew angle is maintained, as is the difference in R values between channels, as both see a rise of $\Delta R \approx 0.04$. 2 hours 36 minutes into the test there is a second skewing impulse, this time in the opposite, negative direction back towards $\theta_{skew} \approx 0\text{deg}$. This impulse is accompanied by a drop in the left side film whilst the right is unaffected.

Figure 6.7b, in which the bearing was run at a higher speed, again shows skew impulses in the $2 \times 10^{-3}\text{deg}$ magnitude range with accompanying film thinning on the edge trying to trail. Comparing plots a and b of Figure 6.7 shows that at a higher bearing speed, there is a much more chaotic pattern to the skew impulses. Additionally, for the higher speed case, between ≈ 0.5 hours and 2.5 hours into the test the skew angle does not seem as stabilised but there are still MRC fluctuations of a comparable magnitude to when there is a skewing impulse, once again suggesting a large skew change is not necessary in altering the film thickness towards either edge.

6.3.3 Grease Churn Results

When investigating skew in the greased roller bearing, there is the added complexity of time dependence due to the churning mechanism. The investigation of this mechanism effect on skew is highlighted in the 2nd test matrix, Table 5.3. Figure 6.8 shows the measured skew angle for all five bearing speeds tested at which churn was occurring. Figure 6.8a is the lowest speed tested, and the very first churn cycle for the grease. There is some fluctuation in skewing angle between 0deg and $0.5 \times 10^{-3}\text{deg}$, however there are no sudden skew impulses as seen in the comparable oil tests of the same speed, see figures 6.6a and 6.7a. Additionally to this, the characteristic drop in reflection that has been associated with a skew impulse is also absent.

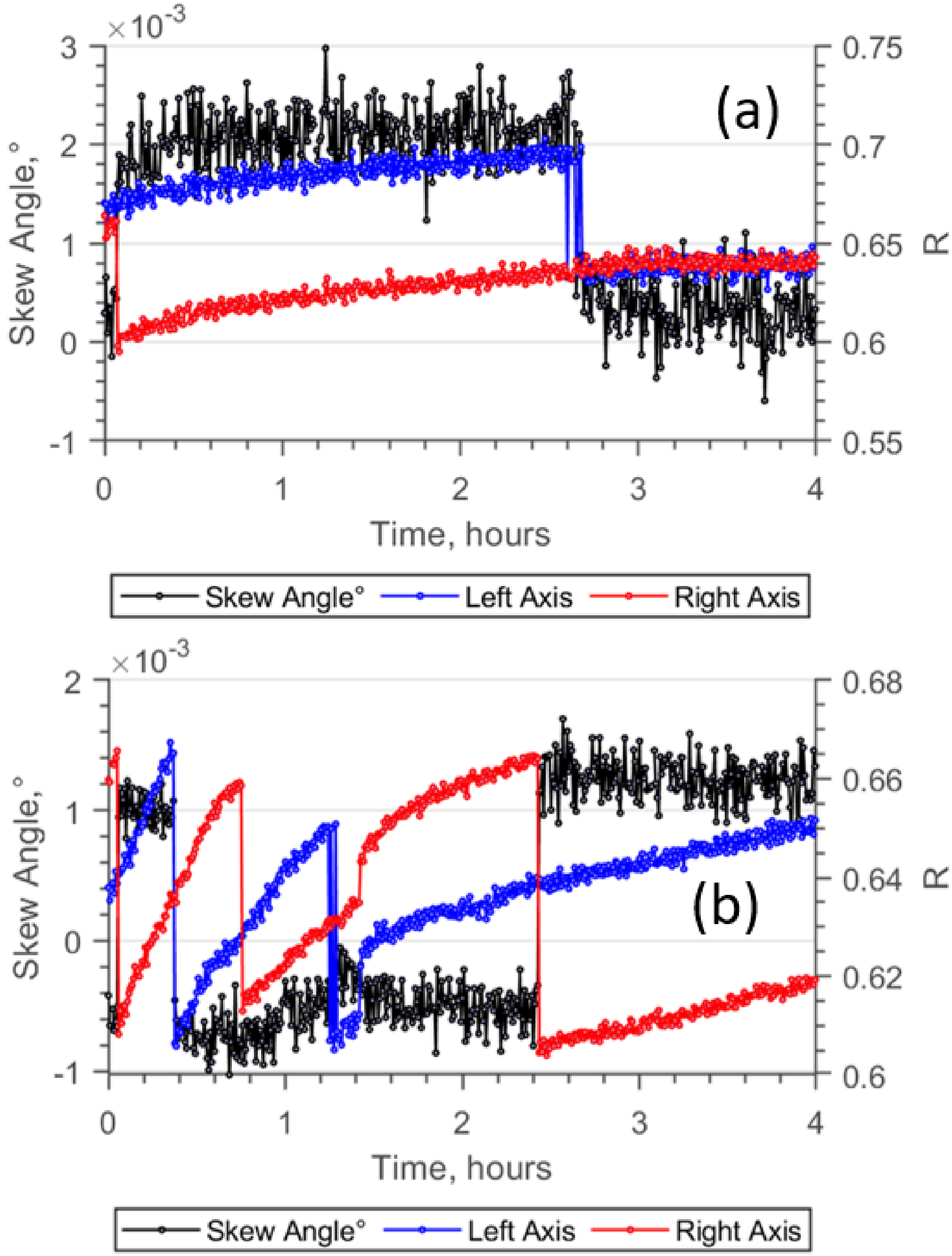

Figure 6.7: Measured skewing angle and minimum reflection coefficient for the VG32 oil lubricated bearing operated under 400kN for (a) $6,200\mathrm{nd_m}$ and (b) $31,000\mathrm{nd_m}$

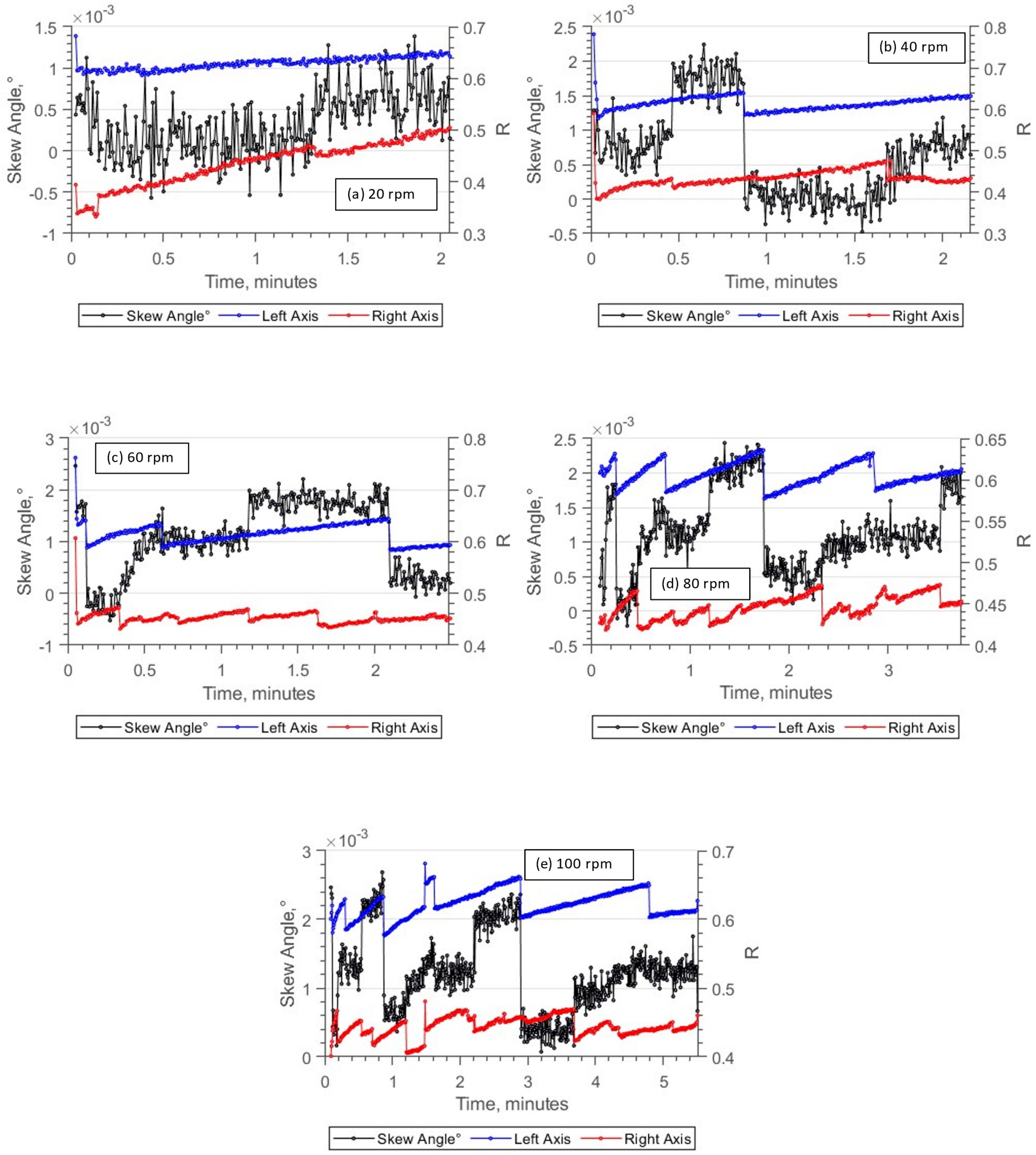

Figure 6.8: Measured skewing angle and minimum reflection coefficient for the 460WT grease lubricated bearing operated under 400kN and a bearing speed of $6,200\mathrm{nd_m}$, $12,400\mathrm{nd_m}$, $18.600\mathrm{nd_m}$, $24,800\mathrm{nd_m}$ and $31,000\mathrm{nd_m}$ respectively from a to e

Looking at comparative speeds between lubricants, figures 6.8a and 6.8e for the grease, and figures 6.6 and 6.7 for the oils, allows for the comparison of a number of patterns. The first is the number of skew impulses. For the lower speed, grease shows no impulses and so is obviously more stable in terms of skewing angle than the oils. However, at the higher speed, per hour there are more impulses for the grease. An increase in the number of skew impulses suggests a more chaotic lubrication pattern within the bearing, as would be expected within grease churn.

When looking at the change in reflection amplitude, interestingly the grease has smaller single sensor changes in the reflection amplitude with quicker bearing speeds. For the 40rpm case $\Delta R = 0.06$, comparable with the oil cases. However, when operated at 100rpm some changes are much more subtle, particularly on the right axis, with $\Delta R = 0.02$. However, there is a more prominent trend when considering the change in R between channels. Table 6.1 shows the mean absolute difference between the channel reflection amplitudes. For the oil tests the change is in the 10^{-2} magnitude and there is no clear pattern between lubricants or speeds. The grease results do show a generally decreasing ΔR trend with an increasing speed, but most noteworthy is the change is an order of magnitude larger than for the oil cases, again suggesting the lubrication pattern is more chaotic than in oil. Uneven R values at either side of the roller also suggest that the skew is accompanied by roller tilt.

Lubricant	Speed, rpm	$\lvert\Delta R\rvert$
VG32	20	4.12×10^{-2}
VG32	100	2.76×10^{-2}
VG320	20	2.41×10^{-2}
VG320	100	5.05×10^{-2}
460WT	20	1.94×10^{-1}
460WT	40	1.81×10^{-1}
460WT	60	1.61×10^{-1}
460WT	80	1.60×10^{-1}
460WT	100	1.78×10^{-1}

Table 6.1: Mean absolute difference in minimum reflection coefficient between channel measurements

Figure 6.9a shows the mean measured skew angle for the 460WT greased bearing in a bar chart. As speed increases, there is a general increasing mean skew angle. The standard error is small due to the high number of data points, and relatively consistent across tests. Figure 6.9b shows a similar trend for the maximum mean skew angle over a single capture window. Both of these subplots then suggest that for greased bearings during churn, a higher speed causes more severe skew.

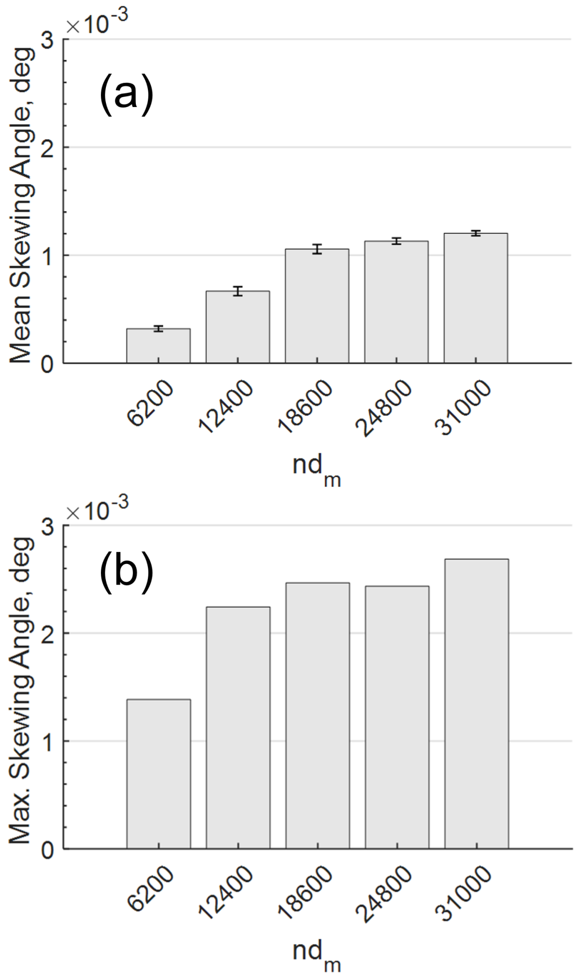

Figure 6.9: Mean and maximum skew angles during the churning phase for the 460WT grease lubricated bearing

Figure 6.10 shows how the mean, maximum and minimum skew values compare for all lubricants tested, under 400kN of radial load at $6,200\text{nd}_\text{m}$ and $31,000\text{nd}_\text{m}$. For oil, an increase in bearing speed leads to a skew shift towards a more negative orientation when considering the mean, maximum and minimum skewing angle recorded. An increase in oil viscosity is shown to shift the skew angle towards a more positive mean orientation at the lower bearing speed of $6,200\text{nd}_\text{m}$, but has a negligible impact at the higher speed of $31,000\text{nd}_\text{m}$. When considering the maximum and minimum skew angle, an increase in oil viscosity shifts the rollers towards a more positive skew angle at both bearing speeds.

Figure 6.10a and b shows grease has the opposite relationship; an increased bearing speed caused a positive shift of the mean and maximum skewing angle. The minimum skew angle shown in Figure 6.10c is lower at the increased speed, the same as with

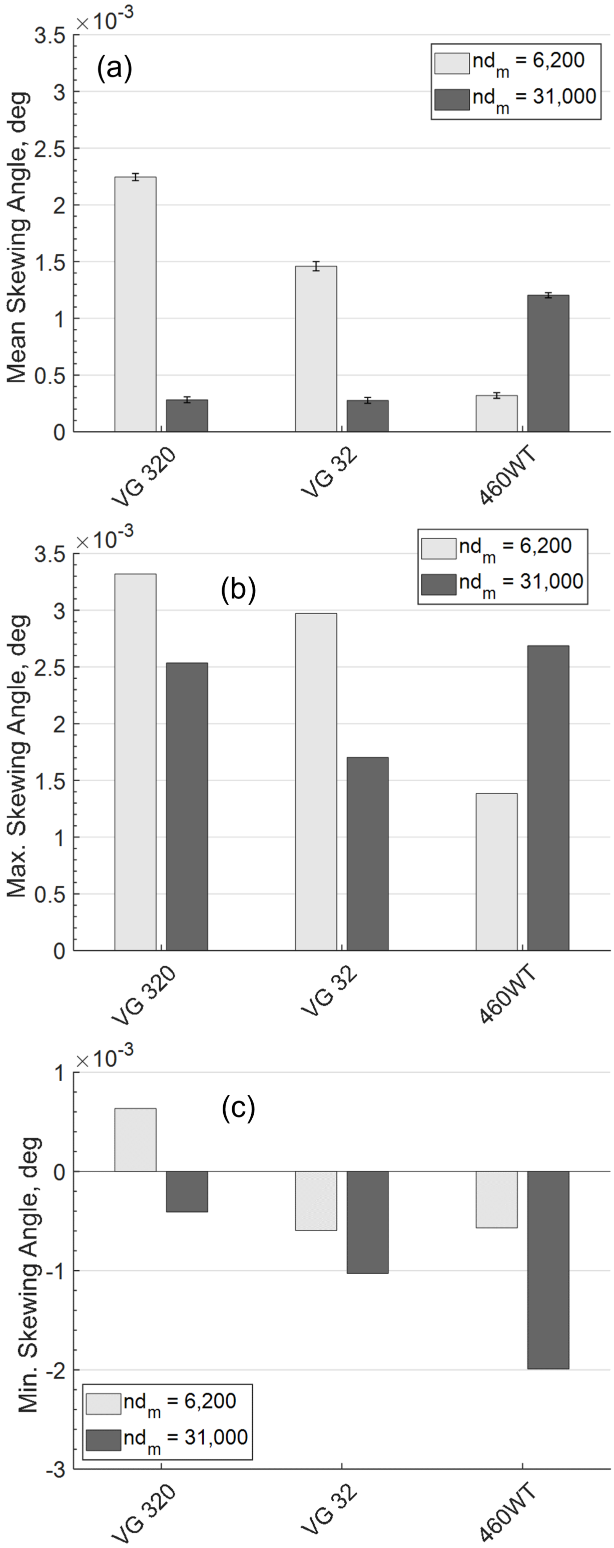

Figure 6.10: (a) mean, (b) maximum and (c) minimum skew angle comparison for all lubricants during the long duration running tests

oil. The difference between the mean capture minimum and maximum recorded skew values is greatest for the 460WT grease at $nd_m = 31,000$ suggesting a more chaotic skewing mechanism. Figure 6.8 agrees with this finding, showing with an increased bearing speed the skewing angle became more erratic, with an increased number of more violent skew impulses. Upon visual inspection of the bearing after testing there were clear visible lumps of dried grease distributed around the bearing surfaces, but appeared to be more clustered near the roller face-flange contacts, see Figure 6.11. The entrainment of this kind of oxidised grease lump into the face-flange contact could feasibly cause this more chaotic skew pattern.

Figure 6.11: Picture of a dried grease clump next to the roller face-flange contact

6.4 Discussion

For both oils tested, increasing the bearing speed is seen to shift the measured mean and maximum skew value closer to 0deg for both the short duration and long duration tests. For VG320 the measured minimum skew angle orientation changed from positive to negative at the higher speed, but still closer to 0deg. Only for VG320 was the minimum skew angle further from 0deg at the lower speed. Chapter 10 shows there is an increased inlet lubricant film at higher bearing speeds. Therefore, there seems to be a correlation between the inlet film and severity of skew in the rollers, with increased inlet oil volumes resulting in less severely skewed rollers.

An opposite trend is seen for grease, with an increased bearing speed shifting the mean, maximum and minimum measured skew value further away from equilibrium. Speed has been shown to cause more violent lubricant distribution during churning [60, 35] and could explain this increase in skew magnitude. Additionally, the grease shows more skew impulses, suggesting more chaotic lubricant movement. Chapter 10 shows that the inlet film for the greased bearing is thinner at higher speeds, an opposite trend to the oil lubricated cases, further explaining why the rollers may have shifted further from equilibrium at the higher speeds.

Skew impulses are seen for both oil and grease lubrication. When operated with oil, the bearing was under steady load and speed conditions with the oil pump constantly turned on. Therefore, there should be do major changes to the availability fo oil or lubrication parameters during the test, such as a sudden lack of lubricant leading to a skew impulse. Therefore, it is more likely that the skew impulse occurs first and is the catalyst for a reduction in film thickness and not the other way around. That is not to say that a reduction in film thickness could not cause a skew impulse, when obviously a sudden change in lubricant conditions could upset the delicate moment balance of a roller. Several things could cause this sudden skew impulse such as load or speed fluctuation, impaired lubrication between the roller face and flange or roller slip. The sensing capabilities of the rig were not adequet to determine the causality and these mechanisms' influence on skew should be the focus of future research.

The dominant issue with the skewing measurements is the alignment of the sensors during instrumentation, meaning that any conclusions drawn from the work relate to the relative change, and when concerning the absolute skew angle are thus far unverified. However, future work could remedy this. In a laboratory setting it would be possible to design and mount a rig that holds a roller in contact with the instrumented raceway, using the raceway faces as parallel guides. Whatever skewing angle this roller is then measured at could be used as a baseline correction value, meaning previous and future skew angle measurements could be corrected for, and the true skewing angle validated.

6.5 Conclusion

- Due to a lack of zero-offset calibration all skew results shown are relative, and not validated as an absolute skewing angle.
- In Figure 6.7a the left and right side MRC values are equal and the skew angle is close to zero actually suggesting that sensor alignment is very good. However, this is an observation and not enough evidence to use the results as more than a relative skew change.
- For short duration tests there is a trend between increased bearing load and speed and an increase in skew in a negative orientation for both viscosity oils tested.
- For longer duration oil tests this negative orientation of skew with increased speed is seen again with mean, maximum and minimum skew angle.
- The mean skew angle is closer to equilibrium with the lower viscosity oil at low speed, but there is a negligible difference at the higher speed.
- Grease shows an opposite trend to the oils; increasing speed gives a more positive mean and maximum skew angle, and a more negative minimum skew angle, further from equilibrium.
- For grease there is a much larger difference in minimum and maximum skew angle recorded at the higher bearing speed, suggesting a more transient skew mechanism with higher rotation rates.
- When operating at an increased bearing speed, it is shown in Chapter 10 that with oil the mean raceway film thickness leading into the contact is increased, so more oil is available to lubricate all contacts. Figures 6.4 and 6.10a suggest increasing bearing speed reduce skew. It can then be concluded with a fair level of confidence that the lubrication state of the rollers and the mean skewing angle are linked, but the mechanism is not clear and there could be a third dominating factor, such as rig vibration, that influences and/or governs both.
- Although the sensors are in a fixed position, the relative skew change does have benefits. To the author's knowledge, the reported skewing impulses have not been recognised as a kinematic mechanism of rolling element bearings, and it has thus far been assumed that under steady state conditions the skewing angle remains constant.

- The purpose of measuring skew was to evaluate if a skew orientation occurred which could alter the lubricant flow to the bearing. To this end, the in-situ measurement was a success. Clearly, the skew angle alters depending on the load, speed, lubricant viscosity and lubricant type. In turn, this could have a beneficial or detrimental impact on lubricant flow to the contact inlet, depending on the flange side and orientation of skew.

Chapter 7

Validation of the Film Thickness - Resonant Frequency Relationship

This chapter begins the work on measuring bearing raceway films by exploring the resonance phenomenon in free surface layer films, defined as a lubricant layer sandwiched between materials of higher acoustic impedance on one side, and a lower acoustic impedance on the other. In this application, that is a solid-lubricant-air contact. Firstly, through a resonance model, it is shown that lubricant film thickness is inversely proportional to a layer resonant frequency, and that for a free surface layer, resonances are present at the fundamental frequency f_0, and all further odd integer multiples $(3f_0, 5f_0, ...)$. These results are then validated using a bench-top rig which mimics both oil and grease lubricant layers on a bearing raceway. Results show that thin layer films are sensitive to ultrasonic waves which cause detectable resonances. Finally, the acoustic velocity of different lubricants is calibrated for, a series of rules for detecting the fundamental frequency is established, and method limits are explored.

7.1 Preliminary Free-Film Oil Resonance Validation

To investigate the relationship between free film thickness and the resonant frequency, the reflection coefficient from a aluminium-oil-air contact was modelled across a 20MHz frequency range using Equation 3.15 given by Haines et al. [94] for the real, amplitude portion of the reflection coefficient. The equation is copied below

$$|R| = \left[\frac{(R_{23} + R_{12}e^{-2\beta h})^2 - 4R_{12}R_{23}e^{-2\beta h}\sin^2 k_2 h}{(1 + R_{12}R_{23}e^{-2\beta h})^2 - 4R_{12}R_{23}e^{-2\beta h}\sin^2 k_2 h}\right]^{1/2}$$

Figure 7.1 shows four different film thicknesses at $25°C$. Two distinct patterns are clear from this figure. Chiefly, increasing the film thickness increases the number of resonances. For the 1μm film there is no dip present at all within the frequency range, the 20μm shows just the single dip at the resonant frequency, and the 100μm and 200μm films both show multiple resonances. Observing the resonance frequencies of the two thickest films, it is clear they occur at the odd integer multiples of the fundamental frequency. This is to be expected as the acoustic impedance of air is lower than that of the oil. Kinsler [95] explains that when a wave travelling through a material reaches the boundary with an acoustically softer material ($z_2 < z_1$) the reflected wave is 180°out of phase with the incident wave, with resonances are only seen at odd harmonics. These odd harmonics occur when the wavelength is an odd integer multiple of the film thickness ($1/4\lambda, 3/4\lambda, 5/4\lambda$, etc.).

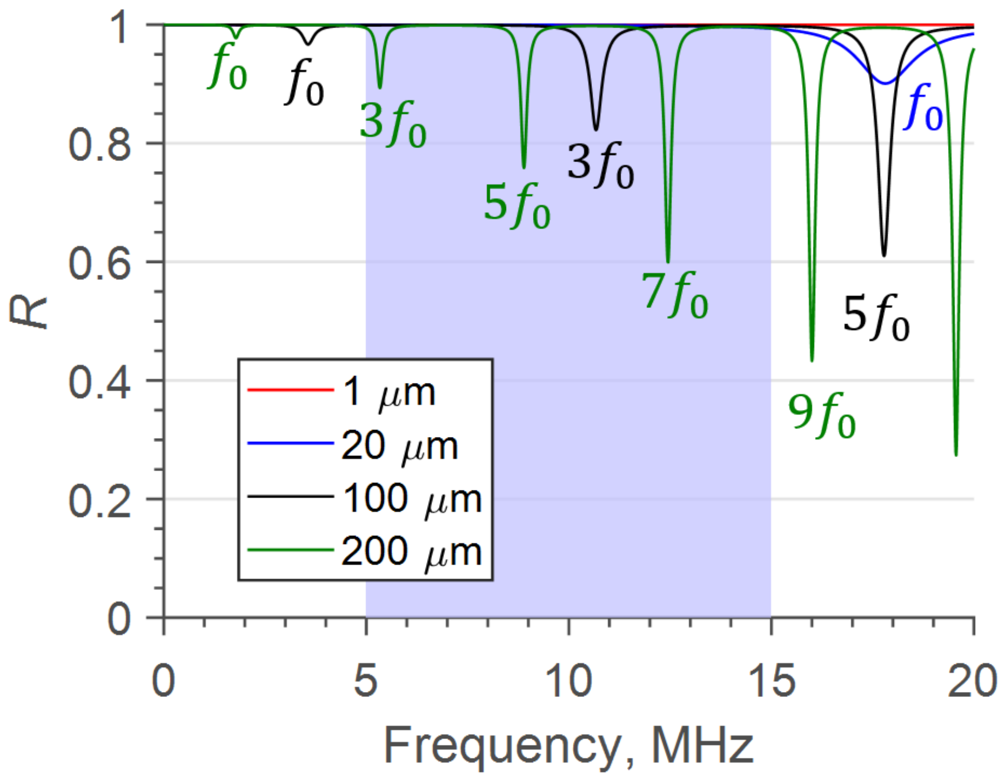

Figure 7.1: Predicted reflection coefficient using Equation 3.15, resonances appear as dips in R. The blue region shows a typical usable bandwidth, centred around 10MHz

To validate the resonance model, and that bare piezoelectric sensors could observe resonances in an oil film, the phenomenon was investigated on a simple spreading oil droplet. An aluminium plate, instrumented with a 10MHz ultrasonic sensor and thermocouple, had droplets of different viscosity oils placed on the plate centre, corresponding with the sensor position, and were allowed to flow unhindered. Two Newtonian calibration oils were used for the experiment, *Cannon s3* and the more viscous *Cannon n10* which have viscosities of 4.6cSt and 21cSt at 20°C respectively. Figure 7.2 shows a schematic of the test set-up. As the oil runs, the film thickness reduces, and so the layer measured becomes thinner over time. During the test the sensor is excited to produce ultrasonic waves which interact with the oil layer, and then 'listens' for the reflections, in a pulse-echo configuration. The ultrasonic test equipment used was a compact low voltage version of the UPR kit used for the bearing test, described in Section 5.2.1.

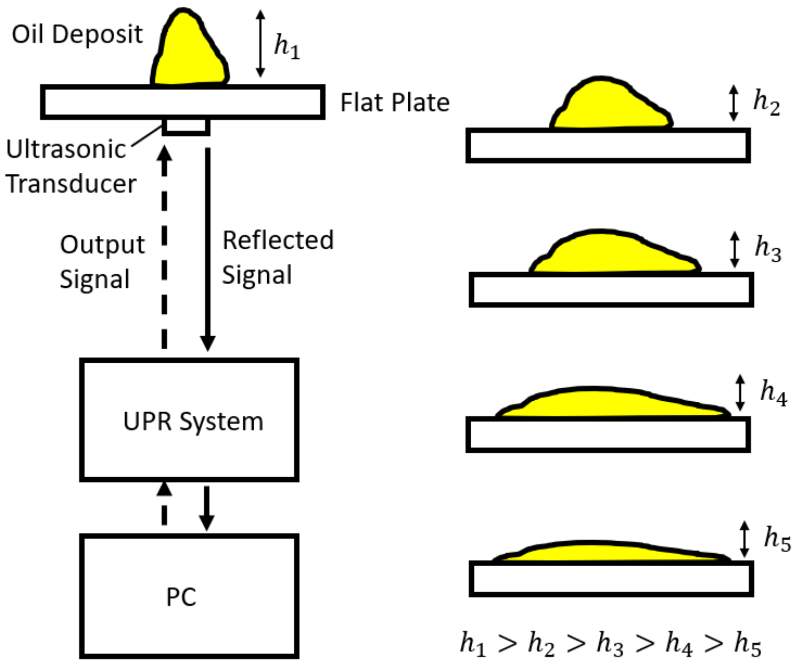

Figure 7.2: Schematic of the thinning oil droplet experiment

Figure 7.3 plots (a) and (c) show reflection coefficient at a single frequency of $\approx$ 11.5MHz. As the oil thins, the film thickness passes through different odd integer multiples of the quarter wavelength, which cause a resonance in the oil layer and thus a dip in reflection coefficient. The resonances occur closer together in (a) as the oil is less viscous and so thins very quickly. In (c) the resonances occur over a long time period as the oil thins slower, and also have a more variable dip pattern. This variability is attributed to shearing in the lubricant by [98].

Plots (b) and (d) show the spectrogram analysis of the same oils thinning. The spectral plot allows analysis simultaneously in the time and frequency domains, with the plot intensity the reflection coefficient. The thinning oil produces horizontal

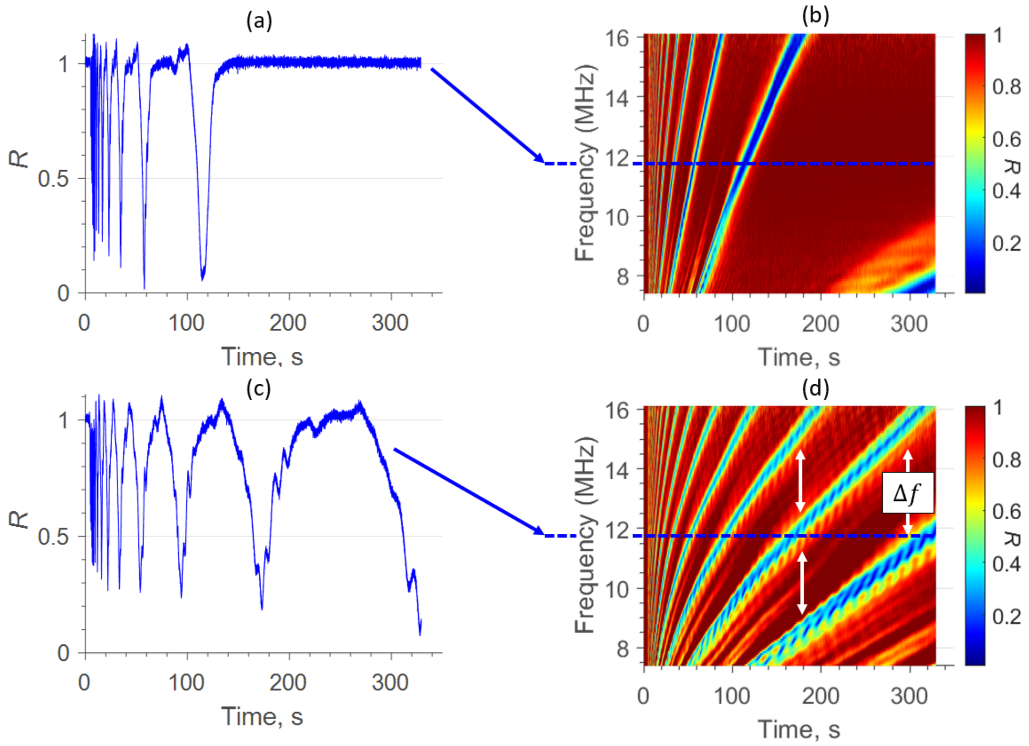

Figure 7.3: (a) & (c) single frequency of 12MHz analysis of s3 and n10 oils respectively. Plots (b) & (d) show the spectrogram oil map of the same oils

fringes which are the resonant odd harmonics, which spread as the oil spreads and h decreases. As the oil thins the fundamental frequency increases along with the odd harmonics, and so the frequency between resonances $\overline{\Delta f}$ increases over time. Plots (a) and (c) are essentially horizontal slices through these spectrograms, and the frequency at which they were taken is observed by the dashed line.

Figure 7.4 shows the ultrasonic measurement of the thinning oil droplets for both viscosity oils. The thickness was calculated by measuring the mean frequency difference between multiple resonances and applying Equation 3.19 with an appropriate acoustic velocity. In the initial reflections, the oil droplet is thick and therefore measurable only by the well established TOF method. As the films continues to thin, reflections from the front and back face of the oil layer overlap and TOF becomes unusable, but the resonance technique is still applicable. For the less viscous s3 oil, the transition occurs at $\approx$ 20s when the film is 300μm thick. The oil film is measured to 112μm after which the film becomes too thin for detection with this particular sensor. For the more viscous n10 oil, the transition does not occur until $\approx$ 80s, and the oil film is measured for the full duration of the test. This test validates that the fundamental resonance is related to the film thickness, and the resonance approach is capable of measuring surface oil films.

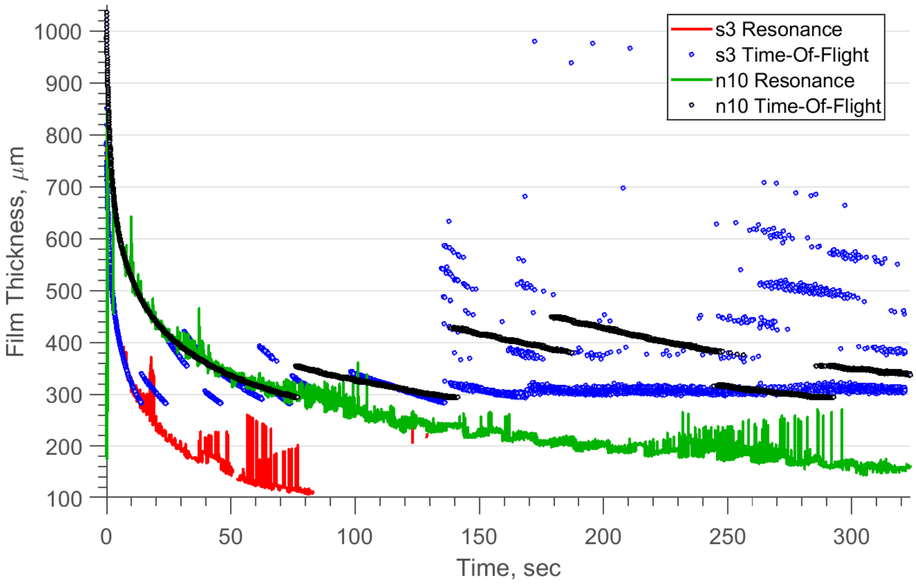

Figure 7.4: Film thickness of thinning oil drops measured by time-of-flight and resonance methods

7.1.1 Effect of Echo Number

Before transferring a time domain signal into the frequency domain, a user decision must be made on the length of signal capture. Figure 7.5 shows a typical ultrasonic reflection, divided into three sections: the nose, the body and the tail:

Nose The nose is the section before the actual signal starts. This section does not contain any data as it is the recording before the wave hits the sensor face. However, it must be sufficiently long, and thus distinguishable from the body of the wave, to ensure that the wave body is not cropped in any way. Any deviation between results from having a shortened reflection nose, so long as the body is not cropped, is most likely due to less measured data points and so more padding and interpolation is required.

Body The reflection body is the main portion of the signal, which is similar to a classic sinusoidal wave, and this region contains the majority of the information data within the signal. In the vast majority of all ultrasonic post processing, it is the body of the signal which is used.

Tail The tail of the signal proceeds the body, but is less a defined length, and more an area where oscillations in the signal are clear, but have amplitudes orders of magnitude smaller than those of the body. Due to the somewhat clouded length of the reflection tail, it leaves the length used for post processing vulnerable to operator judgment. However, due to diminishing amplitude, there is often no gain to be made from greatly increasing the amount of tail incorporated into post-processing, and instead the only effect will be an increased computation time.

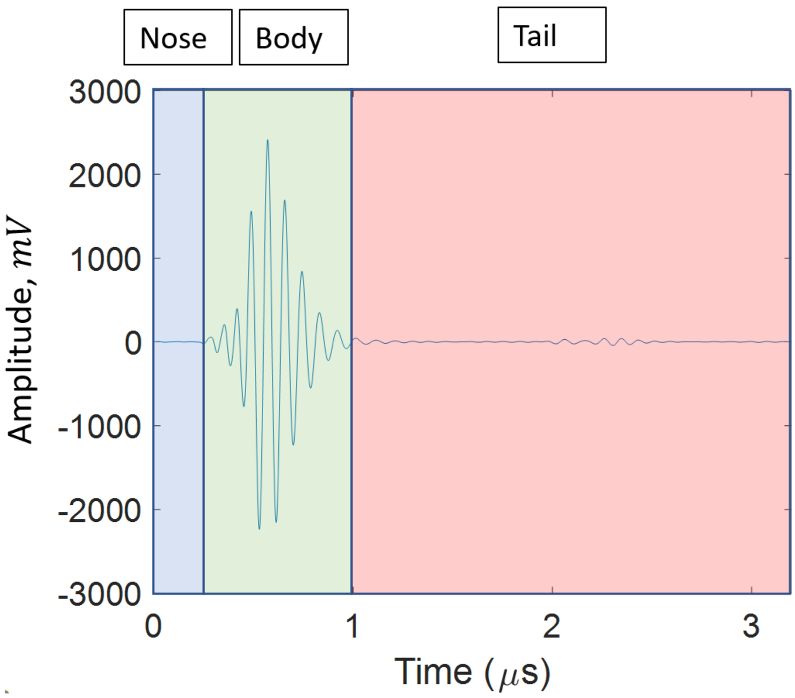

Figure 7.5: Different sections of a typical ultrasonic reflection

Figure 7.6 compares the thickness measurement shown in Figure 7.4 for the n10 oil using the resonance method, but manipulating the length of the tail by clipping the end of the recorded reflection before performing the resonance analysis.

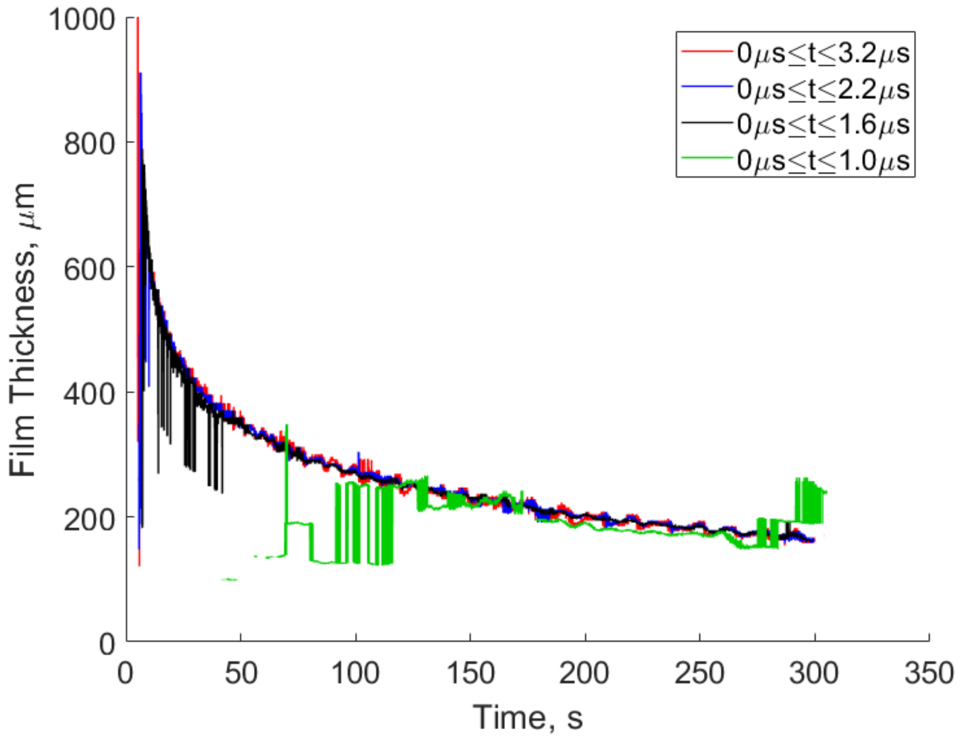

Figure 7.6: Different sections of a typical ultrasonic reflection

The longest reflection analysed is $0 \leq t \leq 3.2\mu$s where t is the analysed reflection time. This incorporates a large tail. The shortest is $0 \leq t \leq 1\mu$s which ignores all of the tail and only incorporates the nose and body in post processing.

Results show that the tail of the signal appears to contain resonance information relating to thicker films. As less and less of the tail is included in post processing, the maximum film thickness calculable reduces. Dou et al. [99] investigated the resonant amplitude with varying numbers of echoes both theoretically and experimentally, and found that as the echo number reduces, the amplitude of resonance decreases. With thicker films, the number of echoes detectable will be reduced as the wave energy reduces due to attenuation, and so naturally the resonant amplitude will decrease. By reducing the tail length included in post-processing, the echo number is synthetically reduced, and thus the resonances of thick films, which already have a lower amplitude than their thinner counterparts, become even shallower until they are indistinguishable from noise. The same manipulation was trialled using a shortened nose, but there was no discernable difference between thickness measurements as expected.

7.2 KOVOT Test Rig Design

The preliminary experiments clearly demonstrate a link between ultrasonic resonances and film thickness of a unconstrained oil film. However, the rig has no way to control the film thickness, and the materials are not representative of a bearing, leaving the validity of the application to a bearing in doubt. Therefore, to develop the work further, the Known Oil Volume Test Rig (KOVOT) was developed.

The purpose of the rig is to perform as an extremely well dimensioned oil bath, of known volume. When a lubricant, whose density and volume are known, is deposited into the bath, the film thickness can be calculated from the dimensions of the rig. The layer thickness can then be measured using ultrasound, and the resonance approach validated against the known thickness. The materials and dimensions used for the rig can also be made representative of a bearing raceway, further validating the use of a resonant approach to measure in-situ raceway films. Additionally, the rig is also of a size suitable to heat on a hot plate or in the oven, so that measurements at different temperatures can be performed. This is crucial as the speed of sound through the lubricant, used for calculating film thickness, is highly dependent on the temperature.

Figure 7.7 shows a rig schematic; the deposited oil layer is representative of a raceway film that may develop in-situ. The rig is made of three main pieces:

- Stand: sole purpose is to support the rig and allow space and protection for sensors and cabling.
- Base plate: This is the most important piece as it is instrumented with ultrasonic sensors and supports the lubricating film.
- Bath Wall: The purpose is to constrain the lubricant film within a known diameter ring, so the film thickness can be calculated from the quantity deposited.

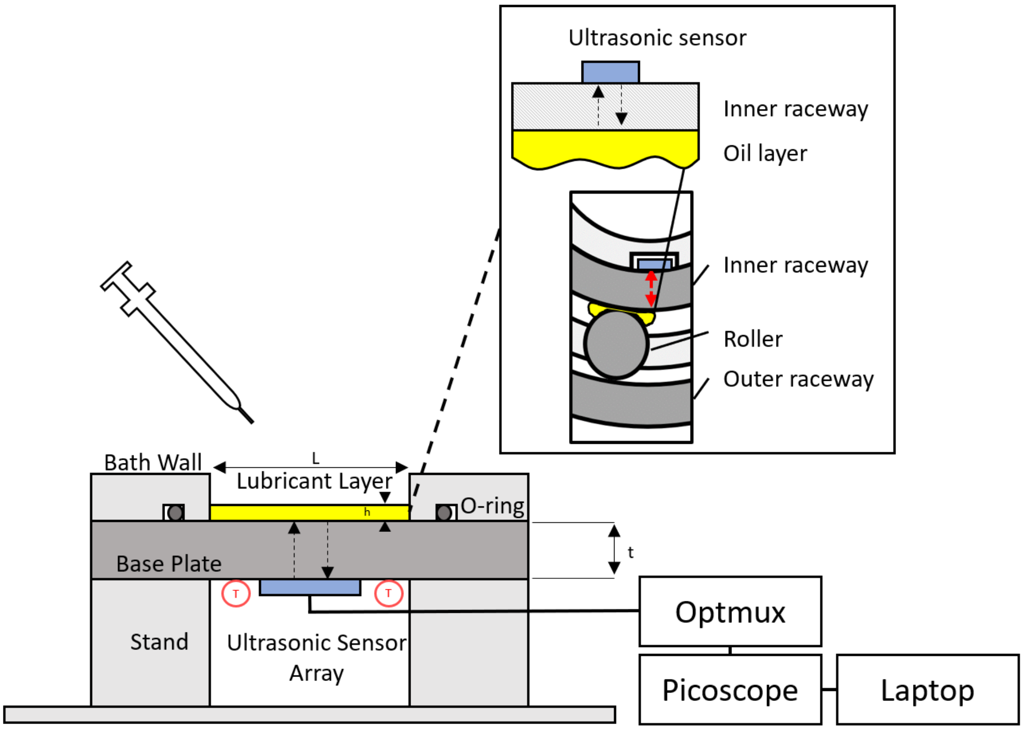

Figure 7.7: Schematic of the KOVOT rig, and the model representation of a lubricated raceway. The red T symbols show where thermocouples are temporarily bonded during testing

Being made in such a fashion, which allows for the rig to be completely disassembled, gives several advantages over oil baths machined into a single substrate block. Chiefly, it means that the base plate can be machined and worked upon without the constraints of bulk material around it. This allows the access of a grinding wheel meaning a far superior surface finish can be achieved. Reducing the roughness is important in reducing the surface tension of deposited liquid films and making the plate more representative of a raceway face. When disassembled, the cleaning operation is made easier as access no longer becomes an issue, and the possibility of contamination of oils is eradicated. Finally, grease layer deposition becomes easier via scraping operations, which again are possible because there are no access constraints.

7.2.1 Rig Commissioning

The intention of the rig was to simulate resonances in lubricants on a bearing raceway. Therefore, the base plate, on which the lubricant rested, was manufactured from EN31 bearing steel. The steel was purchased pre-annealed to allow for machining, after which the plate was then heat treated to increase the hardness, as within real bearings, and the surface was ground to achieve an acceptable roughness.

The stand and bath wall were present only to support the rig and constrain the lubricant respectively, meaning no ultrasonic wave passed through them. For this reason, both parts were machined from the less expensive EN24T. Although other materials were considered, such as a polymer or plastic, the rig must be capable of withstanding temperatures up to $80°C$ for elevated temperature tests. EN24T is capable of operating at this temperature, and has a similar expansion coefficient to EN31, meaning the sealing of the rig was not compromised under expansion when heating due to misalignment.

A single o-ring was used to seal the rig between the base plate and the bath wall. Although only subjected to low, static loads, the ring needed to be resistant to chemical deterioration with high temperature performance. For such an application, hydrogenated Nitrile or Viton are suitable choices [155]. As Viton is more readily available, this was the most suitable choice.

To determine the appropriate plate hardness, to inform the duration and temperature of the heat treatment, the NU2244 bearing was tested using a Vickers Pyramid Hardness Testing Machine fitted with a 2/3" objective size and 20kN load. Due to the curvature of the bearing, the tests were performed along the side face of the inner raceway. Three different locations were selected around the circumference of the bearing, and at each location three tests were taken from towards the inner face to towards the outer face, for a total of 9 tests, as shown in Figure 7.8. The purpose of this was to determine the mean hardness, and also if there was a hardness gradient through the cross-section of the bearing. Table 7.1 shows the raw data and calculated mean.

For each diamond imprint the hardness was recorded in the x and y directions, and the mean was taken of the two. The average was then calculated across the 9 mean results as $785HV20$. There is no pattern to the variation in hardness. Therefore, it was deemed appropriate to specify the base plate to be heat treated to match this value, and the plate was sent to an external supplier to do so. After heat treatment, the plate hardness was tested on the same Vickers Pyramid Hardness Testing Machine, with the same objective size and applied load. Six different locations were tested, between the screw hole locations. Table 7.2 shows the hardness values. The mean KOVOT hardness was $795HV20$, meaning the % difference between the NU2244 and KOVOT hardnesses was 1.27% which is acceptable.

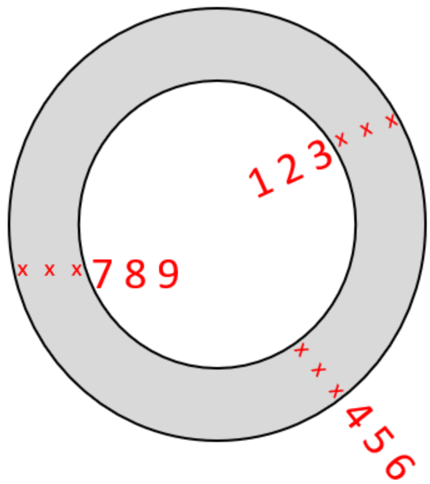

Figure 7.8: Schematic of Vickers test locations on the NU2244 bearing

Test	x HV20	y HV20	$\overline{HV20}$
1	788	739	763.5
2	713	849	781.0
3	695	689	692.0
4	733	810	771.5
5	810	795	802.5
6	841	825	833.0
7	802	833	817.5
8	739	825	782.0
9	795	857	826.0
			785

Table 7.1: Vickers hardness values of NU2244 inner raceway

Test	x HV20	y HV20	$\overline{HV20}$
1	759	849	804.0
2	759	812	785.5
3	817	817	817.0
4	788	817	802.5
5	759	810	784.5
6	733	817	775.0
			795

Table 7.2: Vickers hardness values of KOVOT test plate post heat treatment

The base plate thickness is a crucial dimension as it determines the set path length of the ultrasonic signal. Therefore, this thickness was equal to that of the raceway thickness, 19.50mm. Within roller bearings however, raceway thickness is not a variable that is readily controlled, and instead radial run-out is used. Radial run-out is the variation in either the inner bore of the bearing or the outer diameter of the bearing. The run-out, unlike wall thickness, is very well controlled as large variation can lead to bearing vibration [20] and assembly issues. As bore run-out, outer diameter run-out and element diameter are all very well controlled, an estimate tolerance of the inner raceway thickness, $\Delta t_{raceway}$ can be calculated as:

$$\Delta t_{raceway} = \frac{1}{3} \times \text{total assembly runout} \tag{7.1}$$

According to Timken [156] bearings with a 400mm outer diameter, as the NU2244 has, have an assembly run-out tolerance of $+0\text{mm} - 0.070\text{mm}$. Therefore, according to Equation 7.1 $\Delta t_{\text{i raceway}} = +0\text{mm} - 0.023\text{mm}$. The plate thickness was measured using a pair of digital calipers, the mean plate thickness $\overline{t_{plate}} = 19.50\text{mm} \pm 0.007\text{mm}$, and therefore agreeable with the raceway tolerance.

The roughness of the oil face side of the test plate was investigated using an optical InfiniteFocus SL Alicona. This side was chosen as it is the face in contact with the oil, and as each face had the same finishing procedure the roughness values should be comparable. However, the reverse face of the plate only needed to be smooth to the point that a good bond was made between the ultrasonic elements. As shown in the results section of this chapter, high amplitude clean signals could be seen, showing a good bond was achieved. The oil face side of the plate was measured at five random locations and had a mean $\overline{Ra} = 0.287\mu\text{m} \pm 0.020\mu\text{m}$. This is somewhat rougher than what would be expected of a bearing raceway, however the purpose of a smooth finish on the plate is to achieve optimal oil spread and reduce surface tension, for which the surface finish is acceptable.

7.2.2 Ultrasonic Instrumentation

The underside of the base plate, which does not contact the lubricant film, was instrumented with six ultrasonic sensors with a manufacture stated central frequency of 10MHz. Figure 7.9 shows a picture of the sensors before cabling. Placing sensors at 90° intervals enabled the observation of oil film thickness across the entire plate. The plate centre is furtherest from any edge effects of the bath wall and should therefore be closest to the theoretical deposited film thickness. For this reason two sensors

Figure 7.9: Picture of the KOVOT ultrasonic sensor array before cabling and epoxy was applied

were instrumented at the centre for extra comparison. During tests these sensors were excited, transmitting a wave through the steel base plate to the lubricant film, and the data enriched reflections were recorded on the same pulsing sensor, operating in a pulse-echo configuration as with the bearing testing.

7.3 Experimental Method

7.3.1 Oil Experiments

For the stationary oil layer tests it is critical that the test plate is as level as possible. If there is any kind of tilt, the oil layer will naturally flow, due to the effect of gravity, to the lower point leaving an uneven film thickness. To ensure the levelness of the test plate, Figure 7.10a shows that first a CG60 Cromwell Circular Level was placed at the plate centre. The CG60 is a bullseye style gauge which allows the levelness of the plate to be observed across the full 360°. Shim steel was used to pack up different areas of the plate stand to achieve levelness in all directions. The levelness of the plate was then checked with a Laseriner MasterLevel Box Pro, a digital level reader with a precision of $\pm0.05°$. The plate was deemed level when a reading of 0.00° was achieved in two planes perpendicular to each other, taken from the plate centre, as shown in Figure 7.10b. This meant that maximum deviation the plate could be from true level was essentially $\pm0.025°$ as a greater deviation would have been registered. If the plate was out of level by 0.025° this would give a height variation of 65μm between the diameter extremes, or 33μm between the bath wall and centre point.

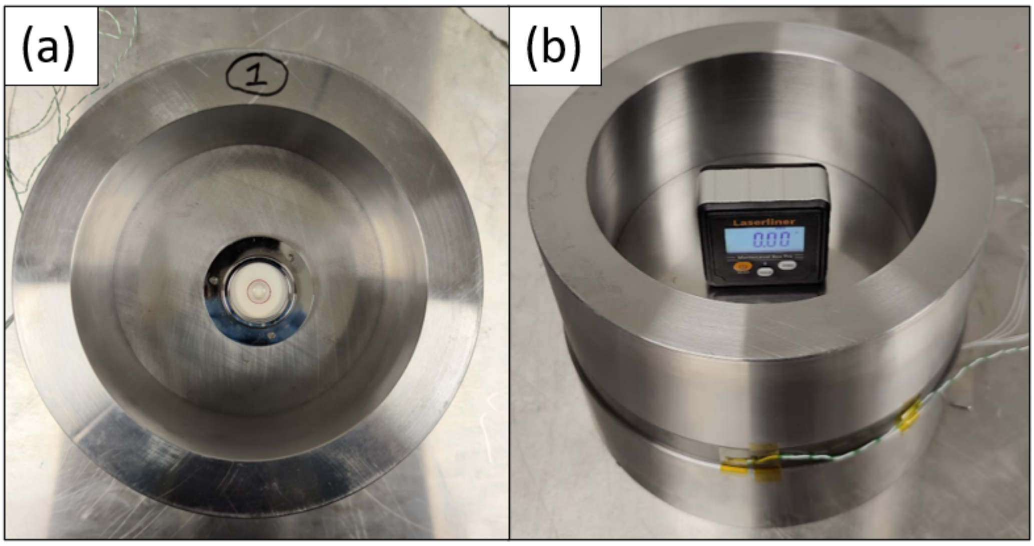

Figure 7.10: Pictures of levelling the KOVOT rig pre-oil tests. Shown in (a) the CG60 Cromwell Circular Level (b) the Laseriner MasterLevel Box Pro

For each test a volume of oil was measured using a syringe with a precision of ± 0.1ml and then deposited at the centre location of the plate and allowed to spread naturally. Once the oil had stopped spreading, the plate surface was visually inspected to ensure that the oil layer made contact with the bath wall across the entire circumference. This ensured an even distribution, and allowed the assumption that the layer thickness was as consistent as possible across the plate face. In practice, surface tension effects at the bath wall will mean some oil will form a meniscus rim, thus lowering the theoretical film thickness h_θ. However, the test area of the plate is large in comparison with the deposited film, the volume of lubricant required to achieve just a $h_\theta = 200\mu$m is 3.53ml. This surface tension effect will only interact with a small volume of lubricant, and thus its effect was assumed negligible.

Once the lubricant film had stabilised, the theoretical film thickness was calculated from a simple volume by area equation:

$$h_\theta = V/A \tag{7.2}$$

where V is volume in $\text{m}^3 = \text{ml} \times 10^{-6}$ and A is area calculated as $A = \pi D^2/4$. The stabilised layer was then measured using a wet film comb gauge, capable of reading films between 25μm and 3000μm, with 25μm increments. The gauge is hexagonal in shape, with different teeth ranges on each side. Thus, before the gauge is used h_θ is calculated from the volume deposited, and the correct comb side is selected. To use the comb, one side is dipped into the oil layer, so that the the edge teeth make contact with the plate. The comb is then removed, and some teeth will have a visible but thin oil layer adhered to them, and others will be dry. The measurement is between the shortest dry tooth and the shortest wet tooth. Looking at the schematic in Figure 7.11, $75\mu\text{m} \leq h \leq 100\mu\text{m}$, or $h = 87.5\mu\text{m} \pm 12.5\mu\text{m}$ where h is the measured film thickness. Figure 7.12 shows a picture of a reading being taken from a stationary oil layer.

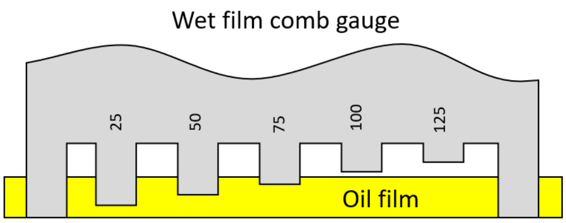

Figure 7.11: Schematic of Vickers test locations on the NU2244 bearing

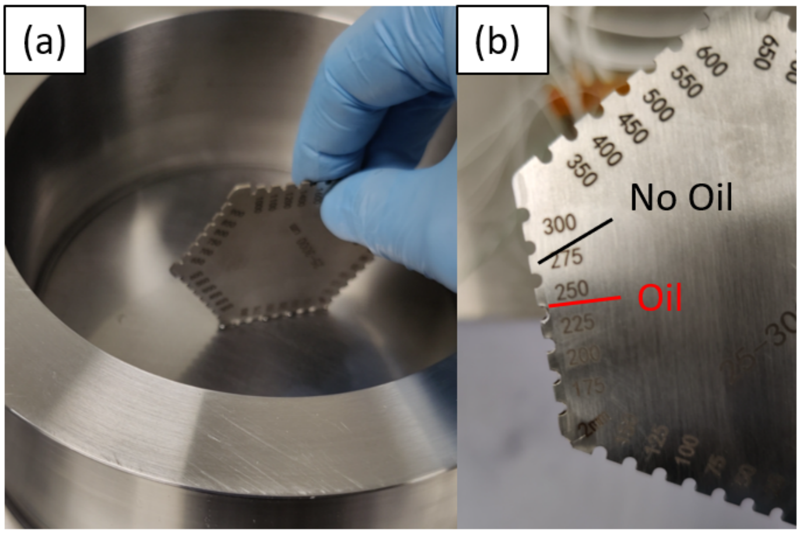

Figure 7.12: Pictures of the comb gauge being dipped into a stationary oil layer. Oil is present on the 250μm tooth but not the 275μm tooth, giving a reading of 262.5μm $\pm$ 12.5μm

When commissioning the KOVOT rig, it was noted that the film did not disperse evenly across the plate and in many cases the oil could not fully cover the plate area. This is due to a combination of surface tension, viscosity and wettability affects. To improve the wettability, a trial test ran where a thin layer of test oil was first wiped onto the plate using a cloth. This greatly enhanced the oil spread, but ultrasonic readings suggested that an even layer was still not formed. Across the six active sensors the measured film thickness ranged from 316.73μm to 455.75μm, although the mean film thickness of 379.14μm was close to the theoretical film 396.12μm. The two most central sensors measured films thinner than most of those around the edge. This phenomenon is likely caused by the previously mentioned meniscus forming at the bath wall and oil adhering to this wall through a capillary action, thus wicking oil away from the contact centre. In some preliminary tests this wicking effect was so dominant that the centre became parched of oil ($< 25\mu$m as checked by the wet film comb gauge) so that the centre sensors detected no film.

In the work of Chen et al. [126] in which a similar test was performed, a surfactant was used to improve the wettability of the surface and was shown to have no impact on the thickness measurements, although the type and quantity of surfactant used is not stated. To improve the surface wettability for the KOVOT tests two different surfactants were trialled. Initially, an off-the-shelf cleaning product which contains a small amount of non-ionic surfactant, but around $15\% - 30\%$ anionic surfactant. Tests showed this impaired oil flow and caused the oil layers to form islands of lubricant more readily, as the anionic surfactant is oil repelling. The second surfactant trialled was Polysorbate 80, a non-ionic surfactant, the type of which is commonly used in wetting agents. A thin layer was applied to the KOVOT test plate before the deposition of an oil droplet, and trial tests showed that this layer greatly improved the oil distribution across the test place. Before all tests, it became standard to apply a thin coating of Polysorbate 80.

7.3.2 Grease Experiments

Grease is a semi-solid at room temperature, and during the test there is inadequate heat to surpass the dropping temperature, thus there is no material flow. This meant that only stationary films could be investigated. To deposit the grease films, an adapted doctor blading method was used.

Doctor blading is typically used for depositing controlled wet or slurry layers onto flat surfaces [157]. The technique is used in casting anodes for batteries and also precisely controlled painting applications. The method involves a doctor blade, which is a straight edge fixed into a adjustable height frame, being drawn along a surface at a controlled speed as a liquid/slurry mixture is deposited in-front of the doctor blade. The set height is how thick the deposited film will be.

Due to the test plate being circular it was not possible to mount a doctor blade for the KOVOT application. Instead, two tape layers of equal thickness were joined to the test face of the KOVOT test plate to form a film channel. The centre of this channel overlapped the measurement area of the two central ultrasonic sensors.

The height of these layers governed the final deposited grease layer thickness, and the height could be adjusted by using multiple overlapped tape layers. A small amount of grease was deposited at one end of the channel and a scalpel blade was drawn across. Constant speed is critical for an even layer deposition, if the draw speed changes the layer can be deposited as wavy and uneven. Many practice attempts were taken until reasonable proficiency was obtained. Figure 7.13 shows a schematic of this doctor blading style technique.

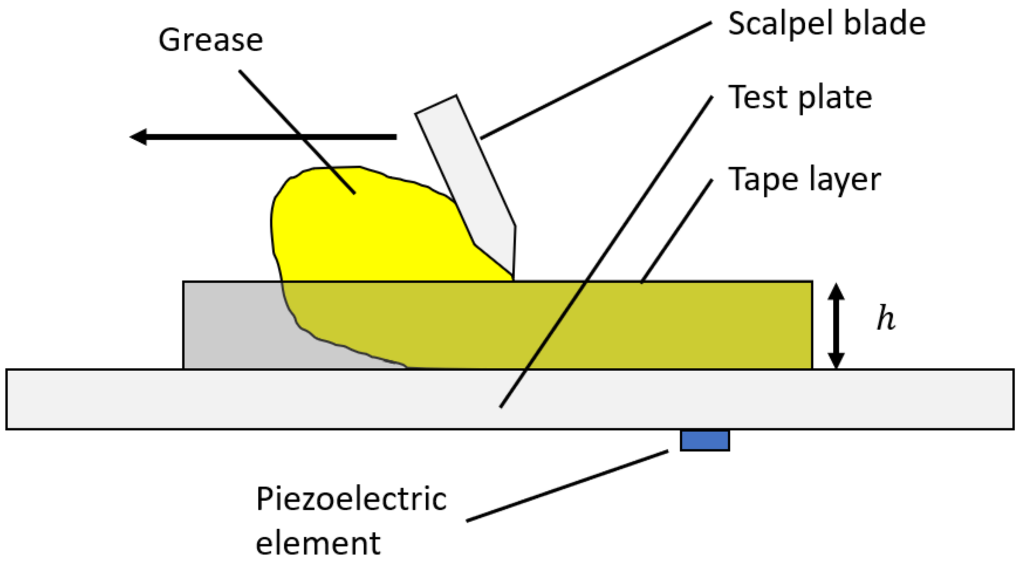

Figure 7.13: Schematic of doctor blading style technique used to deposit grease layers

After the grease layer was deposited, ultrasonic recordings were taken of the film using the two central sensors. Initially an optical InfiniteFocus SL Alicona was used to measure the film step height for comparison, an example plot is shown in Figure 7.14. However, there were significant errors with this approach. Firstly, as the grease is not completely opaque the Alicona struggled to measure the films across the deposited layer. Detection was only achievable on very thin films $< 100\mu$m. The Alicona measurements were then validated using the film thickness comb gauge, which showed that the Alicona under predicted a 67.5μm $\pm$ 12.5μm by approximately 25μm. The reasoning for this is the tape layer, once removed, will leave a slight glue deposit when removed. However, the Alicona references the grease height from this tape layer, which the ultrasound and comb measurements do not. This meant the Alicona was not suitable as a validating measurement method.

Regardless, the Alicona measurements did allow the shape of the grease deposition to be visualised. Figure 7.14 shows an example of a scan, the plotted profile course, and the the profile heights. The profile heights show three different scans of the same layer, but at different positions along the y-axis. The central region thicknesses are consistent across passes, but clearly from the edge of the film there is a large tapering in height. This is due to some flexion in the blade, meaning the edge heights are thicker, and at the centre more grease is removed from the track. In ideal testing the thickness would be consistent across the entire track width, and so based on these preliminary tests the track was widened, meaning greater consistency over the sensor locations.

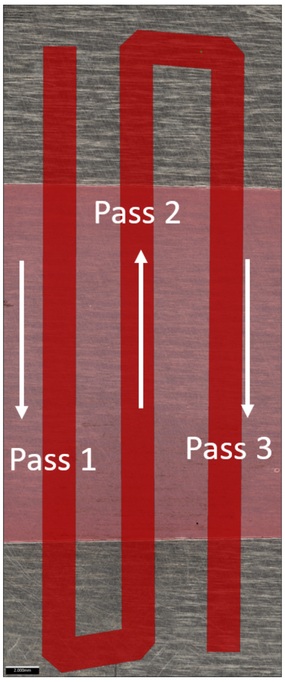

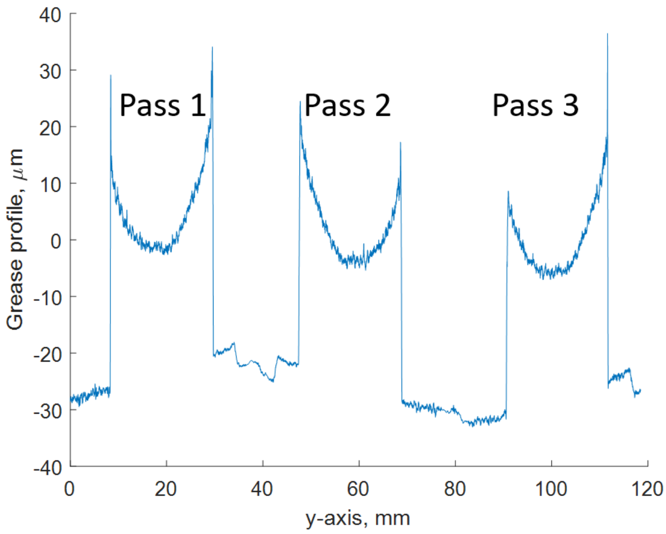

Figure 7.14: Example Alicona scan of a grease layer with the displayed measured profile

As the Alicona measurements were unusable for the grease layers, the film comb gauge was used instead. Figure 7.15a shows a pre test grease layer, deposited via the modified doctor blading technique. Figure 7.15b shows the post test layer, where there are clear indentation marks left from the film comb gauge. On both images there are two thermocouples shown which monitor the grease layer temperature.

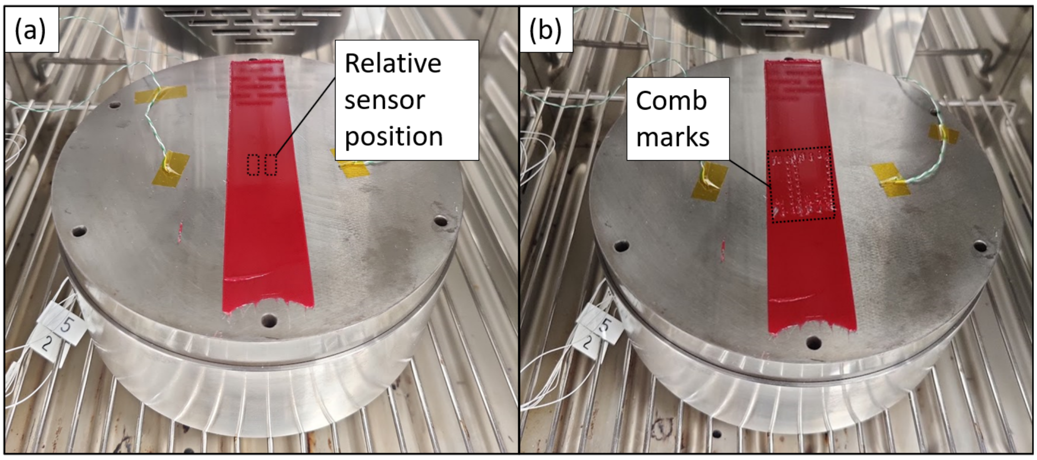

Figure 7.15: Example of a grease layer pre and post oven controlled temperature test

7.4 Oil Film Analysis

7.4.1 Oil Acoustic Velocity Calibration

The resonance method has only two variables; the resonant frequency f_0 of the layer of interest, and the acoustic velocity c through that layer. Resonance detection techniques are universal and can be applied to any free-surface layer. The specificity of a measurement is therefore dependent on the speed of sound through that layer.

The speed of sound is a calculable measurement, and is governed by the bulk modulus and density of a material, as shown by rearranging Equation 3.2:

$$c = \sqrt{B/\rho} \tag{7.3}$$

Wave velocity can be altered by stress fields in stressed materials, as the stiffness of the material will alter when stressed due to the acoustoelastic effect as described by Egle and Bray [82]. This effect was studied by Nicholas [142] in his thesis on measuring bearing load with ultrasonic sensors. Degradation is an additional mechanism that can potentially alter the speed of sound through either a change of bulk modulus or from inclusion of debris particles affecting the homogeneity of the lubricant. However, for all tests run in Chapter 10, the lubricants were fresh and not degraded in any way. Additionally, the raceway films investigated are free-films, meaning they are unconstrained and therefore unstressed. The unpressurised bulk modulus is thus appropriate for the speed of sound of lubricant on the raceway.

Consequently, the acoustic velocity-temperature relationship is what governs the change in the speed of sound. With an increase in oil temperature, there is a decrease in the speed of sound. This has been shown to be very repeatable, and linear in natural oils [158, 159], and a very similar relationship is seen in synthetic oil, as seen for example by Beamish [131].

A bespoke test rig, pictured in Figure 7.16 was used to quantify the acoustic velocity of test lubricants. The rig has different chambers of a very tight tolerance, each with an ultrasonic sensor potted parallel to the bath wall with a Robnor resin epoxy to form an ultrasonic plug. To operate the rig, a chamber was filled with a test fluid, two thermocouples are dipped into the chamber away from the travel path of the ultrasonic wave, and the rig was then placed in the oven. The oven temperature was raised and held until the thermocouples showed temperature stability. The oven was then turned off and allowed to cool, as ultrasonic TOF measurements were taken. The measurements were taken during the cooling phase instead of the temperature ramp as better agreement was seen between the thermocouples, suggesting a more consistent lubricant temperature.

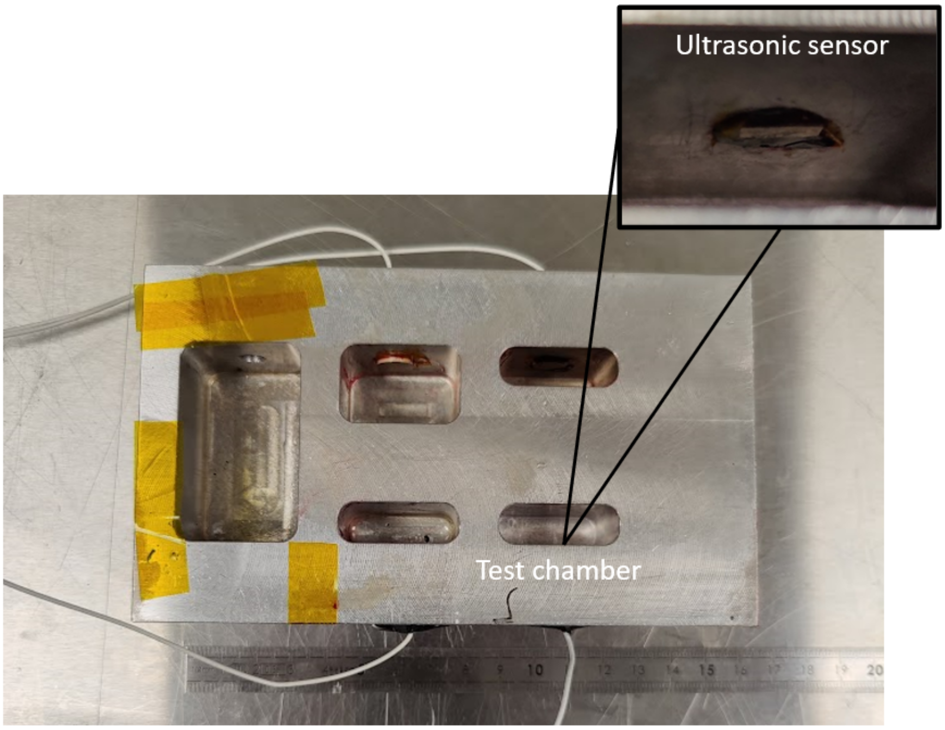

Figure 7.16: Photograph of the acoustic velocity-temperature calibration rig. Enlarged is the ultrasonic sensor embedded in an epoxy puck

To calibrate the rig, the test chamber of choice initially was filled with distilled water, of which the acoustic velocity-temperature relationship is very well documented

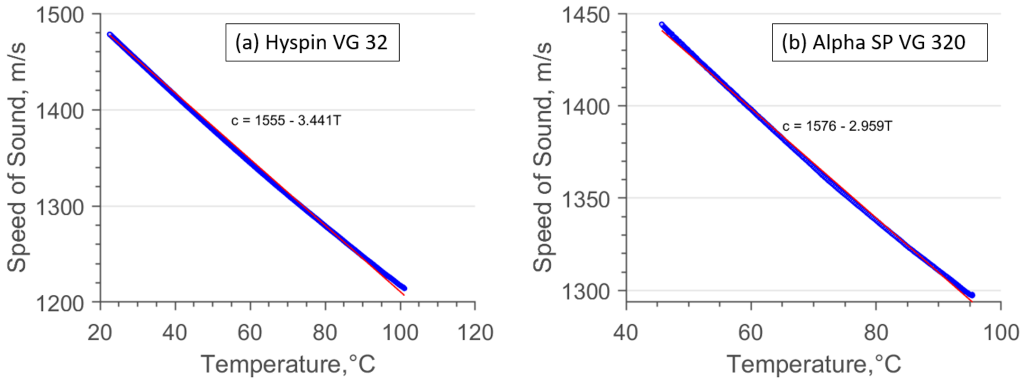

Figure 7.17: Acoustic velocity-temperature relationship of the VG32 and VG320 oils

[160, 161]. Between $25°C$ and $55°C$, the path length changed from 10.03mm to 10.01mm respectively. This change occurs not due to the rig well expanding which would widen the gap, but instead due to the epoxy plug (which has the embedded ultrasonic element) expanding into the chamber. To quantify this error, at $25°C$, c_{water} = 1496.36m/s. Over a chamber length of 10mm the time between reflections (where the wave has travelled twice the path length) is 13.37μs. Assuming then that this is the time measured between reflections, if the path length was actually 10.03mm the speed of sound of water would be calculated as 1500.38m/s, which is a percentage error of just 0.27%. Therefore, it was deemed that the path length change over the course of testing was negligible.

Figure 7.17 shows the velocity-temperature calibration curves for both *Alpha SP VG 320* and *Hyspin VG 32* test oils, derived from the rig shown in Figure 7.16. Clearly, both exhibit a linear decrease in acoustic velocity at increased temperatures. The blue points show the experimental values, and the red line is the derived velocity-temperature relationship for each oil.

In his thesis, Howard [132] also performed a acoustic velocity-temperature calibration for the *Hyspin VG 32* oil, and derived a similar equation of $c_{VG32} = 1507.65 - 3.412T, \text{m/s}$ where T is the temperature in degrees Celsius. Therefore, for bearing tests, the two relationships used for the acoustic velocity calibration were:

$$c_{VG320} = 1576.3 - 2.9586T, \text{m/s} \tag{7.4}$$

and for the *Hyspin VG 32* oil, the mean of the relationship derived in this work, and the relationship derived by Howard [132] were used to form:

$$c_{VG32} = 1531.33 - 3.427T, \text{m/s} \tag{7.5}$$

7.4.2 Oil Film Results

For the KOVOT tests, both the VG32 and VG320 were too viscous to adequately spread over the plate surface at room temperature. Instead, *VWR Avantor calibration oil 85095.260* which has a viscosity $\nu = 4.4$cSt at $20°C$ was used, and found to flow across the entire plate surface and stabilise within 1 hour. A separate acoustic velocity-temperature calibration was performed for this oil using the rig shown in Figure 7.16. Four different volumes of oil were used for the validation tests; 4ml, 5ml, 6ml and 7ml which should form film thicknesses of 264μm, 283μm, 339μm and 396μm respectively, if the layer formed is perfectly stable and level.

During the oil thinning, the film resonance was monitored on a single sensor located at the plate centre. This changing resonance was observed via a spectral plot, as in Figure 7.18, which is similar to those seen in Figure 7.3. To highlight the resonances of importance it is important to place a threshold on the reflection intensity. Figure 7.18 shows the spectrogram for the 4ml case with an upper threshold of 1.1 in (a) and 1 in (b). The resonances of interest have a low amplitude, and are shown in blue in both plots. In Figure 7.18a there is a series of other fringes, much more tightly banded, but also of a much lower amplitude in comparison with the real resonances. Interestingly, these lower amplitude resonances mirror the real resonance pattern, suggesting that there is a dependence on the film thickness.

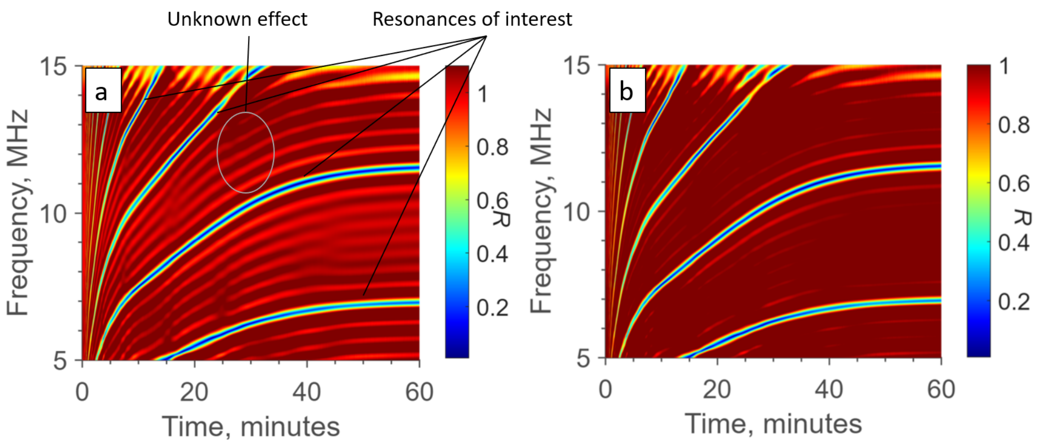

Figure 7.18: Comparison of spectral plots with upper intensity contrast limits 1.1 and 1 respectively for a & b, for the 4ml deposit test on the KOVOT test rig

When the contrast limit is reduced to the theoretical reflection limit in Figure 7.18b, the majority of these lower amplitude reflections are removed, meaning these dips occur above the theoretical limit of total reflection where $R = 1$, and so classically would be considered to be noise within the signal. Therefore, Figure 7.18b shows the true resonance pattern of interest.

At the start of the test, there is an initial parched period where $R = 1$ at all frequencies as there is no oil present. The oil is then applied and initially the fringes are very tightly packed as the film is relatively thick and so f_0 is low. As the oil spreads the fundamental frequency increases and so the fringes 'spread'. Towards the end of the test the oil layer has spread over the entirety of the plate face and formed a stable film, which is why the resonances stop spreading and become parallel for a short duration before the test end.

Figure 7.19 shows the same spectral plots over the same time duration, but for increasingly larger oil deposits. As the deposition volume increases, the time taken to achieve a stable layer, defined by the resonant fringes becoming parallel, shortens as a larger oil volume can cover the test plate quicker and thus achieve stability sooner. The final frequency difference between resonant fringes at the end of each test is related to the thickness of the stabilised layer. Larger oil deposits form thicker films and thus resonant fringes that are more tightly banded. Interestingly, the thicker films have lower amplitude resonances, as shown by the increase in R intensity in one test as the film thickens, and also between the stabilised layers of increasing oil volume deposits. For the 4ml case the resonant amplitude $R \approx 0.2$. However, for the 7ml case $R \approx 0.5$.

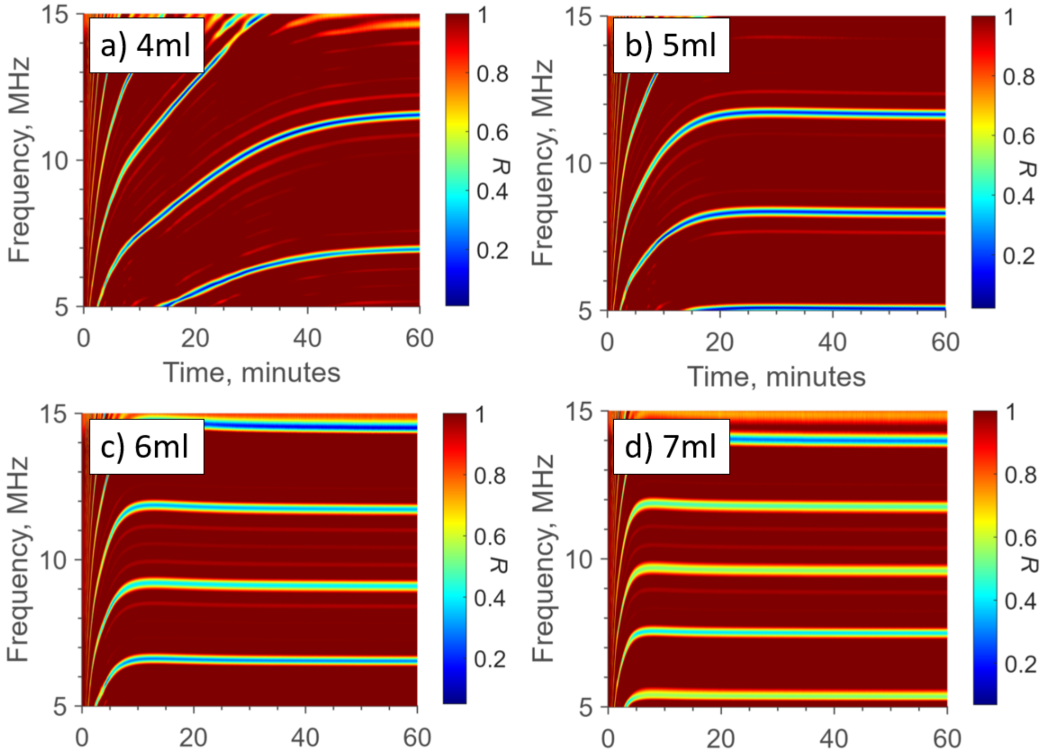

Figure 7.19: Spectral plots of different volumes of oil deposited on the KOVOT test rig

Figure 7.20 shows the ultrasonically measured film thickness at the plate centre, calculated from the resonances shown in Figure 7.19. Initially there is a large scattering for all tests when the oil is first supplied as the film is thicker than the upper measurable limit via the resonance method. This then stops, and all tests show a clear reduction in the film thickness. As expected, the lower volume depositions form thinner films, and take a longer time to stabilise. This is because the internal forces oppose the wetting action of the oil, whereas when the deposition is increased, these forces become somewhat irrelevant as the increased volume means the oil has more inertia and so spreads easier.

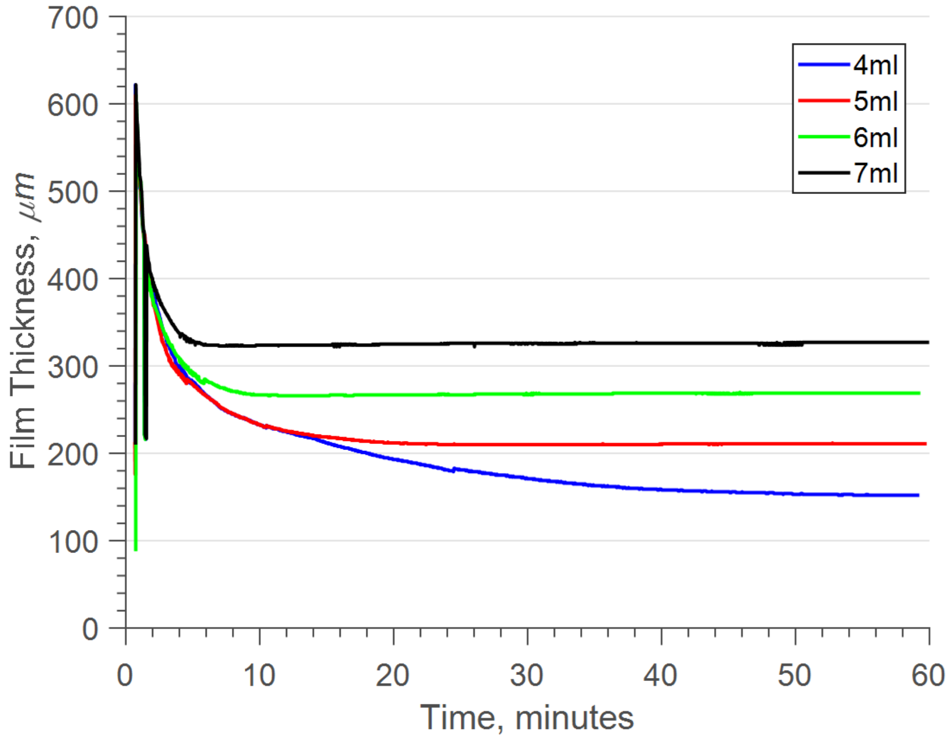

Figure 7.20: Ultrasonically measured central film thickness over a 60 minute duration with four different deposit volumes

For each test, the stabilised film thickness was calculated/measured three ways; the theoretical height calculated from the deposited oil volume, the ultrasonically measured film thickness from six locations around the plate, and film comb measurements from five locations around the plate. Figure 7.21 shows how the measurement techniques compare. The error bar for the volume method is calculated from the precision of calliper used to measure the internal diameter of the bath wall, and the precision of the syringe used to deposit the oil. The ultrasonic measurement and film comb measurement error bars are the standard deviation across the different locations. The fact that the ultrasonic method and film comb method have an error bar at all shows that the film formed was not perfectly level. Between ultrasonic measurements there was a maximum deviation of 11μm from the plate centre to an edge measurement. The film comb measured a maximum deviation of 50μm from the centre to edge, but the relatively low precision of the instrument makes this deviation understandable.

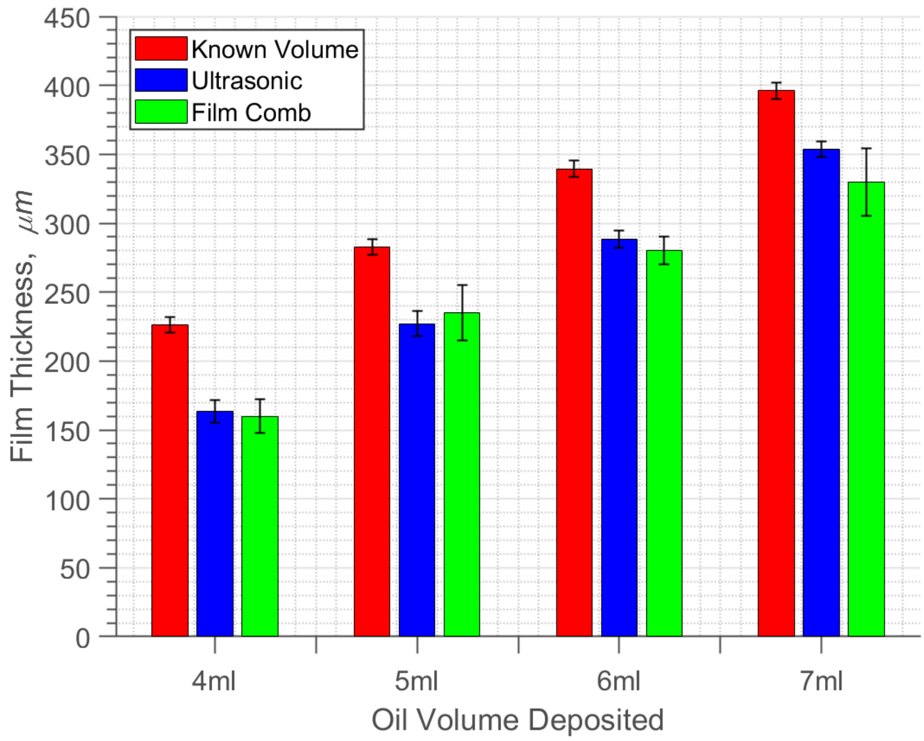

Figure 7.21: Comparison of the mean measured film thickness using ultrasonic sensor, film comb, and known volume deposition method

Across the four volumes tested, there is very good agreement between the mean film thickness measured via the ultrasonic method and film comb method. However, the theoretical deposited film, calculated from the bath wall dimensions, is larger than the other two methods, even when considering what the minimum film may be due to the deposition precision. The % difference between the mean ultrasonically measured film thickness and calculated film thickness from the oil volume is 32%, 22%, 16% and 11% from 4ml to 7ml respectively; that is to say, as the volume of oil increases the agreement between measurement techniques and the calculated volume improves. The most rational explanation for this is a meniscus rim forming around the layer circumference, which wicks up the bath wall due to capillary action, making the deposited film formed thinner than the theoretical prediction. However, if the capillary action is independent on the volume of oil deposited, so long as there is ample oil to wick from, the % difference change would decrease with larger oil deposits, which is seen in the tests. If larger oil deposits were used then it is expected that agreement would improve, but the deposited layer would no longer be representative of a raceway film, and for this reason was not performed.

7.5 Grease Films

7.5.1 Grease Acoustic Velocity Calibration

Grease has a harder to measure velocity-temperature relationship. Initially, fresh tubed grease was used to fill the test chamber of the speed of sound test rig, and a calibration experiment was run in the conventional way. The results of this, seen in Figure 7.22 show similar trends to the oil tests, at higher temperatures the velocity is reduced, and as the lubricant cools the acoustic velocity increases linearly. However, at room temperature the velocity of grease appeared to be twice that of oil, and the gradient much more shallow at -0.638m/s·°C^{-1} meaning there is a velocity change of just 51.040m/s (1.67% decrease) between 20°C and 100°C. This is very small when compared with the VG320 and VG32 oil which have changes of 236.688m/s (15.60% decrease) and 274.160m/s (18.74% decrease) respectively over the same temperature ranges.

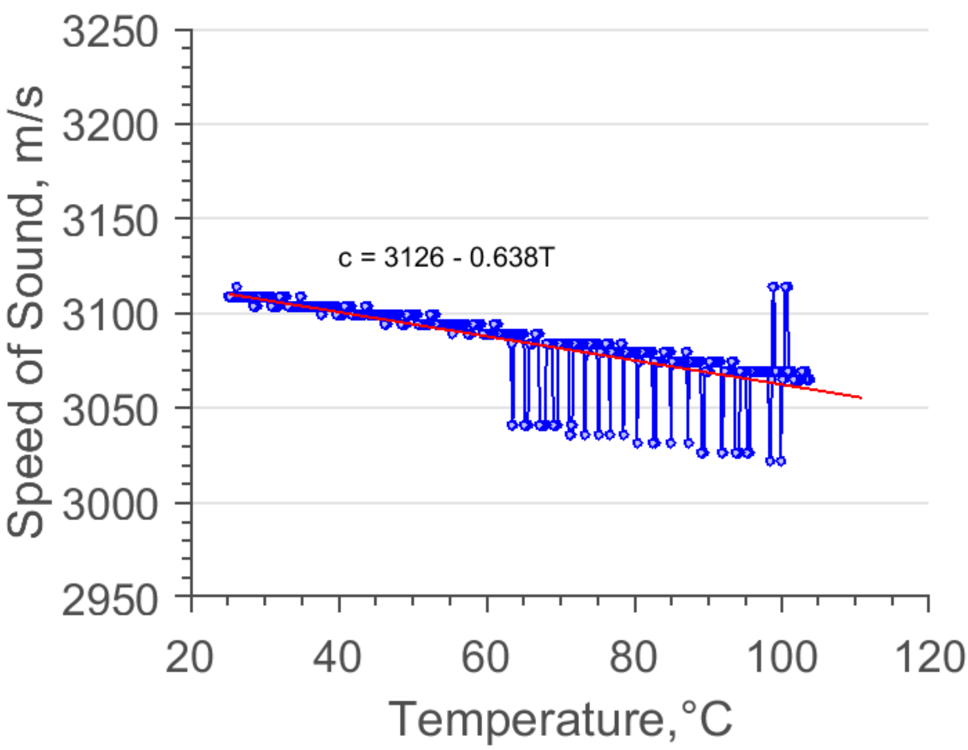

Figure 7.22: Acoustic velocity-temperature relationship of the Mobil SHC 460 WT grease, taken straight from the tube with no air exposure or mixing

During testing, it was found that a signal of measurable amplitude for the calibration test was difficult to obtain, and was not possible at all after it had spent time exposed to air and had been mixed. Even though this process barely stresses the grease, it appears to greatly increase the ultrasonic attenuation.

Figure 7.23 shows results of different thickness grease layers measured at room temperature. Three repeat tests were taken of deposited films, with the height set using 1, 2 and 3 tape layers using the doctor blade method. The fundamental frequency average between the two sensors was calculated. The error displayed is based on the minimum and maximum f_0 value measured between the two sensors, including the tolerance of the frequency precision for each sensor. The film thickness was then calculated using the plate temperature, taken from two thermocouples either side of the grease layer, input into the speed of sound equations for both the 460WT grease, calculated using the acoustic velocity shown in Figure 7.22, and VG320 oil measured using the conventional acoustic velocity chamber shown in Figure 7.16. For each layer, five comb measurements were taken in the direction of grease spread. The average of these was calculated, and the error seen is based on half the range between tooth measurements. It is noted for test 5, one sensor did not properly trigger, and so only a single measurement is available.

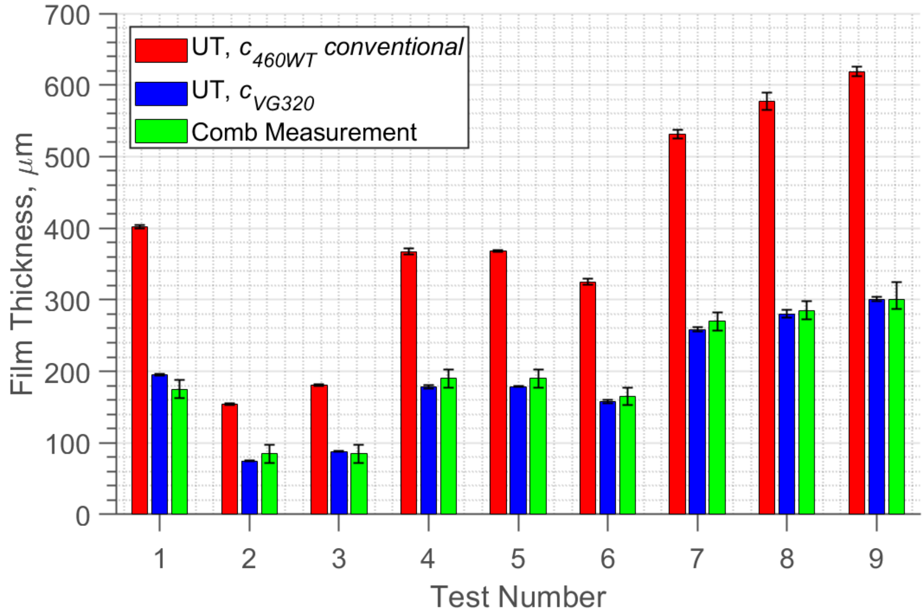

Figure 7.23: Comparison of deposited grease layer thickness measured with a wet film comb gauge, and ultrasonic sensors using the acoustic velocity of the 460WT grease and VG320 oil

When comparing the ultrasound measurements using the acoustic velocity of the 460WT grease, labelled $c_{460WT}conventional$, the measured thickness is roughly twice of that measured via the comb. This trend was seen for all nine tests. However, when using the acoustic velocity of the VG320 oil, labelled c_{VG320} there is excellent agreement between the ultrasonically measured film, and the film measured via the comb for almost all of the tests. For tests 2-8, the ultrasound measurement and variance lies close to the measured comb range. The only test this did not occur for is test 1. This test was performed using a single tape layer to govern the film thickness, but it is clear that the deposited film is much thicker than the repeats in test 2 and 3. Likely, the deposited film was not very consistent, evidence of which this is possible is shown in Figure 7.14. Also, only a single comb measurement was taken of this layer. These two influences combined can plausibly explain the slight disagreement between measured results in test 1.

The grease used for this test had been opened, naturally exposed to air and mixed before application, but there was no deliberate attempt to work or stress the grease, and it was stored properly in a dedicated chemical cupboard. This then suggests that an appropriate acoustic velocity to use for grease in a bearing, which has air exposure and is naturally worked due to its intended nature, should be closer to that of oil than the results in Figure 7.22. When trying to repeat the tests of Figure 7.22 using different tubes of grease a usable signal could not be obtained due to a high level of signal attenuation, and the test could not be completed. It is plausible then that the one test that did work had some form of air pocket in the grease, essentially reducing the thickness measured, or that the sensor had cracked in-situ and the result observed was of some stray reflection and not of the grease layer at all. Both possibilities would make the result null. The inability to repeat the measurement makes drawing reasoning difficult, but it is therefore a conclusion of this work that conventional acoustic velocity test rigs are not appropriate for grease measurements as the results are subject to uncontrollable errors, and a different approach is needed.

To study this phenomenon in more depth over different thickness and temperature ranges, different grease layers were deposited on the KOVOT, and the rig placed in the oven and ramped to $80°C$, the temperature allowed to stabilise, and then ultrasonic measurements were taken during the cooling phase. The test was repeated with no grease present, with measurements of the steel-air boundary, to obtain a reference at all appropriate temperatures. The calculated film thickness, using the c_{VG320} value, for one test is plotted in Figure 7.24. The shaded area shows the measurement range of the film comb used for the thickness validation. Clearly for all temperatures the ultrasonic measurement lies within the comb range. However, as temperature increases so too does the measured thickness. As the test grease has a dropping point of 255°C, and there was no visible bleed from the grease track after testing, it is safe to assume the film thickness was constant during the test. Consequently, the changing measured film thickness must be due to the error between using the c_{VG320} value instead of a true measurement of the grease acoustic velocity.

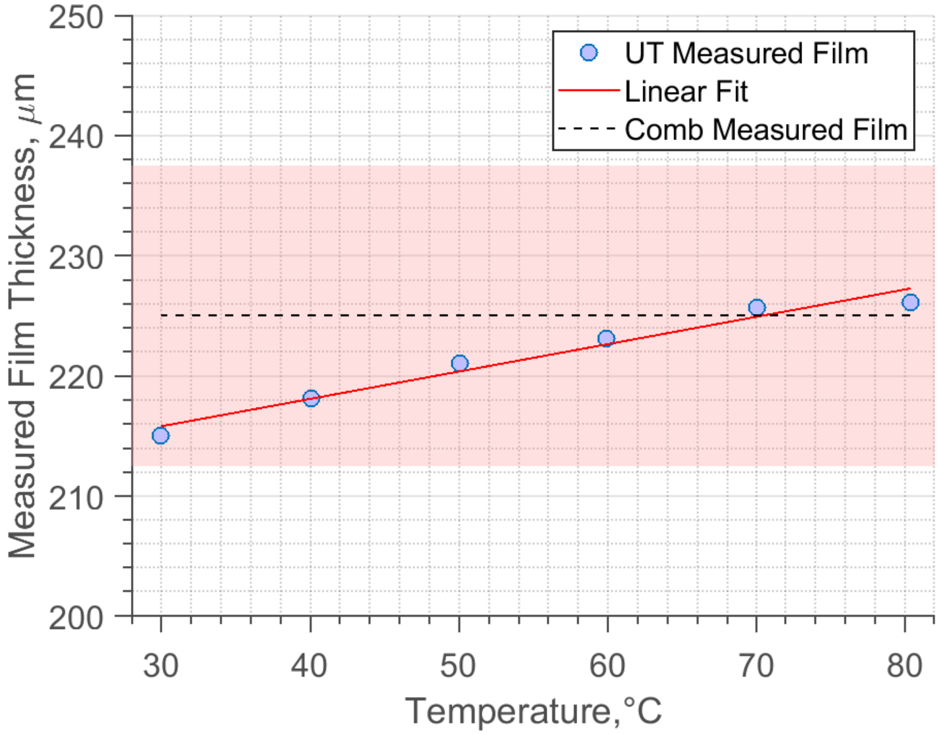

Figure 7.24: Changing measured film thickness with increasing grease temperature

To generate a better acoustic velocity estimation for the grease, which could not be done in the conventional rig due to the previously mentioned attenuation issue, these temperature ramp results were used. For each test, the linear relationship between the temperature and acoustic velocity was measured. Then as:

$$\begin{gathered} h = \frac{c_2}{4f_0} \\ \therefore c_2 = h \cdot 4f_0 \end{gathered} \tag{7.6}$$

For each test temperature the acoustic velocity was calculated, using the mean comb film thickness as h. These new acoustic velocity values could then be plotted against the recorded temperatures to derive a new acoustic relationship. Using this new acoustic velocity relationship, the thickness values from Figure 7.24 were recalculated, the results of which can be seen in Figure 7.25. Although there is still some variance, the linear fit line lies directly over the mean comb measurement line, and the fit has a negligible gradient, as expected for a stable film thickness.

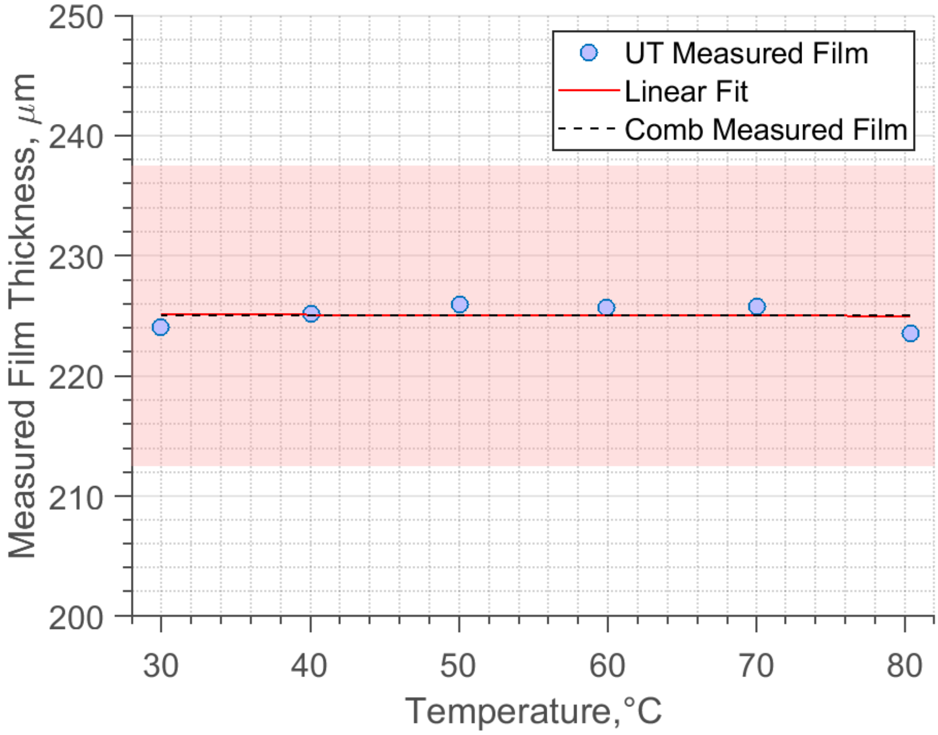

Figure 7.25: Measured film thickness with increasing grease temperature, calculated using modified speed-of-sound calculation technique

To improve the accuracy of this method, six total tests were taken. Three using open and mixed grease, three using completely fresh, tubed grease from a grease gun. The films were determined using 2, 3 and 4 tape layers. Over the temperature range, the fundamental frequency of each layer was measured, and using the mean comb thickness, the speed of sound derived. Obviously, due to the precision of the comb there is some error introduced into this approach. However, the number of repeats aids in reducing this error, and to improve the method would take a large investment of time, with diminishing returns in terms of accuracy improvement. The mean value of the gradient and y-intercept constant was calculated, to derive a relationship applicable for fresh, un-worked grease. Table 7.3 shows the measured velocities at different temperatures and thicknesses, as well as the calculated mean value. These mean values could then be plotted against temperature, as in Figure 7.26, to develop a usable acoustic velocity-temperature relationship for the fresh, unworked 460WT grease, shown in Equation 7.7.

	$c, m/s$						
Temperature, °C	Fresh grease unmixed - 2 tape	Fresh grease unmixed - 3 tape	Fresh grease unmixed - 4 tape	Fresh grease Mixed - 2 tape	Fresh grease Mixed - 3 tape	Fresh grease Mixed - 4 tape	Mean
80	1434	1268	1321	1386	1332	1272	1336
70	1468	1299	1360	1424	1365	1301	1370
60	1494	1340	1397	1470	1411	1341	1409
50	1539	1385	1445	1512	1454	1395	1455
40	1583	1429	1494	1564	1504	1434	1501
30	1640	1482	1549	1619	1557	1486	1555

Table 7.3: Calculated acoustic velocities of different grease layers over a range of temperatures

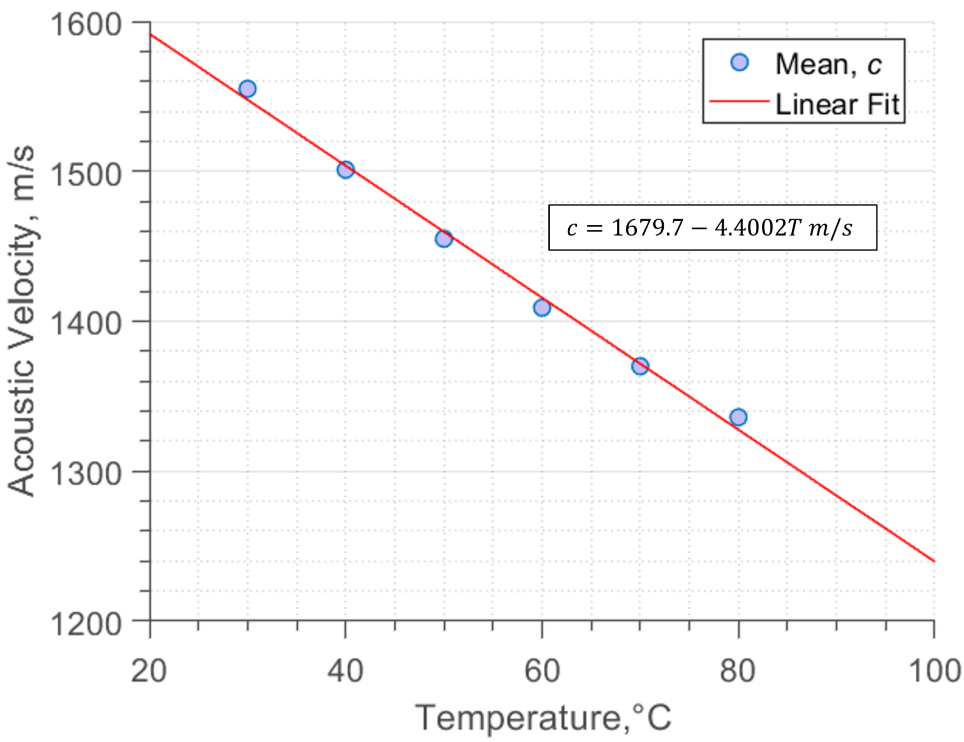

Figure 7.26: Change in 460WT grease acoustic velocity with an increase in temperature

$$c_{460WT} = 1679.9 - 4.4002T, \text{m/s} \tag{7.7}$$

Using this new calculated acoustic velocity relationship, the film thickness trials shown in Figure 7.23 were re-calculated, and compared again with the use of the VG320 acoustic velocity. Results are shown in Figure 7.27. Clearly, the agreement between the ultrasonic measurements and film comb gauge is much better, suggesting the calculated relationship in Equation 7.7 is valid for both unopened and opened and mixed grease.

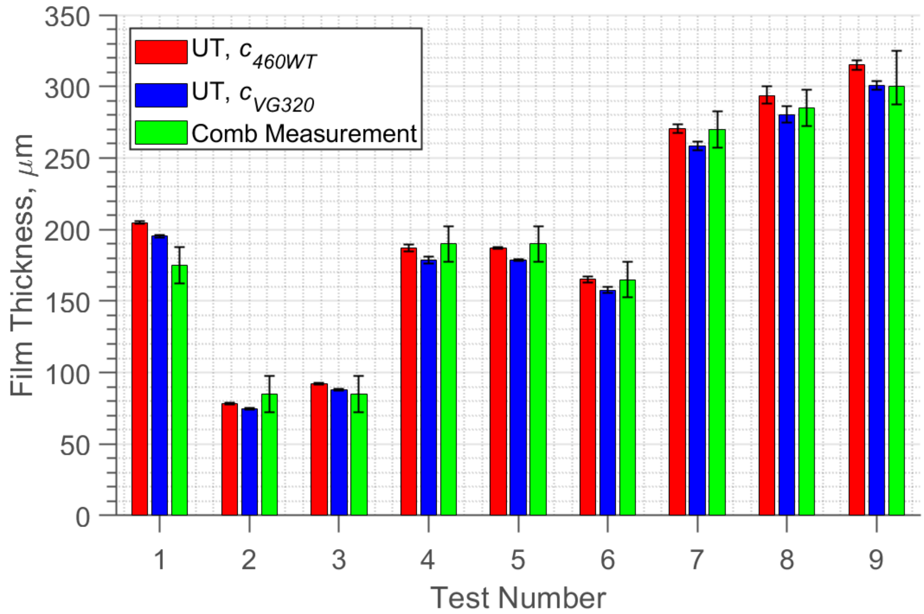

Figure 7.27: Comparison of deposited grease layer thickness measured with a wet film comb gauge, and ultrasonic sensors using the calculated acoustic velocity of the 460WT grease and VG320 oil

7.5.2 Resonance Amplitude Pattern

Figure 7.28 shows the reflection coefficient response of three different grease layers. The thickness shown is the mean thickness of the film comb measurements. All three layers show a clear resonance pattern, with a couple of noteworthy points. Firstly, an increase in film thickens not only reduces the fundamental frequency, but the magnitude of the resonant dip appears to decrease. This pattern of decreasing resonance amplitude with an increasing film thickness is seen in the oil results, Figure 7.19, but is the opposite to Figure 7.1 where different thickness oil layers were modelled through Equation 3.15, and an amplitude increase was seen with thicker films. As there is more material to cause attenuation in a thicker film, this is the most logical answer to explain this decrease in amplitude. However, Equation 3.15 and therefore modelled films also incorporate an attenuation coefficient, and so the change in amplitude is likely not governed solely by this. Dou et al. [99] showed that as echo number reduces, so too does the magnitude of the resonance amplitude. With thicker films,

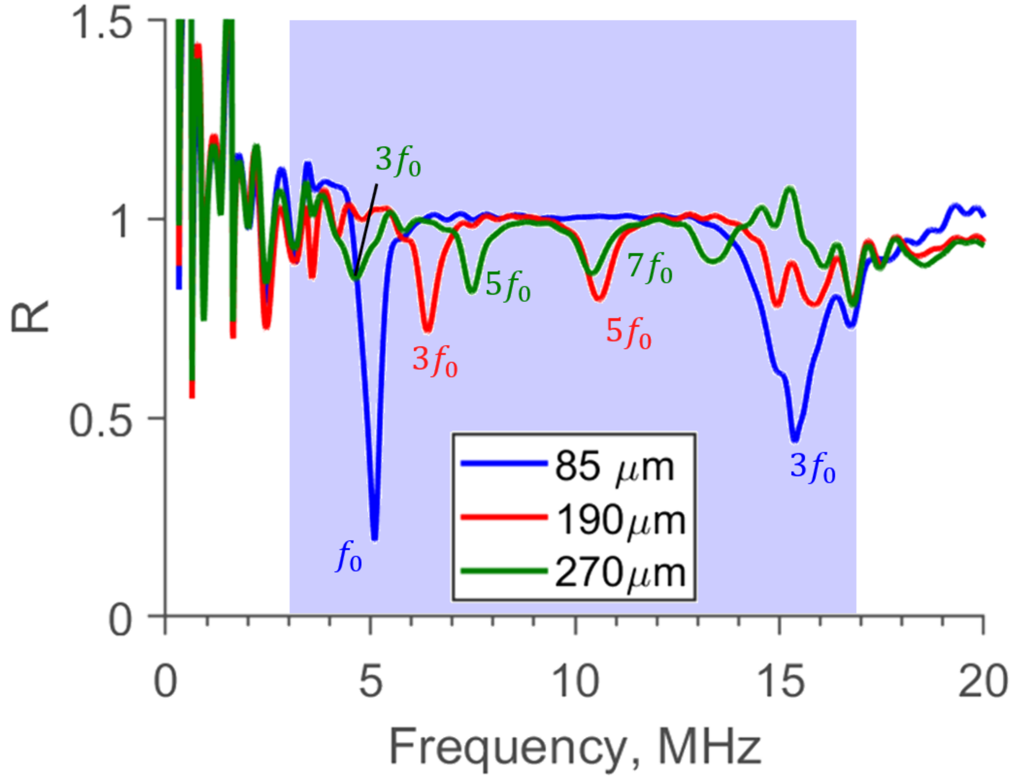

Figure 7.28: Comparison of resonance dips in the reflection coefficient response of three deposited grease layers. The blue area represents a bandwidth of acceptable signal-to-noise ratio

the signal attenuates more, thus reducing the potential number of echoes recorded and so the minima is reduced. This is not observed when using Equation 3.15 plotted in Figure 7.1 as echo number is not considered and the wave is assumed continuos.

The second noteworthy point is within the usable bandwidth, of which the signal-to-noise ratio is agreeable, different order resonances are observed for the different film thicknesses. Only for the thinnest, 85μm film is the first resonance, the fundamental frequency, observed. For the other films, where f_0 is reduced, this first resonance occurs outside of the bandwidth, and only higher order odd harmonics are detected. This highlights the importance of properly understanding the order of resonance detected, which Section 7.6 expands on.

7.6 Measurement Limitations, Interval and Uncertainty

The limits and precision of the resonance method are difficult to define as from Equation 3.19 there is dependency not only on the frequency measurement, but also through the speed of sound value. The speed of sound is affected by several things such as temperature, pressure and aeration and so calculation of the measurement uncertainty of these parameters, which can be very difficult to measure in-situ, should be estimated on a case-by-case basis. However, resonance detection is universal, regardless of the application.

For very thin films, f_0 becomes increasingly large, as too does the required bandwidth to capture multiple resonances, and so only one resonance may be recorded. In this situation [126] suggests that as no other resonances are detectable, the single resonance can be assumed to be f_0. However, this does not hold true for all bandwidths (BW). Take for example the 190μm case in Figure 7.28. The first resonance <u>detectable</u> occurs at around 6.5MHz, but this is actually $3f_0$, not the fundamental frequency. This is known because there is a second detectable resonance at around 10.8MHz. If $f_0 = 6.5$MHz there would be no other resonance until $3f_0 = 19.5$MHz. However, using the frequency at which the first two dips occur, it is seen $\overline{\Delta f} = 4.3$MHz and so $f_0 \approx 2.15$MHz. If it was incorrectly assumed that $f_0 = 6.5$MHz, the thickness measurement would be out by a factor of 1/3.

To address this issue, three conditions are proposed. If only a single resonance is measured of the film, any of the conditions can be met to ensure the resonant frequency detected f_r is the fundamental frequency and not a higher order odd harmonic, which would most likely be $3f_0$ if only a single resonance is observed. The first condition:

$$f_r \leq \frac{BW_{max} - BW_{min}}{2} \tag{7.8}$$

When an oil layer is unconstrained (a steel-oil-air interface) resonances will appear at the fundamental frequency and every odd integer multiple. The second highest frequency resonance is thus $3f_0$, and the main threat to an inaccurate detection is mistaking $3f_0$ for f_0. The first condition ensures that if a single resonance is detected, the bandwidth range is adequate to detect either f_0 or $5f_0$ above or below f_r respectively, if $f_r = 3f_0$. If this condition is met and only a single resonance is present then $f_r = f_0$. This rule is the most encompassing of the three proposed, and when selecting sensors this should be kept in mind.

The second condition is simple:

$$\frac{f_r}{3} \geq BW_{min} \tag{7.9}$$

If the bandwidth minimum is less than a third of the frequency of the detected resonance, and only one resonance is detected, then it is confirmed that the detected frequency is not a higher order harmonic and thus $f_r = f_0$. This condition is used for using lower frequency sensors, such as 5MHz where the BW_{min} is very low, and the user is essentially aiming to only measure one resonance. Although this makes detection easier, the bandwidth is essentially limited to only measuring a single resonance, unless measuring very thick films. This increases the likelihood of f_0 detection error from things such as inadequately detecting the true spike of the dip. With higher central frequency sensors, larger bandwidths are often achievable and so multiple resonances can more often be measured, reducing this kind of error.

The final condition is similar in principle to the second condition, but for the upper bandwidth limit:

$$\frac{f_r}{3} \times 5 \leq BW_{max} \tag{7.10}$$

This rule essentially suggests that a single resonance measured is $3f_0$, and from this calculates the fundamental frequency and thus suggests where $5f_o$ will occur in the bandwidth. Then, if BW_{max} is greater than this predicted $5f_0$ frequency, and no resonance is present, the single resonance is proven to not be $3f_0$ and must instead be f_0.

If any of the above conditions in Equations 7.8, 7.9 or 7.10 are met, the bandwidth is deemed large enough to detect other odd harmonics and therefore if not present it is assumed $f_r = f_0$. However, if the conditions cannot be satisfied, the assumption cannot be made, and at least 2 resonances must be recorded and $\overline{\Delta f}$ calculated and used in Equation 3.19 to make a thickness calculation. The 100μm film in Figure 7.1 is an example of when the single resonance within the measured bandwidth cannot be assumed to be f_0.

7.6.1 Minimum Detectable Film Thickness

In all automated analysis completed in Chapter 10, the bandwidth was not large enough to meet the criteria of Equations 7.8, 7.9 or 7.10, meaning two resonances were required for film thickness calculation via Equation 3.19. The thinnest film measurable therefore occurred when two resonances were observed; the lowest harmonics they could be were $3f_0$ and $5f_0$. The minimum detectable film thickness h_{min} therefore occurs when f_0 is the highest it can possibly be while $3f_0$ and $5f_0$ are still within the bandwidth. This is when:

$$\begin{aligned} 5f_0 &= BW_{max} - df \\ \therefore f_{o_{max}} &= \frac{BW_{max} - df}{5} \end{aligned} \tag{7.11}$$

Where df is the frequency spatial resolution $\approx$ 0.1MHz in the bearing tests. This must be subtracted from BW_{max} so a peak can be detected. As $h = \mathrm{f}(c, \frac{1}{f_0})$ and $c = \mathrm{f}(\text{temperature})$, h_{min} decreases with an increasing temperature. Figure 7.29a shows the changing minimum film thickness for *Alpha SP VG 320* as the resonant frequency increases, with a conservative -6db bandwidth applied. The minimum detectable film is 141μm at 20°C and 119μm at 100°C but this plot is very similar for most oils as the speed of sound value is similar across most grades.

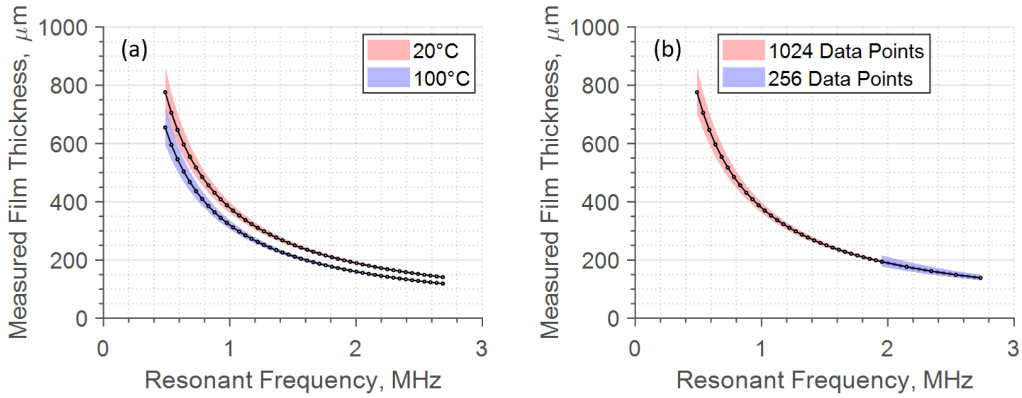

Figure 7.29: Comparison of theoretical measurable thickness and interval with an increasing fundamental resonant frequency, with (a) two temperature extremes (b) different levels of signal padding at 20°C

7.6.2 Maximum Detectable Film Thickness

The maximum detectable film thickness measurable using the resonance method is not as critical as there is an overlap with the Time-Of-Flight (TOF) method. A thicker film corresponds with a lower fundamental frequency and therefore tightly banded resonances. Thus, the frequency discretisation determines the upper limit of film thickness h_{max}. For this work, 10 data points between resonant peaks were deemed an acceptable resolution, giving an adequate measurement interval for a thick film. This gives a maximum detectable film thickness of 776μm, 749μm and 815μm via the resonant method at 20°C for VG320, VG32 oils and 460WT grease respectively.

7.6.3 Measurement Interval

The frequency spatial resolution is $\approx$ 0.1MHz, and so the resonance measurement precision is $\pm$0.1MHz. Through Equation 3.19, it is clear $h \propto 1/f_0$. Therefore, with a thinner film, f_0 is larger, resulting in df being a smaller percentage of the value, and thus the measurement interval is reduced. With thicker films, f_0 is small and so the measurement interval is large. Figure 7.29a plots a model film thickness decreasing with an increasing resonance for 20°C and 100°C. The colour block encapsulating the lines show the potential minimum and maximum film at that resonant frequency due to the precision of the measurement. As discussed, this decreases with a thinning film.

The measurement interval can be improved upon by zero padding the recorded reflection before completing the FFT. This does not change the true resolution, but the interpolation allows for detection closer to the actual resonances. Figure 7.29b shows that by padding the signal further, the frequency resolution is improved, and so the measurement interval is decreased. Also, with the same criterium for the minimum number of data points between resonances, signal padding allows for the detection of thicker films as smaller frequency differences between resonances can be observed.

7.7 Conclusion

- When observing reflections from a pulse-echo ultrasonic sensor in the frequency domain, it is shown that oil layers cause a detectable resonance. The frequency of this resonance is governed by the acoustic velocity and thickness of layer.

- The first resonance is the fundamental frequency f_0, higher order resonances then occur at the odd harmonics $(3f_o, 5f_0, etc...)$ when there is an acoustic impedance gradient of $z_1 > z_2 > z_3$ such as with a steel-lubricant-air boundary.

- The resonance amplitude is influenced by the echo number through the layer. Thicker layers have lower echo numbers, meaning less interference takes place in the oil layer, and thus have smaller amplitude dips, making resonance detection harder.

- The tail of a reflection contains further echo numbers; if not included in post-process the number of echoes is synthetically reduced, reducing the resonance amplitude and thus the maximum film thickness detectable by the resonant method.

- The KOVOT rig was made, a precise oil bath manufactured from an ultrasonically instrumented base plate of a material specification and thickness equivalent to that of the inner bearing raceway in Section 5.1.

- When trialled with oils, the ultrasonic resonance method detected the oil flow and time of full spread across the plate. The equilibrium film was measured three ways: ultrasonic resonance method, film comb gauge, dimensional calculation. There was good agreement between the three methods, particularly the resonance and comb gauge.

- As grease does not flow below its dropping temperature, a modified doctor blading technique was used to deposit consistent grease layers. Grease layers were also found susceptible to the ultrasonic resonance method. The layers were measured using the resonance method and comb gauge with good agreement between the two.

- Grease acoustic velocity cannot be measured in conventional speed-of-sound baths, such as the one shown in Figure 7.16 as it is too attenuative. To develop an acoustic velocity-temperature relationship, films of different thicknesses from grease freshly opened unmixed/mixed and grease exposed to air were measured using the comb gauge and ultrasonic resonance technique over a temperature range from 30°C to 80°C. A relationship was developed from the mean of the results.

- The acoustic velocity of grease is very similar to that of the oils tested. As oils have very similar acoustic velocity-temperature relationships, this suggests the speed of sound through grease is governed primarily by its constituent base oil.

Chapter 8

Scouting for the Entry and Exit Film of a Cylindrical Roller Contact

In this chapter, the ultrasonic measurement method that was validated in Chapter 7 is explored for in-situ raceway film measurements within a full scale wind turbine gearbox bearing test rig. First, the instrumentation of a roller bearing inner raceway is discussed, and the selection process of sensor central frequency and axial position is explained. Then, the scouting tests method is described and a novel way of observing the raceway film via a spectrogram is explained. Results give a qualitative indication as to the presence of a raceway film, and the effect of bearing load, speed and lubricant viscosity on this film.

8.1 Scouting for the Resonant Frequencies of a Raceway Film

Chapter 7 investigated the resonant frequency - film thickness relationship, and validated that film thickness could be monitored in both stationary and dynamic films using the resonant frequency approach. At the centre of the relationship is $h \propto 1/f_0$, and so thinner films have higher resonant frequency values. When tracking a film thickness using this approach, the ideal would be to have an understanding of the film thickness, and then select a sensor with a bandwidth that encompasses a range of frequencies either side of the predicted mode f_0 value. However, the lack of comparative literature for in-situ measurements of a meniscus and raceway films meant a prediction of thickness could not be made. A solution to this problem was the instrumentation of a multi-frequency scouting bearing.

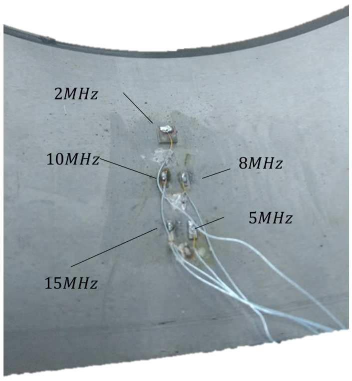

Figure 8.1: NU2244 multi-frequency scout bearing instrumented with bare piezoelectric elements

To scout for the raceway films via the resonance method, an NU2244 inner raceway was instrumented with five bare piezoelectric elements with manufacturer stated frequencies of 2MHz, 5MHz, 8MHz, 10MHz and 15MHz, which can be seen in Figure 8.1. After this picture was taken, the sensors were covered in a thin coating of Robnor epoxy to provide vibration damping and element protection. As an excited element has a finite usable bandwidth either side of the central frequency, by using a range of central frequencies a longer bandwidth can be synthetically analysed across the sensors, improving the chances of detecting a film resonant frequency.

Due to the space restriction within the bearing carrier, the sensors could not be positioned in a single axial location, and were therefore bonded across the rolling axis. The lower frequency elements are thicker, as explained in Chapter 3, and thus were sized accordingly, meaning a constant element size could not be achieved between all sensors.

8.1.1 Experiential Methodology

The scout tests to determine whether raceway film detection was possible were performed with both *Hyspin VG 32* and *Alpha SP 320*. The thicker VG320 oil is typical of what is used to lubricate WTGBs and so was assumed capable of developing a meniscus. The VG32 oil is far less viscous, meaning the raceway film leading to the contact inlet might be assumed to be thinner and/or shorter than the more viscous oil. The oils also have different acoustic properties, and by testing the two oils the resonance application to different oil viscosities could be qualitatively assessed.

The tests were carried out on the full scale WTGB test rig, and comprised of 10 second captures. By keeping test times short, the UPR can record at much higher pulse rates without filling the internal buffer and losing data. Five incremental speeds of 20 to 100 rpm, bearing speed $n.dm$ of 6,200 to 31,000 were tested. As entrainment velocity is a function of bearing speed, this is expected to thicken the film leading to the contact inlet. Load is known to have the smallest affect on central and minimum film thickness within an EHL line contact [49]. However, the load affect on raceway film development and thus inlet meniscus position is not as established. The tests were run at unloaded and at 100kN, 200kN and 400kN to investigate.

8.1.2 Ultrasonic Test Equipment

The ultrasonic test kit used was the FMS, a PC with in-built high speed UPR, as previously described in Section 5.2.1. The reason for this set-up was that as the bearing rotates at ever higher speeds, the circumferential resolution is diminished as the radial distance travelled between reflections increases due to the almost constant pulse rate. Therefore, a low speed UPR kit would not be applicable for bearing tests of this type.

8.2 Piezo Element Frequency Response

During testing, the frequency response of the mode reference signal was monitored, Table 8.1 shows that the central frequencies deviate from those specified by the manufacturer. There are several reasons that could cause this, such as sensor manufacturing error, sensor adhesive layer being too thick, or the sensor not being properly excited during the tests. The result is that the centre frequencies have a smaller range than desired, 2.4MHz instead of 13MHz. However, when comparing the reference amplitudes in the frequency domain in Figure 8.2, there is evidently a larger usable bandwidth across all sensors compared with just a single sensor. The multi-frequency bearing was deemed still fit for purpose for this reason, as a larger frequency range could be observed for detecting resonant frequencies. It is noted in Table 8.1 and Figure 8.2 that the 8MHz sensor is not present. That is because during the installation the sensor failed, meaning no signal could be received, but as it was covered in a Robnor epoxy coating there was no access to fix this. During disassembly of the rig between oil changes from VG320 to VG32 the 5MHz also failed and became unusable.

Channel number	Manufacturer stated frequency, MHz	Measured central frequency, MHz
1	2	5.9
2	5	6.6
3	10	8.3
4	15	7.5

Table 8.1: Stated central frequency and observed central frequency for VG320 tests

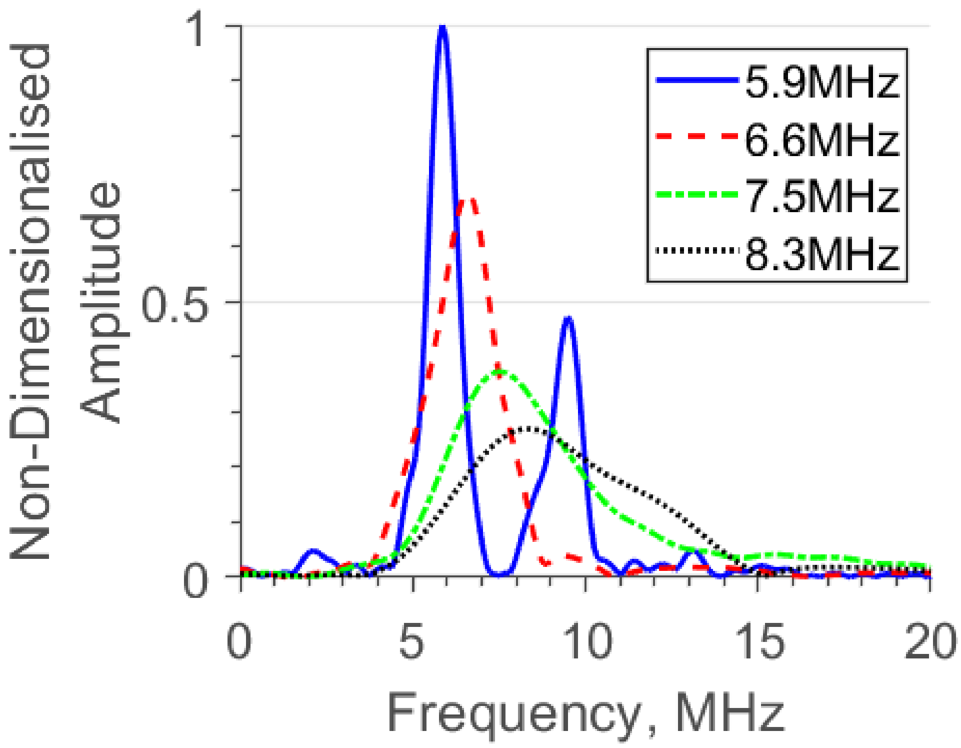

Figure 8.2: Non-dimensionalised frequency response of all active sensors during the VG320 tests

8.2.1 Spectral Analysis of a Single Roller Pass

To assess whether the meniscus films were of a magnitude to be measurable via the resonance approach, the reflections must be analysed across the frequency domain. The process of analysing signals across the frequency domain is the same as the spectral method described in Chapter 7. Figure 8.3 shows how the reflection coefficient changes, across a −18dB bandwidth, as a roller passes over the sensor location. Three key areas have been highlighted:

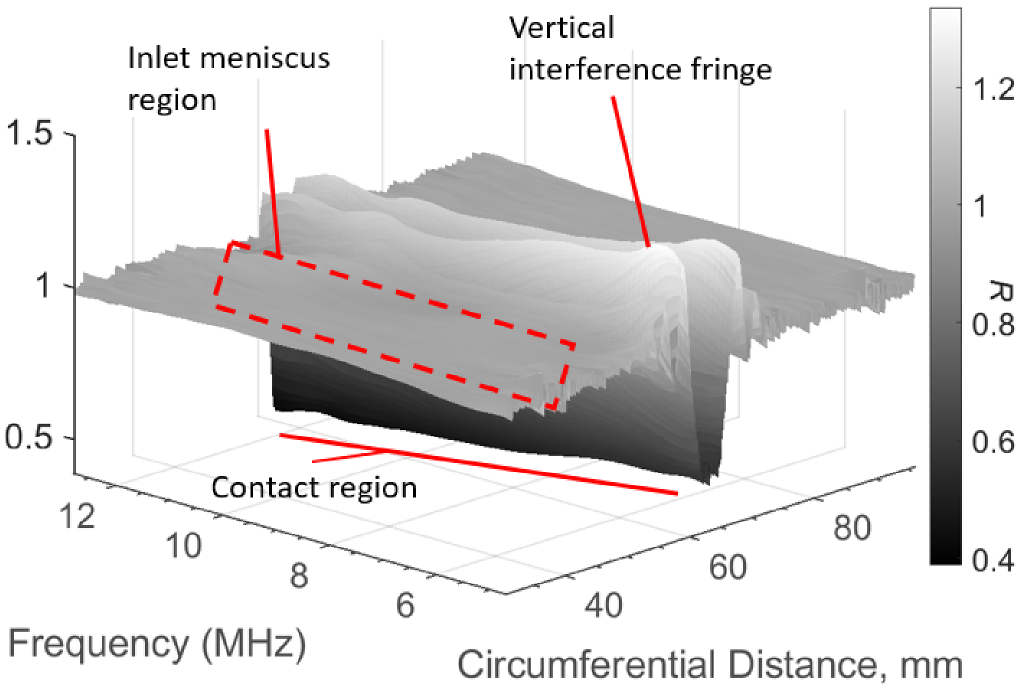

Figure 8.3: Changing reflection coefficient as a single roller passes the sensor location, observed across the usable frequency range

Vertical Interference Fringe As mentioned previously in Section 5.5, wave reverberations occur where complex geometries are close to touching, causing spikes of $R > 1$ which is theoretically impossible [132]. These fringes are viewed as high peaks when analysing in 3D in Figure 8.3, and resonant measurements cannot be taken from these regions.

Contact Region The contact region occurs when the roller is directly over the sensor. Because the oil film is very thin and compressed here, the contact acoustic impedance is closer matched to the steel raceway than a free surface film is, leading to much more transmission and therefore less reflection. Figure 8.4 observes the spectrogram in the yz axis to highlight the relationship between the

MRC and frequency. As the frequency increases, there is a linear decrease in *MRC* from $R \approx 0.5$ to $R \approx 0.4$, because through the spring model (Equation 3.9) $R \propto 1/f$.

Inlet Raceway Region This region is the oil film leading to the inlet of the contact. Within this region, there are fluctuations in R across the bandwidth due to resonances in the oil film, however the contrast is low due to the large reduction in the contact region, and so the frequency at which the resonances appear is blurred.

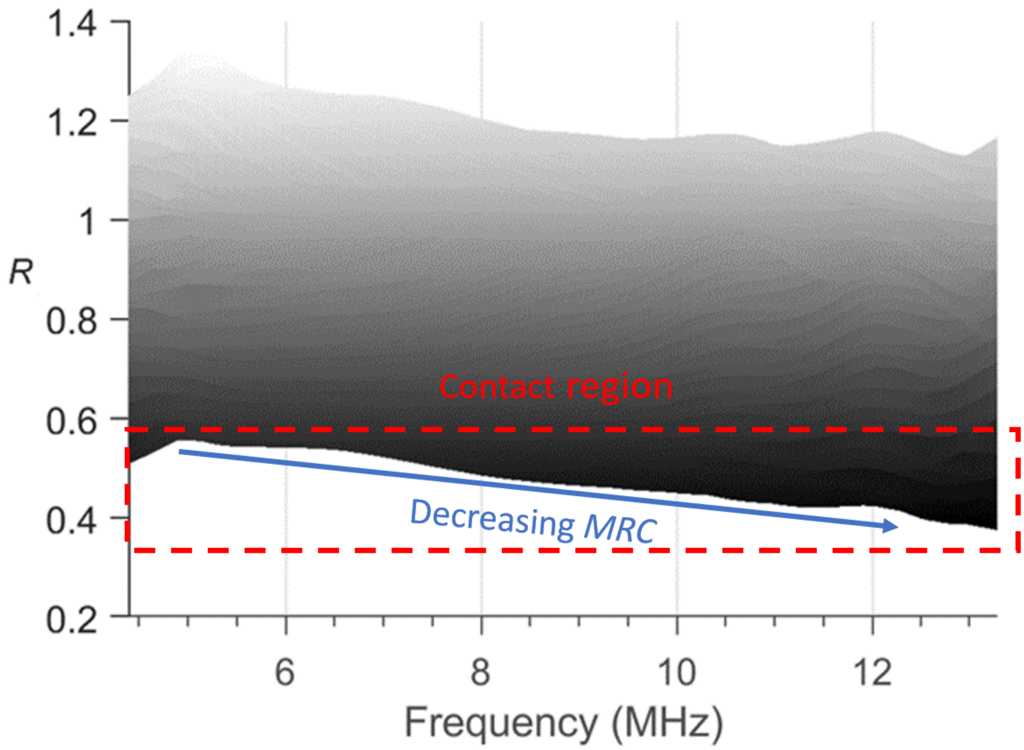

Figure 8.4: Changing minimum reflection coefficient with increasing frequency for a single roller pass

Figure 8.5a shows the same single roller pass as in Figure 8.3, except through the xy plane so that the intensity is R. The central line is the contact region, and there is evidence of the vertical interference fringes also. Within the inlet region marked in Figure 8.3, the intensity is not even, suggesting a resonance presence, but due to the low R values in the contact, and high values in the vertical interference, this intensity difference is blurred.

In Figure 8.5b the intensity is limited to $0.95 \leq R \leq 1$ so that the contrast range is closer to these intensity changes at the inlet and outlet region. In doing so, horizontal

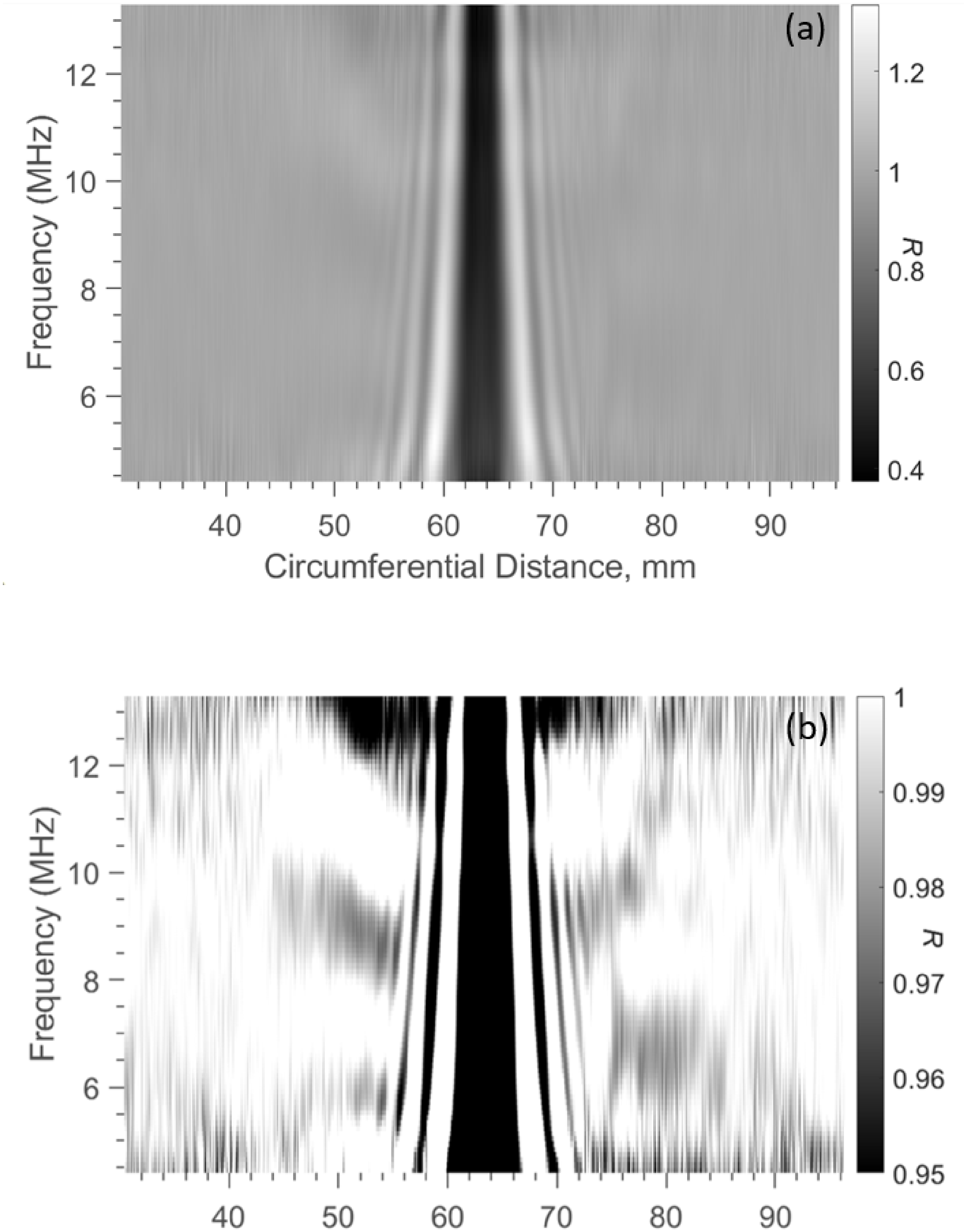

Figure 8.5: a) Spectrogram of a single roller pass b) Spectrogram contrast limited to $0.95 \leq R \leq 1$

bands of resonance become extremely clear. Looking at a single spatial distance such as at 50mm, several resonances are clear across the bandwidth, which are different odd harmonics of the f_0, showing that the oil films in these regions are within the resonance range.

The stand alone spectrogram can be analysed as one would a topographical map. If f_0 reduces, then assuming a constant temperature through the film, all odd harmonics of f_0 will reduce. This will present spectrally as the resonant bands lowering in frequency, and looking more tightly packed. As $f_0 \propto 1/h$, this indicates a film thickening, just as a topographic map presents a mountain incline increasing as tighter contour lines. Counter to this, horizontal resonant bands increasing in frequency and spreading from each other indicates a film thinning. Just as with a topographical plot, further separated contour lines indicate a gradient decreasing.

Figure 8.6 is the same plot as Figure 8.5b, but has overlaid colour blocks, discretising the spectrogram into four distinct regions:

1. Red: outside of the contact and inlet/outlet regions where very little oil is present. The oil has yet to reflow back onto the track from the previous roller pass meaning the measurement is essentially of a steel-air boundary, or an oil film only 10's of microns thick and below the measurement range, and so no resonances are present.

2. Yellow: the inlet zone has horizontal dark fringes showing where the resonance occurs. Closer to the contact, the fringes tighten and the frequency reduces, indicating that f_0 is reducing, and thus the film is thickening into the contact. The oil here is fed by reflow onto the rolling track after the passage of the previous roller.

3. Blue: this is the contact zone where there is a vertical, dark patch since the reflection coefficient is low. The oil is too thin to resonate here and so thickness measurements cannot be taken via resonance analysis. Thinner vertical lines also show evidence of interference within the entry and exit of the contact, due to complex reverberations within the bearing geometry [132]. These interference fringes affect the resonant fringes of interest and so it is difficult to take film thickness measurements within this zone.

4. Green: this is the outlet meniscus region which, antithetical to the inlet region, shows horizontal fringes spreading. This indicates an increase in f_0 and thus a film thinning towards the parched area between rollers. There is likely a

strong oil presence at this outlet region because of enhanced side-flow due to the large quantity of oil that acts as a sump in the bottom of the test bearing, as discussed in Section 5.1. The fact that the oil disperses into the parched red zone suggests this outlet film adheres to, and is dragged around by, the roller.

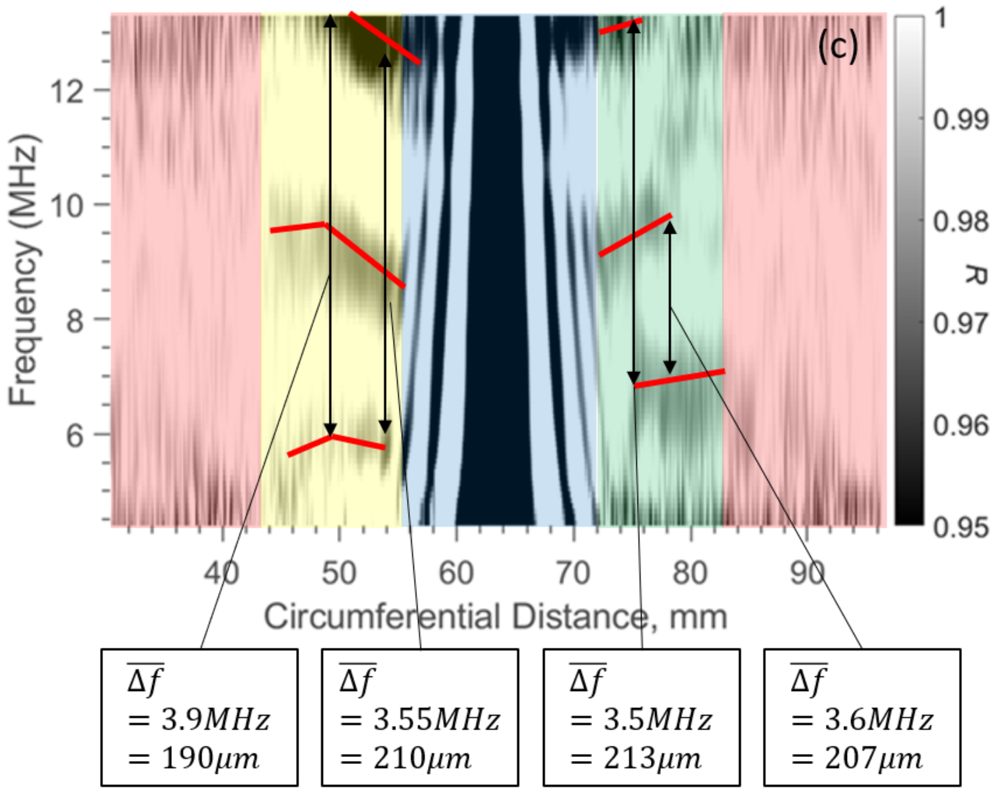

Figure 8.6: Drawn by eye resonances and calculated film thickness at the contact inlet and outlet

Of course looking at the raw spectrograms is a qualitative analysis of the raceway film pattern, but the resonances can be quantified. Figure 8.6 has had the frequency of the resonances drawn by eye, and for single reflections at certain circumferential distances $\overline{\Delta f}$ has been measured across the frequency range. From this the film thickness has been calculated using Equation 3.19. It is clear that for this roller pass thickening takes place in the contact entry and thinning takes place at the exit.

Of note is that the frequency jump between resonant minima is not always exact, as it is in theory, which is why it is important to calculate $\overline{\Delta f}$. There are two likely reasons for this deviation. The first is the digitisation rate of the ultrasonic test equipment being too low, meaning the signal padding increases the resolution 'near' to the true resonance, instead of at the resonance. The second is an uneven film thickness within the sensor measurement area, meaning the resonances from multiple films are being detected. If the films are of a very similar amplitude, such as a raceway inlet film growing into the contact, the resonance minima could be blurred and/or shifted. If this was the case, taking the mean frequency jump would still be an appropriate way to quantify the mean film thickness. Regardless, both of these factors should be explored in future work.

8.2.2 Comparison of Film Patterns Between Sensors

Figure 8.7 shows a comparison of the four different sensors active during the VG320 test, operated under 100rpm and 400kN load. These operating conditions ensured EHL film conditions similar to that of an operating field bearing. All sensors show evidence of the resonance phenomenon to varying amounts.

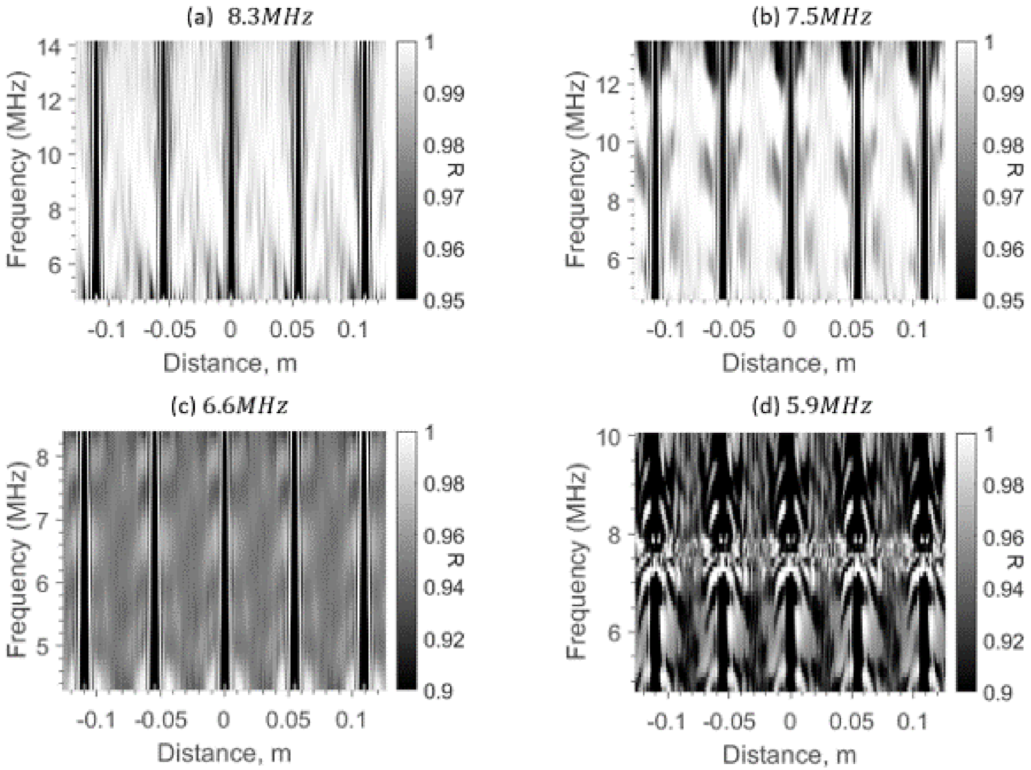

Figure 8.7: Spectral pattern for five roller passes under 100rpm, 400kN load with VG320 oil. The central frequency of each sensor is stated

There are several noteworthy points:

- Figure 8.7a has the highest central frequency, but the weakest resonant pattern. There is a horizontal fringe starting around f = 8MHz which reduces to f = 6MHz at the contact region suggesting film thickening.

- Figure 8.7b has by far the clearest resonant pattern, with fringes present at both the entry and exit to the contact. At the contact entry, the fringes reduce in frequency, indicating a film thickening into the contact. At the outlet, the fringe frequency increases, as the oil film thins away from the contact. Figure 8.2 shows that the amplitude and usable bandwidths of the 7.5MHz and 8.3MHz sensors are very similar, and have large amounts of overlap from 7 to 12MHz.

- Figure 8.7c shows a resonant fringe pattern very similar to that of plot (b), with both having fringes around 6MHz and 8MHz. Both of these sensors were on the same radial axis, as shown in Figure 8.1, and so the measured resonance would be expected to be the same.

- Figure 8.7d has the most chaotic spectral pattern out of the four sensors. Looking at the FFT plot in Figure 8.2, it is evident that a large amount of interference is causing a double spike pattern. This essentially renders the sensor unusable in terms of detecting resonances.

It is noted that (c) and (d) had to be multiplied by 0.95 to lower the amplitude to within the $0.95 \leq R \leq 1$ contrast window to achieve the spectrogram plot. This can be caused by a thin lubricant film covering the raceway being the mode lubrication state. When this occurs, the mode reflection used to generate the live modal reference is of a lubricated raceway, and so when the raceway becomes starved, the reflection coefficient raises from 1 to 1.05 instead of from 0.95 to 1. Making this amplitude adjustment has no affect on the actual resonant frequency presented, it simply allows for a consistent contrast window to be applied to all sensors for a more understandable comparison.

Across the sensors there is a large overlap in bandwidths, but oil resonances measured from sensors not on the same rolling axis occur at different frequencies. This indicates the raceway inlet film was not consistent across the roller length, and instead there were local changes in both the inlet length and thickness. Localised changes were modelled by Chevalier et al. [6, 7] in point contacts which showed that there can be flooding and starvation within a single contact due to localised lubricant supply. Chen et al. [11] monitored the distribution of oil within a transparent resin and glass bearing and also observed a gradient in inlet thickness across the rolling axis, with thinner films towards the centre axis and thicker films at the edges. As rollers have an increased contact length in the axis perpendicular to the rolling direction when compared with point contacts, local deviations in oil supply should expected here also.

8.2.3 Qualitative Analysis of Speed and Load on the Raceway Film

As the clearest meniscus pattern in Figure 8.7, the load, bearing speed and viscosity effect on meniscus formation were assessed qualitatively using the 7.5MHz sensor. Figure 8.8 shows spectral plots of five roller passes at a range of loads and bearing speeds, when the bearing was lubricated with the VG320 oil.

At 20rpm, 000kN (where the bearing had no load applied) there are large dark regions of reduced R across the entire frequency range at the contact inlets. This suggests that a resonance is not observable through this spectral method because either the oil film in this region is above the maximum film thickness measurable by the frequency approach, or the contrast is not low enough to detect the resonant dips. At the contact outlets there is the same thick film present on four out of the five contacts shown. The large dark regions associated with a very thick film are somewhat present at 100kN and 200kN, and very dominating at 400kN. At 20rpm, 000kN and 400kN, single frequency analysis showed the modal reference offset to 1.05, being representative of the entire raceway being covered in oil. As this is seen at the highest and lowest load investigated, but not at loads in-between, the effect is deemed load independent, and the cause is low bearing speed. This oil flood occurs at 20rpm because there is more time between roller passes for the oil to flow around the rollers, and less oil is entrained into the contact at these low speeds, meaning a greater abundance of free oil on the surfaces. Although there are large patches of free oil around the rollers, these may not actually aid in menisci generation, that in turn allow a development of contact pressure to cause separation. This is understood as literature has shown roller bearings operated at low bearing speeds do not generate a pressure build-up that adequately separates contacting surfaces, and so the bearings tend towards boundary lubrication and have higher levels of wear.

From 000kN, 20rpm to 100rpm the large oil patches almost vanish and instead short resonant fringes appear. This is chiefly because at the higher bearing speed there is less time for oil reflow around the rollers, resulting in less free surface oil on the raceway. Secondly, if there is ample oil for fully flooded conditions, a speed increase will entrain more of the oil that is available into the inlet region where the roller and raceway films meet. More oil within this inlet region will also result in less raceway oil availability in the measurement area.

As the load increases to 400kN the horizontal fringes lengthen towards the contact centre, and the frequency decrease becomes less sharp. This indicates the film becoming longer, a symptom of a shorter reflow time, and the gradient thickening at a less severe angle. Nicholas et al. [133] observed changes in lubrication state in a field operation WTGB and observed a relationship between inlet films and load. Their conclusion was higher loaded rollers shear more lubricant off of the raceway surface, resulting in a increased reflow time, the opposite trend to Figure 8.8. The work of Nicholas et al. [133] was done using a similar ultrasonic approach, but only observing in the single frequency domain, what is essentially a slice of a spectral plot. Therefore, what they observed as an inlet film depletion when R raised from 0.95 to 1, may actually have just been a change in the resonant frequency due to a film thickness change. Despite this, the relationship between inlet thickness, reflow time and load is noted.

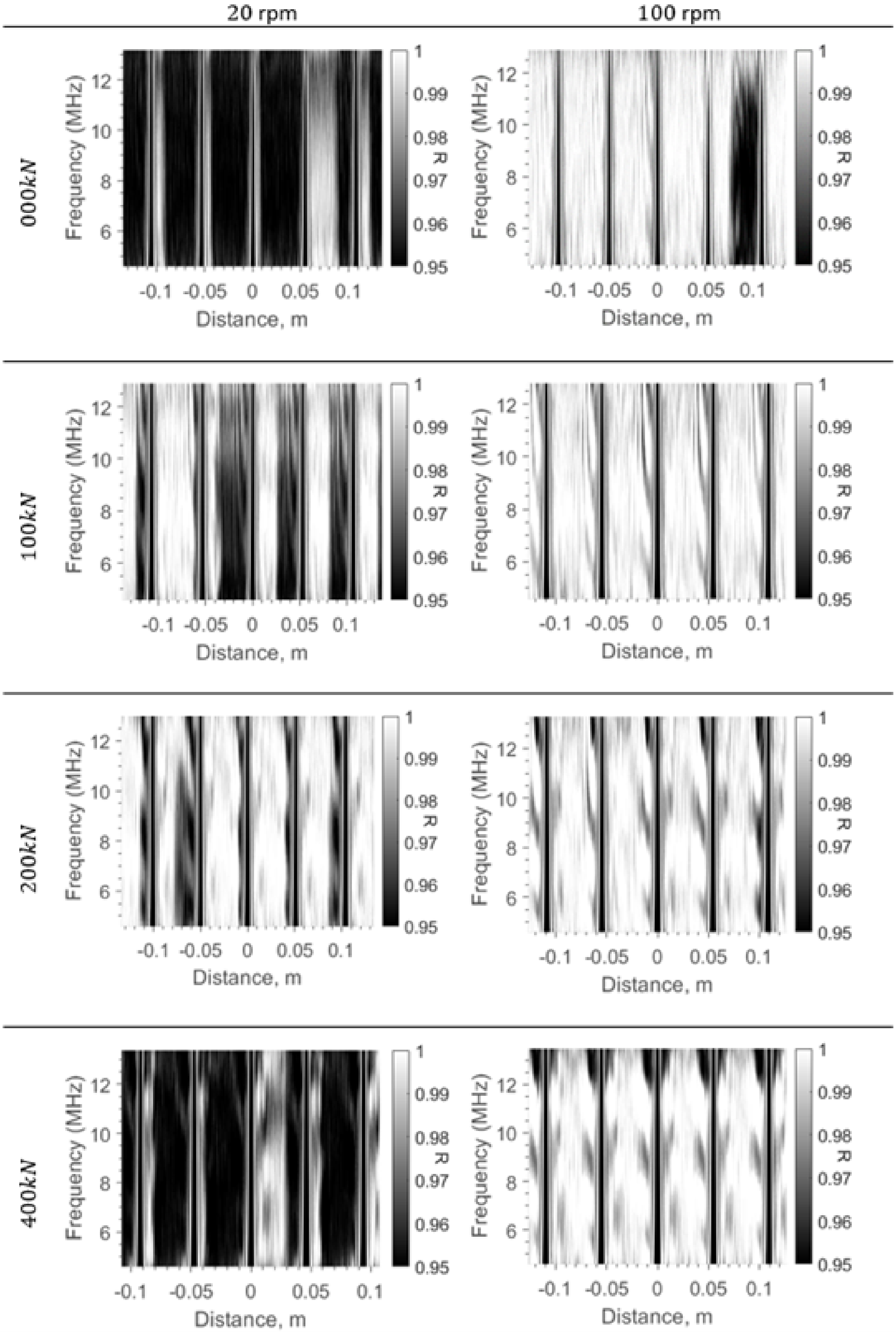

Figure 8.8: Spectral analysis from 7.5MHz central frequency sensor of VG320 oil lubricated bearing under various loads and speeds

Figure 8.9 shows the bearing lubricated with the VG32 oil at the same operating conditions and with the same sensor as Figure 8.8. What is immediately clear when comparing with the VG320 test results is the lack of dark oil patches present at any of the test conditions. As the oil is far less viscous, the lubricant spreads thinner and therefore is less likely to adhere a thick free surface raceway film. There may still have been a film covering the raceway at the low speed conditions, but the result suggests it was below the resonance range.

In general there is a much weaker inlet resonant fringe pattern. At 100rpm, 400kN there is clearly some resonance phenomena occurring, indicative of a raceway film, but the pattern is not nearly as strong, and the film is shorter than with the more viscous VG320 oil. This suggests that raceway films did develop with the less viscous oil, but not as readily. This is counter-intuitive as the less viscous oil should have improved flow characteristics, so although the raceway film could potentially be thinner, the film should have developed sooner after the outlet of the previous contact. However, this analysis method is purely qualitative and governed partially by the contrast settings, and a different contrast setting may be more appropriate for the less viscous lubricant. For the 100rpm, 000kN case a contact patch is completely undetectable as the oil has caused such a large separation suggesting very large contact separation and a fully flooded bearing, although this was not a common theme throughout the entire data set.

Refining the contrast settings for the VG32 oil was not explored as the spectral method was used purely as a tool to observe the presence of the film. The research emphasis of this thesis was to develop quantitative measurement tools and automate the measurement of raceway film thickness, which is discussed in the next Chapter 9.

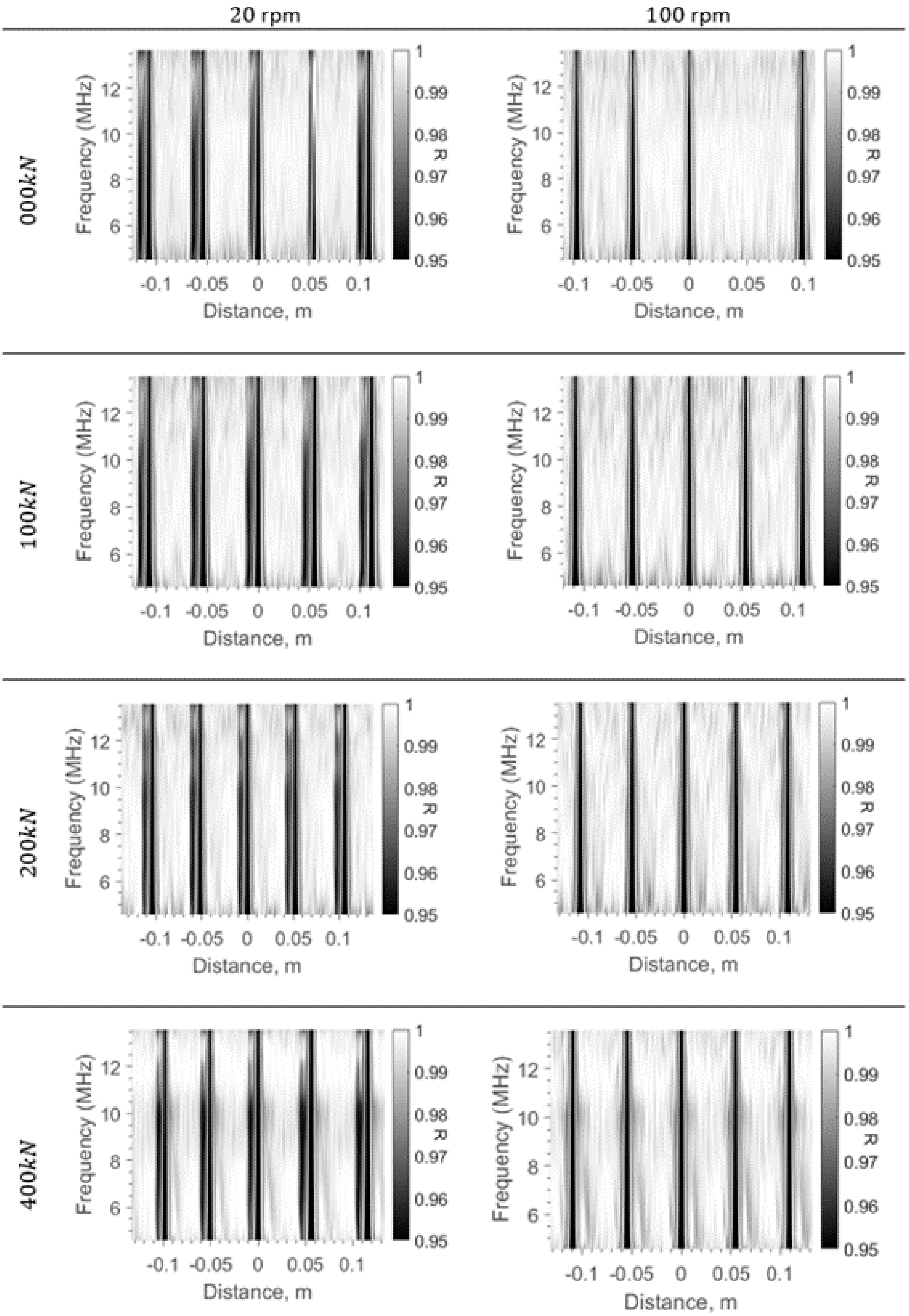

Figure 8.9: Spectral analysis from 7.5MHz central frequency sensor of VG32 oil lubricated bearing under various loads and speeds

8.3 Conclusion

- The purpose of the multi-frequency bearing was to scout for resonances in raceway films at the entry and exit of rolling bearing contacts, and to this end the testing was successful.

- Clear resonant patterns of changing frequency, which have been validated as a function of changing film thickness in Chapter 7, were observed both at the entry and exit to individual roller contacts.

- The presence of these resonances was not intermittent, and instead repeatedly observable for every roller.

- A qualitative analysis of the raceway spectral patterns shows that there is a relationship between the film formation and load, bearing speed and lubricant viscosity.

- With an increase in bearing speed from 20rpm to 100rpm, the spectral pattern suggests less oil was on the raceway between rollers. This is due to a reduced reflow time and an increased volume of oil in the inlet region as the entrainment into the contact is increased.

- With the lower viscosity oil, the spectral film pattern is weaker, but when using the higher viscosity oil there are clearly thicker films formed over greater portions of the raceway.

- The load, which has a minimal theoretical effect on the contact film thickness [49, 42], appeared to lengthen the raceway film leading to the inlet, suggesting a shorter reflow time and more oil availability for lubrication when operated under heavier loads. This is likely due to an internal scraping effect from the raceway or flanges.

- Sensors at different axial locations observe different resonant frequencies, suggesting the inlet raceway film was not consistent across the rolling axis. Inlet deviations have been noted in other works [6, 7, 11] and attributed to localised lubricant supply differences. The length of the roller contact perpendicular to the rolling axis is much larger than the contact width in the rolling direction, and so these localised changes should be expected here also.

- To attempt to understand or quantify meniscus formation based on raceway films, comparable measurements must be taken right across the rolling axis.
- The results presented in this chapter are all qualitative assessments based on spectral plots, meaning that drawn conclusions are not fully validated. As the spectral plots are based on individual reflection coefficient values of single reflections, to fully comprehend the magnitude of raceway films and the impact of test conditions, an automation post-processing method is needed, that will give an output film thickness similar to that given by hand in Figure 8.6. Such an approach is detailed in Chapter 9.

Chapter 9

Measurement Method for the Inner Raceway Film

Chapter 7 introduced an ultrasonic measurement method capable of detecting the resonant frequency of thin oil and grease layers. In Chapter 8 the method was proven to be applicable to bearing raceway films, showing qualitative analysis of in-situ measurements. This chapter explores the more intensive quantitative analysis of such measurements. First, details are given of the instrumentation of a second bearing raceway with seven 10MHz sensors, giving a comparable view of the raceway film across the rolling axis. The discretisation of the ultrasonically recorded rolling bearing pattern is explained, as is the automation method of detecting resonances in-situ, along with the calculation of film thickness. Finally, as the raceway film is only an indicator to lubricant fill within the contact, a volume fill model is proposed which determines a starvation level for the contact at that particular location, based on the film thickness adhering to the raceway.

9.1 Instrumentation of the Inner Raceway

Ultrasonic instrumentation, with the same central frequency transducers, laterally across the bearing inner raceway is necessary to fairly assess the lubricant film across the rolling axis. In order to assess the film thickness at the roller centre, and an even number of points either side of this centre, seven transducers were installed, with the fourth sensor at the axis centre. This also aligns with the FMS limitation of eight channels maximum. Figure 9.1 shows an image of the instrumented raceway and schematic showing the transducer positioning in relation to the roller profile. In the image, two rows of transducers can be seen. The first are shear transducers, which were not used during this testing. The second set are the longitudinal sensors used for the in-situ film measurement. After this image was taken, the transducers were cabled with micro-coax, grounded against the conductive raceway, and then covered in a protective epoxy. A k-type thermocouple was bonded and epoxied at the location of the central sensor to take in-situ temperature readings during testing.

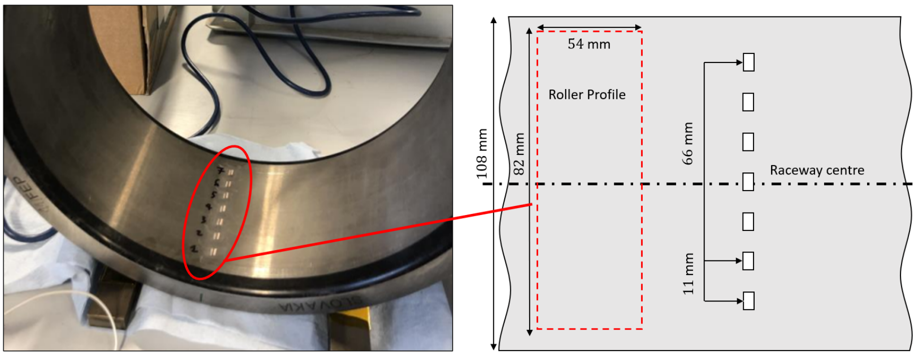

Figure 9.1: Schematic of the instrumented inner raceway of the multi-axis bearing

For a fair comparison it is important that all the transducers were of the same frequency. 10MHz transducers were selected as typically these have bandwidths between 5MHz and 15MHz. The results of Chapter 8 suggest that this is an ideal range for detecting multiple raceway resonances.

9.2 Reflection Pattern Discretisation

Figure 9.2 shows an example spectrogram from the instrumented raceway shown in Figure 9.1. The inlet, outlet and contact regions have again been highlighted, and within these regions are clear horizontal resonances due to a raceway film. Any parched region between contacts has been split between the inlet and outlet regions. From this type of plot the film thickness can be qualitatively assessed, but quantitative analysis is more involved.

During testing the channel pulse rate operated around 9kHz, within a 10s capture across 8 active channels (a single shear sensor was active but the data not interpreted for this study). This high pulse rate increases the resolution of the measurement in the rolling direction but results in a large amount of data stored. Additionally, at higher bearing speeds there are 100's of roller passes within each capture. Considering that captures were taken at several loads, under five different speeds, and with different lubricants, it is implausible to scan by eye the spectral patterns and come to any significant conclusions. Instead, it was necessary to develop a MATLAB script that

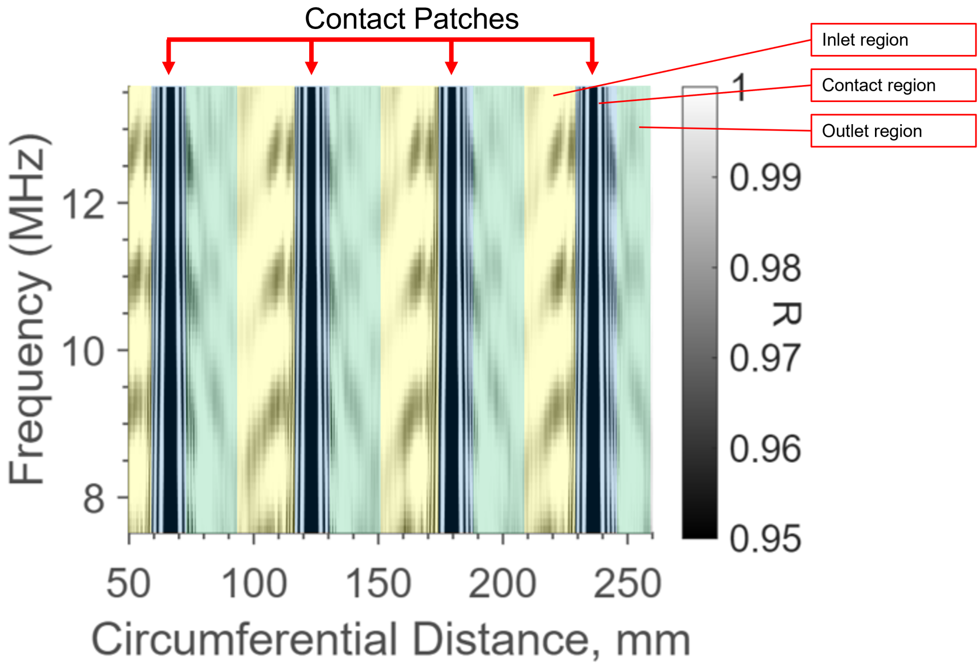

Figure 9.2: Example spectrogram with inlet, outlet and contact regions highlighted

would initially discretise the reflections into different contact regions, and furthermore automatically detect resonances and calculate film thickness.

The purpose of the contact discretisation is to separate the inlet and outlet region reflections from the rest of the reflections, as has been done in Figure 9.2. The resonance method can then be applied to these reflections and the thickness calculated. By the contact being discretised, different roller passes can then be compared with each other, as well as the average raceway pattern calculated.

Chapter 5 details how to generate reflection coefficient plots from the in-situ bearing measurements, an example of which is shown in Figure 9.3a. The x-axis has been left as reflection number as this is the variable used when automating the discretisation. This kind of reflection plot is the starting point for the discretisation.

Six locations are marked, one at each of the contacts. These locations are the centre of the contact region, and do not occur at the *MRC* reflection as this point is shifted towards the left of the contact. However, it is necessary to locate the centre of a contact, so that when the contact region is removed from the analysis, it is done so symmetrically about the contact location, with unnecessary ignorance to reflections taken within the inlet region in particular. Also, the number of reflections between contact locations is not constant, and instead has some variance about a mean value.

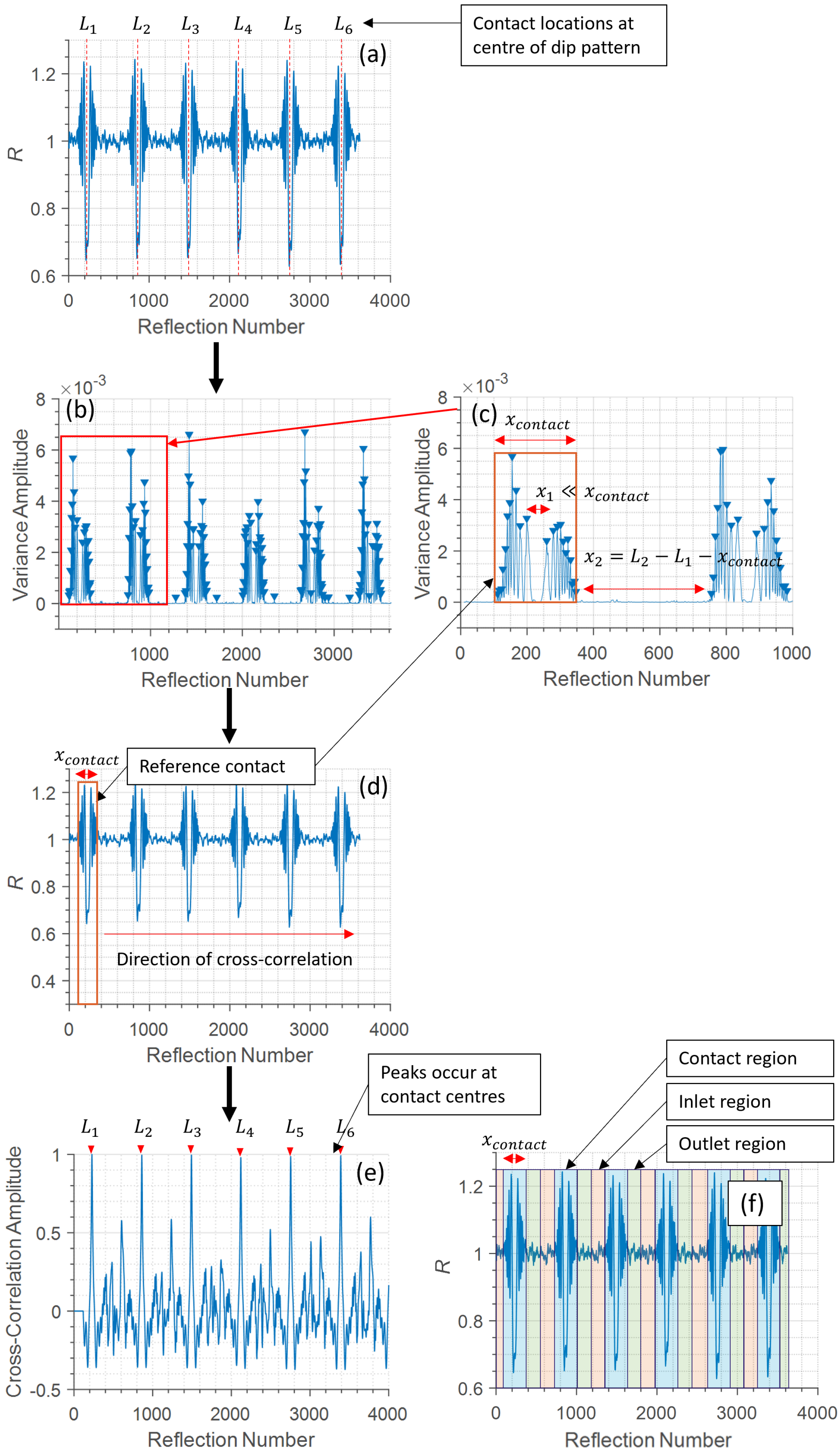

Figure 9.3: Explanation of the contact discretisation steps taken to automate the splicing of a reflection plot with rollers passing in (a) through to the discretised inlet-contact-outlet regions in (f)

This is due to fluctuations in the channel pulse rate of the UPR, and also variance in the bearing speed which fluctuates naturally during the test. Therefore, looking at the locations in 9.3a, $L_2 - L_1 \neq L_3 - L_2$. Consequently, a constant number of reflections between contacts cannot be defined. This means the *MRC* locations alone cannot be used as the contact location in an automation process and a more sophisticated approach is needed.

9.2.1 Detecting a Reference Contact

The first step towards automation is recognising a reference contact pattern, which can then be used later for cross correlation. Looking at Figure 9.3a, despite noise being in-between the contacts, the contact locations clearly have a much greater deviation from the baseline of $R = 1$. Figure 9.3b shows the calculated moving variance with a width of 4 reflections, with Figure 9.3c showing an enlargement across the first two contacts. The peaks in the interim regions between contacts are almost non existent, but the contacts themselves show very clear spikes in variance amplitude. The *findpeaks*[162] function in MATLAB was used to detect the spike in variance amplitude. For a single contact several peaks are seen, mainly due to the vertical interference pattern. However, there is a short period of stabilisation, labelled x_1 at the contact centre, where the roller is directly over the sensor location and where the R change is consistent leading to and away from the *MRC* reflection. The relationship between x_1 and the contact region width $x_{contact}$ is as follows:

$$\begin{aligned} &x_1 < x_{contact} \\ &\frac{x_{contact}}{x_1} = n \end{aligned} \tag{9.1}$$

If L denotes a contact location, the interim region between the first two contact regions (x_2) can be defined as:

$$\begin{aligned} &x_2 = (L_2 - L_1) - 2(\frac{x_{contact}}{2}), \\ &\text{if} \;\; (L_2 - L_1) = \Delta L, \\ &x_2 = \Delta L - x_{contact} \end{aligned} \tag{9.2}$$

As with Equation 9.1 another relationship can be defined with x_1:

$$\frac{\Delta L}{x_1} = m \tag{9.3}$$

The n & m are arbitrary variables, dependent on the two contacts in question, to describe the magnitude difference. Due to the nature of the reflection pattern in Figure 9.3c, $m > n$ for all test cases. n & m can be subbed into Equation 9.2 to form:

$$\begin{aligned} x_2 &= mx_1 - nx_1, \\ x_2 &= x_1(m - n), \end{aligned} \tag{9.4}$$

if:

$$m - n = k \tag{9.5}$$

then:

$$x_2 = kx_1 \tag{9.6}$$

As $m > n$ then $k > 1$, the following is always true:

$$x_2 > x_1 \tag{9.7}$$

Knowing $x_2 > x_1$ allowed minimum peak distance variables to be established, meaning a MATLAB script could differentiate between x_1 & x_2. This allows for the fist contact pattern, highlighted as $x_{contact}$ in Figure 9.3c, to be recorded as a reference contact.

9.2.2 Cross-Correlating the Reflection Pattern

As the tolerance of both the bearing raceway and rolling elements are very well defined, each reflection coefficient contact pattern has a uniform shape. The MATLAB function *corrcoef* [163] was used to cross-correlate the reflection pattern for a single test, against the detected reference contact. Figure 9.3d shows a schematic visualisation of this cross-correlation, and Figure 9.3e shows the correlation amplitude. When the contact reference is aligned with a contact, there is a sharp spike in the correlation amplitude to $A_{corr.} \approx 1$. $A_{corr.} = 1$ only occurs at the contact which was used for the reference, as this is the only perfect match. The maximum peaks then occur at the same contact central locations shown in Figure 9.3a, where the contact pattern is symmetrical about the detected location, not asymmetrical like it is about the *MRC* location. This is crucial for the step shown in Section 9.2.3.

Of note here is that the correlation amplitude is not always as prominent as shown in Figure 9.3e and noisy signals can mean such close correlation is not achievable when noise spikes have a more comparable amplitude to the spike at a contact. To still locate the contact locations for these nosier signals, a series of 'peak finding passes' were deployed. The purpose of these passes were to detect the maximum prominences of peaks, associated with the contact locations, and then develop a new minimum peak prominence that peaks must match in order to be detected for the next pass. This means that with every pass, fewer and fewer noise spikes are detected, and only the true peak locations remain.

9.2.3 Indexing Roller Passes

None of the contact region is suitable for resonance analysis. When the contact is directly over the sensor location, the film is in the sub μm range and therefore does not cause a resonance. Additionally, around ±10mm from the contact centre the vertical interference pattern, discussed in Sections 5.5 and 8.2.1, makes resonance detection due to film thickness difficult and so this region must also be excluded from calculations. This was done by excluding the contact reference reflections, used for the cross-correlation, from the resonance analysis. To ensure a symmetrical contact pattern was removed an *if* function in MATLAB ensured the contact reference reflection number to be odd. If detected as an odd number nothing was done. If even, the end contact reflection, on the outlet side, was removed from the reference, thus ensuring that more of the inlet region was available for detection. Removal of a single reflection from the analysis is not detrimental to the raceway patterns because of the large number of reflections already included in the analysis.

The remaining reflections left for analysis are therefore the regions between contacts, denoted as x_2 in Figure 9.3c. The first half of these reflections is denoted as the 'outlet film region' of the first contact. The second half is then the 'inlet film region' to the second contact. Figure 9.3f shows the reflection pattern discretised into the contact region, inlet and outlet raceway regions.

9.3 Determining the Raceway Film Thickness

9.3.1 Amplitude of In-Situ Resonances

One point of in-situ resonance detection that makes automation difficult is the amplitude of resonant dips. In Figure 7.28 In Chapter 7 resonant dips are seen as low as $R = 0.2$. However, the in-situ dip amplitudes are normally $R \approx 0.95$ as shown in Figure 9.4 which is an example in-situ resonance plot from the bearing measurement.

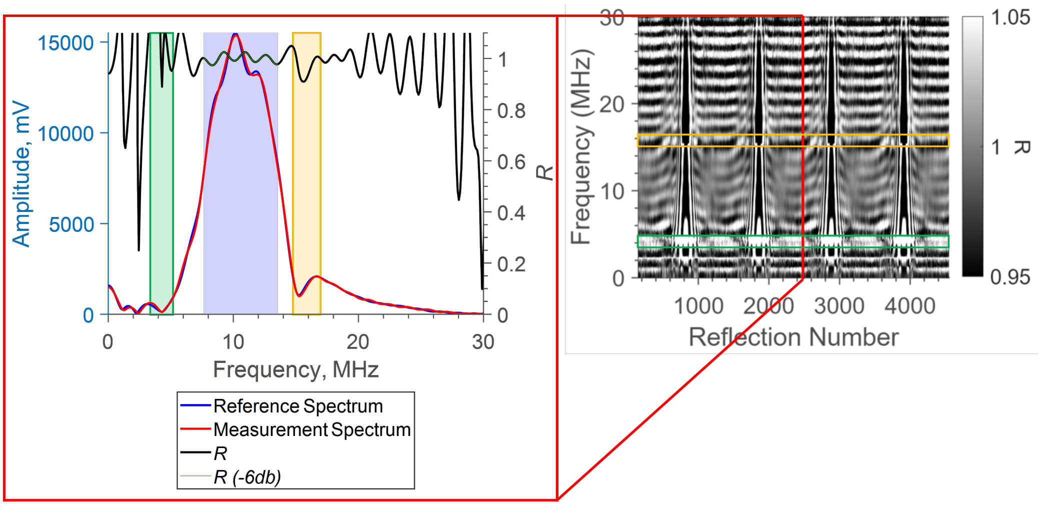

Figure 9.4: Example resonance plot from an in-situ measurement. Shown is the FFT plots of the reference and signal, and from this the calculated reflection coefficient

The number of frequency bins evaluated can be user defined by using different severities of bandwidth, but there is a finite frequency range at which usable measurements can be taken, and bandwidths that include frequencies outside of this range are detrimental to analysis. Figure 9.4 shows the frequency response of the reference signal and a raceway film measurement signal, along with the calculated reflection coefficient, over the first 30MHz. The blue region highlights the −6db bandwidth of the sensor. Outside of this bandwidth, at ≈ 5MHz, 15MHz and 27MHz there are dips in R of a larger magnitude. However, when the location of these dips is assessed against the FFT frequency spectrum, the first two at 5MHz and 15MHz occur near the transition region between frequency lobes, which are governed by the central frequency of the piezo element and the pulse width applied. If there is some form of general decrease or lateral frequency shift in the FFT amplitude of the measurement reflection, these two points when will naturally show a drop in R, but not due to resonance, and should therefore be excluded from resonant analysis. Windows of where these dislocations can occur due to the transition of lobes have been marked on the plot in green and yellow. Likewise, the dip at 27MHz is far away from the central region of the sensor. The further the frequency is from the sensor central frequency the worse the SNR becomes, and the more susceptible the signal is to dips in R of a substantial magnitude, but due to data noise instead of resonance.

When analysing multiple reflections in the spectrogram over the same frequency range, the natural dislocations in data at 5MHz and 15MHz due to the transition region between frequency lobes is again very clear. Above and below these dislocations very rigid noise patterns are seen. These have poor SNR ratios and should be excluded from any kind of resonance analysis as they will incorrectly alter the mean resonant frequency calculation. For the in-situ tests a $-6db$ bandwidth was applied. Within this region there are clear dips in R due to the presence of an oil film, but of a more subtle amplitude than the resonances seen within the validation tests. There are several explanations for the low amplitude of in-situ resonant dips:

Convex Body Contact As highlighted in Section 5.6.4 the convex nature of the contact bodies alters the measurement area of each sensor, essentially meaning that the reflection coefficient is representative of an average area larger than the sensor face. Conceptually, this blurring affect could reduce the amplitude of the resonance dip.

Live Data Mode Reference Section 5.4.3 describes how a live data mode reference is generated from in-situ bearing data. One of the issues highlighted with the method is if the modal lubricant state is of a very thin oil layer, instead of a steel-air reference. This is known to occur within the bearing, and the effect is a reduction in R amplitude, as this was corrected for in some of the scout bearing data, as discussed in Chapter 8.

Thick Raceway Films Film thickness partially governs the amplitude of a resonance dip, with thicker films generally having shallower dips, see Figure 7.28 of Chapter 7. Dow et al. [99] found that as the echo number through a film reduces, the amplitude of resonance decreases. Within a captured reflection, thicker films will have less echoes due to increased attenuation per echo pass through the fluid, and so the dip of amplitude is subdued.

Any of the above mentioned influences, or a combination of all three, could be responsible for the shallower dips seen in the in-situ measurements. Isolating each influence is complex, and would require a large investment of time. Ultimately, the measurement of film thickness relies only on the frequency at which the resonance occurs, shown by Equation 3.18. Therefore, so long as a resonant dip is measurable and can be separated from signal noise, the amplitude is irrelevant.

9.3.2 Detecting Resonant Frequencies

The measured resonant frequency may not always be within the usable bandwidth of the sensor, and instead only the higher order harmonics are visible. To calculate

f_0 then, the mean frequency difference between resonances $\overline{\Delta f}$ is measured, which is known to be equal to $2f_0$. A thickness value is then calculated using $\overline{\Delta f}$, and a calibrated acoustic velocity at the appropriate temperature, in Equation 3.19.

Due to the reduced amplitude of the resonance dips, the processing automation needed to highlight resonances from signal noise. Initially the resonant plots were inversed, so that the dips became peaks and the MATLAB function *findpeaks* [162] could be used for detection. Then the signal was subjected to a series of three peak detection passes, with each pass filtering out more signal noise to leave only the true resonances left to detect. The first pass highlighted all peaks in the signal which include the resonances but also the deviations in R due to noise. For the second pass, a minimum peak prominence value was set to filter out very low amplitude noise. Additionally, the maximum peak from the first pass was found, which if the reflection was from a free oil film location would be due a resonance peak. A 10% threshold of this peak width and height were then used as the minimum peak width and height for the second pass. Peaks which surpassed this threshold are due to resonance, and below this are most likely signal noise. Additionally, a minimum peak distance of 10 data points was set for this second pass, to adhere to the maximum film thickness tolerance defined in Section 7.6.2. For the third pass the frequency differences between detected peaks remaining, which are assumed at this point of processing to be due to resonances, were examined by the *isoutlier* function [164], which defined outliers as values exceeding more than three median absolute derivations. All outliers were excluded, and the remaining frequency differences between peaks were averaged to calculate $\overline{\Delta f}$. The resonance detection function used for the in-situ measurements can be seen in Section A.1 of Appendix A.

9.3.3 Measured Resonant Frequency Drift

It is noted that integer multiples of the f_0 value, calculated from $\overline{\Delta f}/2$ do not always align with the measured frequencies, and that the measured harmonics are higher. Figure 9.5 shows an example of this. In black are the measured harmonics from an in-situ test. f_0 has been calculated from these and multiplied by 9, 11 and 13, the values of which are shown in red. Clearly there is a discrepancy between the two sets. The most likely cause for this is the relatively large sensor measurement area, meaning multiple thicknesses are being measured at one time. These different thicknesses will have slightly different resonant frequencies which could cause the shift in measured resonance. The same kind of shift is seen in the validation data presented in Chapter 7 but to a lesser extent. In Figure 7.19 the shift of the measured harmonics compared with the theoretical harmonics is larger during the thinning stage, where there is a larger gradient of oil film across the measurement area, which then reduces as the film stabilises. This shift is another reason larger bandwidths capable of measuring multiple harmonics are beneficial, so a mean measurement can be taken of f_0.

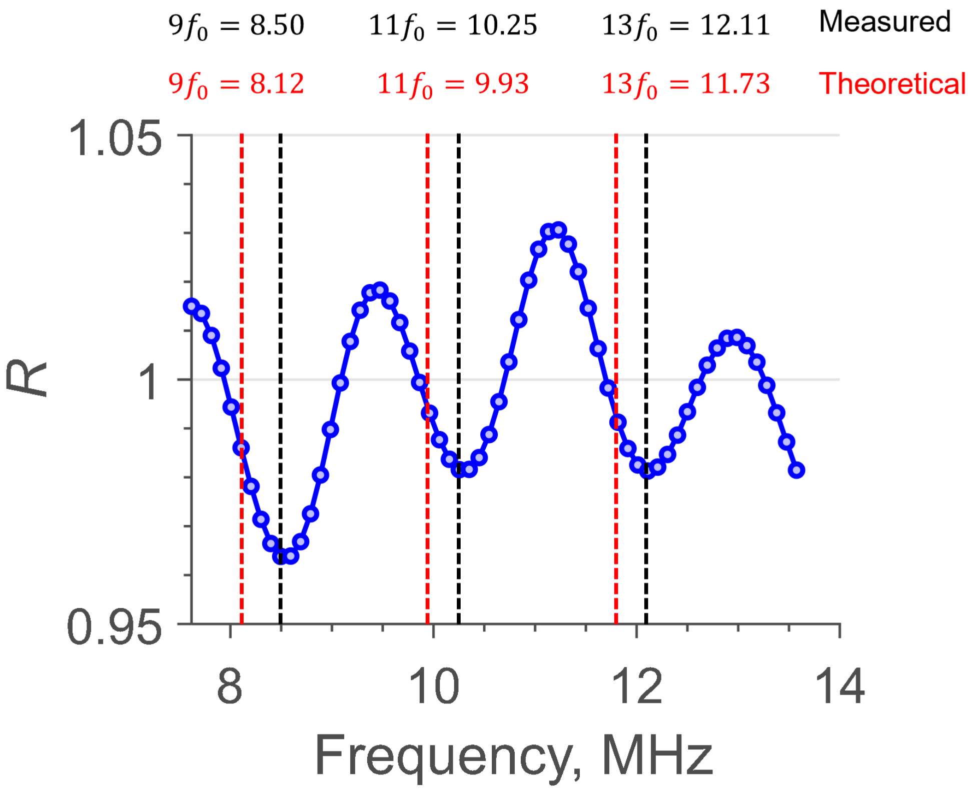

Figure 9.5: Example of measured higher order harmonics compared with the theoretical value, calculated from $\overline{\Delta f}$

9.3.4 Visualising the Raceway Film

Discretisation of the recorded roller passes allows for the inlet and outlet to be viewed at a single contact; Figure 9.6 shows such an example. The film thickness values shown are from the fundamental frequency measurement of the reflections, and the acoustic velocity value at the oil temperature, used in Equation 3.19.

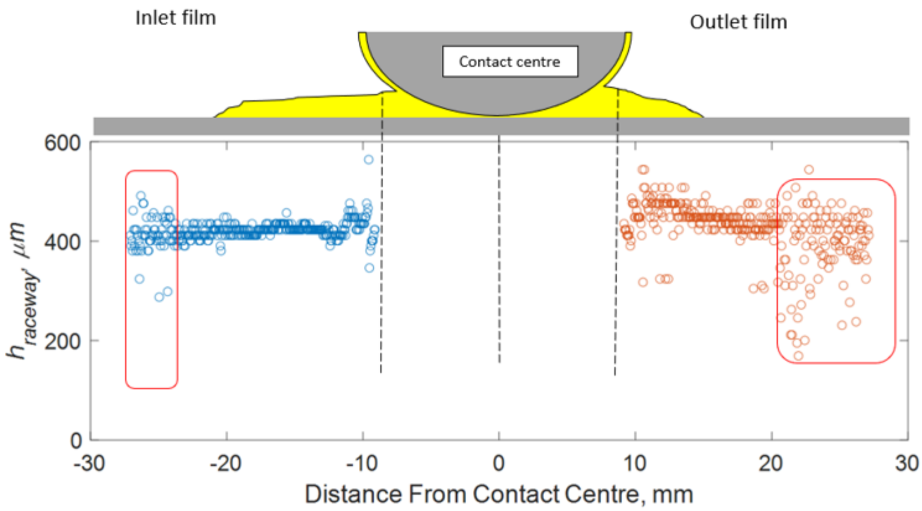

Figure 9.6: Visualisation of the raceway film at the contact inlet and outlet regions. Highlighted are regions of scatter where a stable film is not present

Some film plots show large variance in the measured film thickness, with a large scattering of film thickness values. Such regions have been outlined in Figure 9.6, and an example plot highlighted in red in Figure 9.7a. These values vary so much from reflection to reflection that such a film could not exist. Investigation into the resonance plots shows that this occurs when the script fails by detecting noise dips as resonant dips, suggesting in this location there is no film present, or a film below the minimum detection threshold. In automating the detection of the mean raceway thickness these scatter values should be excluded from any kind of thickness analysis, otherwise the mean will be impacted. The green region of Figure 9.7a shows a stable raceway film, leading to the contact inlet. In the yellow region, there is some ambiguity about where the film forms, and transitions to a stable one.

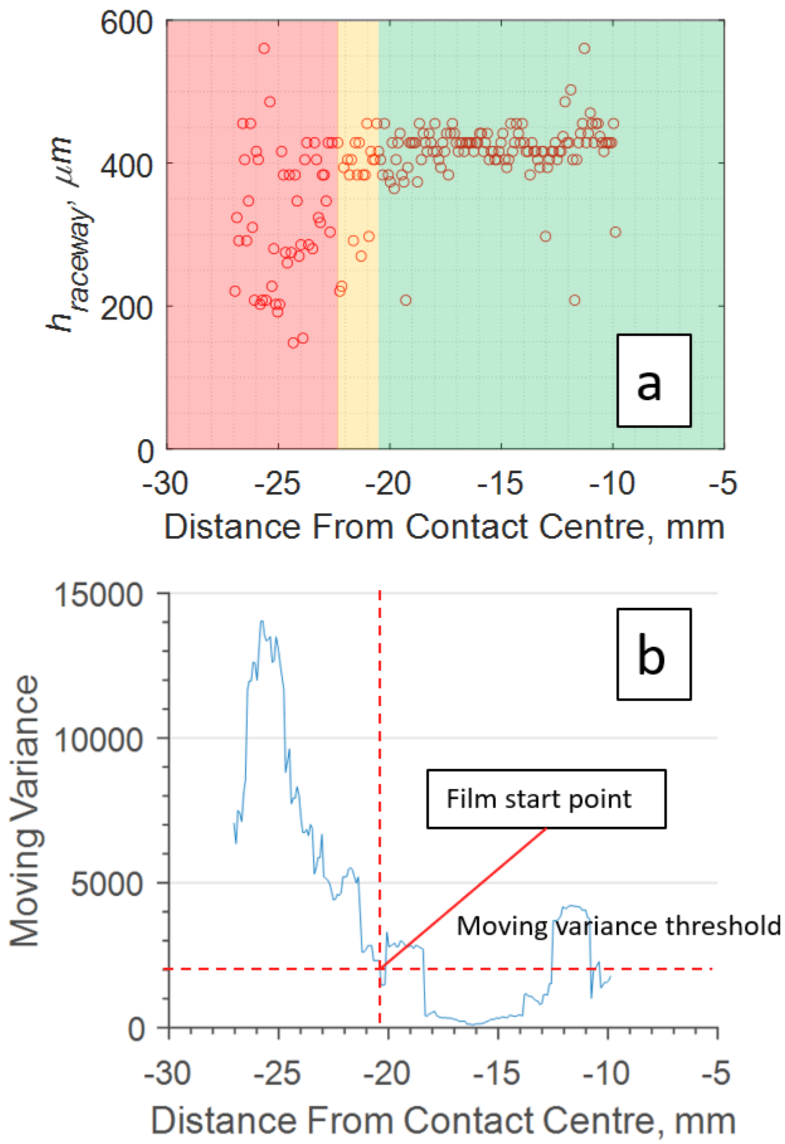

Figure 9.7: (a) shows the measured raceway film at the inlet to a contact with some scatter far away from the contact inlet. (b) shows the moving variance and determination of the raceway film detection area

To standardise the detection of the stable region across roller passes, a moving standard variance window was used. A window of a set number of reflections was selected; a trial and error approach deemed 20 reflections gave repeatable results. The reflections within a window, for example reflections 1 to 20, were selected and the variance calculated. The window was then moved one reflection along, and the variance of the next window was calculated (reflections 2 to 21). The process was repeated until the last reflection was included within a window. Figure 9.7b shows an example plot of the moving variance window of the film in Figure 9.7a. From analysing different roller patterns, a variance threshold of 2000 was deemed acceptable to define a stable raceway film. The acoustic velocity of a lubricant influences the precision of the thickness measurement, and therefore by extension the variance in films. As the acoustic velocities of all lubricants tested were very similar, a single threshold value could be used across all tests.

Once the variance value falls below this threshold, a stable film is assumed to be formed, and all values after are included in analysis. Before this value, the raceway is too thin/non-present and the scatter values are ignored.

Figure 9.8a shows a second inlet raceway film that does not contain scatter, and visually is much more stable than the film of Figure 9.7a. When looking at the complementary moving variance plot, all initial values are below the 2000 threshold. There is a peak in variance around -12mm from the contact centre, which moves the variance above the threshold. But, because previous thickness values were below the threshold, the film is assumed relatively stable, and so these peak values are included in further analysis.

The thickness spike peak is not always present in film plots; for example Figure 9.7 does not have one. There are two potential causes for this shape change. The first, the detected film genuinely has a thickness spike within that region which is plausible considering the chaotic nature of oil flow within the bearing. The second, the measured contact is wider than the reference contact, and so some of the vertical interference region which is not appropriate for resonance detection has been included in the raceway plot. Figure 9.9 shows the film thickness plot of Figure 9.8 against the single frequency reflection coefficient; the film spike occurs in an area still influenced by vertical interference. However, the raceway mean and median have good agreement, validating that inclusion of the spike is not detrimental to the data. This is because the spike is just a small portion of the overall film shape.

9.4 Calculating the Position of the Inlet Meniscus

9.4.1 Defining Contact Starvation

A complex starvation parameter was given by Cann et al. [109], shown in Equation 4.1. The issue with this method is that it is impractical to measure, requiring a lot of meta information about the contact and lubricant properties, and is not necessarily applicable to both oil and grease lubricated bearings due to the input parameters.

Wolveridge et al. [3] defined starvation based on the distance of the inlet meniscus position away from the contact centre. Dowson [41] found that when the inlet distance

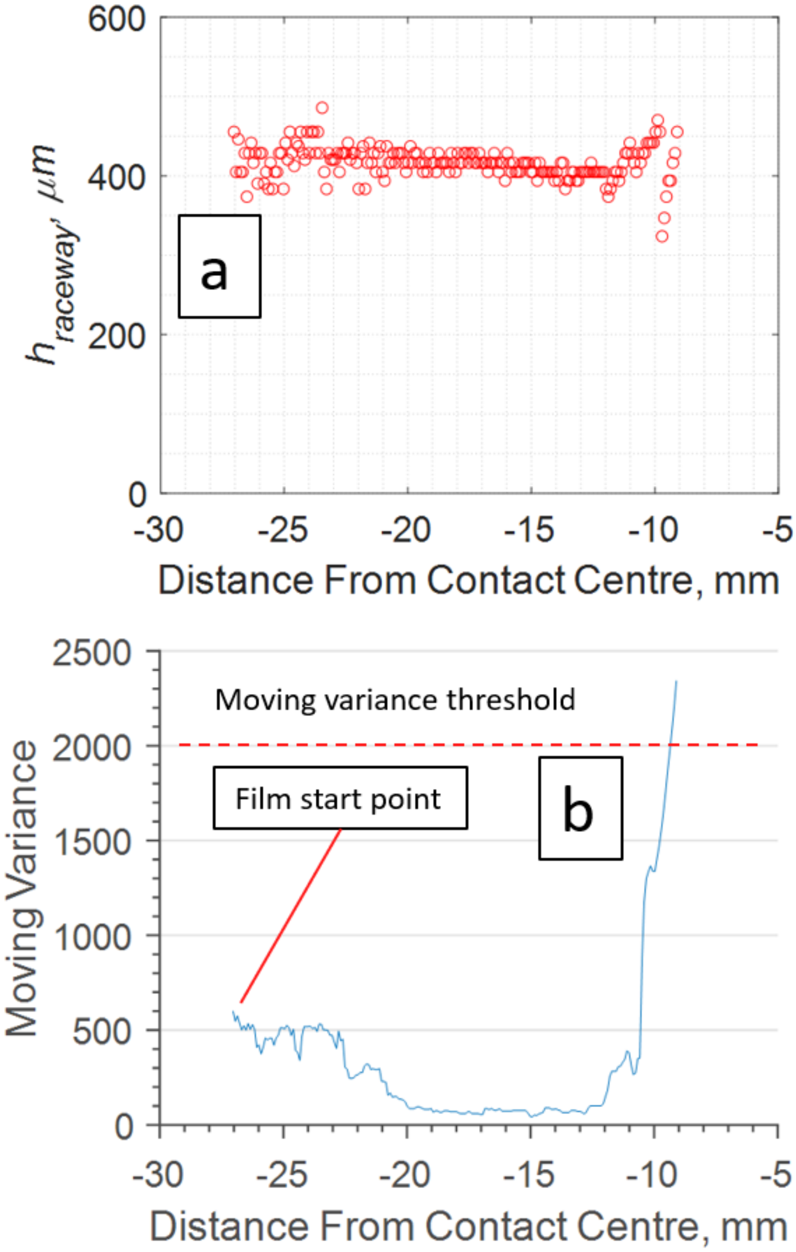

Figure 9.8: (a) shows the measured raceway film at the inlet to a contact, which appears very stable. (b) shows the moving variance which confirms the stability

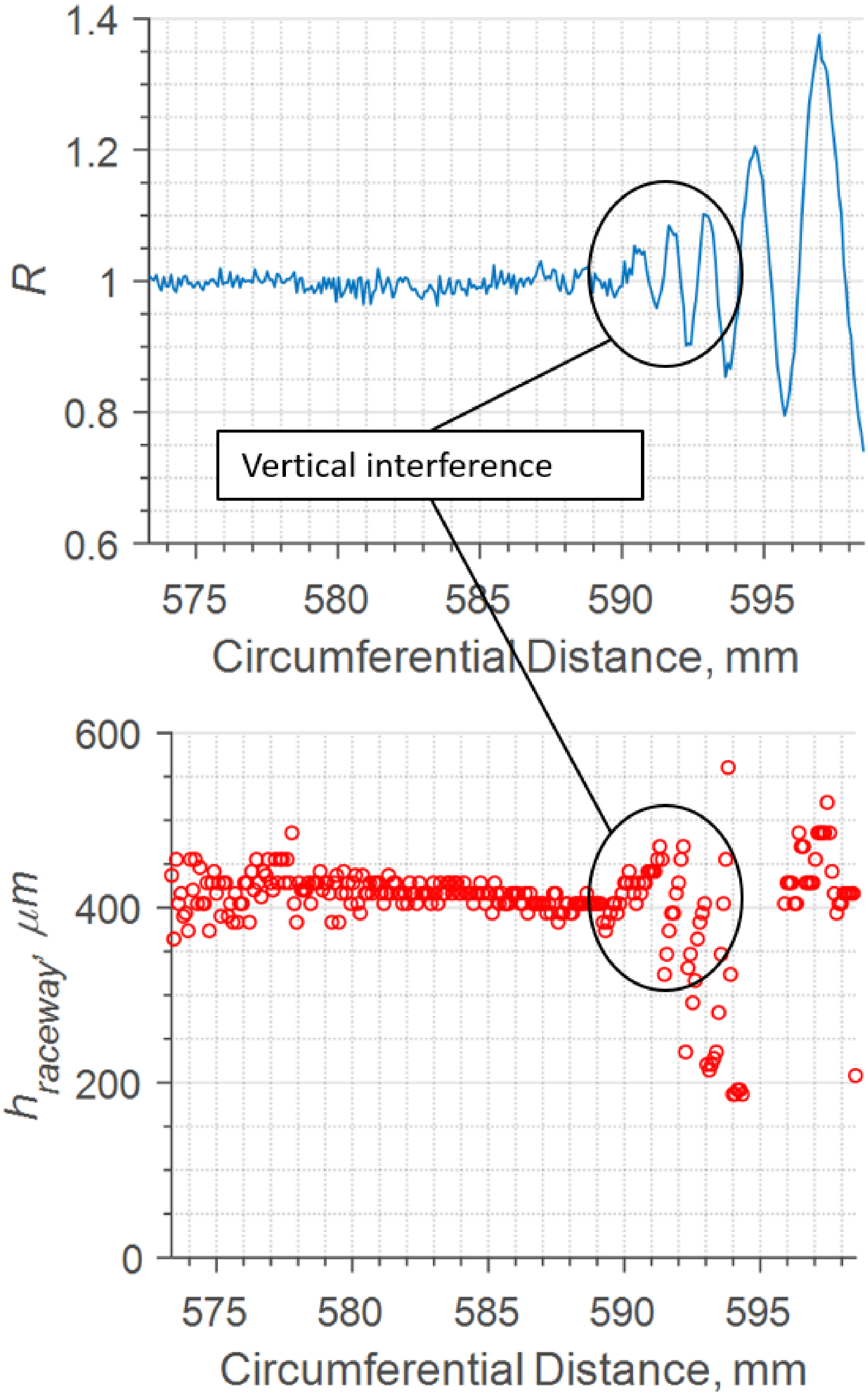

Figure 9.9: Observation of measured raceway film shape in area influenced by vertical interference

was 5× greater than the Hertzian contact half-width ($s/b = 5$) $h_c = h_{c\infty}$ and thus the infinite meniscus assumption can be made, essentially stating that there is adequate length for the contact pressure to develop and so no starvation occurs. When $s/b < 5$ starvation begins and h_c is reduced; when $s/b = 1$ then the zero reverse flow boundary condition is true, and $h_c = 0.7h_{c\infty}$. Thus, between $1 < s/b < 5$ the contact film thickness varies between $0.7h_{c\infty} \leq h \leq h_{c\infty}$.

The work of Cen & Lugt [60] shows that a greased contact thickness can be as low as $0.25h_{c\infty}$ as bearing speed increases. In this instance, it is likely $s/b < 1$ due to impaired reflow time and the contacts were severely starved. Regardless, inlet length and s/b ratio are more practical parameters to comprehend and compare, and so were the focus of this thesis.

9.4.2 The Volume Fill Model

The inlet meniscus position, as shown by Figure 4.2 occurs when the separation between the rolling surfaces is completely filled with oil. As discussed in Chapter 5, in this region, the concave nature of the opposing surfaces allows for constructive and destructive interference of ultrasonic waves. The calculated reflection coefficient then becomes an extremely complex plot, and film thickness measurements in this region are not possible. Therefore, to calculate the inlet meniscus position, the Volume Fill Model (VFM) is proposed. At the contact inlet, the films adhering to the roller and raceway will join, forming the meniscus inlet, when the added volume of lubricant of both films matches the separation at a particular distance away from the contact centre. The purpose of the VFM is therefore to use a measured raceway film and theoretically calculated roller film to determine the meniscus location based on the combined film matching the raceway-roller separation.

For simplicity the dry, undeformed contact between roller and raceway is modelled as two simple circles, touching at an infinitely small point at the contact centre. This is shown schematically in Figure 9.10. The separation of the two circles at a distance x away from the contact centre is dependent solely on their radii in this undeformed case. At a given x, this half chord length can be used with the known radius to calculate k, the distance from the circle centre to the chord, via Pythagoras theorem.

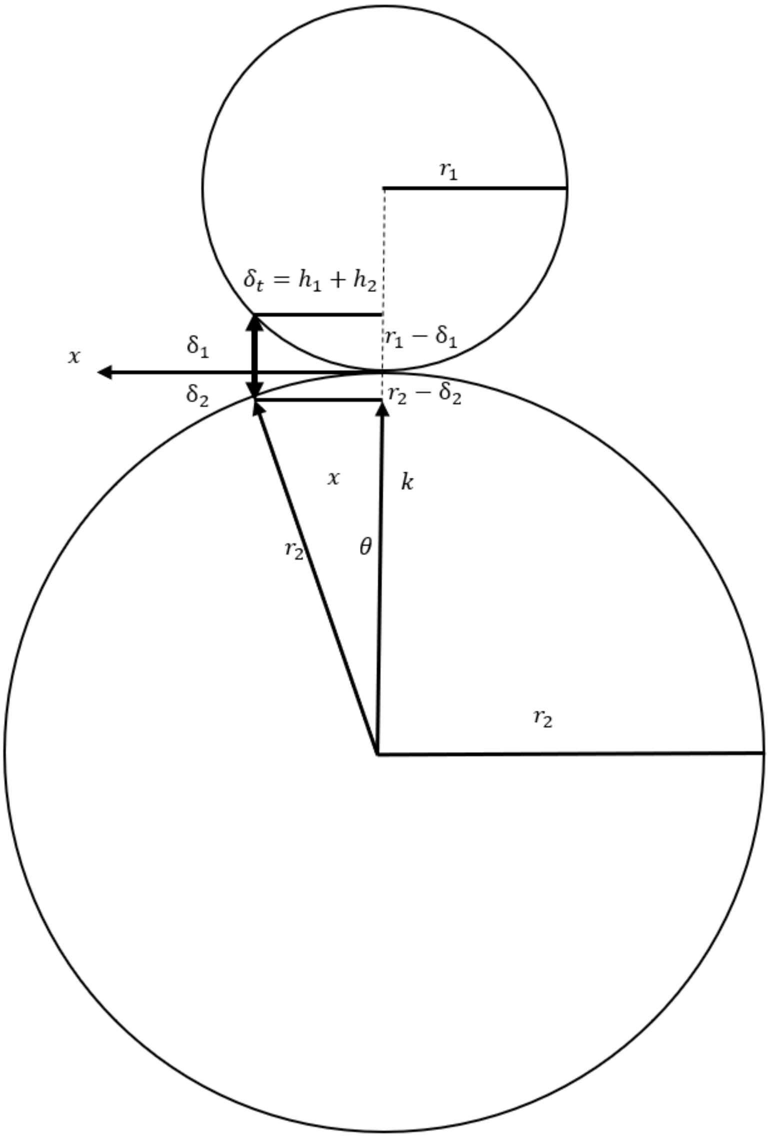

Figure 9.10: Schematic of the circle separation which governs the volume fill model approach

$$k = \sqrt{r^2 - x^2} \tag{9.8}$$

and so the separation of a radius to the centre line at a arbitrary position x is

$$\begin{aligned} \delta &= r - k \\ &= r - \sqrt{r^2 - x^2} \end{aligned} \tag{9.9}$$

The total separation δ_t is as follows, where the subscripts 1 and 2 refer to either circle:

$$\delta_t = \delta_1 + \delta_2 = r_1 - \sqrt{r_1^2 - x^2} + r_2 - \sqrt{r_2^2 - x^2} \tag{9.10}$$

The inlet meniscus position will then occur at a position x_i where the inlet film thickness is equal to the total circle separation ($h_i = \delta_t$). this can be written as:

$$h_i = r_1 - \sqrt{r_1^2 - x_i^2} + r_2 - \sqrt{r_2^2 - x_i^2} \tag{9.11}$$

This relationship is useful for understanding how thick an oil layer must be to achieve a meniscus at a given distance away from a contact, when using a non-deformed contact assumption. However, with a measured film, Equation 9.11 must be solved for x_i with h_i known. This is an implicit relationship, so no analytical value exists, and x_i must be solved numerically.

This can be solved using the Newton-Raphson method, which is an iterative function used to find successively more accurate solutions to the derivative of a function. The method begins with an initial 'guess' at the solution x_0. From hand calculations using Equation 9.11, $x_0 = 10$mm was selected, although the only influence this initial guess has is on computation time, and so the value is essentially arbitrary so long as it is within a similar magnitude to the real solution. A first approximation of the root is given by:

$$x_1 = x_0 - \frac{f(x_0)}{f'(x_0)} \tag{9.12}$$

and successive iterations, each of which makes a more accurate estimation of the true value, are calculated as:

$$x_n + 1 = x_n - \frac{f(x_n)}{f'(x_n)} \tag{9.13}$$

Applying this method to Equation 9.11:

$$f(x_i, h_i) = r_1 - \sqrt{r_1^2 - x_i^2} + r_2 - \sqrt{r_2^2 - x_i^2} - h_i \tag{9.14}$$

and

$$f'(x_i, h_i) = x_i(r_1^2 - x_i^2)^{-1/2} + x_i(r_2^2 - x_i^2)^{-1/2} \tag{9.15}$$

The method is deemed complete to an acceptable accuracy when $|x_{n-1} - x_n| < 10^{-3}$.

9.4.3 Volume Fill Model Improvement Parameters

In the basic iteration of the VFM in Equations 9.14 and 9.15 two governing parameters are excluded: the roller film thickness and the cylinder compression. These are excluded as it leaves the model simple, and still a good predictor of the inlet meniscus position. To include them requires more data about the contact conditions. However, both can be included in the VFM if needed to improve the accuracy of the calculated meniscus position.

9.4.3.1 Roller and Raceway Films

The position of the oil-air boundary at the inlet to the contact is formed from the joining of the films adhering to the roller and to the raceway. Therefore, it is necessary to determine both of these films to calculate the inlet meniscus position. The film adhering to the roller is not directly measurable as the only point it is positioned over the sensor location is when in contact with the raceway, and there is no other sensing position where this film can be isolated from other film measurements. However, by calculating the theoretical film thickness from Equation 2.5 and applying the rupture ratio formula given by Koštǎl et al.[9] as shown in Equation 4.3, the film adhering to the roller (h_{roller}) can be estimated.

Although the rupture ratio is dependent on the SRR, the in-situ measurements are within the heavy load zone, and so it is assumed that SRR = 0 [38], and thus the rupture ratio $\Delta = 0.0108 \cdot 0 + 0.5 = 0.5$ and the contact film is evenly split between the roller and raceway at the outlet. Under test conditions that would give the theoretical thickest central film thickness, an applied load of 100kN and bearing speed of 100rpm, and assuming the bearing has sufficient lubricant such that starvation does not occur, $h_{c\infty} = 1.52\mu$m at the recorded oil temperature of $27.4°C$. Then using the assumption that $\Delta = 0.5$ the thickest film during testing that will adhere to the roller surface is 0.76μm. The thinnest measurable raceway film for the *Alpha SP VG 320* oil using the resonance approach is 141μm at $20°C$ and 119μm at $100°C$.

If the roller film h_{roller} is included in the inlet film thickness h_i (i.e. $h_i = h_{raceway} + h_{roller}$ where $h_{raceway}$ is the thickness of the film adhering to the raceway), there is only a 0.64% difference to if just the raceway film is used, at those minimum values. This % difference decreases even further with both thicker raceway films, higher temperature tests which alter the inlet viscosity, and heavier loaded, lower bearing speed tests. Therefore, the impact of the roller film on the position of the meniscus at the contact inlet is small, and the assumption $h_i \simeq h_{raceway}$ is valid in most, well lubricated cases. Although this assumption is valid in this case, the bearing is large, with a reduced radius $R' = 22.3$mm, meaning the measurable raceway thicknesses shown in Figure 7.29 are only 0.4% to 4% of R'. This assumption may not be appropriate for much smaller bearings run at much higher speeds, where the R' is reduced and raceway films starts to become comparable to the central film thickness. For smaller bearing geometries, or if a reduction in complexity is not necessary, h_{roller} can be included in the calculation of the x_i position, as will be done later in this chapter.

A secondary note of caution is that oil splash onto the roller, which would increase h_{roller}, is not considered but in this situation, where the measured contact is ploughing through an oil sump, could potentially be expected. It would be hard to incorporate the random nature of this oil splash and therefore difficult to comment on its level on impact, but the assumption that $h_{raceway}$ is the governing film in this case should still stand. That is because the inner raceway here is stationary and therefore more likely to collect these oil droplets, which can be detected if they land within the sensor measurement area, than the moving rollers are. However, this assumption may not be true for other contact and lubrication conditions.

9.4.3.2 Bearing Cylinder Compression and Separation

When lubricated a thin film forms in the rolling contact that separates the metal surfaces. Although this separation is within the sub-micron range for EHL, it does increase the oil volume needed to achieve $s = 5b$. Cylinder compression has a more prominent effect as increased load increases the contact width. Between $0 \geq x \geq b$ the contact separation is constant, and calculable from the Dowson equations. In his book "Principles of Lubrication" [165] Cameron gives formulae for the separation of deformed cylinders, outside of the contact zone, for a dry contact in Eq. (8.23). In his approach, within the contact region the deformation is governed by load and material properties. Outside of this region, the separation is governed by the undeformed geometry of the cylinders, with the crucial detail being that separation is non-existent within the contact region. This Cameron style approach can be accommodated in a more complex form of the VFM, but using the theoretical contact central film thickness as the separation value within the contact area, the dimensions of which are calculated by the Hertz equations. With increased load b will increase, shifting the start of the separation further away from the contact centre, but also meaning the s parameter must be larger to reach the $s/b = 5$ fully-flooded criteria.

9.4.3.3 Inclusion of Contact Compression and Raceway Film

When including the roller film and contact separation, the inlet meniscus position will occur when the product of the films are equal to the dry separation value plus the separation in the contact:

$$\delta_t = \delta_1 + \delta_2 + h_c \tag{9.16}$$

The film adhering to the roller is calculated from the central film thickness multiplied by the rupture ratio, which at the point of maximum load with $SRR = 0$ gives $\Delta = 0.5$:

$$h_{roller} = h_c \Delta \tag{9.17}$$

and so using Equations 9.16 and 9.17 the separation relationship can be defined as:

$$\begin{aligned} \delta_t &= h_{raceway} + h_{roller} \\ \delta_1 + \delta_2 + h_c &= h_{raceway} + h_c\Delta \end{aligned} \tag{9.18}$$

Subbing in Equation 9.9 gives an expanded form of the relationship:

$$r_1 - \sqrt{r_1^2 - x_i^2} + r_2 - \sqrt{r_2^2 - x_i^2} + h_c = h_{raceway} + h_c\Delta \tag{9.19}$$

This equation can be set to zero and simplified:

$$r_1 - \sqrt{r_1^2 - x_i^2} + r_2 - \sqrt{r_2^2 - x_i^2} - h_{raceway} + h_c(1 - \Delta) = 0 \tag{9.20}$$

A function of the inlet meniscus position can then be written as:

$$f(x_i, \delta_t) = r_1 - \sqrt{r_1^2 - x_i^2} + r_2 - \sqrt{r_2^2 - x_i^2} - h_{raceway} + h_c(1 - \Delta) \tag{9.21}$$

And the differentiation of this as:

$$f'(x_i, h_i) = x_i(r_1^2 - x_i^2)^{-1/2} + x_i(r_2^2 - x_i^2)^{-1/2} \tag{9.22}$$

It is noticed that the differentiated from of this equation is the same as in the simple model, shown in Equation 9.15 as the additional parameters are not governed by x_i or δ. Thus, when the Newton-Raphson method is applied, a very similar x_i value is calculated. However, as with the dry contact analysis presented by Cameron, within the Hertzian contact zone the separation is assumed constant. In this lubricated case, this separation is calculable as the fully-flooded central film thickness, presented by Dowson in Equation 2.5.

This means $0 \leq x \leq b$ the separation $\delta_t = h_c$. Therefore, the x_i position calculated from the separation values will be an additional b distance away from the contact centre. Thus, the inlet meniscus position, calculated from the roller and raceway films, will be equal to the position calculated from applying the Newton-Raphson method added to the Hertzian contact half width.

$$x_i = x_{i_{non-deformed}} + b \tag{9.23}$$

In Equation 2.5 there are three variables dependent on the test. The process of calculating these is already described in Chapter 5 Section 5.6.4.1 and will not be repeated here. With known bearing geometries and measured test parameters these can all be calculated to find the theoretical h_c for each test.

Figure 9.11 shows how the mean s/b ratio across sensors changes with increasing bearing speed and load within the VG320 oil lubricated test case with different VFM parameters included. The data trend in terms of load and speed effects will be discussed in Section 10.1, but of note here is how the VFM model values vary with the same raceway film input value. The blue line is the basic VFM model of a dry, undeformed contact. With the red line, the contact separation and roller film is included, but deformation is still neglected. It is most clear in Figure 9.11(a) that these additional considerations give a slight decrease to the s/b ratio. Although there is the additional roller film consideration providing more oil to the inlet, this is smaller than the contact separation which increases the demand for oil, and thus reduces s/b. When considering the geometry deformation shown with the green line, there is a much larger increase in the s/b ratio. The reason for this is that $0 \leq x \leq b$ the separation $\delta_t = h_c$ which is lower than the undeformed geometry across the same area. Thus, the separation value at a set distance from the contact centre for a deformed contact is lower than that of an undeformed contact, meaning a thinner raceway film can fill it. This increase in s/b ratio, when deformation is considered, increases with load as it proportionally widens the contact.

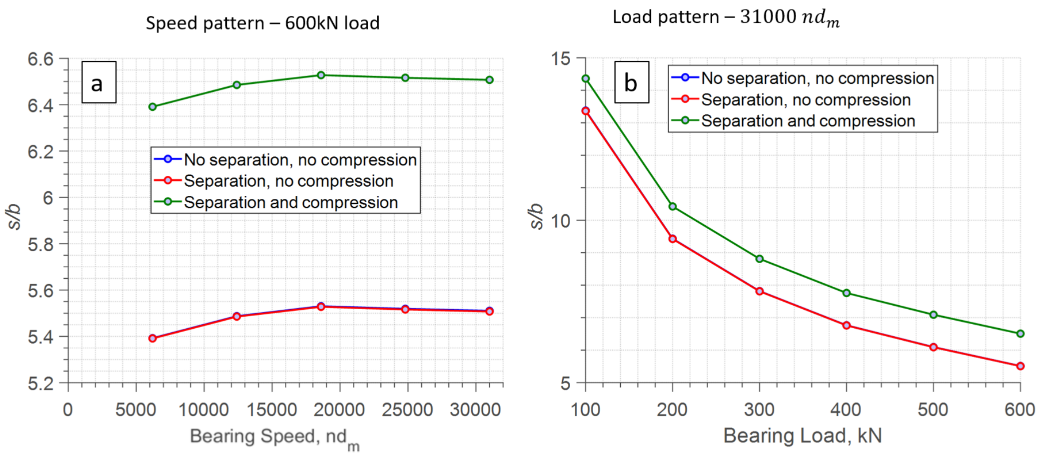

Figure 9.11: Change in s/b ratio with different complexities of the volume fill model. both plots are of the VG320 oil with (a) total bearing load of 600kN with increasing bearing speed (b) bearing speed of $31,000\mathrm{nd_m}$ and increasing load

9.4.4 Volume Fill Model Assumptions

There are two main assumptions to the VFM model, the first being the inlet film shape. The inlet meniscus position is determined by where the product of the raceway and roller films are equal to the cylinder separation. Thus, the shape assumption dictates that where the raceway film and roller film join, there will be a sharp meeting point. In reality, this meeting point would be softened because the surface tension of the two films would naturally find an equilibrium, and form a bubble like shape, much like an oil droplet does on a hard surface. In theory, this would slightly shift the inlet meniscus position away from the contact centre, but to determine by how much would take a complex model to resolve all film forming effects, which is beyond the scope of this thesis.

The second assumption is in regard to the stability of the inlet raceway film. The determination of the inlet meniscus is dependent on the measured raceway film thickness. This thickness value is determined by the mean thickness measured within the detected film area which is assumed to be stable up to the inlet point. However, some raceway film plots show that there is a gradient, where $dh/dx \neq 0$. Theoretically, these gradients could be used to calculate a more precise inlet location for each individual roller pass by analysing the gradient of the detected film and extrapolating the thickness to locations closer to the contact zone. However, this is a very complex operation that would greatly increase computing time. Additionally, as the gradients of the film can vary between roller passes, an average gradient may be close to $dh/dx = 0$ meaning that the stable film assumption would be valid. Ultimately, the time and computer resource investment is not deemed worthwhile in this case, but this could be the subject of future work.

9.5 Conclusion

- Within any rolling bearing there are a large number of rolling contacts per second, the frequency of which only increase with quicker bearing speeds. Therefore, the analysis of the raceway film thickness was automated and applied to all capture windows for a full assessment of lubricant conditions.

- Due to minor variability in rotational speed and unsymmetrical contact reflection pattern, the MRC value cannot be used to discretize the contact pattern. A cross-correlation method was instead developed.

- The amplitude of in-situ raceway resonances is less than those seen in bench top testing. This is likely due to a combination of a varying film thickness over the sensor measurement area, the reference being a live data mode signal and the fact that the observed films are relatively thick which is seen to cause lower amplitude resonances in the KOVOT testing in Chapter 7.

- There is an observed frequency drift form the theoretical resonant frequencies; this is attributed to the measurement of an uneven film across the sensor measurement area. When this occurs it is beneficial to capture multiple harmonics of the resonance and take the average frequency difference to calculate f_0.

- Areas of large scatter are due to a script failure to recognise signal noise. To highlight just the film portion measurable by the resonant technique a threshold approach was taken of the moving variance. A single threshold value could be used for all lubricants as they have comparable acoustic velocities.

- The VFM was developed which inputs a measured raceway film thickness and outputs the distance away form the contact location at which the meniscus occurs, based on a Newton-Raphson numerical approach. The model incorporates both contact deformation and roller film, calculated from the applied load and theoretical contact film thickness respectively.

- The level of contact starvation can be defined by the ratio of inlet meniscus length to contact width. When $s/b = 5$, $h_c = h_{c\infty}$ [41]; when $s/b = 1$, $h_c = 0.7h_{c\infty}$ [113, 2] and so between $1 \leq s/b \leq 5$, $0.7h_{c\infty} \leq h \leq h_{c\infty}$. The VFM allows the calculation of this ratio across the rolling axis for contacts in-situ.

Chapter 10

Measurement of the Lubricant Meniscus Across the Rolling Axis

In this chapter the results from the in-situ measurement of the lubricant meniscus are presented and discussed. Tests were run at different bearing loads and speeds for two different viscosity oils. Grease tests were completed at a single load but multiple speeds to observe lubricant distribution during the churning phase. Test condition effect on lubricant pattern and mechanisms are discussed. Using the previously introduced Volume Fill Model, critical loads and film thicknesses are given as practical guidance for bearing engineers.

10.1 Oil Lubricated Bearing Results

To appreciate how the inlet meniscus position changes, first the change in the raceway film thickness must be appreciated, as this governs the local supply of lubricant. Within the oil area that is highlighted as a stable film leading into the contact region, for each sensor the mean film thickness is calculated per roller pass, to give a single thickness measurement that quantifies and describes the lubricant film for that particular pass. Then for an axial location and test condition, the mean is taken across multiple roller pass mean thicknesses, to quantify the average thickness of film leading into the contact at that particular axial location. This enables the analysis of several phenomenon.

10.1.1 Cross-Axial Inlet Film Shape

Figure 10.1 shows a schematic illustration of how the measured raceway film thickness leading into the contact varies across the axis of a roller. The values shown are the mean raceway thickness, up to around 10mm away from the contact centre as shown by Figures 9.7 and 9.8, which is the limit of the measurement area due to previously mentioned vertical interference fringes, as detailed in Section 5.5. Although the bearing rollers do have crowning, the sensors central positions lie within the middle 66mm of the 82mm long roller, and so deviations from flat at the outer sensors are not considered. Error bars are standard error for the sensor at that axial location. As the capture duration is constant, between sensors there is naturally an equal number of roller passes, but with quicker bearing speeds the number of roller passes recorded is increased, giving a smaller error. The number of roller passes captured, rounded to the closest 10, is 30, 60, 90, 110 and 140 for 20, 40, 60, 80 and 100rpm respectively. Above the plot is a schematic to help visualise the film shape. For this test case, both the VG320 and VG32 oils show thicker bands of oil towards the roller end faces, and a thinner film in the central region.

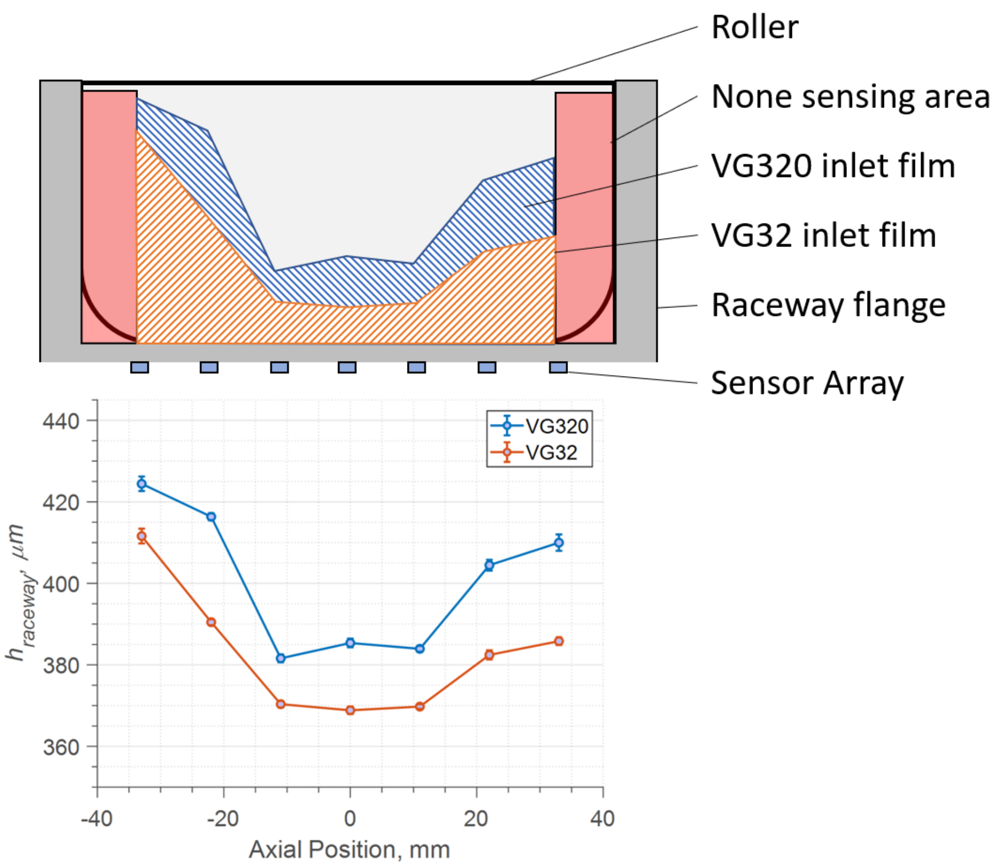

Figure 10.1: Mean raceway thickness leading into the contact inlet at different axial locations when the bearing was lubricated with VG320 and VG32 oils

Figure 10.2 shows how the raceway film thickness changes across the roller axis for the VG320 and VG32 oil when operated under 100kN of load and increasing bearing speed from $6,200\mathrm{nd_m}$ to $31,000\mathrm{nd_m}$ (20rpm to 100rpm). Plotted error bars are standard error over for each mean thickness measurement over the 10s capture duration.

Under this load, both oils show a ‘U’ shaped pattern, where there are thicker oil bands towards the roller end faces, and a depletion towards the axial centre. However, at the lowest speed, the minimum seems to be shifted towards the left side of the centre. As bearing speed increases, this minimum point shifts through the centre, then towards the right side of the roller. The pattern is present for both oils, suggesting the observed effect is not governed by viscosity, and instead some kind of centrifugal force of the bearing. Figure 6.4 shows that for both oils tested, there was a skew change in a negative, counter-clockwise direction with an increase in speed. It could be then that the mean skewing angle and point of minimum film thickness are correlated, but cause and symptom are not clear. Either the minimum thickness location partially governs the skew angle, and by increasing speed the minimum location and skew angle are altered; or a skew angle change, which is known to alter the lubrication state of rollers from the work of Liu et al. [140, 141] then determines the location of the minimum film. Alternatively, some other kinematic mechanism could govern both the skew angle and axial location of the minimum film. Further research is needed to investigate.

The presence of oil bands and a depleted centre within the contact area have been observed both experimentally and theoretically for starved contacts [6, 8, 11]. Figure 10.2 shows that at a relatively low load oil bands can be observed in-situ, at the contact inlet region. Later in this chapter, in Section 10.3.1, the critical raceway films required to achieve $s/b \geq 5$ are derived. At 100kN load this film is 36μm; the inlet films in Figure 10.2 are clearly thicker than this at all recorded axial positions, and so starvation was not present within these contacts. This then suggests that contact side bands can form before the onset of starvation, for a fully flooded contact, but once starvation occurs, the axial distribution is governed primarily by the localised lubricant flow. The fact that there is an observable thicker film at the roller edges with a fully flooded contact also suggests that the roller will be churning lubricant, but again with a distribution across the roller axis, with the least churn occurring at the contact centre.

It is also clear that for every axial location and speed, the more viscous VG320 oil developed a thicker film on the raceway, and that the thickness increase is reasonably consistent across the rolling axis. The oils were subjected to the same kinematic forces, such as the centrifugal force applied from the bearing rotation and the shearing

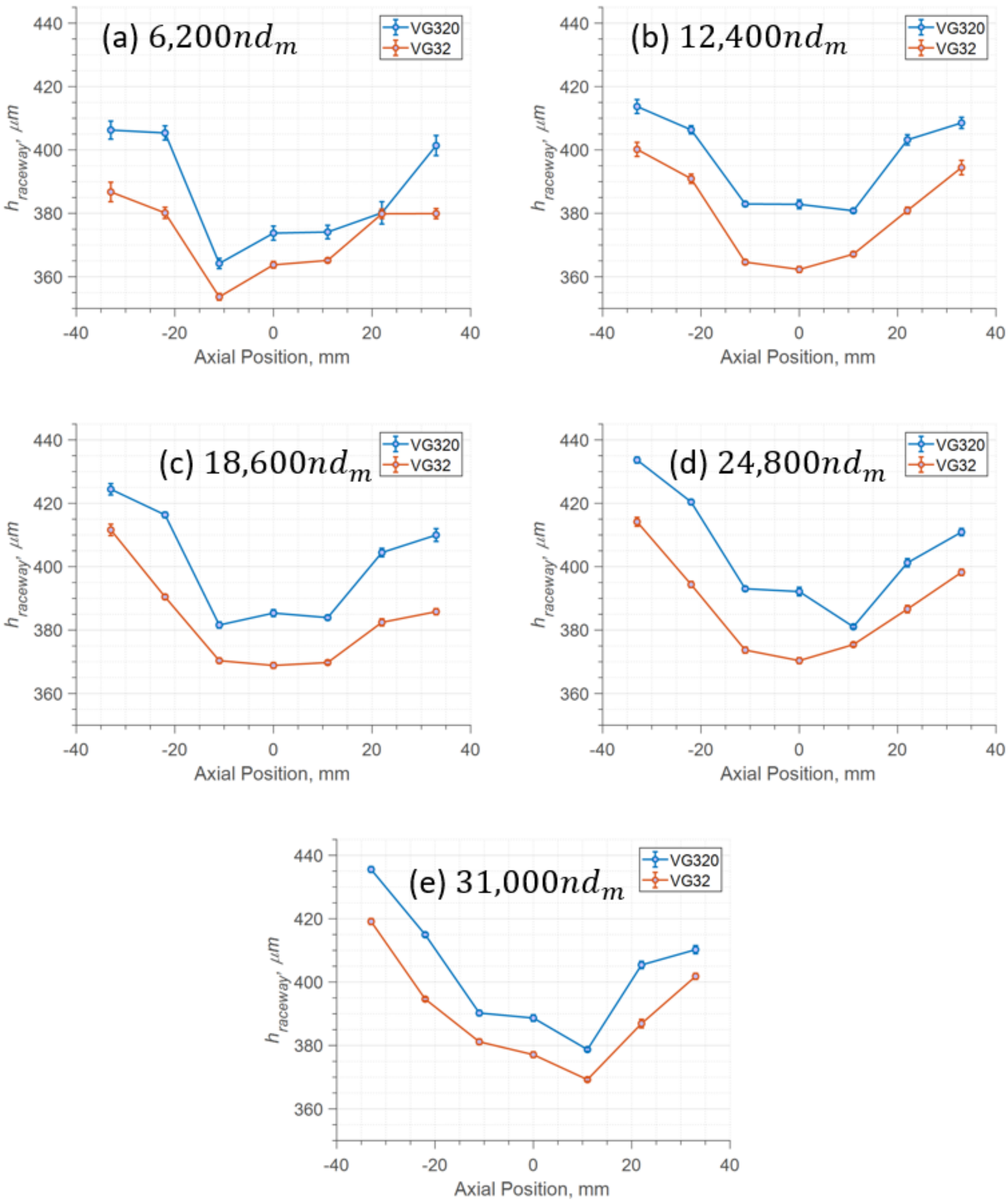

Figure 10.2: Mean raceway thickness leading into the contact inlet at different axial locations when the bearing was lubricated with VG320 and VG32 oils. The test conditions were 100kN load, operated at bearing speed of $6,200\mathrm{nd_m}$, $12,400\mathrm{nd_m}$, $18,600\mathrm{nd_m}$, $24,800\mathrm{nd_m}$ and $31,000\mathrm{nd_m}$ respectively from a to e

force applied at the roller face-flange contact. The mean temperature was calculated from readings from the inner-raceway mounted thermocouple over the test capture, a duration of 10s. There is a maximum deviation of just $0.4°C$ between the tests using the two different oils at the same test conditions. This then suggests the thicker inlet film developed by the VG320 oil is a direct result of its increased viscosity; most likely it has a stronger capillary effect and is therefore able to form thicker films easier.

Figure 10.3 shows how the cross-axial film changes under a constant speed of $31,000\mathrm{nd_m}$ but with increasing load. The pattern change is more chaotic than with the increasing speed plot, but for loads of 100kN to 400kN the 'U' shape film pattern is maintained. When operated at 500kN however, this pattern becomes blurred, and the cross-axial thickness tends towards a somewhat linear decrease from left to right.

Figure 10.4 shows the same increasing load patterns, but for the bearing operating at $6,200nd_m$. Here there is a much weaker film thickness pattern with both oils, and the increase in thickness with oil viscosity pattern that is so clear in Figures 10.2 and 10.3 is lost. Although reflow is enhanced with less viscous oils, inlet film growth with increasing speed suggests there was adequet supply with the VG320 and so it could develop a thicker film than the VG32 due to its increased viscosity. However, at lower bearing speeds the entrainment seems to be reduced to the point that there is minimal enhancement from the increased viscosity.

With increasing load the 'U' film shape is lost and Figure 10.4 shows the distribution tends towards a linear decrease from left to right, as it did for the $31,000\mathrm{nd_m}$, 500kN case in Figure 10.3. With an increased load from 100kN to 500kN there is a temperature increase of just $4°C$ and $4.2°C$ for the VG320 oil at 20rpm and 100rpm respectively. For the VG32 oil the change is $4°C$ and $3.8°C$. The viscosity decrease from this temperature raise is far less dramatic than the inherent viscosity difference from comparing the VG320 and VG32 oils, meaning the more chaotic pattern is not a result of lubricant property changes.

In Figure 6.4 of Chapter 6 it was shown that as the radial load increases, there is an observed trend for the skewing angle to shift towards a more negative orientation, but closer to the 0deg position. However, the skew angle was measured as positive for all cases other than VG32 running at $31,000\mathrm{nd_m}$ under loads of 400kN and upwards. This means, the roller with the largest measured skew angle, which occurs under the lighter loads, has the most symmetrical oil distribution pattern according to Figures 10.2, 10.4 and 10.3. This is counter-intuitive as a larger skew angle would be expected to give a great non-uniformity to the lubricant flow around the roller. However, as discussed in Chapter 6, minor misalignment should be expected in the

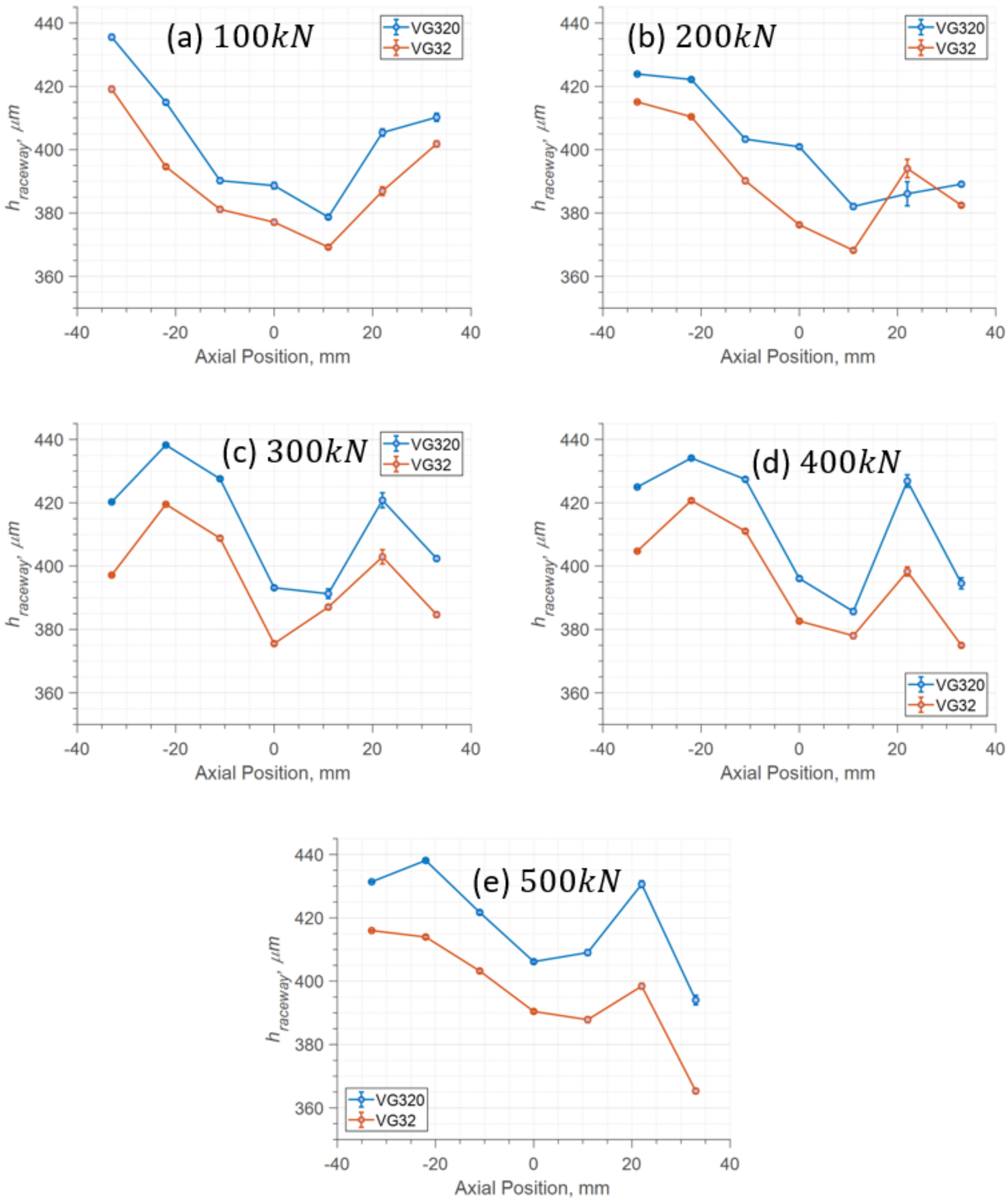

Figure 10.3: Mean raceway thickness leading into the contact inlet at different axial locations when the bearing was lubricated with VG320 and VG32 oils. The test conditions were $31,000\mathrm{nd_m}$ bearing speed, operated at applied loads of $100\mathrm{kN}, 200\mathrm{kN}, 300\mathrm{kN}, 400\mathrm{kN}$ and $500\mathrm{kN}$ respectively from a to e

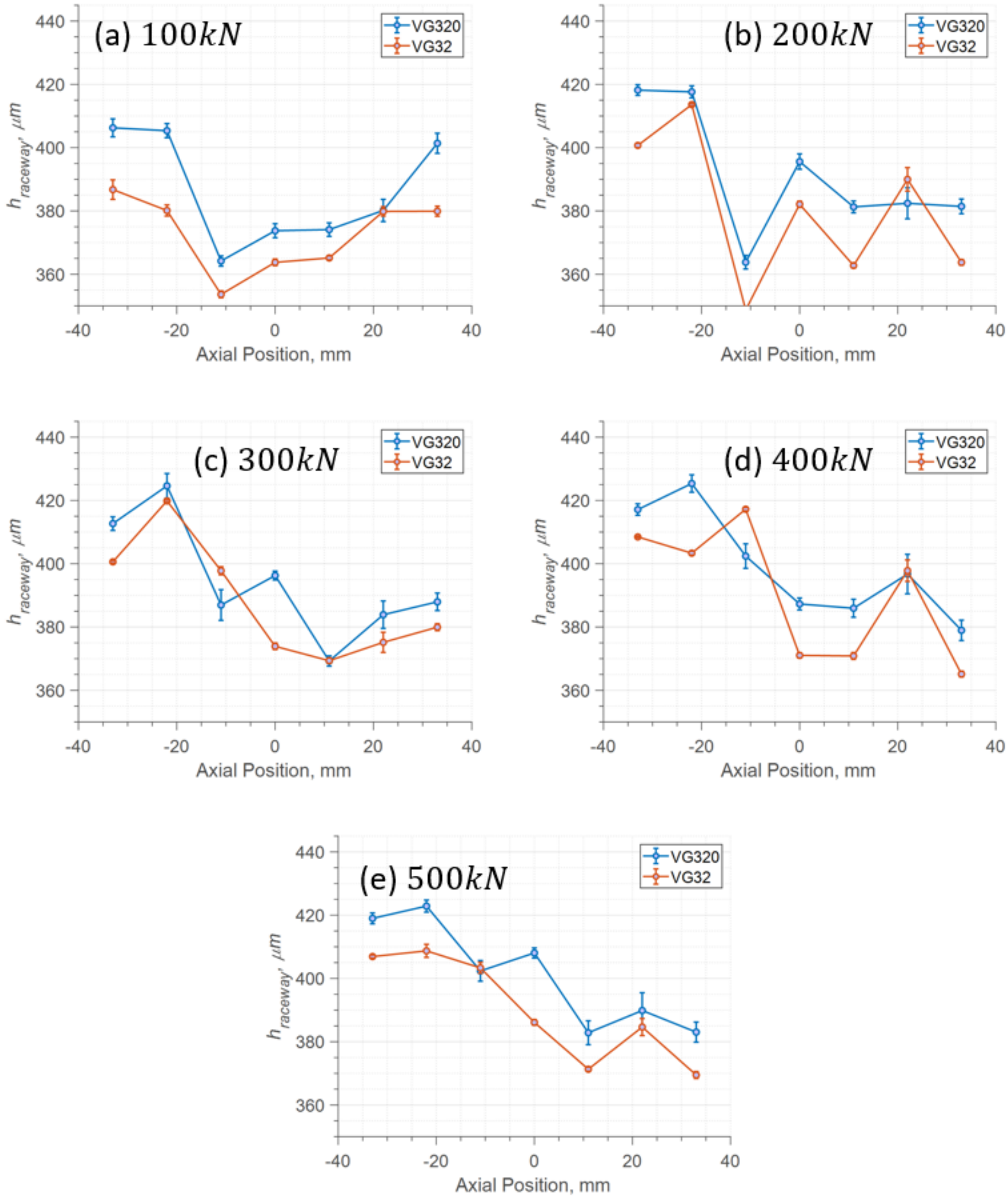

Figure 10.4: Mean raceway thickness leading into the contact inlet at different axial locations when the bearing was lubricated with VG320 and VG32 oils. The test conditions were $6,200\mathrm{nd_m}$ bearing speed, operated at applied loads of 100kN, 200kN, 300kN, 400kN and 500kN respectively from a to e

sensor instrumentation, meaning only skew angle changes should be appreciated, rather than the absolute measured skew angle. Therefore, it can be concluded that there is a relationship between skewing angle and the axial distribution of oil at the contact inlet. However, from this work alone, the nature of the relationship cannot be determined.

An alternative cause for the loss of 'U' shape may be the inlet film being closer to the critical raceway film thickness, which Section 10.3.1 shows is 180μm at 500kN to achieve $s/b \geq 5$. The results of Figures 10.3 and 10.4 suggest that the rolling contacts were fully flooded, but the inlet films were closer to the minimum need to achieve this fully flooded condition. Potentially, this approach to a starved condition upset the classical 'U' shape that is seen in other works, albeit for a ball not roller, and that is seen in Figure 10.2.

10.1.2 Localised Film Deviations

In the previous Section 10.1.1 it was shown that raceway thickness and thus the meniscus position varies depending on the axial location. Thus, there is potential for a contact to be both fully flooded and starved at the same time. Consequentially, the minimum mean single roller pass film thickness recorded for each sensor within one particular test was investigated. These minimum values, and the load and bearing speeds at which they occurred, are shown in Tables 10.1 and 10.2 for the VG320 and VG32 oils respectively. Looking at both tables, there is no clear load or speed at which the minimum value occurred, which gives an insight into the somewhat chaotic nature of the oil flow along the raceway during operation. Comparing the two tables, the minimum films recorded with the VG32 oil are <u>thicker</u> than the minimum films when lubricated with the VG320 oil, despite the VG32 oil having an overall thinner average film. This suggests that more viscous oils tend to develop thicker films on average, but films that are potentially less stable and therefore more prone to isolated starved roller passes within an otherwise well lubricated operation. This somewhat agrees with the findings of Cen & Lugt [123] who found that greased bearings with a higher base oil viscosity are more prone to starvation due to impaired lubricant flow.

	VG320 - Sensor Axial Position, mm						
	-33	-22	-11	0	11	22	33
Min. Thickness, μm	371	352	302	286	272	268	260
Load, kN	400	600	600	400	300	200	600
Bearing Speed, n_{dm}	31,000	31,000	6,200	18,600	18,600	6,200	6,200

Table 10.1: Minimum mean single roller pass raceway thickness values and test conditions at which they were recorded for the VG320 lubricated case

	VG32 - Sensor Axial Position, mm						
	-33	-22	-11	0	11	22	33
Min. Thickness, μm	357	361	337	348	346	311	339
Load, kN	100	100	200	100	200	300	500
Bearing Speed, n_{dm}	6,200	6,200	6,200	6,200	31,000	18,600	31,000

Table 10.2: Minimum mean single roller pass raceway thickness values and test conditions at which they were recorded for the VG32 lubricated case

10.1.3 Mean Frontal Shape Change

To understand the more general relationship between bearing load, speed and raceway film thickness, the mean film thickness was calculated across sensors for an average frontal raceway thickness for a single test condition. Figure 10.5 shows how this mean frontal raceway thickness varies with an increasing bearing speed under different loading conditions for both oils tested. Figure 10.5a shows that at each load tested, increasing the bearing speed leads to an increase in the VG32 mean raceway film thickness. This is expected as the oil has flow properties that enable it to move around rollers and reach the next contact inlet, and with the increased speed the entrainment velocity into the contact is increased, creating a pressure differential that draws oil towards the contact inlet, and thus forms a thicker film.

However, in Figure 10.5b with the more viscous VG320 there is a general raceway film increase up to $18,600\mathrm{nd_m}$ but above this the trend plateaus and decreases. The more viscous oil has impaired reflow properties, and so after a certain bearing speed, further increases mean less oil can flow around the roller to join the inlet of the next contact. However, as this is the raceway film, the decrease does not mean the contact is starved, simply that the lubrication feed is reducing. It is possible for this feed to reduce and the contact to still have ample lubrication for fully flooded conditions.

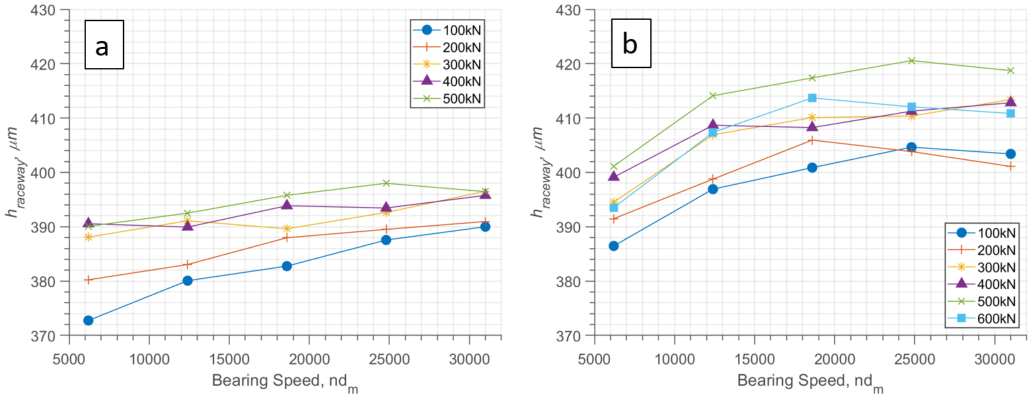

Figure 10.5: Change in frontal inner raceway film thickness with increasing speed under different loads for (a) VG32 (b) VG320

Figure 10.6 shows the same results, but instead with an emphasis on how increasing load affects the mean raceway thickness. Increased bearing load also seems to enable a thicker raceway film to form at the contact inlet up to 500kN. Figure 10.6b shows that with VG320 oil which was able to run at 600kN there was a decrease, the magnitude of which varied with speed.

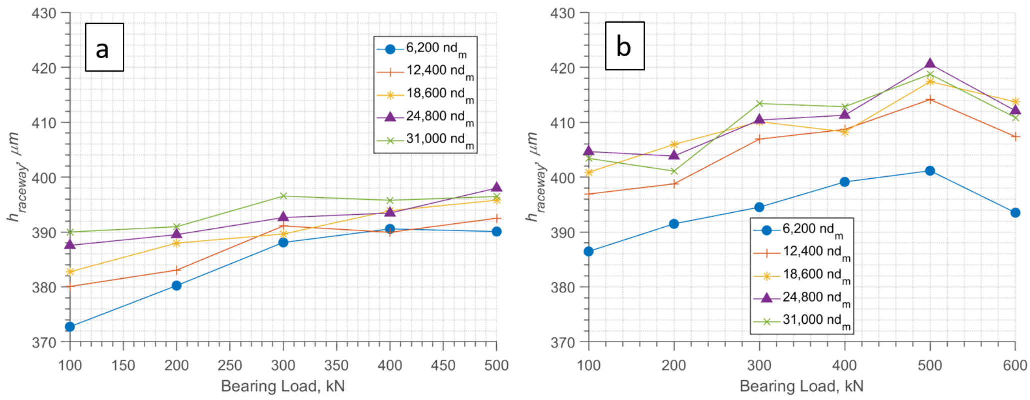

Figure 10.6: Change in frontal inner raceway film thickness with increasing load under different speeds for (a) VG32 (b) VG320

In Figure 8.8 of Chapter 8, where spectral plots of the scouting bearing were used to qualitatively infer load and speed effects on raceway film formation, it was noted that higher loads seemed to additionally lengthen the film leading into the inlet location. This result is unexpected as the measured film is not within the contact, and thus is not pressurised. Theoretically then, there is no direct mechanism in which load could cause this effect. The three alternative mechanisms by which load could alter this film thickness:

Temperature Increase With higher load there is naturally a raise in temperature due to internal bearing friction. This causes a lubricant viscosity decrease, which has already been shown to reduce film thickness, and so is not the cause of film thickening with load.

Contact Size and Separation As load increases, so too will the contact size. This would mean a larger volume of oil is entrained, resulting in less available on the raceway. However, Equation 2.5 shows that contact separation decreases with an increased load, which would cause more oil available on the raceway. Considering these two effects opposing each other, and the very small volume of oil that is in the EHL contact, it can be said with confidence that this is not the cause of film thickening with load.

Increased Skew Magnitude Harris et al. [137, 20, 24] discussed how geometry imperfections, along with an increased bearing loading can cause a skewing motion of rollers, which in turn truncates the roller face-flange contact. This could potentially scrape more oil away from the flange and onto the running track, and Chapter 6 of this thesis clearly demonstrates that skew occurs in this particular test bearing when lubricated with oils, with a magnitude governed partially by load. Nicholas et al. [133] concluded there is a relationship between bearing load and lubrication reflow time, and thus mean raceway thickness. They saw impaired lubricant performance with increasing load, which they attribute to shear off of the raceway surface. In this work it appears as though the load/skew mechanism is linked with increased lubricant on the raceway surface, and that some internal scrape effect is the most likely explanation for film thickening with an increased bearing load.

Figure 10.7 plots the Figure 10.5 and Figure 10.6 results as a bar chart, allowing for the variation in raceway thickness with speed and load to be appreciated. For each load group there is again a clear monotonic increasing pattern in film thickness for VG32 and an increase then decrease for VG320. Generally there is an increase for a single speed across loading groups. The error bars shown on the plot are the standard errors, calculated between the mean sensor values at different axial locations. As only seven sensors are present, the sample size is relatively limited, and in many cases there is error bar overlap between test results. This means that although there is an observable trend of increasing raceway thickness with bearing speed and load, the statistical $P > 0.05$ and the result cannot be deemed statistically significant.

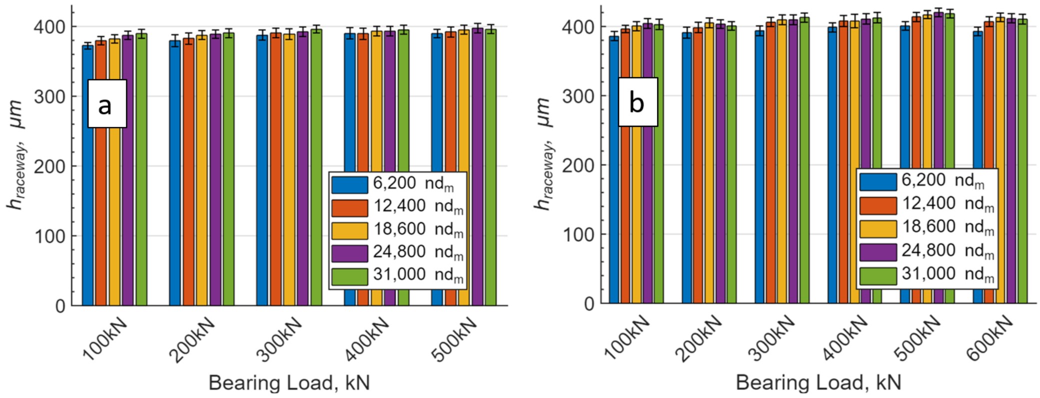

Figure 10.7: Comparison of frontal inner raceway film thickness for various load a speed cases for (a) VG32 (b) VG320

This P value could theoretically be improved upon, but would require more in-situ sensors, for which there was not space or sensing capabilities for within these tests.

10.1.4 Starvation Ratio

The raceway film thickness fed into the VFM gives the theoretical inlet meniscus position. The distance to the inlet meniscus position from the contact centre is defined as s, which is then non-dimensionalised by dividing by the calculated Hertzian contact half-width in the rolling direction b to calculate a starvation ratio and make results comparable. The calculation of the Hertzian half-width is dependent on the known material properties of the bearing and the applied load. When calculating s/b it is assumed that the Hertzian half-width is the same at each sensor location, and was calculated from the set total load applied. Figure 10.8 shows the width increase in the rolling direction from unloaded to 600kN total load applied, calculated using Equation 2.4.

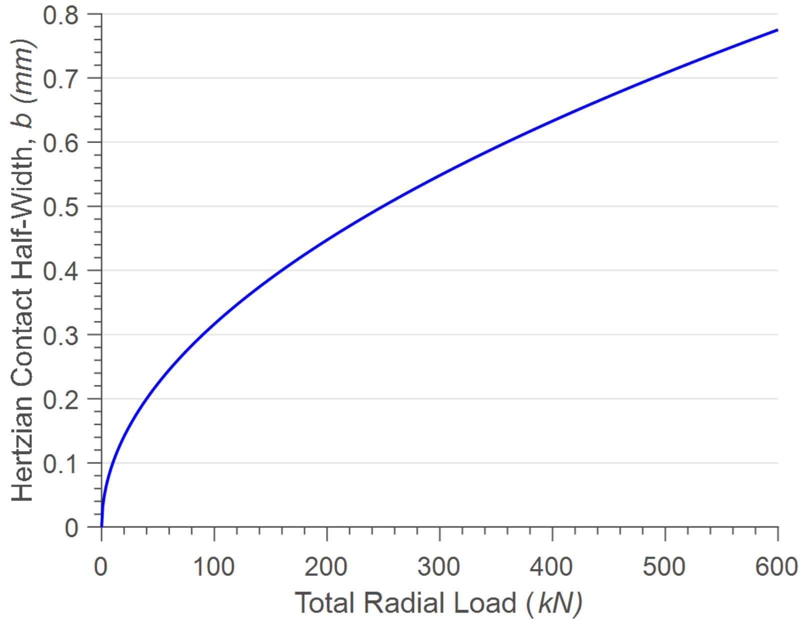

Figure 10.8: Theoretical Hertzian contact half-width with increasing load, calculated using Equation 2.4

There are several phenomenon and mechanisms that can be investigated using the VFM. The first is the s/b ratio with an increasing bearing speed. Figure 10.9 plots the s/b ratio as the bearing speed increases for the VG320 lubricated bearing under 600kN total load. Because the load is constant, the contact size is also constant, but Figure 10.5 shows an increasing raceway film thickness up to $18,600\mathrm{nd_m}$. Therefore, as the rotation of the bearing increases up to this speed, the raceway film thickens, as too does the less impactful roller film as the central contact separation is increased, and thus more of the inlet area is filled. This results in a larger s value as the meniscus position is further away from the contact centre. The accompanying schematic shows that the increase in raceway thickness shifts the inlet meniscus position further from the contact centre.

However, at the top two speeds there is a decrease in the s/b starvation ratio. Although $s/b \geq 5$ at these two speeds, meaning central contact separation will still increase as per the Dowson equations, the raceway film, which is the starvation governing factor, decreases. Therefore the meniscus forms closer to the contact centre, as shown by the schematic. It is important to note again that this decrease is still above the theoretical limit of $s/b \geq 5$ and so the decrease is not contact starvation; likely there was contact film growth at these two increased speeds as there was still adequet lubricant supply. However, it does show that the raceway film is decreasing, likely due to impaired oil reflow at the higher speeds. This decreasing trend likely presents itself pre-starvation, and acts as a precursor to contact starvation at even higher bearing speeds. Figure 4.14b adapted from Chennaoui et al. [12] shows that in a deep groove ball bearing, the onset of starvation was detected at the comparable value of $s/b = 7.1$.

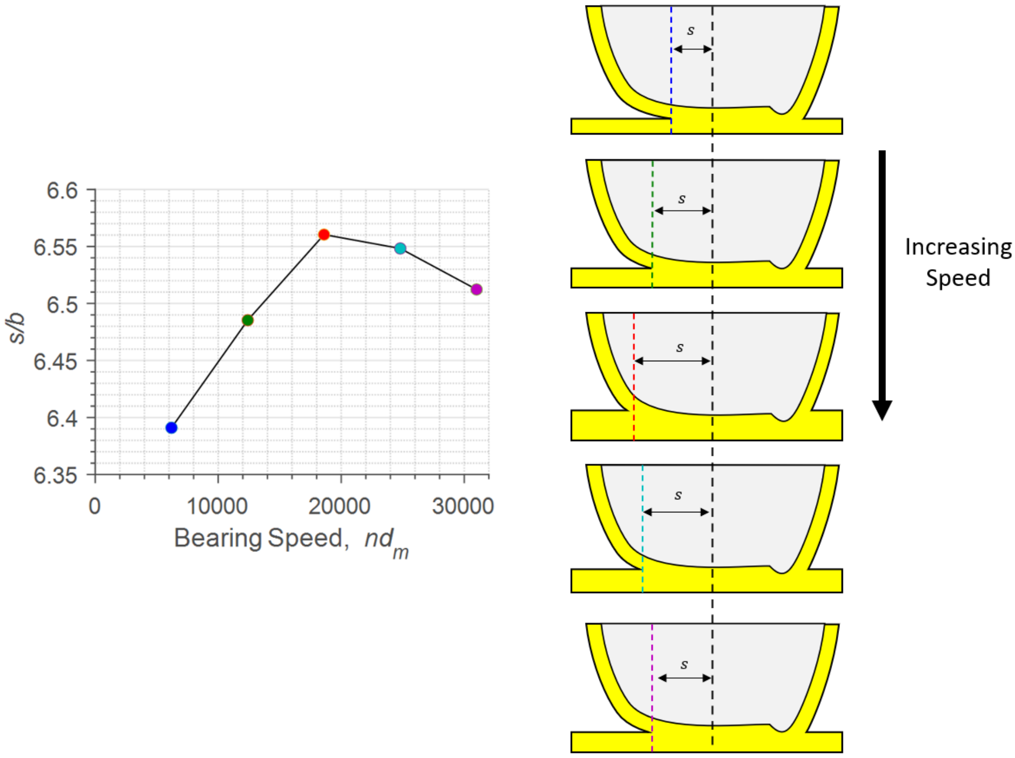

Figure 10.9: Change in inlet meniscus position with an increased bearing speed under 600kN total load, lubricated with VG320 oil

Figure 10.10 shows the variance in s/b ratio for all loads tested, for both (a) the VG32 oil (b) the VG320 oil. All results do show a slight increase in s/b with bearing speed, and then a decrease beyond $18,600\mathrm{nd_m}$ with VG320, but the pattern is subdued when compared with the pure raceway thickness values seen in Figure 10.5. This is because the separation of the roller and raceway increases non-linearly away from the contact centre; thicker raceway films have a minimum influence upon the position of the inlet meniscus once $s > 5b$ is achieved.

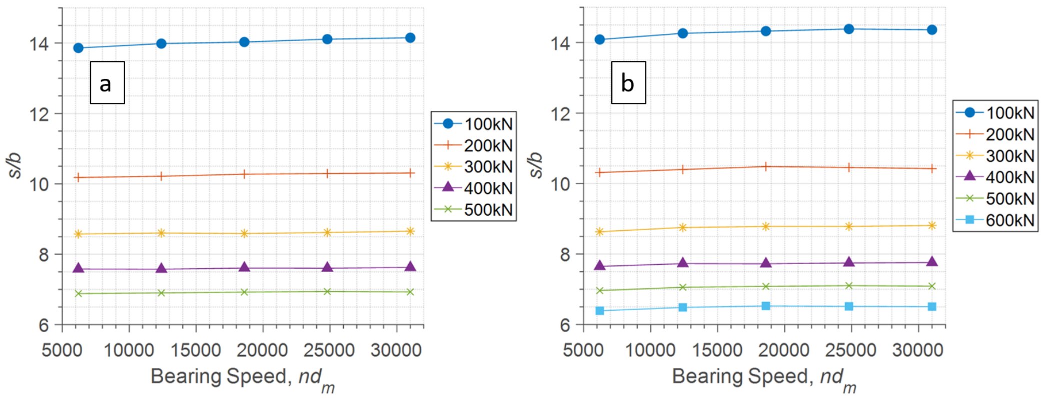

Figure 10.10: Change in s/b ratio with increasing bearing speed for (a) VG32 (b) VG320

What is stark is the clear separation between different loads. To investigate this pattern further, the same data was plotted against a load axis in Figure 10.11. Both oils show a large decrease in the s/b ratio as bearing load is increased, from ≈ 14 to ≈ 6.5 from 100kN to 600kN for the VG320, suggesting load has a greater role in governing the level of contact starvation than bearing speed does. The relationship between increased load and starvation was previously made by Cann et al. [109] where a model showed a decreased contact film thickness with increasing load, and a larger decrease than is predicted from using the fully flooded assumption with the Dowson equations. The authors attributed this reduced contact film thickness to increased starvation due to an increase in the contact radius and track width. Cen & Lugt [123] studied starvation and replenishment in greased bearings and observed higher starvation rates with increased load, which they attributed to the increased contact size meaning that more time is required for replenishment to the contact centre. The caveat to that conclusion is grease has different flow properties to oil.

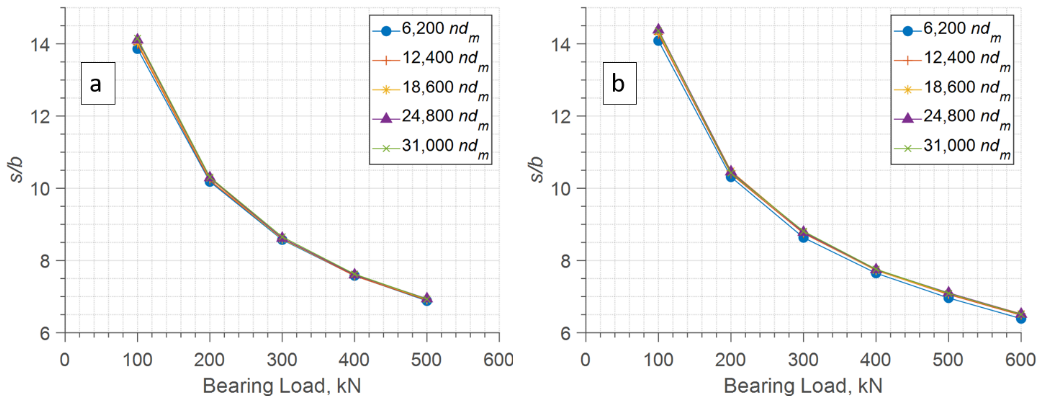

Figure 10.11: Change in s/b ratio with increasing bearing load for (a) VG32 (b) VG320

Figure 10.6 shows that heavier loaded bearings have thicker films form on the raceway leading towards the contact inlet, which will shift the meniscus position further from the contact centre. However, as with the increasing bearing speed case, this film thickening has minimal influence on volume fill at distances $> 5b$ away from the contact centre. However, a far more dominating effect is the increase in contact size with load.

Individual roller load is related to the total radial load through Equation 5.1. The load per unit width is calculated through Equation 2.3. By modelling the roller-raceway contact as twin cylinders, with the roller load as the applied load, the relationship between roller load per unit width and Hertzian contact half-width is described by Equation 2.4. Subbing Equation 5.1 into Equation 2.3 and in turn Equation 2.4 gives the relationship between the Hertzian half-width and total radial load W:

$$b = \sqrt{\frac{20W \cdot l \cdot R'}{\pi E^* z}} \tag{10.1}$$

Thus, it is shown that $b = \mathrm{f}(W^{1/2})$. Although this may not appear to be a dominating effect, the required inlet position to achieve fully flooded conditions is five times the b value. If the raceway film thickness is similar from low loads to high loads, which Figure 10.7 shows to be true, the higher load case with the larger contact half-width will have a much lower s/b ratio. This is because of an increase in b rather than a decrease in s.

10.1.4.1 Singular Starved Contact

Tables 10.3 and 10.4 show the mean s/b ratio for the VG32 and VG320 oil respectively, calculated using the mean frontal raceway film. The s/b trend at a given load with

	6,200nd_m	12,400nd_m	18,600nd_m	24,800nd_m	31,000nd_m
100kN	13.861	13.984	14.030	14.110	14.151
200kN	10.182	10.216	10.275	10.293	10.310
300kN	8.575	8.604	8.589	8.618	8.656
400kN	7.580	7.575	7.608	7.605	7.624
500kN	6.883	6.901	6.925	6.941	6.930

Table 10.3: The s/b ratio, calculated from the mean frontal raceway film thickness for the VG32 lubricated bearing

	6,200nd_m	12,400nd_m	18,600nd_m	24,800nd_m	31,000nd_m
100kN	14.088	14.263	14.325	14.386	14.363
200kN	10.313	10.399	10.482	10.457	10.423
300kN	8.634	8.753	8.782	8.784	8.811
400kN	7.649	7.728	7.723	7.748	7.760
500kN	6.963	7.059	7.082	7.104	7.091
600kN	6.391	6.485	6.528	6.516	6.507

Table 10.4: The s/b ratio, calculated from the mean frontal raceway film thickness for the VG320 lubricated bearing

increasing speed mirrors the raceway thickness trend. With increasing load, there is again a large decrease s/b due to contact widening.

However, these are the mean s/b values for capture windows. There of course exists a natural fluctuation between rollers. The minimum s/b ratio observed was 6.4862 for the VG32 oil at 500kN and 5.3887 for the VG320 oil at 600kN, which according to Dowson's empirical starvation criteria [41] means there were no isolated starved incidents observed. However, for some roller passes such as the one shown in Figure 10.12, the moving variance criteria could not be met due to the scatter of data points meaning that no stable measurable film, according to the script, was detected.

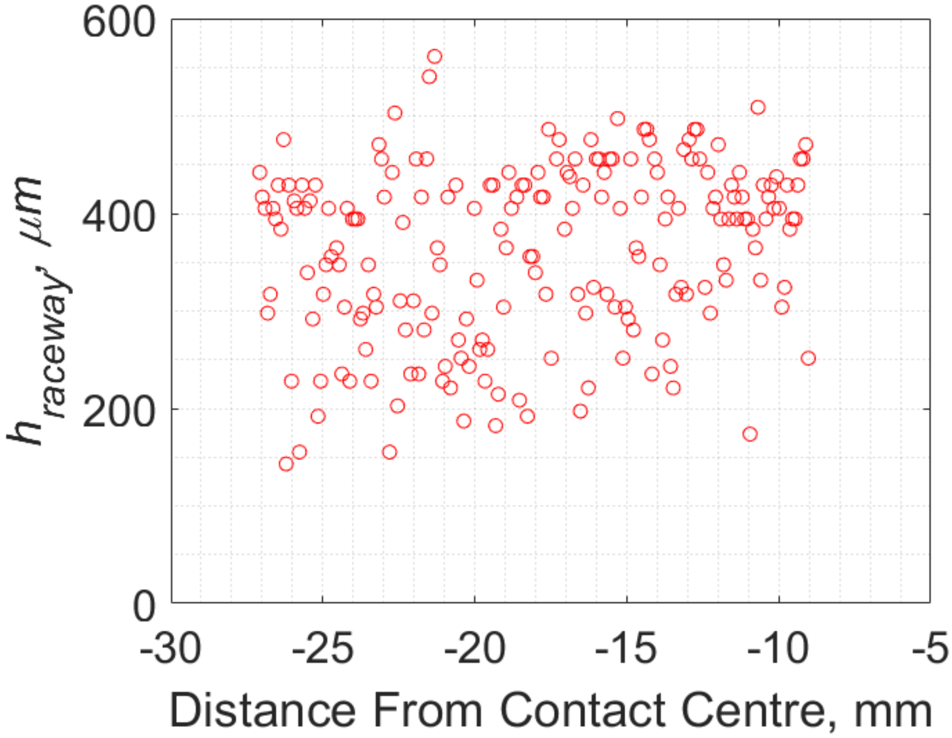

Figure 10.12: A raceway film thickness pattern at the inlet of a roller pass where the moving variance threshold was not met, and so a NaN film thickness is detected

The explanation for a non-detection is however unclear. Primarily, it could be due to a genuine lack of oil on the raceway, or a film below the detection threshold, for that particular roller pass, which would cause localised starvation at that axial position. Alternatively, lubricants within bearings operate in very dynamic conditions, and so equally the lack of detection could be due to a very unstable, but relatively thick film, which could still lubricate a bearing but is much more difficult to detect. Because of this, these films which are measured as having a NaN raceway thickness are excluded from the mean frontal film calculations and minimum film detection analysis. Further work would be needed to infer if these contacts were truly starved.

10.1.4.2 Bearing Stalling

Tables 10.3 and 10.4 show that for all test conditions the bearing is considered adequately lubricated when using the empirical starvation criteria as $s/b > 5$. Interestingly, when operating the bearing lubricated with less viscous VG32, the bearing stalled at $6,200nd_m$, 600kN, meaning there was inadequate contact separation and the contact frictional force was greater than the motor torque. The bearing could be operated under the same load at an increased speed of $12,400nd_m$. When looking at the oil trends of Figure 10.5 the results show that lower speeds have thinner raceway films and therefore form menisci closer to the contact inlet. Despite this, the relationship between raceway film thickness and bearing speed suggests slowing from $12,400\mathrm{nd_m}$ to $6,200\mathrm{nd_m}$ would still form a raceway film $h_{raceway} \approx 390\mu$m. In turn, this would still achieve a $s/b \geq 5$. Likewise, when observing minimum raceway films in Section 10.1.4.1 that shows the somewhat chaotic nature of single roller passes, no roller pass was detected as starved. It is worth noting that at 600kN the extrapolated s/b ratio would be < 6.883 which in turn is lower than $s/b = 7.1$, the ratio calculated from Chennaoui et al. [12] at which starvation onset was observed. From this then, it can be concluded that the raceway had ample oil to form a lubricating meniscus, even if the contact was in pre-starvation. This stall then suggests it is not sufficient to simply swamp the inlet with lubricant. The lubricant must be adequately entrained into the contact, and of an appropriate viscosity to cause ample separation, as was the case with the VG320 oil which did not stall at the most extreme test condition.

10.1.5 Discussion

It had already been established from literature that oil films could be measured via ultrasonic resonances, see Section 4.5.1 of Chapter 4. These results have shown that this method can be applied to raceway films, and from these measurements the lubrication state of the bearing inferred. The measurements give an insight into the localised lubricant supply across a rolling axis. Clearly, even under steady state conditions the film leading into the contact is not symmetrical, and generally the centre region has a reduced oil supply, causing a 'U' shaped distribution with thicker oil reservoir bands towards the roller faces. Comparison with other in-situ bearing measurements are difficult due to a lack of comparative work. However, Chen et al. [11], who studied oil films of a ball bearing using a glass and resin bearing, also note the 'U' pattern towards the contact inlet.

The measured film distribution shape is affected by load, speed and viscosity. The viscosity relationship is complicated; the lower viscosity oil has a thinner mean film thickness across the entire raceway, but more stable inlet films than the higher viscosity oil. Quicker bearing speeds increase the contact film thickness, as shown via Equation 2.5, and as there is a constant lubricant supply during the test with the VG32 oil it is intuitive that there is a comparable affect at the raceway inlet. However, the more viscous VG320 oil saw a decrease in raceway thickness at quicker bearing speeds, likely due to impaired oil reflow.

Increasing load is seen to interrupt the 'U' shaped pattern of the film, thinning the film on one side of the roller and thickening it on the other to make an almost linear distribution, but overall Figure 10.6 shows there is a mean increase across the frontal film. Classically it is thought load has a minimum impact on film thickness as the load parameter in Equation 2.5 has an exponent of -0.1. However, these results show as load increases the s/b ratio drastically decreases due to an enlargement of the contact area. Consequently, fully flooded conditions are much harder to achieve under heavy loads.

The starvation ratio across the roller axis was larger than $5b$, the minimum ratio Dowson [41] shows is needed for fully flooded lubrication, for all test conditions. However, when loaded at 500kN and 600kN, $s/b < 7.1$, the value calculated from Chennaoui et al. [12] which shows the onset of starvation. Despite this, a bearing stall occurred under 600kN with the VG32 oil, even with an expected raceway film that would meet the $s/b \geq 5$ criteria. This then suggests that an ample oil supply is simply a pre-requisite for adequate separation, but oil choice is still of paramount importance. In other words, all separated contacts have a healthy lubricant supply, but not all contacts with a healthy lubricant supply are well separated.

10.2 Grease Lubricated Bearing Results

Much like the oil tests, the mean distribution across the rolling axis for a grease lubricated bearing can be assessed over a single capture window, which for the grease tests was 5s. Figure 10.13 shows such a plot, for the early stages of grease churn where the contact is fully flooded. Much like the oil plots, there is no constant film thickness, and instead the centre appears more depleted. However, single plots like this cannot fully describe raceway thickness within the greased bearing as grease lubrication has the added complexity of time-dependence during the churning phase, which is not the case with oil lubrication. Figure 10.13 shows a transverse distribution after the churn-temperature criteria was met; clearly there has been a distribution change, with a general film thinning. Therefore, the most logical way to assess the data is with the incorporation of that time dependence.

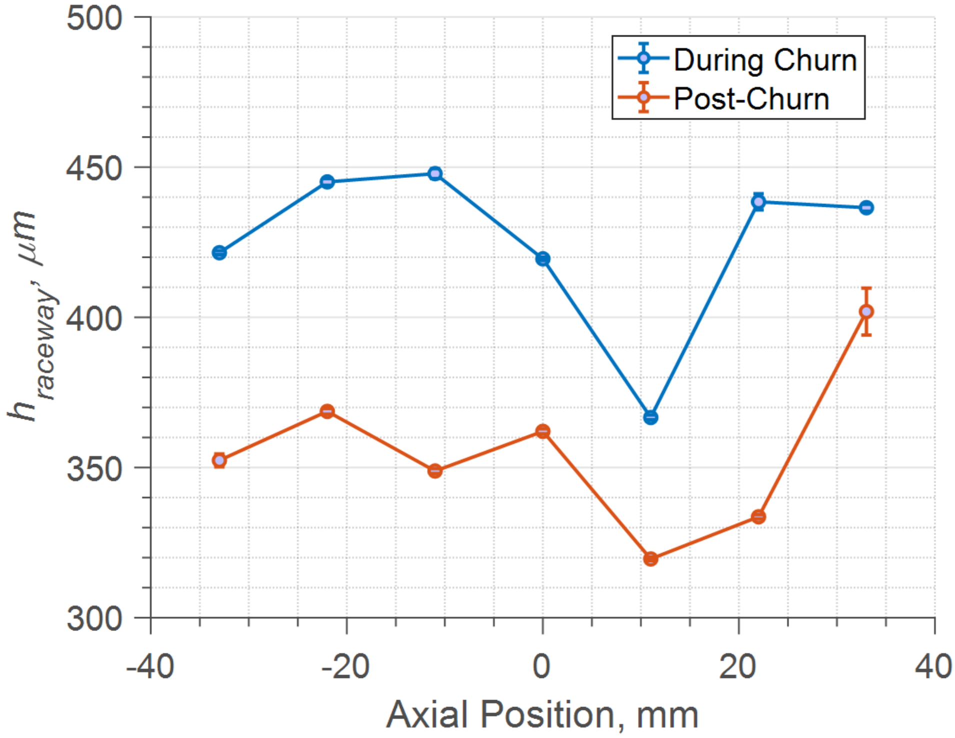

Figure 10.13: Comparison of the inlet distribution across the rolling axis during and post-churn

To assess how this distribution changes during the churning phase, mean distributions for each capture window are stacked together to form a 3-dimensional matrix with axes of time, raceway axial position and raceway inlet film thickness. Figure 10.14 shows a 3-dimensional map of the inlet film across the raceway inlet location over a number of hours. The lighter yellow colour indicates a thick film, and the deeper blue a thinner film. The plot has been overlaid onto a raceway schematic to indicate where the film occurs, but the distinction is made that this is not from a single roller pass, but many hundreds of passes over the duration of the test. The figure shows that as the grease churns there is an overall decrease in film thickness right across the rolling axis. However, at the beginning of the test the film is thicker towards the roller faces, and so the film reduction is more dramatic in this region. Although observing the plot in this 3D format is beneficial to observe film change in a qualitative manner, the result can be quantitatively analysed by observing as a 2D spectrogram. Figures 10.15 to 10.20 show the film change during churning for the different speeds tested. As only seven sensors were present across the rolling axis the spectrogram has been interpolated to better appreciate the thickness change.

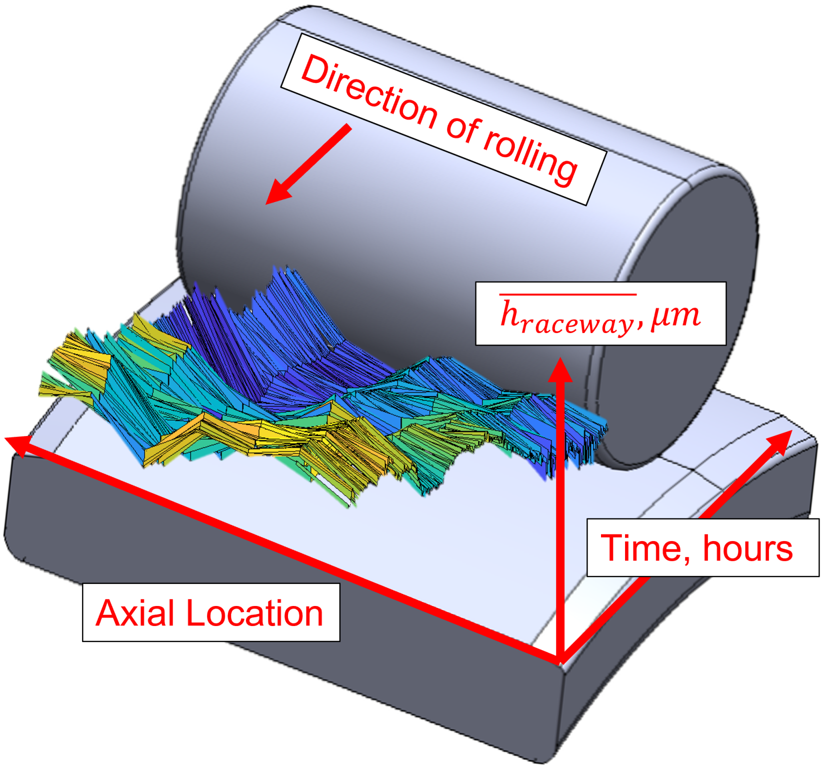

Figure 10.14: 3D spectrogram plot of grease churn across the rolling axis

At the lowest bearing speed of 20rpm two tests were run. The first test, shown in Figure 10.15, was run for an extended period after the churning-temperature criteria had been met due to a desire to monitor the grease film in what is theoretically steady state. A second test was completed the day after, see Figure 10.16, to investigate the grease distribution after relaxation, and to see if the same kind of temperature rise, which indicates churn, would be seen.

In the first test, the churning-temperature criteria was met after 1.742±0.008 hours. After this time the temperature does continue to rise, but not at a level that indicates churning is still in progress. After $\approx$ 0.5 hours Figure 10.15a shows evidence of grease channel formation, with some raceway film thickening to the negative side of the axis centre and film thinning towards the middle of the running track. Figure 10.15b shows the mean frontal thickness $\overline{h_{raceway}}$, calculated as the average across the rolling axis. The mean frontal thickness remains relatively constant suggesting there is more a redistribution of grease across the axis rather than a change in available lubricant volume.

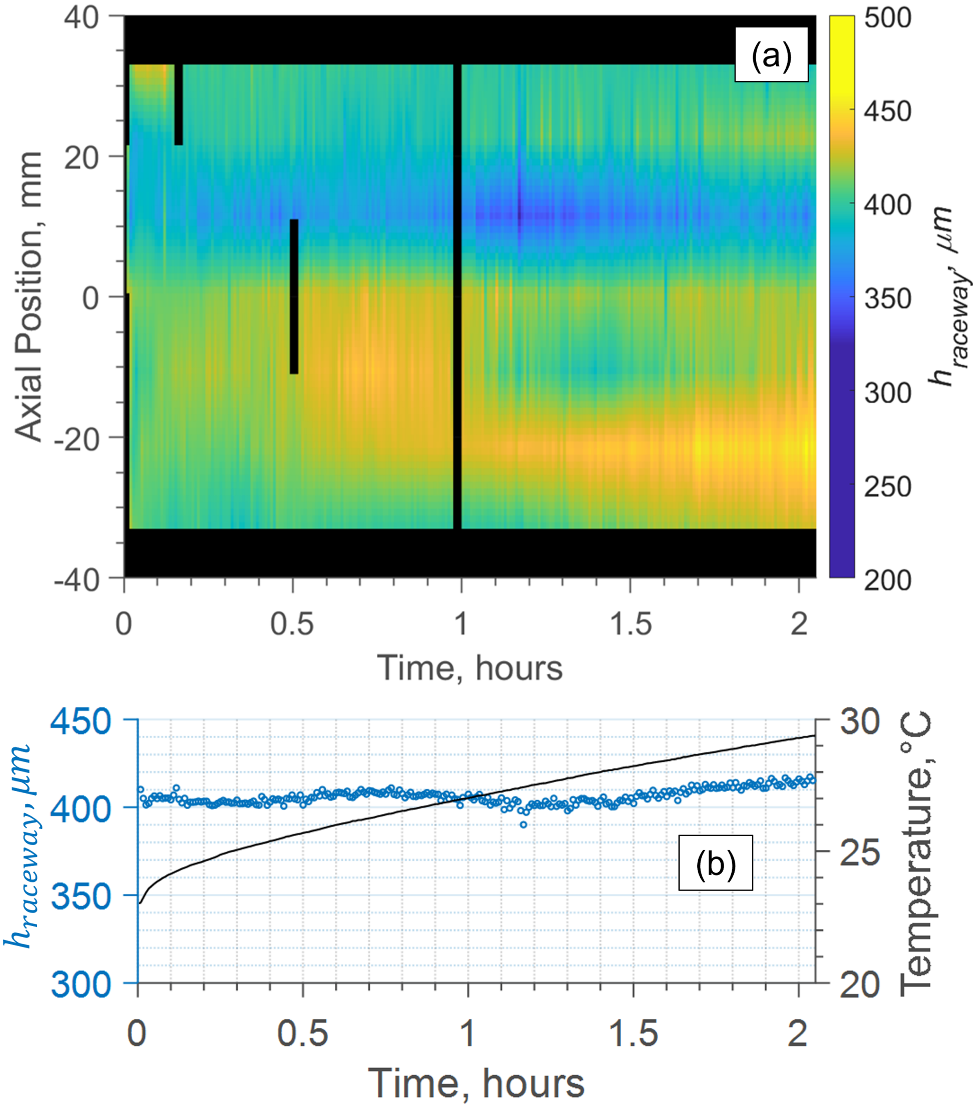

Figure 10.15: Results of the grease churn when operated at $6,200\mathrm{nd_m}$ (a) shows the spectral plot of inlet thickness across the raceway (b) shows the change in mean frontal raceway film thickness

When the second test was performed, the next day after the grease had a chance to relax, under the same speed conditions, there was a temperature rise that exceeded the churning-temperature criteria, and therefore indicative of churn. However, some temperature increase is always expected when running a bearing regardless of the lubricant, and the criteria was met in the much shorter 0.508 ± 0.008 hours. Interestingly, Figure 10.16a shows a much more consistent cross-axial distribution compared to Figure 10.15a, although still with a thinner centre, and the film distribution change seen at ≈ 0.5 hours in Figure 10.15a is not present. Additionally, Figure 10.16b shows the mean frontal film thickness is very comparable to that of Figure 10.15b, and is stable across the test duration. This indicates then that a grease channel was formed during the first churning test, and that when the bearing was left overnight, the grease relaxed into a more even distribution. Then, upon re-running, as no actual channelling took place, the distribution remained consistent.

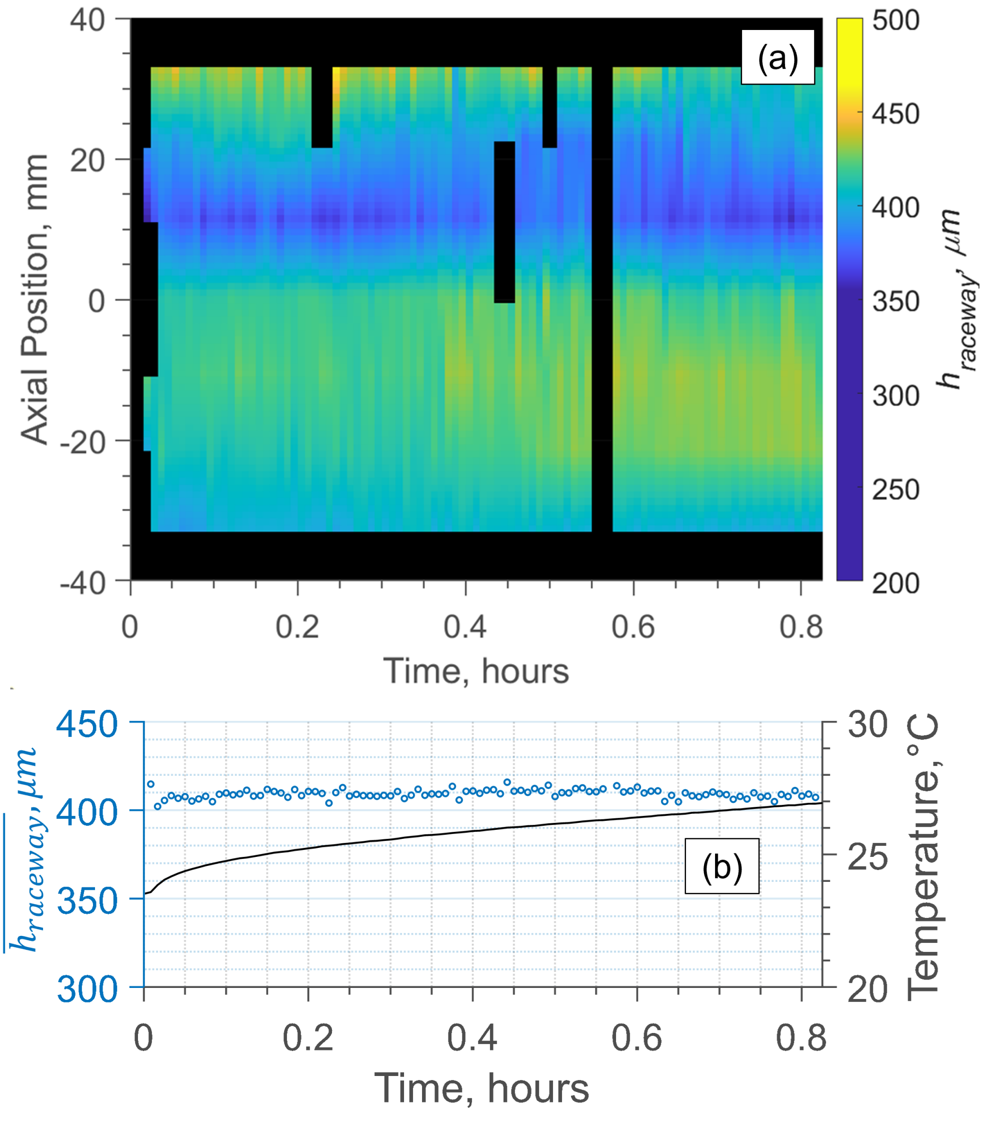

Figure 10.16: Results of the second grease run operated at $6,200\mathrm{nd_m}$ (a) shows the spectral plot of inlet thickness across the raceway (b) shows the change in mean frontal raceway film thickness

Figure 10.17a shows the spectral results for the 40rpm, $12,400\mathrm{nd_m}$ test, and the pattern is similar to Figure 10.15a where the grease was churned at a lower speed. There is an initial redistribution of grease towards the edge of the contact as a channel is formed, causing contact centre depletion, and this distribution remains stable for the duration of the churn. At 40rpm the grease was deemed churned after 1.842 ± 0.008 hours which is very similar to the first 20rpm test. Figure 10.17b shows that the bearing did run at a hotter temperature, as would be expected at a higher bearing speed, but also that the mean film thickness is increased from 406μm in Figure 10.15b to 418μm.

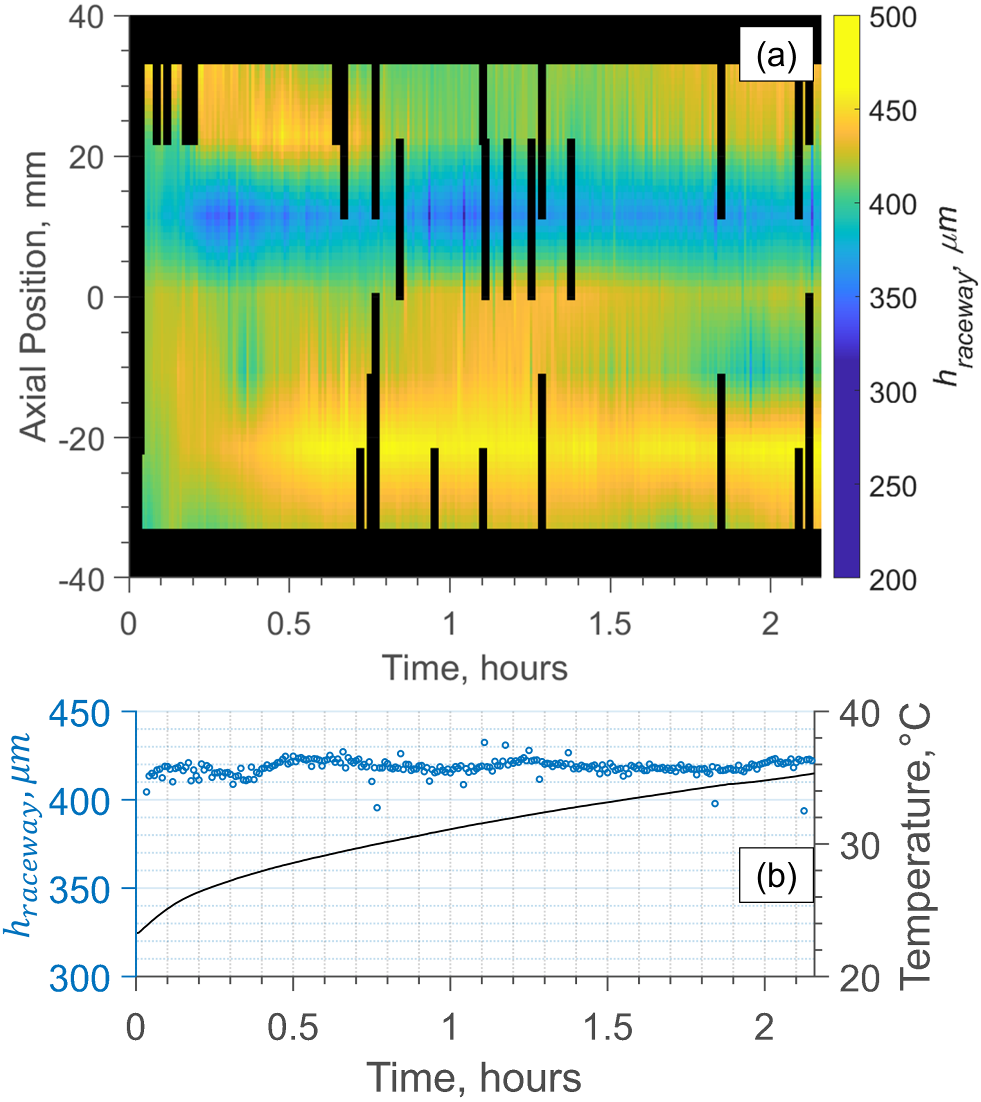

Figure 10.17: Results of the grease churn when operated at $12,400\mathrm{nd_m}$ (a) shows the spectral plot of inlet thickness across the raceway (b) shows the change in mean frontal raceway film thickness

With the first two speeds, the only indication that churning has taken place is a high rate of temperature increase and a redistribution of lubricant across the rolling axis showing channel formation. Figure 10.18 shows the churn result when operated at 60rpm, $18,600\mathrm{nd_m}$ and unlike the previous two slower speeds, the evidence of churn is much more stark. Plot (a) shows that initially there is a much thicker film at the edges of the raceway, with $h_{raceway} > 450\mu$m in some instances, and the film feeding the centre of the contact is $< 400\mu$m. This is again indicative of the grease channel formation mechanism. However, after 1 hour the film on the positive axial position has greatly thinned to values similar to that seen in the centre. After approximately 1.5 hours the measured thicker side reservoirs substantially diminish. The churn-temperature criteria was reached at 2.175 ± 0.008 hours, after which there is still a film gradient across the rolling axis, but the distribution is more equal, with the film being $< 400\mu$m at every measurement location. Figure 10.18b shows that up to 0.6 hours into the test, where the spectrogram shows a large variation in film thickness across the raceway, there is an increase in the mean frontal film from 420μm to 430μm. However, for the remainder of the churn time, $\overline{h_{raceway}}$ steadily decreases to 372μm due mainly to a loss of lubricant from the side reservoirs to the un-swept areas of the bearing.

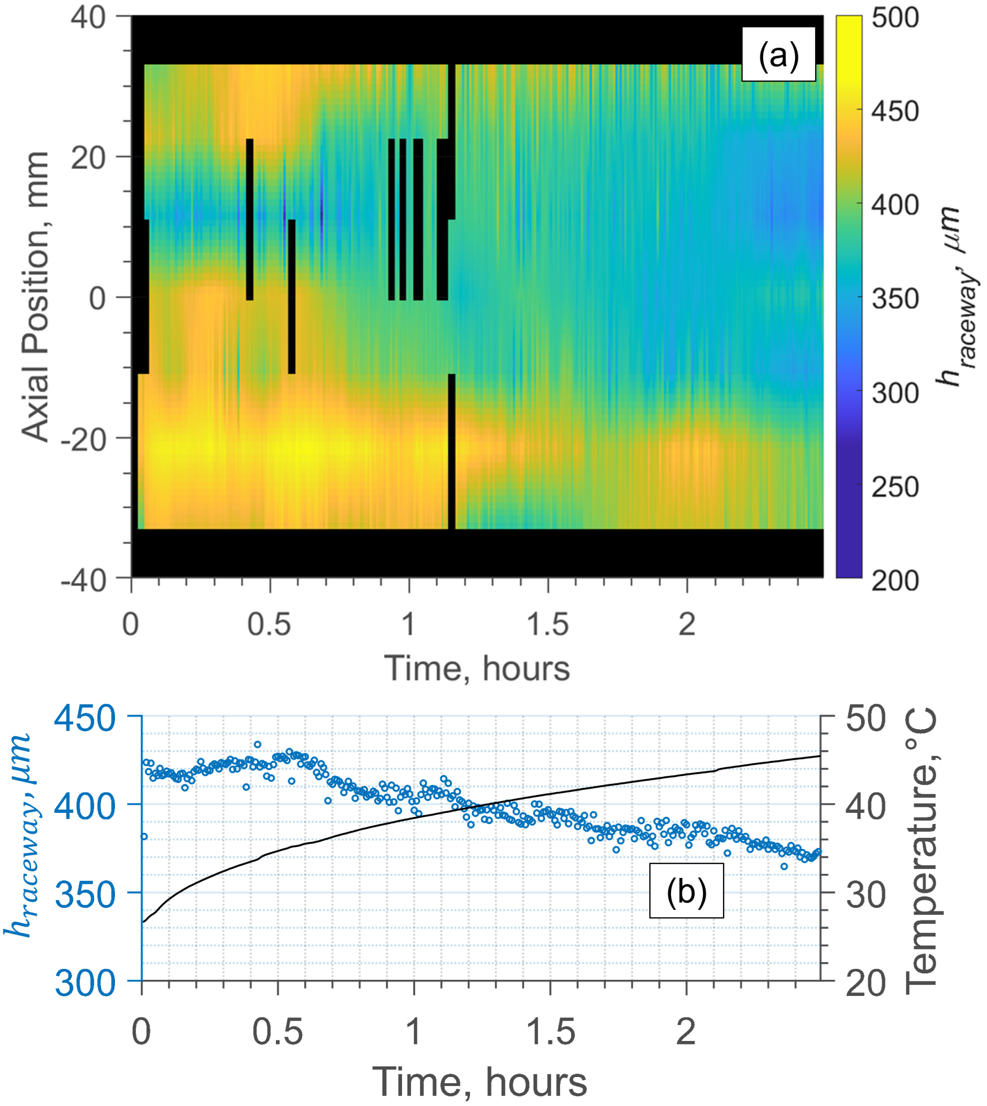

Figure 10.18: Results of the grease churn when operated at $18,600\mathrm{nd_m}$ (a) shows the spectral plot of inlet thickness across the raceway (b) shows the change in mean frontal raceway film thickness

Figure 10.19 shows the churn result when operated at 80rpm, $24,800\mathrm{nd_m}$ which was deemed churned after 3.425 ± 0.008 hours. In Figure 10.19a there is again the same reservoirs seen towards the raceway edges which suggests channel formation, that after ≈ 1 hour begin to decay. Unlike with the previous tests, after ≈ 2 hours not only are the reservoirs severely thin, but still present, but there is a clear further depletion towards the contact centre, with the raceway films $\leq 300\mu$m occurring. Plot (b) shows that in the first half an hour there is again a slight film increase from around

410μm to 428μm. The rise is followed by a continuous decay in mean frontal film thickness, that mirrors the depletion seen in the spectrogram, but some stabilisation occurs after 3 hours where $\overline{h_{raceway}} = 350\mu$m, an 18.2% decrease in film thickness.

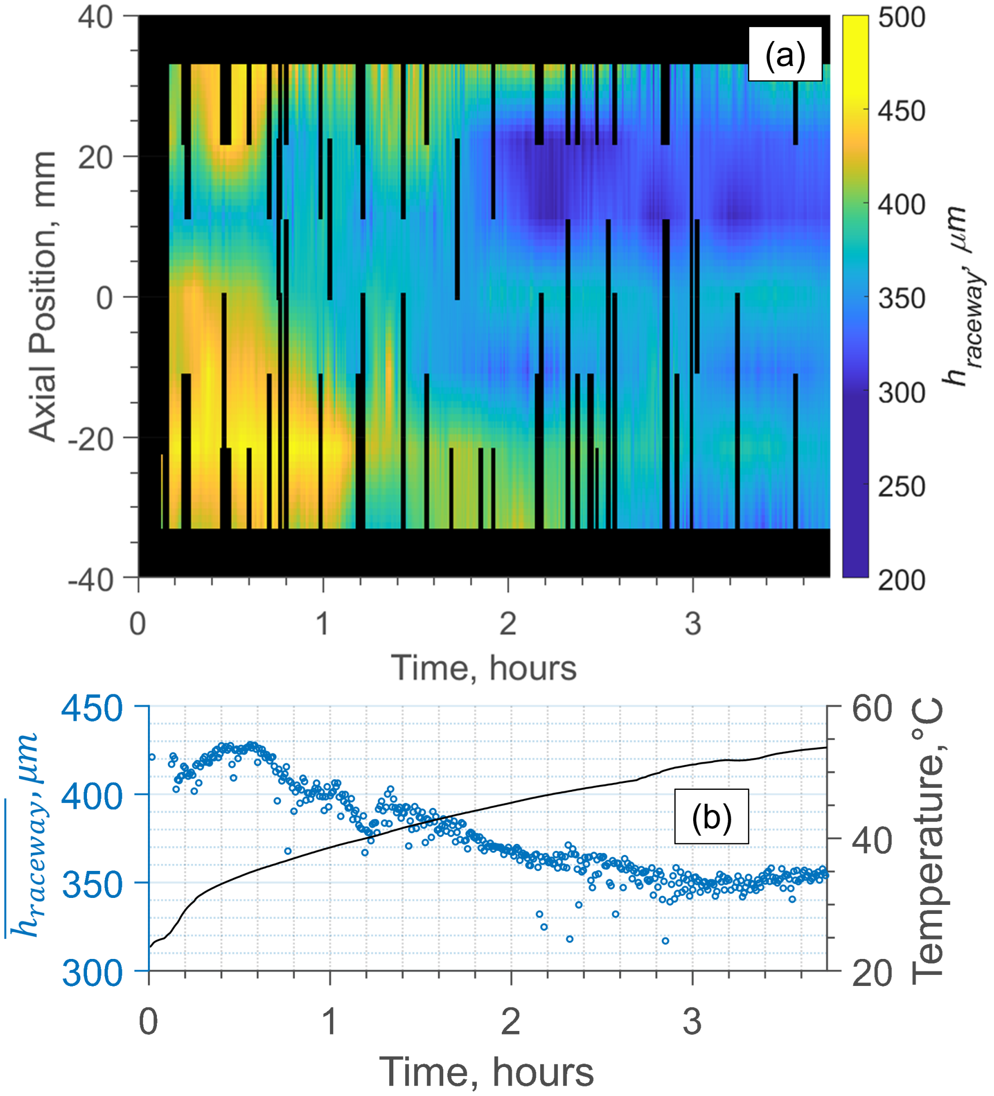

Figure 10.19: Results of the grease churn when operated at $24,800\text{nd}_\text{m}$ (a) shows the spectral plot of inlet thickness across the raceway (b) shows the change in mean frontal raceway film thickness

Figure 10.20a shows the spectral pattern for the 100rpm, $31,000\text{nd}_\text{m}$ test. In the first hour of the test there is the same channel formation pattern seen for the previous speeds. The side reservoirs then deplete to outside the measured area. To a lesser extent there is central region film thinning also. After this redistribution there is a period of stabilisation. Interestingly, churning was ongoing until the very end of the test, at 5.192 ± 0.008 hours, despite the decline of the measured side reservoirs after approximately 1 hour. Although Figure 10.20a shows almost visual stability of the film until the end of the test, there is an observed tendency for the film to grow and deplete, particularly towards the negative side of the axis. It is known that in the clearing phase grease leaks back into the swept area of the rollers [166], which would explain this pattern.

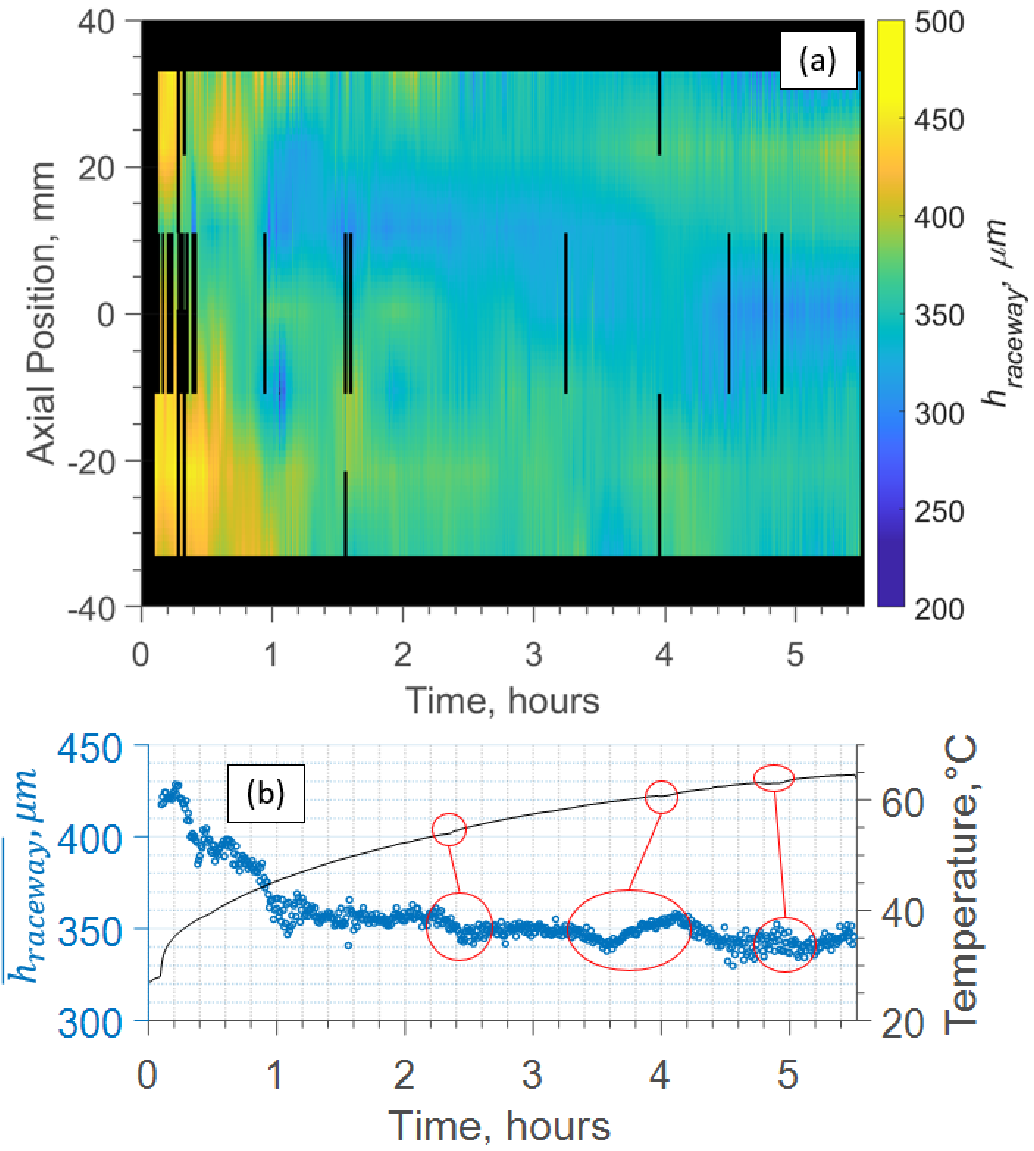

Figure 10.20: Results of the grease churn when operated at $31,000\mathrm{nd_m}$ (a) shows the spectral plot of inlet thickness across the raceway (b) shows the change in mean frontal raceway film thickness

Looking at Figure 10.20b there are three distinct patterns that can be identified, which are the same as in Figure 10.19b but more pronounced. First, there is a slight rise in the mean frontal film thickness from 417μm to 428μm. After 0.1 hours to 1 hours, there is a sudden sharp drop in film thickness to 360μm, a 15.9% decrease; the film semi-stabilises at $t = 1$ hour. At 2.2 hours there is another drop in film thickness to 330μm $\leq \overline{h_{raceway}} \leq$ 360μm, with a maximum mean frontal film thickness decrease of 22.9%. From $t = 2.2$ hour to the end of the test this undulation in the thickness pattern persists. This corresponds with the growth and depletion of the side reservoirs shown in Figure 10.20a. Of note is that a similar undulation is seen in the temperature plots, marked at the time stamps (2.358, 3.992 and 4.818 hours) that correspond with the film undulation.

10.2.1 Starvation Ratio

Figure 10.21 shows how the mean starvation ratio changes during the churning tests at the five different test speeds. As this is calculated from film thickness, the plots are similar in nature to the mean frontal film thickness subplots shown earlier. As with the oil results, at no point is $s/b < 5$ suggesting fully flooded conditions, as expected within the churning phase [54]. However, there is a clear shift towards a starved lubrication state as the fibres are broken down and the grease is expelled from the rolling track, shown by a thinner inlet film thickness. This trend towards starvation is governed entirely by a loss of lubricant at the contact inlet.

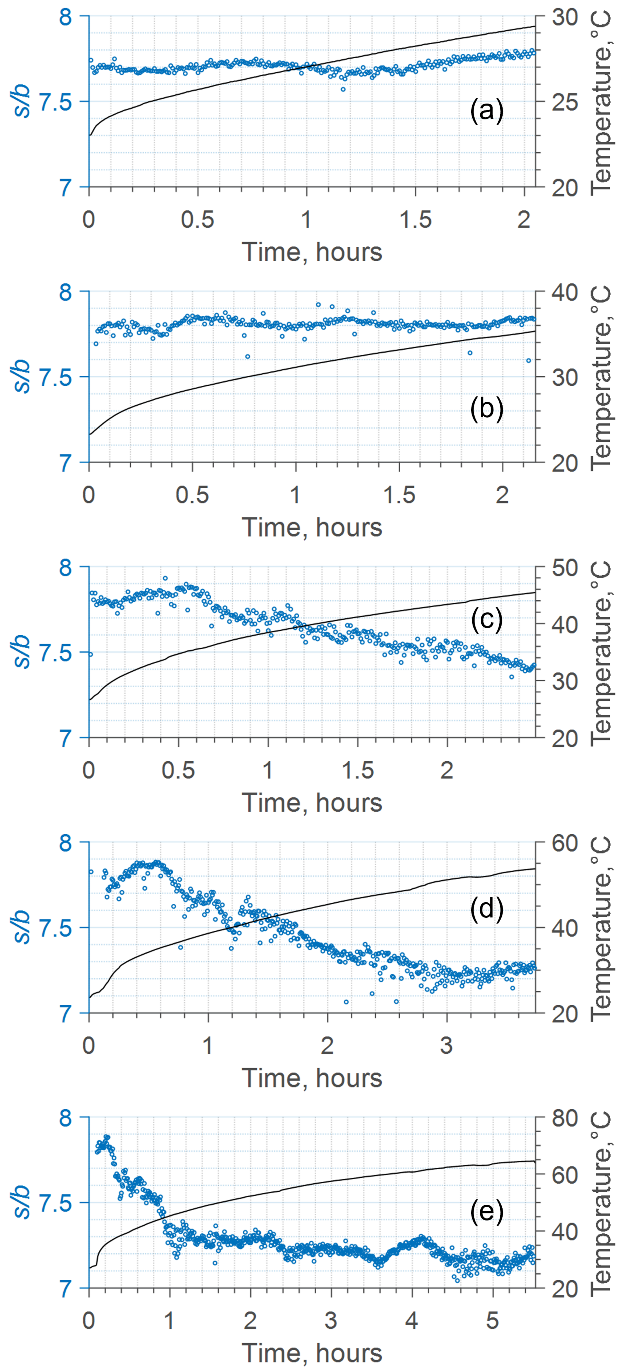

Figure 10.21: Mean starvation ratio during 460WT churn tests operated at bearing speeds of $6,200\mathrm{nd_m}$, $12,400\mathrm{nd_m}$, $18.600\mathrm{nd_m}$, $24,800\mathrm{nd_m}$ and $31,000\mathrm{nd_m}$ respectively from a to e

The 80rpm and 100rpm test cases shown in Figure 10.19b and Figure 10.20b both show that there was an initial thickness rise, followed by film decay, and then a period of stabilisation. Cann et al. [110] saw a similar pattern in the contact film thickness when using thin film optical interferometry techniques, as shown in Figure 4.8. This patterns was accredited to three zones of grease starvation and replenishment, as discussed in Section 4.2.

Cen & Lugt [123] again saw a similar pattern to this in the contact film thickness in a full-scale grease lubricated bearing when operated up to $97,500\text{nd}_\text{m}$ which is over $3\times$ greater than the max nd_m used in this thesis of work. In [123], when testing at $162,500\text{nd}_\text{m}$ and greater, an opposite initial trend is seen, with an increasing contact film rather than decreasing, suggesting that the initial trend is governed by bearing speed. The fact the pattern of the raceway inlet film and contact film mirror each other suggests that the contact film is primarily governed by the raceway lubricant flow. However, during the grease tests Figure 10.21d & e show the mode frontal film is enough to satisfy the $s/b > 5$ criteria, and thus the inlet flow fluctuations should have no impact on the contact film thickness.

Potentially then, the $s/b > 5$ criteria which was determined by single contact optical methods is not stringent enough to assure fully flooded conditions in a bearing. Alternatively, the VFM model proposed in this work needs accuracy improvements, and the real meniscus length was shorter than calculated.

10.2.2 Discussion

At the lowest test speed of 20rpm ($6,200\text{nd}_\text{m}$), the entrainment velocity was 0.16m/s, based off of the cage revolution speed. Therefore, all tests were completed above the quoted 0.01m/s grease transition speed [56]. Thus, with ample lubrication, the grease contact thickness pattern would be expected to mirror that of the base oil. However, these tests focused deliberately on the churning phase, where steady state conditions were held for a prolonged duration during which complex rheological mechanisms take place, and so such a clear pattern is not seen.

The spectral plots show that there is an abundance of NaN values across the test duration, which are presented as black lines in the spectral plots. These occur either due to an actual breakdown of lubricant film and individualised starvation event where the film is out of the measurable range due to being too thin or not present at all, or due to an algorithm failure to detect the film in that particular instance, and it is important to distinguish between the two. The former is obviously of great interest as isolated starvation events could potentially lead to catastrophic failure modes. For such a volume of data it was not feasible to investigate each individual NaN value separately. A relaxation of the algorithm is possible by either increasing the bandwidth analysed, allowing for thinner films to be detected, or by increasing the acceptable variance at which a stable raceway film is defined. The issue with both approaches is they each make the data more susceptible to false positives, that is incorporating a random noise value as a resonant plot, and thus giving an incorrect thickness value. If this approach is taken, it is the opinion of the author that a false thickness value is more detrimental to the data analysis than no value given (a NaN result). However, future work could reduce the number of NaN values due to algorithm failure by better potting of the piezo elements. This would provide damping and an improved signal to noise ratio, thus increasing the frequency range within a -6db bandwidth, and therefore lowering the minimum film measurable without increasing the risk of a false positive.

For all tests the churn time was determined by the stability of the temperature; potentially this stability criteria should have been narrowed and the test duration extended. Chatra & Lugt [55] define the end of churning by the sudden transition of the clearing phase to the bleeding phase, and in [166] determine the end of churning by the homogeneity of grease yield stress throughout the bearing. In this chapter results show channels are clearly formed, but as a film is still detectable along the raceway the clearing phase was potentially still ongoing. It may be expected that NaN values would be detected right across the rolling axis, or there was a sudden thinner steady state film, to indicate churning had finished and bleeding begun. Extending the test duration may therefore have resulted in further findings, but at the time of test, the full-scale CRB test rig was not able to be operated without supervision, limiting test duration to lab opening hours, meaning the churn criteria used in this work were appropriate.

During the prolonged running of the bearing there is clear channel formation, but also observed depletion of these side reservoirs. However, all sensors are positioned to measure within the running track. Therefore it is feasible that much thicker reservoirs still exist, but outside of the running track within the un-swept areas.

One caveat to the grease measurement is the acoustic velocity, used to determine film thickness, is calibrated against fresh, un-bled grease. As the grease churns and oil is released, this will alter the speed of sound. An attempt was made to use Fourier transform infrared spectroscopy (FTIR) on grease samples after the churn tests to determine the level of bleed, and thus identify a new calibration curve, but the results obtained were not accurate enough to perform this kind of analysis. This is not to say FTIR could not be used in this manner in the future, potentially the issue was with the grease samples. However, as the grease and oil acoustic velocities are comparable, it is a fair assumption in this work to use the fresh grease as a calibrating sample.

10.3 A Model of Cylindrical Rolling Element Bearing Lubrication

In Sections 10.1 and 10.2 the measured lubricant film thickness adhering to the raceway was used with the theoretical roller film to determine a starvation ratio. As $h_{roller} << h_{raceway}$ the lubrication state of a rolling contact is governed primarily by the film thickness on the raceway leading to the inlet. In this section, equations are developed to calculate the critical raceway film thickness ahead of the roller, required to lubricate a bearing under a given load, or the maximum film thickness applicable if the raceway film is known.

10.3.1 Calculating Critical Raceway Films

To avoid extreme, accelerated wear of rolling surfaces a bearing must be lubricated, with the intention of this lubricant to create separation of opposing surfaces within the contact. The results presented in this thesis suggest that the governing theory of which lubricant to use for a fully flooded bearing is whichever one forms a raceway film that enables $s = 5b$, a critical raceway film thickness.

In Section 9.4 geometry was used to calculate the inlet position, and from that the s/b ratio. An alternative method of modelling the starvation is defining the angle θ from each cylinder centre to the inlet meniscus position. This angle relates to each separation value as:

$$\delta = r - r \cdot cos\theta \tag{10.2}$$

subbing Equation 10.2 into Equation 9.18 gives:

$$r_1 - r_1 \cdot cos\theta_1 + r_2 - r_2 \cdot cos\theta_2 + h_c = h_{raceway} + h_c\Delta \tag{10.3}$$

The x position is related to θ through:

$$x = r \cdot sin\theta \tag{10.4}$$

As stated previously, $0 \leq x \leq b$ the separation $\delta_t = h_c$. Therefore, where the inlet meniscus position x_i occurs can be calculated from Equation 10.4 with the additional b value to include the region of constant separation:

$$x_i = r \cdot sin\theta + b \tag{10.5}$$

This can then be rearranged to calculate the necessary θ angle to achieve $s/b = 5$:

$$\theta = sin^{-1}((x_i - b)/r) \tag{10.6}$$

Subbing Equation 10.6 into Equation 10.3 and rearranging gives an equation relating the raceway film thickness to an inlet meniscus position:

$$h_{raceway} = r_1 - r_1 \cdot cos(sin^{-1}((x_i - b)/r_1)) + r_2 - r_2 \cdot cos(sin^{-1}((x_i - b)/r_2)) + h_c(1 - \Delta) \tag{10.7}$$

When the bearing is fully flooded $s/b = 5$ and so $x_i = 5b$. Subbing this relationship into Equation 10.7 gives the raceway film thickness needed to fully flood the bearing, allowing the infinite meniscus assumption to be made:

$$h_{raceway_\infty} = r_1 - r_1 \cdot cos(sin^{-1}((5b - b)/r_1)) + r_2 - r_2 \cdot cos(sin^{-1}((5b - b)/r_2)) + h_c(1 - \Delta) \tag{10.8}$$

A similar equation can be presented for a raceway film thicknesses needed to achieve zero reverse flow, where $s = b$:

$$h_{raceway_{crit}} = r_1 - r_1 \cdot cos(sin^{-1}((b - b)/r_1)) + r_2 - r_2 \cdot cos(sin^{-1}((b - b)/r_2)) + 0.7h_c(1 - \Delta) \tag{10.9}$$

The $0.7h_c$ term is used as it has been experimentally validated that under starved conditions, when zero-reverse flow takes place, this relationship is true [113, 2]. As:

$$cos(sin^{-1}((b - b)/r_1)) = 1 \tag{10.10}$$

Equation 10.9 can be simplifies to:

$$h_{raceway_{crit}} = 0.7h_c(1 - \Delta) \tag{10.11}$$

Given then the bearing geometry and operating conditions, Figure 10.22 plots Equations 10.8 and 10.11 at $31,000\mathrm{nd_m}$ from unloaded to 600kN to understand how the film needed to achieve fully flooded and zero reverse change with an increasing contact width. The contact width has been non-dimensionalised against the reduced radius for future work comparison.

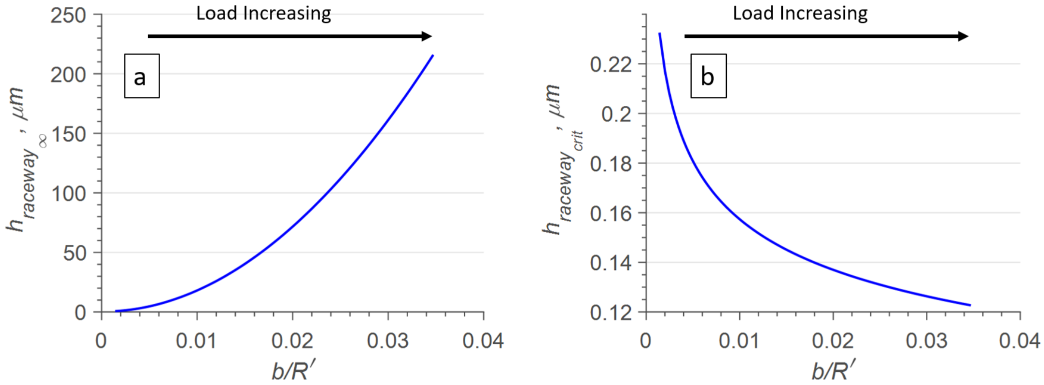

Figure 10.22: Film thickness required to meet the (a) $5b$ and (b) zero reverse flow conditions, with the bearing operated at $nd_m = 31,000$

Figure 10.22a shows that as load, and therefore b/R' ratio, increases the raceway thickness needed to achieve fully flooded conditions is thicker. This is because the contact width is increased, meaning the meniscus must form that much further away to achieve $s = 5b$. Increasing bearing speed would have a negligible impact on this plot as the increase in contact thickness is non-impactful as $h_{roller} << h_{raceway}$.

Figure 10.22b shows that with the same load increase, the raceway film needed to achieve the zero reverse flow condition actually reduces. This is because the film thickness required to achieve zero reverse flow is independent on contact size, and is directly proportional to the starved contact film thickness. With increasing load, there is a reduction in the contact thickness, and therefore $h_{raceway_{crit}}$ reduces. However, the contact width is wider and so a comparable lubricant volume would be necessary to maintain this condition. This film would be heavily impacted by bearing speed as the film is directly governed by the central film thickness.

Using Equations 10.8 and 10.11 two critical raceway film thicknesses are calculable with minimal input. All that is required is an understanding of the bearing geometry, and simple contact width and thickness calculations. If then it is possible to measure the raceway film thickness in-situ, as has been shown possible within this thesis, a series of relationships can be expressed to appreciate the lubrication state:

Relationship	Meaning
$h_{raceway} = h_{raceway\infty}$	Bearing is fully flooded
$h_{raceway} > h_{raceway\infty}$	Bearing is amply lubricated and thicker films will cause churning
$h_{raceway\infty} > h_{raceway} > h_{raceway_z}$	Bearing is partially starved resulting in a central film thickness $h_{c\infty} \geq h_c \geq 0.7h_{c\infty}$
$h_{raceway} = h_{raceway_z}$	Zero reverse flow occurs and $h_c = 0.7h_{c\infty}$
$h_{raceway} < h_{raceway_z}$	The bearing is severely starved and wear is likely

Table 10.5: Impact of the relationships between the measured raceway thickness and critical raceway thickness values

10.3.2 Calculating Critical Bearing Loads

Alternatively, a more practical case may be a measurement of the raceway thickness, and an understanding is needed of the maximum applicable load to achieve optimal lubrication where $s/b = 5$. In this case, given the raceway film thickness, the inlet meniscus position can be calculated from following the Newton-Raphson method between Equations 9.12 and 9.15. The heaviest load applicable where fully flooded conditions are still achieved occurs when:

$$b = s/5 \tag{10.12}$$

Subbing this into the Hertzian contact Equation 2.4:

$$\sqrt{\frac{4P'_\infty R'}{\pi E^*}} = s/5 \tag{10.13}$$

where P'_∞ is the load at which fully flooded conditions are still possible.

$$\frac{4P'_\infty R'}{\pi E^*} = \frac{s^2}{25} \tag{10.14}$$

$$P'_\infty = \frac{\pi E^* s^2}{100R'} \tag{10.15}$$

With cylindrical rollers the load per unit width is defined in Equation 2.3 and so:

$$P_\infty = \frac{\pi E^* s^2 L}{100R'} \tag{10.16}$$

A similar derivation can be made for the max load at which zero reverse flow is achieved. This occurs when $b = s$. Subbing this into Equation 2.4:

$$\sqrt{\frac{4P'_{crit}R'}{\pi E^*}} = s \tag{10.17}$$

where P'_{crit} is the load at which zero reverse flow is still possible. Expanding and rearranging:

$$\frac{4P'_{crit}R'}{\pi E^*} = s^2 \tag{10.18}$$

$$P'_{crit} = \frac{\pi E^* s^2}{4R'} \tag{10.19}$$

$$P_{crit} = \frac{\pi E^* s^2 L}{4R'} \tag{10.20}$$

10.4 Conclusion

10.4.1 Oil Lubricated Bearing

- It had already been established from literature that oil films could be measured via ultrasonic resonances. This chapter has shown that this method can be applied to raceway films, and from these measurements the lubrication state of the bearing inferred. The measurements give an insight into the localised lubricant supply across a rolling axis.

- Under steady state conditions the film leading into the contact is not symmetrical, and generally the centre region has a reduced oil supply, causing a 'U' shaped distribution with thicker oil reservoir bands towards the roller faces.

- Comparison with other in-situ bearing measurements are difficult due to a lack of comparative work. However, Chen et al. [11], who studied oil films of a ball bearing using a glass and resin bearing, also note the 'U' pattern towards the contact inlet.

- Calculating s/b values from the deep groove roller bearing work of Chennaoui et al. [12] shows that their bearing tended towards starvation at $s/b = 7.1$. A comparable s/b ratio is seen for both oils in this chapter when loaded at 500kN and 600kN.

- The measured film distribution shape is affected by load, speed and viscosity. The viscosity relationship is complicated; the lower viscosity oil has a thinner mean film thickness across the raceway, but more stable inlet films than the higher viscosity oil.

- Quicker bearing speeds increase the contact film thickness, as shown via Equation 2.5, and if there is a constant lubricant supply during the test it is intuitive that there is a comparable affect at the raceway inlet. VG32 saw a constant raceway thickness increase with speed but the more viscous VG320 saw a decrease at the top two bearing speeds, most likely due to impaired oil flow.

- Increasing load is seen to interrupt the 'U' shaped pattern of the film, thinning the film on one side of the roller and thickening it on the other to make an almost linear distribution, but overall Figure 10.6 shows there is a mean increase across the frontal film.

- Classically it is thought load has a minimum impact on film thickness as the load parameter in Equation 2.5 has an exponent of -0.1. However, this chapter shows as load increases the s/b ratio drastically decreases due to an enlargement of the contact area. Consequently, fully flooded conditions are much harder to achieve under heavy loads.

- The observed starvation ratio across the roller axis was larger than $5b$, the minimum ratio Dowson [41] states is needed for fully flooded lubrication, for all test conditions. Despite this, a bearing stall occurred under 600kN, even with an expected raceway film that would meet this criteria. This then suggests that an ample oil supply is simply a pre-requisite for adequate separation, but oil choice is still of paramount importance. To reiterate an earlier point, all separated contacts have a healthy lubricant supply, but not all contacts with a healthy lubricant supply are well separated.

10.4.2 Grease Lubricated Bearing

- As shown by a change in the reflection amplitude across a frequency range, grease films on roller bearing raceways are sensitive to ultrasonic waves, and the resonant frequency of these films can be measured and converted into a layer thickness. This is an important step towards more sophisticated in-situ monitoring techniques of large roller bearings, and thus a greater understanding of film movement, both of which enable better lubricant and bearing designs.

- Grease raceway thickness clearly has a dependence on time. All spectrograms show that initially there are large side bands of grease that are thicker than the central region, meaning that the lubricant flow to the contact is not uniform across the axis. This is indicative of the channelling phase and shows that ultrasonic sensors have the capabilities to monitor these complex churning subphases in-situ. As the grease continues to churn there is a decrease in film thickness across the axis, but in particular at these side regions, meaning that the measured cross-axial distribution moves towards stabilisation. However, it is likely that the thicker side bands still existed outside of the sensor measurement area, in the un-swept regions of the bearing.

- The bearing speed affected the onset of raceway film decay, and if present, the time duration of decay. For the lowest two speeds, the mean frontal raceway film is constant during the churn test, at around $400\mu\text{m} \leq \overline{h_{raceway}} \leq 410\mu\text{m}$.

- The lowest speed at which a change in $\overline{h_{raceway}}$ is observed was 60rpm, $\text{nd}_\text{m} = 18,600$. The decay started around 0.6 hours into the test, and did not stabilise during the churn time. The case could be made to extend this test or reduce the stability criteria, but as the test was run in accordance with *The Timken Co.* standard laboratory procedure for churning greases this was deemed unnecessary.

- When comparing the mean frontal raceway films between different tests, only the quickest two speeds of 80rpm and 100rpm saw stabilisation at $\overline{h_{raceway}} \approx 350\mu\text{m}$. The quicker of these two saw film thickness undulation about this mean value. The slower of the two at 80rpm, $24,800\text{nd}_\text{m}$ took ≈ 3 hours to stabilise. At the quicker test speed this is reduced to just 1 hour. This then suggests that the raceway film decay, and thus starvation, is governed partially by bearing speed, as noted also in [123]. Oil bleed is a function of the shear force through mechanical churn and grease temperature through chemical churn. As both of these increase with bearing speed, it is logical that the oil bleed, and thus raceway film decay increases with bearing speed.

- Although only the quicker two speeds saw film stability, the churn time was increased with an increasing bearing speed, but the channel formation time was reduced. Therefore, the extended churning period at higher speeds is due to an increase in the clearing phase duration. It was noted that there is a more dynamic and violent side flow at higher bearing speeds [60, 35] which agrees with the churn results presented in this chapter.

- At the two quickest bearing speeds, although the films stabilised, there is an undulation in both the spectral and mean frontal film thickness plots. This is more pronounced at the quickest, 100rpm test. This is most likely caused by the clearing phase, a sub-phase of channelling, where grease flows into the running track and is pushed back out into the un-swept area until stabilisation occurs with the onset of the bleeding phase [35].

- Although the calculated s/b during all churn tests was greater than 5, suggesting the bearing was fully flooded, the quickest two bearing speeds of $24,800\mathrm{nd_m}$ and $31,000\mathrm{nd_m}$ show a mean frontal inlet film pattern similar to the contact film pattern of a starved contact, presented by Cann et al. [110]. At these speeds the s/b ratio is comparable to the $s/b = 7.1$ at starvation onset calculated from the work of Chennaoui et al. [12]. Potentially then, $s/b > 5$ does not guarantee fully flooded conditions as starvation is expected in bearing churn, or the meniscus length was shorter than that calculated using the VFM.

10.4.3 Lubrication Model

- The meniscus forms when the roller film and raceway film join, the meniscus location is governed primarily by the thickness of the raceway film.
- Equations 10.8 and 10.11 can be used practically to determine what raceway film needs to be developed to achieve fully flooded or zero reverse flow conditions respectively. If the raceway film is known, Equations 10.16 and 10.20 can be used to determine how much load can be applied to the bearing to achieve the two different lubrication states.
- Section 10.1.5 discusses how the amount of lubricant fed into the contact is simply a pre-requisite for proper contact separation, and not a guarantor.
- An ideal contact lubricant therefore has two qualities. Firstly, it has an atmospheric viscosity and pressure-viscosity coefficient capable of causing adequate separation within the contact conditions. Secondly, it has other surface tension and wettability effects enabling a thick film to form at the inlet region. If a lubricant lacks either property, film breakdown and ultimately surface wear can be expected.

Chapter 11

Discussion

This chapter covers three main themes. The first is the general data trends seen within this thesis of work. The second gives guidance to industry based off of the new data trends. The third explores how the technology would scale to other rolling element bearings with different sizes, speeds and lubricant supplies.

11.1 General Discussion on Thesis Trends

11.1.1 Skew Measurements

The implementation of ultrasonic sensors on the inner raceway of a bearing has shown that by monitoring the contact pass time of a roller along the transverse axis, the level of roller skew can be appreciated. The main limitation to the technology in this thesis is the accuracy of sensor positioning, as microscopic misalignment can lead to errors orders of magnitude larger than the actual skew value. However, as the sensors are in a fixed position, there is a tangible benefit from monitoring the skew trend under different running conditions or over an extended period of time.

A novel finding of this work is that there exists skew impulses, where there is a large change in skew magnitude over a very short duration of less than 1 minute, which is accompanied by a contact film thinning on the roller side that is trying to trail. These impulses were observed under steady-state conditions. It is not clear from this work alone whether the uneven lubricant distribution, and therefore assumed roller tilt, is a cause or symptom of the roller skew, or indeed whether there is a separate governing mechanism altogether. However, such a violent change in skew angle is almost certainly detrimental to long term bearing health. Extrapolating this finding, the observation of this phenomenon in the field could be an indicator that a bearing is not going to meet its expected life.

The application of ultrasound for this measurement could obviously be improved upon by the design and creation of high tolerance instrumentation jigs to reduce alignment errors and extensive calibrations to generate accurate zero-offset values, both of which would push the technique to a quantitative measurement instead of qualitative. But, even at its current technology level, the sensors could potentially be used as a binary indicator of bearing imbalance and therefore highlight a need to perform some kind of preliminary maintenance or inspection. With an adequet data set of skew impulses from several field bearings over an extended duration, which contains failures and those which met their expected life, a threshold value of skew impulses over a duration of hours could be defined. Other bearings could then be assessed against this threshold, with those exceeding the value highlighted for inspection.

11.1.2 Relationship Between Inlet Film and Skew

Two key themes of this thesis are the measurement of the contact inlet film adhering to the bearing raceway, and the skew value of the rollers. From this thesis alone it cannot be determined which is the cause or symptom of the other, or if there is a third governing mechanism. However, from extrapolating data trends, some impressions can be drawn.

When considering the skew impulses, these are observed under steady state load and speed. Therefore, the most likely influencing factor on the impulse is a sudden, unpredictable change in lubrication conditions. Conditions are known to be chaotic during the grease churning phase, and with the splashing affect of oil it is intuitive that random, transient changes to inlet thickness could occur. If it is assumed then that inlet film thickness changes can cause skew impulses, it is an intuitive assumption that a trend change to inlet film conditions, which was achieved in this work through altering the lubricant type, lubricant viscosity, bearing load and bearing speed, would also govern the general skew trend.

Considering a potential third mechanism that governs inlet film and skew, the most obvious candidate would be a vibrational effect. Although it is plausible such an effect could cause general trend changes between test conditions, it does not help to explain the impulse occurrence, the frequency of which occurs in μHz, orders of magnitude smaller than other known bearing vibrational phenomenon. Therefore, it is the opinion of the author that there is a direct correlation between inlet film thickness and distribution, and the skew magnitude, with the former initially governing the latter, but it could well be the case that a random change in flow causes a certain skew magnitude, which in turn continues to alter the inlet film. As previously stated, further work is needed to validate this theory, but this thesis suggests that the inlet film and skew are strongly linked.

11.1.3 Detecting Starvation

Results from this thesis show that the calculated $s/b \geq 5$ suggesting fully flooded contacts at all test conditions. However, Chennaoui et al. [12] saw starvation onset, which they defined by a reduction in the contact film thickness vs. bearing speed gradient followed by plateauing, at $s/b \leq 7.1$. The most reasonable explanation for the discrepancy between transition values is starvation onset not occurring at a single s/b value but instead over a window. As the ratio considers oil directly at the contact inlet, bearing design should not alter this window as fundamentally the oil is lubricating a rolling contact and whether point or line based, on a small enough scale the lubricant is subject to similar, high pressure conditions. What is likely to govern the window is the lubricant properties, particularly viscosity at the inlet and the pressure-viscosity coefficient, and entrainment into the contact.

In Chapter 10 the less viscous VG32 oil stalled under high load, low speed despite likely exceeding $s/b \geq 5$ based off of an extrapolation of previous raceway thicknesses. The more viscous VG320 could operate at this condition, with similar raceway films, and so oil properties are clearly crucial. What this suggests is that although there is likely a window of starvation onset, having ample lubricant at the inlet does not guarantee adequet lubricating conditions. To state a previous point again, all well separated contacts have an adequet lubricant supply, but all contacts with an adequet lubricant supply are not well separated. The supply is a pre-requisite to healthy separation but not the only governing factor.

In this thesis, the raceway film leading to the inlet has been measured and for the more viscous VG320 oil a pattern of increase, plateauing, and then thickness decrease has been observed. This is mostly due to impaired reflow at higher speeds. This pattern occurred whilst the bearing was fully flooded, but mirrors the contact starvation plot with increasing speed. Therefore, if the rig was run at even greater speeds, this inlet film would likely decrease to a condition where $s/b < 5$ and contact starvation would take place. Currently, it is not possible to have an in-situ measurement of contact film thickness in field bearings, but as proven by this work, the inlet film measurement is possible. Therefore, this technology could work as a traffic light sensor where the inlet pattern is extrapolated to infer future contact conditions. If a decreasing thickness trend is seen at the inlet, this acts as a pre-cursor to contact starvation and allows preventative action to be taken to alleviate the issue.

Figure 11.1 depicts this relationship between the raceway film and contact film with increasing bearing speed. Initially, both films increase together until $s/b \geq 5$ is achieved at speed V_1. This trend continues until V_2 where oil reflow around rollers is impaired due to the high bearing speeds and there is a plateau of raceway thickness. Between V_2 and V_3 there is an eventual decrease in raceway thickness. However, as there is still ample lubricant at the inlet, the contact film can still continue to grow with bearing speed, but the bearing is now operating in the pre-starvation zone. A further speed increase beyond V_3 leads to a greater reduction in the raceway thickness where $s/b \leq 5$. As this threshold is passed, the contact film plateaus and then begins to decrease as starvation begins and intensifies with even greater speeds. The values of V_1, V_2 and V_3 are arbitrary and will depend on the lubricant, bearing type and running conditions. Figure 10.9 shows a plot that would fit the pre-starvation zone, and if applied to an industrial field bearing could be an indicator to perform an inspection, maintenance or reduce operating speed.

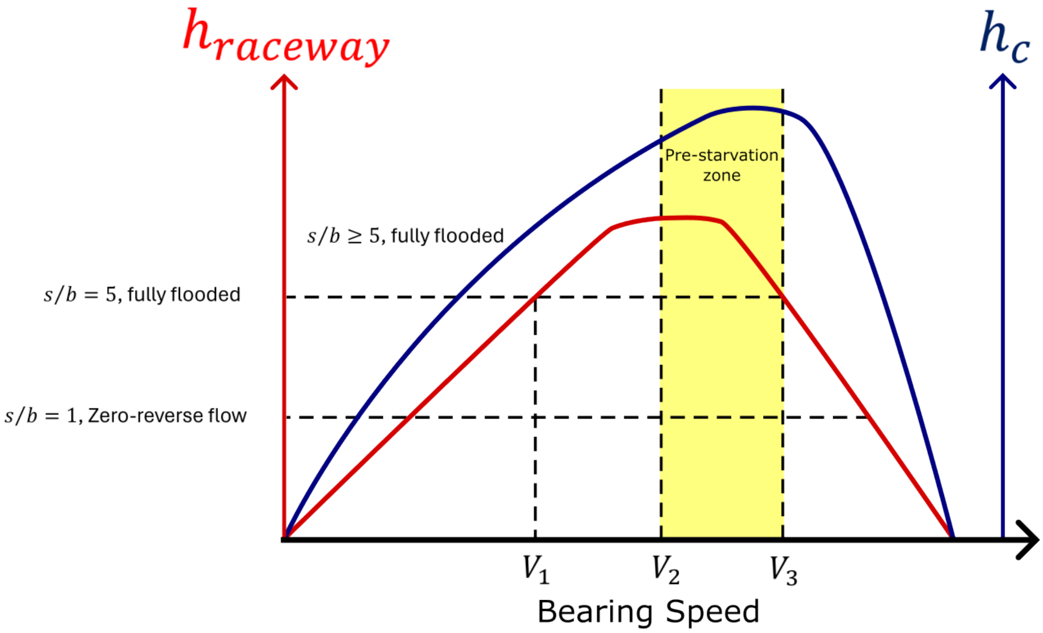

Figure 11.1: Theorised relationship between raceway thickness and contact thickness, showing a detectable pre-starvation window of detection

11.2 Guidance to Industry

Wind turbine bearing failures typically occur due to micropitting, smearing or white etch cracking (WEC), symptoms of rolling contact fatigue, which are caused or worsened by an inadequate contact film [16, 22, 23, 21]. For the contact film to develop the lubricant meniscus must form an ample distance upstream of the contact centre. This thesis of work has shown that for both oil and grease lubricated bearings there is an uneven distribution of lubricant flowing into the contact, typically with thicker oil reservoirs towards the roller edges and a more depleted centre. Therefore, rolling contacts will have uneven churn losses across the roller axis when fully flooded. When in a starved regime, it is not only possible but highly likely that the contact film thickness will be non-uniform across the contact length due to localised flow differences. This irregular contact film thickness is often not accounted for in rolling bearing models, and would be difficult to detect with other in-situ measurement techniques such as the capacitance method where a mean film thickness is measured over the contact length both between the inner and outer raceways. Bearing and lubrication engineers should be aware of this non-uniformity of film thickness as it may help to explain other observed phenomenon.

Results clearly show that with an increased load the bearing lubrication state shifts towards starvation, not because of a higher contact pressure, but instead due to the enlargement of the contact size. Additionally, the 'U' shape distribution of lubricant is hindered at higher loads, most likely due to a skewing motion of the rollers, which leads to an almost linear decrease in inlet film thickness, and therefore meniscus length, from one side of the roller to the other. This has the potential to cause serious consequences to bearing health under prolonged operation. As turbines are trending towards larger swept areas, with the same gearbox architecture bearing loads will only increase, and so likely the failures that are common now and due to an inadequate meniscus formation will increase in number.

One emerging field this work is applicable to is electric vehicles (EV's) lubrication. EV's are gaining in popularity, driven by an increase in cultural desire to reduce personal carbon footprint [167] and through government policy that drives a shift towards non-internal combustion (IC) engine vehicles [168]. However, EV's have a host of different lubrication issues when compared with conventional IC engines as they have to contend with increased operating temperatures and electrical currents but also higher bearing speeds and loads [169]. These last two points have severe consequences on the development of the inlet meniscus. Section 10.2 shows that with increased bearing speed the grease churns quicker and forms inlet films that are thinner, meaning the bearing is closer to starvation. Section 10.1 shows that an increase in bearing load drastically reduces the starvation ratio. As EV drivetrains are susceptible to relatively high speeds and loads, starvation is a likely mechanism that will take place within the greased bearings over prolonged use.

As already highlighted in literature [170], typical IC lubricants may not be appropriate for EV drivetrains. Kwak et al. [170] suggest higher viscosity base oils have superior molecular cooling properties and a lower electrical conductivity, although an ideal electrical conductivity for EV lubricants has not yet been defined. However, due to the high bearing speeds, low viscosity oils with enhanced reflow properties are typically recommended for EV drivetrain bearings; Gupta [171] found a 17% increase in engine efficiency with a lower viscosity oil compared to a factory transmission oil.

Based on the findings of this thesis, lower viscosity oils form thinner raceway films and are therefore more prone to starvation when subjected to higher loading at low bearing speeds. However, at higher bearings speeds, which EV engines operate at, the improved reflow of lower viscosity oils helps avoid starvation. Therefore, when deciding on the viscosity of an EV drivetrain lubricant, or any bearing lubricant for that matter, there is a trade off that should be assessed case by case, and a single oil or grease may not be appropriate. Higher viscosity oils potentially have better thermal properties molecularly but likely more prone to starvation in a high speed EV engine; but they are appropriate for lower speed, high load contacts. Low viscosity oils have an impaired molecular cooling performance but increased flow rate, meaning their overall cooling performance is likely enhanced. Additionally, in high speed scenarios their improved reflow means they are more likely to avoid starvation and instead operate in the maximum efficiency region of the Stribeck curve where the coefficient of friction is the lowest.

11.3 Application of Technology to Other Bearings

This thesis has shown that the developed ultrasonic resonance method is capable of detecting raceway films and thus predicting the starvation level of rolling element contacts in a large rolling element bearing. A technology limitation is the measurement area of the sensor being relatively large when compared with the contact size. Therefore, application to even larger bearings should be easier as the measurement area of the sensor will be relatively comparable but the scale of contact and inlet region is beneficially scaled up. Application to smaller bearings is more difficult because contacts and meniscus dimensions are scaled down. To apply this technology to smaller bearings, beam focusing should be implemented to reduce the measurement area. Unfortunately, current sensors capable of focusing are water bath based, bulky, and therefore impractical. However, this is a limitation that will likely be overcome with future development into ultrasonics.

This work uses a bearing with a relatively low speed, but bearing speed is not a major limitation to the technology. Bearing raceways are typically steel based, with an acoustic velocity of around $5,900$m/s. Taking the raceway thickness of 19.5mm used in this work as an example, a wave can transmit through the raceway and reflect back to the sensor face to be recorded in approximately 6.6μs. Assuming the sensor measurement area length of 3mm^2 found in this thesis, a contact could pass at 453m/s and a capture would still be possible. The inner raceway outer face diameter of this work was 259mm meaning that the rate of rotation could be as high as $33,000$rpm and a single contact point would be measured. Obviously, there will be greater concentrations of data at lower speeds, but within practical bearing operation speed is not a limitation.

In this work load was seen to have a greater influence than viscosity or speed on the starvation s/b ratio. This is due to the test conditions having a small effect on the raceway thickness and thus inlet meniscus position when compared with the contact widening effect of increased load. This is a noteworthy point as load has the lowest effect on central film thickness according to the Dowson equations and so is often overlooked in terms of detrimental effects to lubrication. However, with higher speed bearings, load will likely be replaced by entrainment velocity as the primary starvation governing factor as lubricant flow around the rollers is impaired further.

One noteworthy point is the results discussed in this work are of the heavy loaded zone, but that sits within an oil sump and so there is an advantageous supply of lubricant to the contact. Although results show that fully flooded conditions are not a guarantee, mechanisms such as reflow around the roller are promoted and the raceway film is far thicker than the roller film. If in another bearing the load direction was flipped, so that the heavy load zone was not where the sump was, then contact lubrication would be far more dependent on the oil that adheres to the roller and what is dragged around on the raceway. In this instance the raceway and roller films may be more comparable in magnitude. As roller films are naturally thin due to the rupture at the contact outlet, this means the contacts in these lubrication scenarios are more susceptible to starvation.

Chapter 12

Conclusions

This chapter concludes all of the thesis work. The motivation, novelty and key contributions of the work are discussed, along with the main data trends seen from the in-situ measurements. Based on the thesis findings some advice is given to industry on lubricant selection for avoiding bearing starvation. Finally, limitations of the resonance method for measuring raceway films are discussed and several future research directions are highlighted.

12.1 Thesis Motivation

Lubricant flow to a rolling contact inlet is crucial in determining adequate separation, thus avoiding wear and eventually catastrophic bearing failure. When there is adequate lubricant flow an inlet meniscus can form upstream of the contact centre. The inlet meniscus is the position at which the raceway and roller films join at the contact entry, and determines the position at which the contact pressure, needed to cause separation, can begin to form. If there is not enough lubricant at the inlet, the meniscus position forms closer to the contact centre, delaying the pressure rise. If this pressure rise is delayed to the point where the full separation can not be achieved, the bearing is said to be starved and premature wear is expected. Counter to that, too much oil at the inlet can create a secondary drag force known as churn. This is also detrimental as it can lead to temperature spikes and thermal degradation of the bearing as well as a general reduction in efficiency. Therefore, an in-situ measurement of where the inlet meniscus position occurs is highly desirable. However, this measurement is extremely difficult to take. The menisci are very thin (in the μm range), occur over very small working areas (in the mm range), are hidden deep within the working components of the bearing and occur between complex geometries.

The position of the meniscus is directly related to the lubricant film feeding the contact. Therefore, a measurement technique that can non-invasively measure that lubricant film can be used to infer the meniscus position. However, there are limitations on what technologies can be used. Optical methods are not feasible due to the opacity of bearing materials. Capacitance and eddy current methods require access to either side of the material. As the raceway film is in a steel-oil-air boundary these are also not applicable. This thesis has focused on an ultrasonic approach, the benefits being that ultrasonic waves can propagate through solid and liquid media meaning direct access to the film is not necessary, and that reflections are sensitive to films in the micron range. This works towards developing a robust in-situ monitoring technique for both industry and academic research.

12.2 Main Conclusions of Work

12.2.1 Validation Measurement of Lubricant Resonant Frequencies

Previous research has determined a fundamental link between the thickness of a material and the frequency at which it resonates. This relationship has been proven with solid materials and a range of liquids such as oils and water. Chapter 7 of this thesis explored this link between thickness and resonances, with the results re-validating the relationship. Results in Section 7.4.2 show that ultrasound has the capability to accurately track the fundamental frequency of an unconstrained oil film of changing thickness. This is a development of the resonant tracking of distilled water films presented by Chen et al. [126] and opens ultrasonic sensing to in-situ monitoring of more complex lubrication phenomenon.

In Section 7.5 two advancements were made. Firstly, it was shown that grease is a very attenuative substance; despite this, resonances still occur and are governed by the mean grease layer thickness over the sensor measurement area. Secondly, from the known thickness of the grease layer and the frequency of resonance harmonics, a temperature calibration was performed to obtain a acoustic velocity-temperature relationship for grease. This allows the measurement of a grease film via acoustic velocity dependent techniques such as TOF and the resonant method.

12.2.2 Presence of Resonances in Bearing Raceway Films

To date there has previously been no in-situ monitoring of bearing raceway films that are practically applicable in the field. Chen et al. [11] developed a glass and resin ball bearing, and were able to use optical methods to monitor lubricant films. However, these sensing technologies are bulky and fragile, and could not be deployed in actual bearings. In Chapter 8 it was shown that ultrasonic reflections are sensitive to the resonant frequency of the oil film on the inner raceway, and that the shifting frequency due to oil film thickness changes could be monitored. A spectral method was developed to visualise this change in frequency, examples in figures 8.8 and 8.9, which can be used as a stand-alone analysis technique. The spectrograms are read in a similar fashion to contour lines on a map, tight horizontal fringes which decrease in frequency indicate a film thickening; spreading fringes with a frequency increase indicate film thinning. The conclusions from the scouting bearing in Chapter 8 were that resonance sensitive films form on the raceway, but the thickness distribution across the axis is not even, meaning there are localised changes to lubricant flow. A second inner raceway was instrumented and introduced in Chapter 9 with the same central frequency sensor at seven axial locations. Spectral plots again showed the presence of resonances, and as the sensors were of the same frequency the results are comparable.

12.2.3 Measuring the Raceway Film Thickness

The spectrogram plots allow for a qualitative assessment of a raceway film for a given time, but it is hard to comprehend the full lubrication picture from these. A script that automates the processing of raw ultrasonic reflections into film thickness has been created and introduced in Chapter 9. Initially, the signal is discretised into contact inlet and outlet regions as this is where the resonance method is applicable. Resonant film thickness calculations are then applied to these two areas.

One of the main project difficulties was in this automation and detection of resonances, as their amplitudes are very shallow and noise artefacts outside of a reasonable bandwidth can be interpreted as usable resonances without caution, discussed in Section 9.3.1. The detection was solved by a series of peak detection runs that use several passes to filter out dips due to noise and highlight the repeatable resonance, applied to a restrictive -6db bandwidth. This reflection discretisation and measurement automation has allowed for a comprehensive insight into the raceway film thickness within a rolling bearing during oil and grease lubrication, without lubricant mechanism altering intrusion. This means the measurement method developed in this thesis is practically applicable to large rolling element bearings in the field.

12.2.4 Raceway Lubricant Flow

For both oils tested, at low load there was a clear 'U' shape pattern to the inlet film, with thicker reservoirs of oil towards the roller end faces and a thinner central region. This characteristic of side reservoirs has been highlighted in single contact and modelling work, but the results presented in this thesis are the first in-situ measurements which confirm the mechanism is still apparent in full-scale cylindrical rolling element bearings. It is also the first observation performed of any bearing that is fully metallic. Comparing the two oils, the more viscous oil generally formed a thicker film right the way across the rolling axis. When the load was increased on the bearing this 'U' shape was lost, and a more linear increase from one face to another formed. In Chapter 6 a skew magnitude change was seen with increasing load, and this is the likely cause of the film shape change.

Analysing the mean frontal film change, a generally increasing trend was seen with viscosity, bearing speed and load. However, due to space restriction in the rig meaning only seven sensors could be instrumented, the result can not be deemed statistically significant from this work alone due to a comparatively large standard error. The increase with viscosity and speed is likely due to the capillary affects and entrainment velocity respectively. With the thinner of the two oils the raceway film thickness increase with speed was constant. However, the more viscous oil initially increased with speed before presenting a decreasing trend above $18,600\mathrm{nd_m}$. The cause of this pattern is likely the impaired reflow due to the increased viscosity at higher speeds, and the trend is potentially a precursor to contact starvation. It is feasible that the skew change and increased roller-flange scrape effect is the cause for the increase thickness due to load.

Grease is time dependent, with the most chaotic lubrication period during the initial running stage, where the grease is churned or said to be 'broken-in'. During this churning phase, the results in Chapter 10 show there is a redistribution of lubricant across the axis at the contact inlet. For all churn tests, spectrograms of film thickness across the rolling axis clearly show the grease channelling mechanism, which has been highlighted as the first sub-phase of the churning process by Chatra et al. [35, 55, 166]. Previously, this channelling mechanism has been described/observed via temperature change of the bearing. This work shows the first in-situ observation of the grease distribution forming these channels during churn.

For lower bearing speeds of $6,200\mathrm{nd_m}$ and $12,400\mathrm{nd_m}$ there was a redistribution of grease from large side reservoirs, similar to those seen for oil, to a more uniform distribution, although there was still a 'U' shape pattern to the data. It is likely that thicker channelled ridges were still present, but were out of the sensing area in the un-swept zones. At the lower test speeds there was no change in the mean frontal film thickness during churn, just a redistribution of grease.

At the higher bearing speeds of $18,600\mathrm{nd_m}$, $24,800\mathrm{nd_m}$ and $31,000\mathrm{nd_m}$ a similar redistribution was seen, but also apparent was a drop in the mean thickness across the rolling axis, meaning there was less lubricant available over prolonged running of the bearing. For the quickest two speeds tested, the decrease is not continuous, and ends with a period of semi-stabilisation around $\overline{h_{raceway}} \approx 350\mu\mathrm{m}$ for both speeds. However the highest speed tested shows a greater undulation in the film thickness, with the film dropping to $\overline{h_{raceway}} = 330\mu\mathrm{m}$, a maximum mean frontal decrease of 22.9% when compared with the thickest film in the early stages. The highest speed case mean thickness, shown in Figure 10.20b, interestingly has a very similar pattern to the three zones of grease lubrication identified by Cann et al. [110] for fresh grease being worked in a single contact. The fact that inlet pattern matches the pattern of film thickness within the contact indicates some governance by the supply film.

12.2.5 Calculated Meniscus Position and Starvation Ratio

The meniscus position is defined as the location where contact pressure can begin to develop, and occurs where the roller and raceway film join at the inlet location. The roller film is governed by the EHL contact film thickness and the rupture ratio, which is based on the amount of roller slip, both of which can be theoretically calculated. Therefore, by measuring the raceway film thickness, the meniscus length can be calculated by determining the position that the summation of the roller and raceway films match the separation of the roller and raceway. This thesis has introduced a Volume Fill Model where the position of the inlet meniscus is determined from the meniscus height using the numerical Newton-Raphson method. This model, combined with the in-situ raceway film thickness method developed in this thesis, allows for the calculation of the meniscus position and thus a starvation level to be determined by comparing the position to the theoretical Hertzian contact half width.

For the oil lubricated bearing the rolling contact was fully flooded for all operating conditions and both viscosity oils tested. However, the method developed is capable of measuring thinner films at which starvation would occur, but such films were not re-creatable with the oils used and rig limitations. In this work the starvation ratio had minimal dependence on the bearing speed. Quicker rates of rotation only had a small increase on the raceway thickness for lower speeds; at higher bearing speeds there was a decrease in film thickness with the thicker oil due to impaired reflow, but the speed was not severe enough to cause starvation. With quicker bearing rotation rates that would further impair lubricant reflow, it is assumed that the speed would have much more influence.

Under increasing loads there is a slight increase in raceway thickness, likely due to internal skew and scraping effects, and thus the meniscus position moves away from the contact centre. However, as there is an increase in the contact size, heavy loads drastically decrease the s/b and push the bearing towards starvation. Therefore, at lower bearing speeds, load is a primary governor of starvation as higher loaded bearings have larger contact areas and thus require longer menisci to develop the adequet contact pressure.

For the grease churn tests the bearing was fully flooded on the whole. This is to be expected as the fresh grease is still swamping the contact in this churning phase. However, Figures 10.15 to 10.20 show NaN values where there are potentially periods of starvation within an otherwise well lubricated condition. For the quicker bearing speeds there is a decay of the mean frontal inlet thickness during churn. As the load is constant during the tests this leads to a reduction in the starvation ratio over the same time, see Figure 10.21.

12.3 Novelty Statement

The novelty of this thesis is in developing an ultrasonic resonance method to measure raceway films in-situ with both oil and grease lubrication. No prior work has been able to measure this film in-situ without serious modifications to bearing rigs such as making raceways out of transparent, unrealistic to the field materials. This allowed for the in-situ measurement of the meniscus position, and thus determination of the starvation ratio, in both oil and greased bearings. With grease lubrication the phenomenon of channelling and clearing was observed. This work therefore provides a research foundation to develop on for future in-situ monitoring technologies.

Results suggest that within this thesis starvation was not repeatedly achievable. However, a trend of decreasing contact inlet film thickness has been observed which could be a pre-cursor to contact starvation. This is a novel observation and could provide the foundation of a starvation sensor. A set of new equations have been developed which practically can be used to assess and understand the requirements for fully flooded conditions.

12.4 Future Work

The work presented in this thesis demonstrates the capability of ultrasonic sensors to in-situ monitor the previously unmeasurable raceway film thickness, and from this determine the position of the inlet meniscus. This has allowed the distribution of oils and grease to be viewed across the rolling contact as the bearing is running. There are limitations to the research and areas that require further investigation. These are some suggestions of future work packages to continue this research:

1. With the raceway measurements it is noticeable that the resonant dips have a lower amplitude than the validation experiments. This is caused by an uneven film thickness across the sensing area, the use of a live modal reference instead of an air reference and thick film presence which reduces the number of echoes. There are three main ways to improve this amplitude; firstly by using steered beam sensors which reduce the measurement area and thus reduce film deviation over the sensor area. Secondly, a standing wave method such as the one described by Kanja et al. [172] could be implemented to create a continuous resonance, thus increasing the echo number through the film. Thirdly, using an air reference over an operable temperature range. All of these suggestions should be explored in future work.

2. The resonant approach would benefit from a larger investment of time into researching how different material properties are related to the acoustic velocity and frequency of resonances. For grease specifically, research should focus on oil bleed and thickener breakdown. For oil, the effect of aeration and degradation should be investigated. For both lubricant types, the effect of material property deviation over the sensing area is of primary importance, including film thickness variation and temperature gradients through measured lubricant layers.

3. A large sensor bandwidth is crucial in detecting multiple resonances which improves the accuracy of film thickness measurements. Additionally, higher frequency bandwidths can capture single resonances of much thinner oil films,

increasing the limits of the resonance approach. Better backing materials and potting compounds which have superior damping should be investigated to increase the bandwidth of a single sensor. A second approach would be to use a sensor pair with close central frequencies, such as a 5MHz and 10MHz, which will have overlapping bandwidths and 'stitch' the bandwidths together in post-processing. However, this has a drawback that the two sensors do not occupy the same spacial location.

4. Section 9.3.4 of Chapter 9 details how the mean film thickness is used to determine raceway thickness, which then leads to the inference of the meniscus location. However, some raceway patterns show a gradient to the film, such as the one in Figure 9.6. Therefore, the meniscus detection point could theoretically be improved upon by determining the linear gradient of the meniscus line, and using a numerical model to calculate where the roller and raceway films would join.

5. The focus of this thesis was to develop a method to measure raceway films in-situ, to which the work has been a success. A limitation of the project is that time was focused into method development, and so conclusions on oil and grease flow are based on a limited number of lubricants and test repeats. Literature has shown that base oil types, thickener types, thickener ratios and additive packages can all affect the lubricating properties. An obvious continuation of this research is in investigating how all of these properties affect the oil flow and grease distribution in both the churning phase and over an extended period of time by trialling a larger number of lubricants.

6. Future research would benefit from a bearing rig with temperature control and more in-situ temperature recording positions. Temperature control would allow the viscosity of lubricants to be manipulated over a temperature spectrum, as well as allow for a better comparison between lubricants by operating at certain, defined temperatures. More in-situ sensing locations would allow a better picture for lubricant temperature to be recorded through the bearing, enabling a more accurate calculation of lubricant acoustic velocity and thus film thickness. Secondary to this, the process of grease churn could also be better monitored.

7. In Section 10.3 of Chapter 10, equations 10.8, 10.11, 10.16 and 10.20 give critical film thicknesses and loads that relate to fully flooded or starved contacts where

zero reverse flow is achieved. In this body of work, all contacts were measured as being fully flooded and so these theoretical values could not be tested. With new research making use of transparent material bearings, such as that presented by Chen et al. [11], these theoretical limits could be validated. Doing so would add further confidence to the practical lubrication limits to achieve fully flooded conditions.

8. For greased tests, the churn time was based on *The Timken Co.* temperature assessment for churning greases. Chatra & Lugt [55] mark the end of churning by the sudden transition of the clearing phase to the bleeding phase, and in [166] it is suggested that the end of churn could be characterised by a homogeneity of yield stress around the bearing, which temperature measurements are potentially not sensitive to. Ideally then, the bearing tests completed in this thesis of work should be repeated, but run for much longer durations to ensure that the grease has truly finished the churning phase, which should be quantified with rheological measurements.

9. Using seven sensors along the rolling axis gives a relatively coarse discretisation of lubricant flow conditions. Future work could develop sensor arrays, increasing the measurement point by an order of magnitude and giving a more insightful picture of lubricant distribution. The excitation and recording of these sensors would require an oscilloscope of higher sampling rate and increased channel number, but such devices have reduced in price recently.

10. An obvious future step would be to instrument bearings of different rolling element shapes, cage designs and load directions to understand their influence on lubricant distribution. This could progress to a field bearing with the intention of measuring the raceway film thickness during the normal daily cycle. Mechanisms such as wind turbine stop-start events could be then assessed based on their impact on lubrication state, allowing for greater knowledge gain of in-situ lubricant state and potentially wear mechanisms.

Appendix A

Appendix

A.1 Resonance Detection Script

The purpose of this function is to detect the resonant frequencies from a reflection, and separate the resonances from signal noise.

The peak detection algorithm includes peak width, as this is a key indicator of a resonance and not noise, and amplitude

There are now 3 peak detection sweeps so that the calculation becomes more accrate with every pass

This function receives an input signal of reflection coefficient across an entire frequency spectrum and detects if there are resonant dips present, how many there are, and if there are 2 or more, what

input

x = R in frequency spectrum B = bandwidth

output

y = 2F0

```
function y = Detect_2f0(x,B)

sampleinv = x*-1; %Inverse sample so dips become peaks
sampleinv = sampleinv+abs(min(sampleinv)); %Baseline correct

%first peak detection pass

[PKS, LOCS, W, P] = findpeaks(sampleinv);
if isempty(PKS)==1
    y=nan;
else

    %second peak detection pass

    MPP = 0.001; %minimum Peak Prominence was 0.005, 0.0001, 0.001 for oil, 0.005 for grease
    MPW = 0.1*max(W);;
    MPH= 0.1*max(PKS);


    [pks,locs,widths,proms] = findpeaks(sampleinv,...
        'MinPeakProminence',MPP, 'MinPeakHeight',MPH, 'MinPeakWidth',MPW);

    %third peak detection pass

    MPD= 10;

    [pks,locs,widths,proms] = findpeaks(sampleinv,...
        'MinPeakProminence',MPP, 'MinPeakHeight',MPH, 'MinPeakWidth',MPW,...
        'MinPeakDistance',MPD);

    LocVar = numel(locs); %number of locations

    a = ge(LocVar,2) & le(LocVar,10);

    if a==1
        peakInterval = diff(locs);
        FreqModeVal = B(locs);
        DiffFreqModeVal = diff(FreqModeVal); %calculate difference in resonant frequencies
        Rout = isoutlier(DiffFreqModeVal);
        DiffFreqModeVal(Rout)=[]; %delete outlier values
        y = mean(DiffFreqModeVal); %Mean resonant frequency jump
    else
        y = nan;
    end

end
end
```

Figure A.1: Matlab script developed to detect resonances on bearing raceways. A series of peak passes show how noise is filtered to reduce the chance of a false detection

References

[1] W. Guorong, J. Long, H. Xia, Z. Lin, Y. Changhai, Z. Min, and C. Fei. Effect of rectangular surface texture on tribology properties of beryllium bronze/20CrNiMo under different loads. *J. Balk. Tribol. Assoc.*, 21(2):329–338, 2015.

[2] S. Aihara and D. Dowson. A study of film thickness in grease lubricated elastohydrodynamic contacts. In *5th Leeds-Lyon Symp. Tribol.*, pages 104–115, London, 1978. Mechanical Engineering Publications.

[3] P. E. Wolveridge, K. P. Baglin, and J. F. Archard. The Starved Lubrication of Cylinders in Line Contact. *Proc. Inst. Mech. Eng.*, 185(1):1159–1169, jun 1970.

[4] B. J. Hamrock and D. Dowson. Isothermal Elastohydrodynamic Lubrication of Point Contacts: Part 1—Theoretical Formulation. *J. Lubr. Technol.*, 98(2):223–228, apr 1976.

[5] P. Svoboda, D. Kostal, I. Krupka, and M. Hartl. Experimental study of starved EHL contacts based on thickness of oil layer in the contact inlet. *Tribol. Int.*, 67:140–145, 2013.

[6] F. Chevalier, A. A. Lubrecht, P. M. E. Cann, F. Colin, and G. Dalmaz. Starved Film Thickness: a Qualitative Explanation. In D. Dowson, C. M. Taylor, T. H. C. Childs, and G. Dalmaz, editors, *Lubr. Lubr.*, volume 30 of *Tribology Series*, pages 249–257. Elsevier, 1994.

[7] F. Chevalier, A. A. Lubrecht, P. M. E. Cann, F. Colin, and G. Dalmaz. Starvation Phenomena in E.H.L. Point Contacts: Influence of Inlet Flow Distribution. In D. Dowson, C. M. Taylor, T. H. C. Childs, G. Dalmaz, Y. Berthier, L. Flamand, J. M. Georges, and A. A. Lubrecht, editors, *Third Body Concept Interpret. Tribol. Phenom.*, volume 31 of *Tribology Series*, pages 213–223. Elsevier, 1996.

[8] F. Chevalier, A. A. Lubrecht, P. M.E. Cann, F. Colin, and G. Dalmaz. Film thickness in starved EHL point contacts. *J. Tribol.*, 120(1):126–133, 1998.

[9] D. Kostal, P. Sperka, P. Svoboda, I. Krupka, and M. Hartl. Influence of Lubricant Inlet Film Thickness on Elastohydrodynamically Lubricated Contact Starvation. *J. Tribol.*, 139(5):1–6, 2017.

[10] D. Kostal, P. Sperka, I. Krupka, and M. Hartl. Experimental comparison of the behavior between base oil and grease starvation based on inlet film thickness. *Tribol. Ind.*, 39(1), 2017.

[11] H. Chen, W. Wang, H. Liang, and X. Ge. Observation of the oil flow in a ball bearing with a novel experiment method and simulation. *Tribol. Int.*, 174(June):107731, 2022.

[12] M. Chennaoui, M. Fowell, H. Liang, and A. Kadiric. A Novel Set-Up for In Situ Measurement and Mapping of Lubricant Film Thickness in a Model Rolling Bearing Using Interferometry and Ratiometric Fluorescence Imaging. *Tribol. Lett.*, 70(3):1–17, 2022.

[13] Energy & Industrial Strategy Uk government: Department for Business. National Statistics Energy Trends: renewables. Technical report, Department for Business, Energy & Industrial Strategy, 2020.

[14] Global wind energy council. Annual Wind Report. Technical report, Global Wind Energy Council, 2022.

[15] Office of Energy Efficiency & Renewable Energy. Wind Turbines: the Bigger, the Better — Department of Energy, 2021.

[16] M. N. Kotzalas and G. L. Doll. Tribological advancements for reliable wind turbine performance. *Philos. Trans. R. Soc. A Math. Phys. Eng. Sci.*, 368(1929):4829–4850, 2010.

[17] W. Musial, S. Butterfield, and B. Mcniff. Improving wind turbine gearbox reliability. *Eur. Wind Energy Conf. Exhib. 2007, EWEC 2007*, 3:1770–1779, 2007.

[18] T. Bruce, E. Rounding, H. Long, and R. S. Dwyer-Joyce. Characterisation of white etching crack damage in wind turbine gearbox bearings. *Wear*, 338-339:164–177, 2015.

[19] S. Faulstich, B. Hahn, and P. J. Tavner. Wind turbine downtime and its importance for offshore deployment. *Wind Energy*, 14(3):327–337, apr 2011.

[20] T. A. Harris and M. N. Kotzalas. *Essential Concepts of Bearing Technology.* CRC Press, 1000 20th Street, Bellingham, WA 98227-0010 USA, oct 2006.

[21] Z. Liu and L. Zhang. A review of failure modes, condition monitoring and fault diagnosis methods for large-scale wind turbine bearings. *Meas. J. Int. Meas. Confed.*, 149:107002, 2020.

[22] M. H. Evans. White structure flaking (WSF) in wind turbine gearbox bearings: Effects of 'butterflies' and white etching cracks (WECs). *Mater. Sci. Technol.*, 28(1):3–22, 2012.

[23] M. H. Evans. An updated review: white etching cracks (WECs) and axial cracks in wind turbine gearbox bearings. *Mater. Sci. Technol. (United Kingdom)*, 32(11):1133–1169, 2016.

[24] T. A. Harris and M. N. Kotzalas. *Advanced Concepts of Bearing Technology.* CRC Press, 1000 20th Street, Bellingham, WA 98227-0010 USA, oct 2006.

[25] G. Nayler. *Dictionary of Mechanical Engineering.* SAE International, Warrendale, PA, feb 1996.

[26] SKF. Bearing damage and failure analysis. *SKF-the Knowl. Eng. Co.*, 2017.

[27] SKF. NU 2244 ECML.

[28] SKF. *Rolling bearings.* SKF, 2018.

[29] H. Hertz. On the contact of rigid elastic solids and on hardness. In *Misc. Pap.*, pages 163–183. MacMillan and CO., LTD, London, 1896.

[30] M. MacHado, P. Moreira, P. Flores, and H. M. Lankarani. Compliant contact force models in multibody dynamics: Evolution of the Hertz contact theory. *Mech. Mach. Theory*, 53:99–121, 2012.

[31] K. L. Johnson. ONE HUNDRED YEARS OF HERTZ CONTACT. *Proc. Inst. Mech. Eng.*, 196:363–378, 1982.

[32] K. Radil, S. Howard, and B. Dykas. The role of radial clearance on the performance of foil air bearings. *Tribol. Trans.*, 45(4):485–490, 2002.

[33] G. Gao, Z. Yin, D. Jiang, and X. Zhang. Numerical analysis of plain journal bearing under hydrodynamic lubrication by water. *Tribol. Int.*, 75:31–38, 2014.

[34] T. Tevrüz. Tribological behaviours of carbon filled polytetrafluoroethylene (PTFE) dry journal bearings. *Wear*, 221(1):61–68, 1998.

[35] S. C. KR and P. M. Lugt. Channeling behavior of lubricating greases in rolling bearings: Identification and characterization. *Tribol. Int.*, 143(July 2019):106061, mar 2020.

[36] J. Fitch. The Enduring Grease vs . Oil Debate In Favor of Grease In Favor of Oil. *Mach. Lubr.*, 2006.

[37] LANXESS. Grease versus Oil - which one to use for lubrication.

[38] J. A. Williams. *Engineering Tribology.* Cambridge University Press, 2005.

[39] G.W. Stachowiak and A.W. Batchelor. *Engineering Tribology.* Elsevier, 1993.

[40] A. N. Grubin. *Investigation of the contact of machine components.* Central Scientific Research Institute for Technology and Mechanical Engineering, Moscow, 1949.

[41] D. Dowson. The inlet boundary condition. pages 143–152, 1974.

[42] D. Dowson and A. Toyoda. A central film thickness formula for ehd line contacts. In *Proc. 5th Leeds-Lyon Symp.*, London, 1978. Mechanical Engineering Publications.

[43] D. Dowson and G. R. Higginson. A Numerical Solution to the Elasto-Hydrodynamic Problem. *J. Mech. Eng. Sci.*, 1(1):6–15, jun 1959.

[44] D. Dowson and G. R. Higginson. The Effect of Material Properties on the Lubrication of Elastic Rollers. *J. Mech. Eng. Sci.*, 2(3):188–194, 1960.

[45] D. Dowson and G. R. Higginson. New Roller-Bearing Lubrication Formula. Technical report, 1961.

[46] D. Dowson, G. R. Higginson, and A. V. Whitaker. Elasto-Hydrodynamic Lubrication: A Survey of Isothermal Solutions. *J. Mech. Eng. Sci.*, 4(2):121–126, 1962.

[47] D. Dowson. Paper R1: Elastohydrodynamic Lubrication: An Introduction and a Rexview of Theoretical Studies. *Proc. Inst. Mech. Eng. Conf. Proc.*, 180(2):7–16, 1965.

[48] B. J. Hamrock and D. Dowson. Isothermal Elastohydrodynamic Lubrication of Point Contacts: Part II—Ellipticity Parameter Results. *J. Lubr. Technol.*, 98(3):375–381, jul 1976.

[49] B. J. Hamrock and D. Dowson. Isothermal Elastohydrodynamic Lubrication of Point Contacts: Part III—Fully Flooded Results. *J. Lubr. Technol.*, 99(2):264–275, apr 1977.

[50] A. W. Crook. The Lubrication of Rollers II . Film Thickness with Relation to Viscosity and Speed. *Philos. Trans. R. Soc. London*, 254(1040):223–236, 1961.

[51] P. M. Cann, B. P. Williamson, R. C. Coy, and H. A. Spikes. The behaviour of greases in elastohydrodynamic contacts. *J. Phys. D. Appl. Phys.*, 25(1):A124–A132, 1992.

[52] National Lubricating Grease Institute. *Lubricating Grease Guide.* National Lubricating Grease Institute, Kansas, 2nd edition.

[53] R S Components Ltd. Everything You Need To Know About Greases — RS Components — RS Components.

[54] P. M. Lugt. *Grease Lubrication In Rolling Bearings.* John Wiley & Sons, Ltd, 2013.

[55] S. C. KR and P. M. Lugt. The process of churning in a grease lubricated rolling bearing: Channeling and clearing. *Tribol. Int.*, 153(September 2020):106661, 2021.

[56] H. Cen, P. M. Lugt, and G. Morales-Espejel. On the Film Thickness of Grease-Lubricated Contacts at Low Speeds. *Tribol. Trans.*, 57(4):668–678, 2014.

[57] P. M. Lugt, S. Velickov, and J. H. Tripp. On the chaotic behaviour of grease lubrication in rolling bearings. *Tribol. Trans.*, 52(5):581–590, 2009.

[58] A. Rezasoltani and M. M. Khonsari. On monitoring physical and chemical degradation and life estimation models for lubricating greases. *Lubricants*, 4(3), 2016.

[59] S. C. KR, J. A. Osara, and P. M. Lugt. Impact of grease churning on grease leakage, oil bleeding and grease rheology. *Tribol. Int.*, 176(September):107926, 2022.

[60] H. Cen and P. M. Lugt. Film thickness in a grease lubricated ball bearing. *Tribol. Int.*, 134(January):26–35, 2019.

[61] Piet M. Lugt, Marco T. van Zoelen, Charlotte Vieillard, Frank Berens, Robert Gruell, Gerwin Preisinger, and Paul Meaney. Grease Performance in Ball and Roller Bearings for All-Steel and Hybrid Bearings. *Tribol. Trans.*, 65(1):1–13, 2021.

[62] N. Xu, X. Wang, R. Ma, W. Li, and M. Zhang. Insights into the rheological behaviors and tribological performances of lubricating grease: Entangled structure of a fiber thickener and functional groups of a base oil. *New J. Chem.*, 42(2):1484–1491, 2018.

[63] ExxonMobil. Understanding oil bleed and grease separation, 2017.

[64] B. Damiens, A. A. Lubrecht, and P. M. Cann. Influence of Cage Clearance on Bearing Lubrication. *Tribol. Trans.*, 47(1):2–6, 2004.

[65] W. J. Bartz. *Schmierfette, Zusammensetzung, Eigenschaften, Prüfung undAnwendung*. Expert-Verlag, Renningen-Malmsheim, 2000.

[66] T. Cousseau, B. Graça, A. Campos, and J. Seabra. Experimental measuring procedure for the friction torque in rolling bearings. *Lubr. Sci.*, 22(4):133–147, apr 2010.

[67] T. Cousseau, M. Björling, B. Graça, A. Campos, J. Seabra, and R. Larsson. Film thickness in a ball-on-disc contact lubricated with greases, bleed oils and base oils. *Tribol. Int.*, 53:53–60, 2012.

[68] L. Huang, D. Guo, and S. Wen. Starvation and Reflow of Point Contact Lubricated with Greases of Different Chemical Formulation. *Tribol. Lett.*, pages 483–492, 2014.

[69] S. Y. Poon. An Experimental Study of Grease in Elastohydrodynamic Lubrication. *J. Lubr. Technol.*, 94(1):27–34, jan 1972.

[70] P. M. Cann. Starvation and reflow in a grease-lubricated elastohydrodynamic contact. *Tribol. Trans.*, 39(3):698–704, 1996.

[71] S. Hurley and P. M. Cann. IR Spectroscopic Analysis of Grease Lubricant Films in Rolling Contacts. In D. Dowson, M. Priest, C. M. Taylor, P. Ehret, T. H. C. Childs, G. Dalmaz, Y. Berthier, L. Flamand, J.-M. Georges, and A. A. Lubrecht, editors, *Lubr. Front.*, volume 36 of *Tribology Series*, pages 589–600. Elsevier, 1999.

[72] J-S. Mérieux, S. Hurley, A. A. Lubrecht, and P. M. Cann. Shear-degradation of grease and base oil availability in starved EHL lubrication. In D Dowson, M Priest, C M Taylor, P Ehret, T H C Childs, G Dalmaz, A A Lubrecht, Y Berthier, L Flamand, and J.-M. Georges, editors, *Thinning Film. Tribol. Interfaces*, volume 38 of *Tribology Series*, pages 581–588. Elsevier, 2000.

[73] O. Saita. Evaluation of greases contributing to maintenance interval extension of shinkansen's traction motor. *NLGI Spokesm.*, 73(5):38, 2009.

[74] W. S. Zhu and Y. T. Neng. A theoretical and experimental study of EHL lubricated with grease. *Trasnactions ASME*, 110, 1987.

[75] Y. Kanazawa, R. S. Sayles, and A. Kadiric. Film formation and friction in grease lubricated rolling-sliding non-conformal contacts. *Tribol. Int.*, 109(January):505–518, 2017.

[76] P. M. Cann. Starved grease lubrication of rolling contacts. *Tribol. Trans.*, 42(4):867–873, 1999.

[77] B. Allison and A. Pandkar. Critical factors for determining a first estimate of fatigue limit of bearing steels under rolling contact fatigue. *Int. J. Fatigue*, 117(March):396–406, 2018.

[78] NDT Resource Centre. Wave Propagation.

[79] J. Krautkramer and H. Krautkramer. Ultrasonic Testing of Materials, 2012.

[80] J. A. Gallego-Juárez and K. F. Graff. *Power Ultrasonics : Applications of High-Intensity Ultrasound.* Elsevier, 66 edition, 2014.

[81] K. J. Langenberg, R. Marklein, and K. Mayer. *Ultrasonic Nondestructive Testing of Materials: Theoretical Foundations.* Taylor & Francis, 2012.

[82] D. M. Egle and D. E. Bray. Measurement of acoustoelastic and third-order elastic constants for rail steel. *J. Acoust. Soc. Am.*, 60(3):741–744, 1976.

[83] G. S. Schajer. *Practical Residual Stress Measurement Methods*. John Wiley & Sons, incorporated, 2013.

[84] R. S. Dwyer-Joyce, B. W. Drinkwater, and C. J. Donohoe. The measurement of lubricant- Film thickness using ultrasound. *Proc. R. Soc. A Math. Phys. Eng. Sci.*, 459(2032):957–976, 2003.

[85] K. Kendall and D. Tabor. An Ultrasonic Study of the Area of Contact between Stationary and Sliding Surfaces. *Proc. R. Soc. London, Ser. A*, 323(1554):321–340, 1971.

[86] T. R. Thomas and R. S. Sayles. Stiffness of Machine Tool Joints : A Random-Process Approach. *ASME J. Eng. Ind.*, 99(1):250–256, 1977.

[87] H. G. Tattersall. The ultrasonic pulse-echo technique as applied to adhesion testing. *J. Phys. D. Appl. Phys.*, 6(7):305, may 1973.

[88] B. W. Drinkwater, R. S. Dwyer-Joyce, and P. Cawley. A study of the interaction between ultrasound and a partially contacting solid-solid interface. *Proc. R. Soc. A Math. Phys. Eng. Sci.*, 452(1955):2613–2628, 1996.

[89] R. S. Dwyer-Joyce, T. Reddyhoff, and J. Zhu. Ultrasonic Measurement for Film Thickness and Solid Contact in Elastohydrodynamic Lubrication. *J. Tribol.*, 133(3):031501, 2011.

[90] B. Hosten. Bulk heterogeneous plane waves propagation through viscoelastic plates and stratified media with large values of frequency domain. *Ultrasonics*, 29(6):445–450, 1991.

[91] S. S. Bair. *High Pressure Rheology for Quantitative Elastohydrodynamics*. Elsevier, 2007.

[92] R. S. Dwyer-Joyce, P. Harper, and B. W. Drinkwater. A method for the measurement of hydrodynamic oil films using ultrasonic reflection. *Tribol. Lett.*, 17(2):337–348, 2004.

[93] L. M. Brekhovskikh. *Waves in layered media*. Academic Press, New York ; London, 1960.

[94] N. F. Haines, J. C. Bell, and P. J. McIntyre. The application of broadband ultrasonic spectroscopy to the study of layered media. *J. Acoust. Soc. Am.*, 64(6):1645–1651, 1978.

[95] L. E. Kinsler, A. R. Frey, A. B. Coppens, and S. V. Sanders. *Fundamentals of Acoustics*. John Wiley & Sons, Incorporated, 2000.

[96] T. E. G. Alvarez-Arenas. Acoustic Impedance Matching of Piezoelectric. *IEEE Trans. Ultrason. Ferroelectr. Freq. Control*, 51(5):624–633, 2004.

[97] M. Schirru, R. Mills, R. S. Dwyer-Joyce, O. Smith, and M. Sutton. Viscosity Measurement in a Lubricant Film Using an Ultrasonically Resonating Matching Layer. *Tribol. Lett.*, 60(3):1–11, 2015.

[98] T. Pialucha, C. C. H. Guyott, and P. Cawley. Amplitude spectrum method for the measurement of phase velocity. *Ultrasonics*, 27(5):270–279, 1989.

[99] P. Dou, T. Wu, Z. Luo, Z. Peng, and T. Sarkodie-Gyan. The application of the principle of wave superposition in ultrasonic measurement of lubricant film thickness. *Meas. J. Int. Meas. Confed.*, 137:312–322, 2019.

[100] NDT Resource Centre. Radiated Fields of Ultrasonic Transducers.

[101] NDT Resource Centre. Transducer Beam Spread.

[102] P. Dou, Y. Jia, T. Wu, Z. Peng, M. Yu, and T. Reddyhoff. High-accuracy incident signal reconstruction for in-situ ultrasonic measurement of oil film thickness. *Mech. Syst. Signal Process.*, 156:107669, 2021.

[103] A. Hunter, R. S. Dwyer-Joyce, and P. Harper. Calibration and validation of ultrasonic reflection methods for thin-film measurement in tribology. *Meas. Sci. Technol.*, 23(10), 2012.

[104] A. W. Crook. The Lubrication of Rollers. In *Philos. Trans. R. Soc. London*, volume 250, pages 387–409. 1958.

[105] P. M. Lugt. A review on grease lubrication in rolling bearings. *Tribol. Trans.*, 52(4):470–480, 2009.

[106] L. D. Wedeven, D. Evans, and A. Cameron. Optical Analysis of Ball Bearing Starvation. *J. Lubr. Technol.*, 93(3):349, jul 1971.

[107] A. Cameron and R. Gohar. Theoretical and experimental studies of the oil film in lubricated point contact. *Proc. R. Soc. London. Ser. A. Math. Phys. Sci.*, 291(1427):520–536, apr 1966.

[108] R. Kumar, P. Kumar, and M. Gupta. STARVATION EFFECTS IN ELASTO-HYDRODYNAMICALLY LUBRICATED LINE CONTACTS. *Int. J. Adv. Technol.*, 1(1), 2010.

[109] P. M. E Cann, B. Damiens, and A. A. Lubrecht. The transition between fully flooded and starved regimes in EHL. *Tribol. Int.*, 37(10):859–864, 2004.

[110] P. M. E. Cann, F. Chevalier, and A. A. Lubrecht. Track Depletion and Replenishment in a Grease Lubricated Point Contact: A Quantitative Analysis. *Tribol. Ser.*, 32:405–413, 1997.

[111] Xingnan Zhang and Romeo Glovnea. Grease film thickness measurement in rolling bearing contacts. *Proc. Inst. Mech. Eng. Part J J. Eng. Tribol.*, 235(7):1430–1439, 2021.

[112] W. Lauder. Hydrodynamic Lubrication of Proximate Cylindrical Surfaces of Large Relative Curvature. *Proc. Inst. Mech. Eng. Conf. Proc.*, 180(2):101–112, 1965.

[113] W. Y. Saman. *A Study of Starved Elastohydrodynamic Lubrication with Particular Reference to Gyroscope Bearings.* University of Leeds (Department of Mechanical Engineering), 1974.

[114] H. G. Elrod. A cavitation algorithm. *Trans. ASME*, 103(July), 1980.

[115] B. Damiens, C. H. Venner, P. M. E. Cann, and A. A. Lubrecht. Starved lubrication of elliptical EHD contacts. *J. Tribol.*, 126(1):105–111, 2004.

[116] H. Moes. *Lubrication and Beyond.* Twente University Press, Twente, 2000.

[117] Y. P. Chiu. An Analysis and Prediction of Lubricant Film Starvation in Rolling Contact Systems. *Tribol. Trans.*, 17(1):22–35, 1974.

[118] M. T. van Zoelen, C. H. Venner, and P. M. Lugt. Free surface thin layer flow on bearing raceways. *J. Tribol.*, 130(2):1–10, 2008.

[119] M. T. van Zoelen, C. H. Venner, and P. M. Lugt. Prediction of film thickness decay in starved elasto-hydrodynamically lubricated contacts using a thin layer flow model. *Proc. Inst. Mech. Eng. Part J J. Eng. Tribol.*, 223(3):541–552, 2009.

[120] V. Bruyere, N. Fillot, G. E. Morales-Espejel, and P. Vergne. A two-phase flow approach for the outlet of lubricated line contacts. *J. Tribol.*, 134(4):1–10, 2012.

[121] D. Koštál, D. Nečas, P. Šperka, P. Svoboda, I. Křupka, and M. Hartl. Lubricant Rupture Ratio at Elastohydrodynamically Lubricated Contact Outlet. *Tribol. Lett.*, 59(3):1–9, 2015.

[122] N. Marx, J Guegan, and H. A. Spikes. Elastohydrodynamic film thickness of soft EHL contacts using optical interferometry. *Tribol. Int.*, 99:267–277, 2016.

[123] H. Cen and P. M. Lugt. Replenishment of the EHL contacts in a grease lubricated ball bearing. *Tribol. Int.*, 146(September 2019):106064, 2020.

[124] K. Sakai, Y. Ayame, Y. Iwanami, N. Kimura, and Y. Matsumoto. Observation of grease fluidity in a ball bearing using neutron imaging technology, 2021.

[125] P. Dou, Y. Jia, P. Zheng, T. Wu, M. Yu, T. Reddyhoff, and Z. Peng. Review of ultrasonic-based technology for oil film thickness measurement in lubrication. *Tribol. Int.*, 165(August 2021):107290, 2022.

[126] Z. Q. Chen, J. C. Hermanson, M. A. Shear, and P. C. Pedersen. Ultrasonic monitoring of interfacial motion of condensing and non-condensing liquid films. *Flow Meas. Instrum.*, 16(6):353–364, 2005.

[127] Y. A. Al-Aufi, B. N. Hewakandamby, G. Dimitrakis, M. Holmes, A. Hasan, and N. J. Watson. Thin film thickness measurements in two phase annular flows using ultrasonic pulse echo techniques. *Flow Meas. Instrum.*, 66(January):67–78, 2019.

[128] H. J. Park, Y. Tasaka, and Y. Murai. Ultrasonic pulse echography for bubbles traveling in the proximity of a wall. *Meas. Sci. Technol.*, 26(12), 2015.

[129] H. Tohmyoh and M. Suzuki. Measurement of the coating thickness on the back side of double-sided coated structures by means of acoustic resonant spectroscopy. *Surf. Coatings Technol.*, 204(4):546–550, 2009.

[130] S. Beamish and R. S. Dwyer-Joyce. Measuring Oil Films in Dynamically Loaded Journal Bearings via the Ultrasonic Technique. 2015.

[131] S. Beamish. *Oil Film Thickness Measurements in Journal Bearings under Normal , Severe & Dynamic Loading Conditions using Ultrasound*. PhD thesis, The University of Sheffield, 2021.

[132] T. Howard. *Development of a Novel Bearing Concept for Improved Wind Turbine Gearbox Reliability*. Phd thesis, University of Sheffield, 2016.

[133] Gary Nicholas. *Development of Novel Ultrasonic Monitoring Techniques for Improving the Reliability of Wind Turbine Gearboxes*. Phd thesis, University of Sheffield, 2021.

[134] M. Schirru and M. Varga. Tribology Letters A review of ultrasonic reflectometry for the physical characterization of lubricated tribological contacts : history , methods , devices , and technological trends. *Tribol. Lett.*, pages 1–22, 2022.

[135] M. K. Wan Ibrahim, D. Gasni, and R. S. Dwyer-Joyce. Profiling a Ball Bearing Oil Film with Ultrasonic Reflection. *Tribol. Trans.*, 55(4):409–421, 2012.

[136] M. Schirru, R. S. Dwyer-Joyce, and L. Vergoz. A new ultrasonic rheometer for space exploration in lander missions. *Rheol. Acta*, 58(1-2):47–61, 2019.

[137] T.A. Harris, M. N. Kotzalas, and W K. Yu. On the causes and effects of roller skewing in cylindrical roller bearings. *Tribol. Trans.*, 41(4):572–578, 1998.

[138] Y. Yang, S. Danyluk, and M. Hoeprich. A study on rolling element skew mearsurement in an tapered roller bearing with a specialized capacitance probe. *J. Tribol.*, 122(3):534–538, 2000.

[139] D. Osorno. *Rolling Element Skew Measurement in a Spherical Roller*. PhD thesis, Georgia Institute of Technology, 2005.

[140] X. Liu, S. Li, P. Yang, and P. Yang. On the lubricating mechanism of roller skew in cylindrical roller bearings. *Tribol. Trans.*, 56(6):929–942, 2013.

[141] X. Liu, D. Song, and P. Yang. On transient EHL of a skew roller subjected to a load impact in rolling bearings. *Key Eng. Mater.*, 739 KEM:108–119, 2017.

[142] G Nicholas, B P Clarke, and R. S. Dwyer-Joyce. Detection of Lubrication State in a Field Operational Wind Turbine Gearbox Bearing Using Ultrasonic Reflectometry. *Lubricants*, 9(1):6, jan 2021.

[143] S. Kihong and J. K. Hammond. *Fundamentals Of Signal Tracking Theory*. John Wiley & Sons, Ltd, 1996.

[144] M. G. Silk. *Ultrasonic Transducers for Nondestructive Testing*. Adam Hilger Ltd, 1984.

[145] P. Harper. *Measurement of Film Thickness in Lubricated Components using Ultrasonic Reflection*. PhD thesis, The University of Sheffield, 2008.

[146] G. Nicholas, T. Howard, H. Long, J. Wheals, and R.S. Dwyer-Joyce. Measurement of roller load, load variation, and lubrication in a wind turbine gearbox high speed shaft bearing in the field. *Tribol. Int.*, (March), 2020.

[147] G. Nicholas, T. Howard, R. S. Dwyer-Joyce, J. Wheals, and D. Benchebra. Direct load measurement of a Wind Turbine High Speed Shaft Bearing in the Field. *1st World Congr. Cond. Monit.*, 0(2):879–886, 2017.

[148] J. Zhu. *Simulation Model and Ultrasound Study for Engineering Interfaces*. PhD thesis, The University of Sheffield, 2012.

[149] B. P. Clarke. *Development of Ultrasonic Techniques for Rolling Element Bearing Monitoring*. PhD thesis, The University of Sheffield, 2022.

[150] J. A. Greenwood and J. B. P. Williamson. Contact of nominally flat surfaces. *Proc. R. Soc. London. Ser. A. Math. Phys. Sci.*, A295(1289):300–319, 1966.

[151] ASTM. D341, 2015.

[152] M. M. Khonsari and E. R. Booser. *Applied Tribology: Bearing Design and Lubrication*. John Wiley & Sons, Incorporated, 2017.

[153] A. A. Lubrecht, C. H. Venner, F. Colin, Université De Lyon, and Université Claude Bernard. Film thickness calculation in elasto-hydrodynamic lubricated line and elliptical contacts : the Dowson , Higginson , Hamrock contribution. *Proc. Inst. Mech. Eng. Part J J. Eng. Tribol.*, 223(3):511–515, 2009.

[154] R. B. Randall and J. Antoni. Rolling element bearing diagnostics-A tutorial. *Mech. Syst. Signal Process.*, 25(2):485–520, 2011.

[155] E. Oberg, F. D. Jones, H. L. Horton, and H. H. Ryffel. *Machinery's Handbook*. Industrial Press, INC., New York, 29 edition, 2012.

[156] TIMKEN. Aerospace Design Guide for Precision Metric Ball and Cylindrical Roller Bearings, 2010.

[157] A. Berni, M. Mennig, and H. Schmidt. *Doctor Blade*, pages 89–92. Springer, 2004.

[158] P. A. Oliveira, R. M. B. Silva, G. C. Morais, A. V. Alvarenga, and R. P. B. Costa-Félix. Speed of sound as a function of temperature for ultrasonic propagation in soybean oil. *J. Phys. Conf. Ser.*, 733(1), 2016.

[159] N. A. Azman and S. B. Abd Hamid. Determining the Time of Flight and Speed of Sound on Different types of Edible Oil. *IOP Conf. Ser. Mater. Sci. Eng.*, 260(1):0–6, 2017.

[160] N. Bilaniuk and G. S. K. Wong. Speed of sound in pure water as a function of temperature. *J. Acoust. Soc. Am.*, 93(3):1609–1612, 1993.

[161] W. Marczak. Water as a standard in the measurements of speed of sound in liquids. *J. Acoust. Soc. Am.*, 102(5):2776–2779, 1997.

[162] MATLAB. findpeaks, 2016.

[163] MATLAB. corrcoef, 2019.

[164] MATLAB. isoutlier, 2017.

[165] A. Cameron. *PRINCIPLES OF LUBRICATION*. Longmans, London, 1966.

[166] S. C. KR, J. A. Osara, and P. M. Lugt. The lubrication mechanism behind the transition from churning to bleeding in grease lubricated bearings – Experimental characterization. *Tribol. Int.*, 183(December 2022):108375, 2023.

[167] SWNS. The steps people are taking to reduce their carbon footprints, 2023.

[168] J. Ambrose. UK plans to bring forward ban on fossil fuel vehicles to 2030, 2020.

[169] M. Waleed Ahmed Abdalglil, F. Dassenoy, M. Sarno, and A. Senatore. A review on potentials and challenges of nanolubricants as promising lubricants for electric vehicles. *Lubr. Sci.*, 34(1):1–29, 2022.

[170] Y. Kwak, C. Cleveland, A. Adhvaryu, X. Fang, S. Hurley, and T. Adachi. Understanding Base Oils and Lubricants for Electric Drivetrain Applications. Technical Report December, Afton Chemical Corporation, 2019.

[171] A. Gupta. *Characterization of Engine and Transmission Lubricants for Electric, Hybrid and Plug-in Hybrid Vehicles*. PhD thesis, The Ohio State University, 2012.

[172] J. Kanja, R. Mills, X. Li, H. Brunskill, A. K. Hunter, and R. S. Dwyer-Joyce. Non-contact measurement of the thickness of a surface film using a superimposed ultrasonic standing wave. *Ultrasonics*, 110, 2021.